TESSELLATED CONTINUUM MECHANICS: VIBRATION OF PERFORATED PLATES

A thesis submitted to The University of Manchester for the degree
of Doctor of Philosophy
in the Faculty of Science and Engineering

2019

Zainab M. Sedqi

School of Mechanical,
Aerospace and Civil Engineering

List of Contents

List of Figures

List of Tables

Nomenclature

B_{ij} Projected viscous damping matrix

$\underline{b}^{\psi}$ Source term

C^{pqrs} Stiffness modulus (N/m)

D Hausdorff fractal dimension

D_o Topology dimension

$\hat{E}_k$ Pre-fractal domain

E Young's modulus (N/m^2)

e Internal energy (J/Kg)

F Jacobian matrix for the hole fill-map

f_t Magnitude of force (N)

J Matrix determinant

$\underline{J}^{\psi}$ Flux term

H Kinetic energy (Kg.(m/sec)^2)

I Second moment of inertia (m^4)

G^{ψ} Invertible scaling matrix

G Shear modulus (N/m^2)

g^{pq} Metric tensor

k Pre-fractal complexity level

$\underline{M}$ Momentum ((m/sec).N)

M Potential energy

M Mass (Kg)

$\underline{n}$ Outward unit normal vector

N Strain energy

P Affine map on the tessellated space

Q Load vector

$\ddot{q}$ Generalised coordinate at mode i (m)

$\underline{r}$ Position vector

S Affine map on the pre-fractal space

$\hat{T}_k$	Corresponding tessellated domain
th	Thickness (m)
t	Time (sec)
u	Displacement vector that represents the components of u, v, w
V^*	Volume (m^3)
x	Coordinate vector that represents the components of x, y, z
X	Coordinate vector of undeformed reference
x	Coordinate vector of deformed reference
α^ψ	Constant scalar
β^k	Constant scalar equal to matrix determinate
Γ^*	Control boundary reference
δ^{ij}	Kronecker delta
$\underline{\underline{\varepsilon}}$	Strain tensor
θ	Slope (deg)
ℓ_o	Initial length on the pre-fractal space (m)
η	Eigenvalue
λ	Frequency constant parameter
μ	Bulk modulus (N/m^2)
ν	Poison's ratio
ρ	Density (Kg/m^3)
$\underline{\underline{\sigma}}$	Cauchy's Stress tensor
τ	Shear vector
ϕ	Coordinate of a point in (x,y,z)
φ	Mode of vibration
ψ	Specific field variable
Ω^*	Control volume reference
ω	Angular frequency

Abbreviations

1-D	One dimensional space
2-D	Two dimensional space
3-D	Three dimensional space
CV	Control volume
DN	Discontinuity Network
FDM	Finite difference method
FEM	Finite element method
FS	Finite Similitude
Fs	Fourier series
FZP	Fresnel zones plate
IFS	Iterated Function System
PDE	Partial differential equation
ps	Pre-fractal space
OWL	Overwhelmingly Large Telescope
TCM	Tessellated Continuum Mechanics
ts	Tessellated space
SEI	Secondary electron imaging

Abstract

An important method for lightening the weight of structures is with the incorporation of perforated materials but a good understanding of their dynamic behaviour is required. The more interesting types of perforated structure in the field of engineering are those representable by fractals. Fractals permit the representation of intricate perforated geometries, but their application is recognised to be beset with difficulties, which stem from an inability to define traditionally derived physical quantities such as stress.

The presented research provides a novel methodology based on transport theory for pre-fractals, which facilitates the modelling of complex perforated structures. This approach is called tessellated continuum mechanics, which has recently been developed at the University of Manchester. Tessellated continuum mechanics is an approach that enables known analytical and numerical continuum solutions to be immediately applied to the fractal space. A feature of the approach is the representation of fractal structures in equivalent continuum spaces, which can be readily analysed by available numerical techniques. The tessellated approach links pre-fractal elements to tiles in a tessellated continuum by means of a hole-fill map; so called because when applied to a perforated structure (i.e. a pre-fractal) it closes all holes to form a tessellation. It is shown in the thesis how pre-fractals and tessellations can be created independently and very efficiently using iterated function schemes. Such schemes when used in tessellated continuum mechanics involve the recursive application of contraction maps and the exact same number of maps is required for forming tessellations and pre-fractals. To accommodate any discontinuous physics that arises on a tessellation it is necessary to imbue it with a discontinuity network. Jumps in displacement, velocity and derivatives are permitted on a discontinuity network.

The research presented in the thesis tests the hypothesis that the dynamic behavior of perforated plates and beams can be analysed to high accuracy on a tessellated continuum. The work also examines the role of similitude, which is an integral feature of the tessellated approach. Similitude enables the physics of a tile on a tessellated continuum to be related to an element of a pre-fractal. In this way it can be demonstrated that a collection of tiles which forms a tessellation has the same behavior as a pre-fractal structure.

The work confirms the validity of tessellated continuum mechanics by means of extensive numerical trials using commercial FE software on pre-fractal beams and plates along with corresponding tessellations.

Declaration

No portion of the work referred to in the thesis has been submitted in support of an application for another degree or qualification of this or any other university or other institute of learning.

Copyright

1. The author of this thesis (including any appendices and/or schedules to this thesis) owns certain copyright or related rights in it (the 'Copyright') and s/he has given The University of Manchester certain rights to use such Copyright, including for administrative purposes.

2. Copies of this research, either in full or in extracts and whether in hard or electronic copy, may be made only in accordance with the Copyright, Designs and Patents Act 1988 (as amended) and regulations issued under it or, where appropriate, in accordance with licensing agreements which the University has from time to time. This page must form part of any such copies made.

3. The ownership of certain Copyright, patents, designs, trademarks and other intellectual property (the 'Intellectual Property') and any reproductions of copyright works in the thesis, for example graphs and tables ('Reproductions'), which may be described in this thesis, may not be owned by the author and may be owned by third parties. Such Intellectual Property and Reproductions cannot and must not be made available for use without the prior written permission of the owner(s) of the relevant Intellectual Property and/or Reproductions.

4. Further information on the conditions under which disclosure, publication and commercialisation of this thesis, the Copyright and any Intellectual Property and/or Reproductions described in it may take place is available in the University IP Policy (see http://documents.manchester.ac.uk/DocuInfo. aspx?DocID=487), in any relevant Thesis restriction declarations deposited in the University Library, The University Library's regulations and in The University's policy on Presentation of Theses (see http://www.manchester. ac.uk/library/aboutus/regulations).

Acknowledgements

Chapter 1

Introduction

1.1 General view

This chapter presents the background of this research and discusses the importance of exploring the tessellated method in vibration analysis. This is completed by introducing: a catastrophic failure of a telescope using a mirror in a fractal arrangement. The scope and methodology of the project are also discussed. This Chapter ends with a brief description of the aims and objectives of the research and thesis outlines and summarising the publishing work.

1.2 General background and motivation

Perforated plates and sheets are used in a broad number of applications for sorting and screening any substance, such as sugar and spices to sand and gravel. Additionally, they are used widely in heating and ventilating installations, also in blending different practicals. Moreover, they are extensively used in panel as a noise absorber, besides porous panel configurations are substantial due to environmental and cleaning considerations.

Due to their vast use in industry there is also a particular type of irregular perforated structures known as fractal. These irregular perforated panels are also widely used in industry as heat exchanger applications, antenna configurations and architectural designs, etc. These irregular perforated plates have unique systematic shapes. Fractals, in general, are usually used to describe random objects

in nature, such as the snowflake, clouds, tree, etc. Mainly, these geometries can not be represented by the Euclidean coordinate system. But they can be represented in fractal space by creating a primary object then be iterated through mathematical manipulations.

It is clear that, the uses of fractal in industry are vast and to give a clear demonstration of their use with advantages and disadvantages extremely important. So, the most significant uses of fractal in the industry are in designing the Overwhelmingly Large (OWL) telescope mirror. The mirrors are conceived in a honeycomb design that is illustrated in Figure 1.1 and 1.2, where *V* shows the number of mirror's segments that are needed to form the main mirror. The mirrors are designed in such a way to reduce the curvature of the lenses where the main mirror is better to be separated through a significant length [1]. For this reason and because a telescope image is a high-energy light or particles, it needs to minimise any vibration sources as much as reasonable. On the other hand, a telescope that is installed on earth is suffering from all the dynamic loads from wind and earthquakes [2], etc. In 1990, the Hubble space telescope was launched into space and settled in its orbit. At the first testing to the telescope, it was found that the information quality that was received on earth had a lower accuracy compared to the designed plans. Later on, it was found that the problem was in the positioning of one of the primary lenses where it had been incorrectly shifted about 1.3 mm out of position [3]. Although the number appears insignificant, the effect was huge on such equipments. So, the effect of the dynamical loads, due to lunch the equipments into the space, can cause a lot of damage to such sensitive and finished designs. Also, the best way to avoid such issues in the future is by improving the vibration analysis in an irregular structures by using untraditional methods [4]. Moreover, the application of using such structure is widely implemented in the industry as mentioned earlier; this gives more motivation to carry this work.

This is lead to a curious question what is Fractal? Fractals are irregular structures as mentioned earlier. These structures were firstly suggested by Mandelbrot as been cited in [5]. Usually, fractals are used to represent better cellular objects
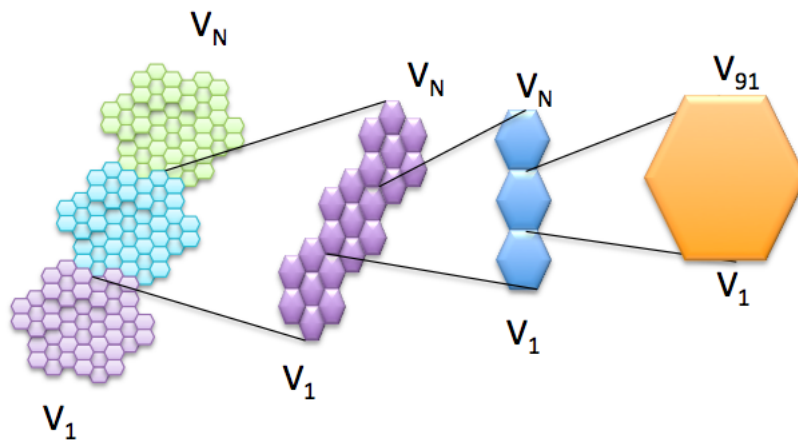
Figure 1.1: The formations of a pre-fractal mirror in each mirror segment in the OWL telescope.
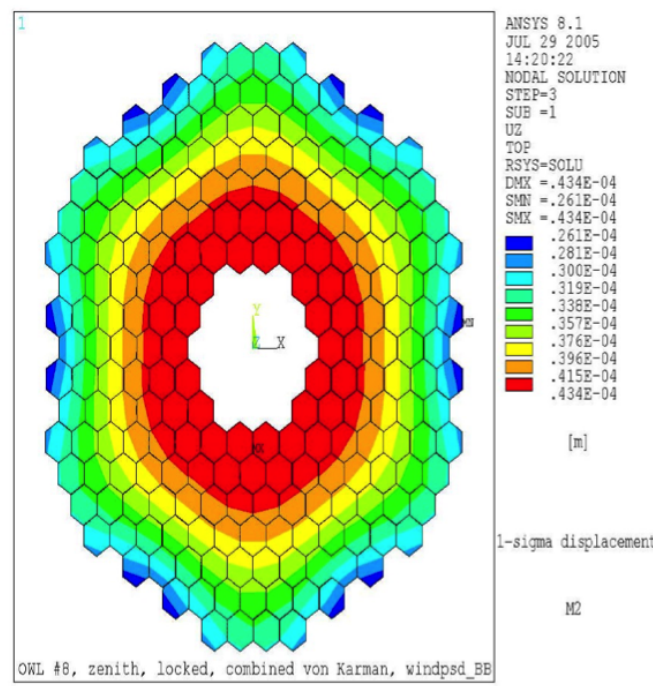
Figure 1.2: The honeycomb in the primary mirror of the OWL telescope mirror under analysis [3].

[6]. Since that time the researchers irritated to find methods to analysis physical quantities on these spaces. For example, Tarasov [7] and Ostoja- Starzewski [8] studied the implementation of transport approaches in fractals. Their strategies were founded on the application of fractional derivatives. These methods were untested and physically impenetrable in many aspects since fractional derivatives do not readily arise from the governing physics. The other option to avoid, is the need for fractional derivatives which are the indirect use of fractal quantities [9]; this type of solutions have severe limitations akin to those arising with the calling of parameters in empirical expressions, For this reason, it was not considered further here [10].

To avoid using fractional derivative and what companies them from the heavy mathematics skills to form the equations of motion to the implement of undeveloped section of mathematics. All these difficulties of analysing vibration in a fractal structure, this work introduces the idea of implementing a Tessellated Continuum Mechanics (TCM) method. The first official introduction to the transport equations theory was in 2013 by Davey and Prosser [11]. In a brief description, a transport equation is used as a general theory to analysis different types of 1-D applications. This theory is built on the concept of creating a number of maps to construct an alternative space that has the ability to mirror the physics on the original model. The mapped model is totally different from the original model but can be scaled back to the real model. This is the concept behind the general method which is called the Finite Similitude theory. One of the branches of this theory is TCM. The TCM theory is simply directed to find a solution on the fractal space on a local basis. All the other branches of the Finite Similitude theory (FS) used the global scaling procedure while this is the first time to consider the uses of local scaling procedure in applied mechanics. Precisely, this work is devoted developing the TCM method in the fractal analysis as structures in applied mechanics.

1.3   Scope and methodology

In the field of mechanical fluid and architectural engineering, the need for high efficiency, high functionality, and high profitability have led to the use of irregular perforated structures. For instance, irregular plates can be found in nuclear reactors, which provide both structural support and flow passage of a coolant [12]. These structures are required to stand various external loadings such as an earthquake and loading design basis, for example, due to a pipe break. Therefore, it is vital to ensure structural integrity [13]. And especially for objects such as fractal designs.

In general, fractal objects and phenomena in nature such as mountains, coastlines and earthquakes signature are an area well studied by Mandelbrot sets [14] . Two of the most essential properties of fractals are self-similarity; and non-integer dimensions. A fractal can be described as an object less regular than ordinary geometrical objects. The term fractal came in use late 1975, by Mandelbrot (as been cited in [5]) who also gave the first mathematical definition of what should be considered as a fractal. The use of fractal analysis is wide. It ranges from probability theory, physical theory and applications, stock market and to a number of theories among many others.

Fractal analysis is a valuable tool when the researcher needs to study eccentric geometrical objects, e.g. a set with a non-integer dimension value (Lightening, tree branches, etc.). Fractal analysis has developed intensively over the last 30 years, which gives a hint to its young age as a branch of mathematics.

There are mainly two favourite types of fractals: complex number fractals see Figure 1.3 , and Iterated Function System (IFS) fractals see Figure 1.4. This work is concerned with IFS fractals. IFS fractals are created on the basis of simple plane transformations: scaling, dislocation, and plane's axes rotation. Creating an IFS fractal consists of the following steps [6]:

1. Defining a set of plane transformations.

2. Drawing an initial pattern on the plane (any pattern).

3. Transforming the initial pattern using the transformations defined in the

first step.

4. Transforming the new model (combination of initial and transformed patterns) using the same set of transformations.

5. Repeating the fourth step as many times as possible (in theory, this procedure can be repeated an infinite number of times). More details are explained in Appendix A.
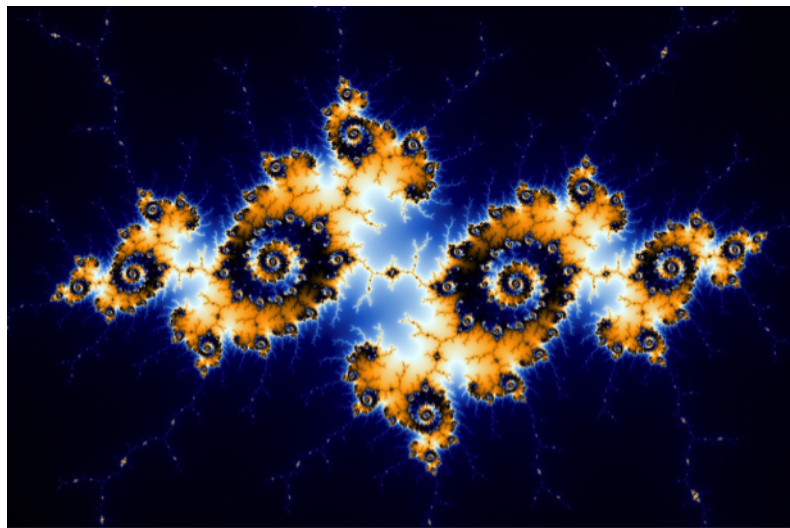
Figure 1.3: Complex fractal geometry [6].

Iteration is one of the most powerful tools in mathematics, because it can simply transfer a process from discontinuity into continuity. This can clearly revealed in sketching a continuos function (by any method such as by hand or computer) by drawing a discrete sets of points then refines the distance between the selected points and reconnecting them will lead to create a finer continuous function. The interpolating process lays at the heart of the mathematics, because interpolating redefines the continuity itself and makes it depends on the chosen limits of the function's independent variables. This enables researchers to choose wisely their necessary limits when plotting their functions. This enforced researchers to carefully chose their satisfactory limits of iteration while studying fractals as a structure.

At this point, it is essential to introduce an alternative method to solve problems in the fractal space. So the tessellated continuum mechanics approach in a brief
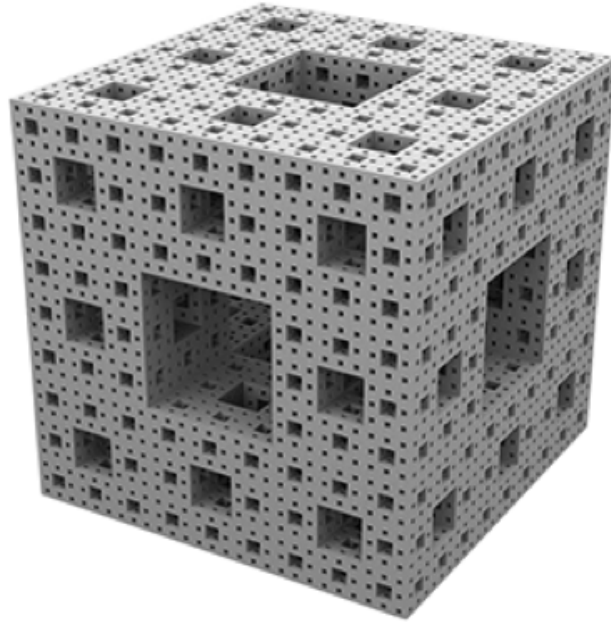
Figure 1.4: IFS fractal geometry (Sierpinski Carpet) in three-dimension (3-D) [6].

explanation: It is an alternative representation to specific physical subjects (such as heat transfer [11] and vibration [15]) into a second hypothetical domain. This domain is called 'Tessellation'. To create such a domain transport equations must be implied to define the physics of the hypothetical domain, where, conservation laws must be preserved and proportioned at both spaces. This study is focusing on studying the physical problem in the shape of fractal structures.

Moreover, as mentioned earlier these geometries have random holes perforation in a systematic means, which means it involves the application of iteration function schemes using affine contraction and expansion maps. Highly complex geometries can be produced using a modest number of contraction mappings.

For the current time, the formation of the tessellation geometries is more constrained with the initial meshes that are built on the fractal spaces. Besides, the TCM method has been significantly modified by introducing some techniques such as hole-filling maps and the discontinuity network that will be presented extensively in the next chapters. However, briefly, the hole filling-maps are deforming the associated mesh on the tessellation that is initially created from initial mesh on the fractal. The hole-fill maps are constructed using an iterated function scheme similar to the one applied in the fractal generation process

The discontinuity network is tested in providing a proper representation of the physics relating to cellular beam structure designs, a general scheme explaining the TCM method is presented in Figure 1.5. It is necessary to explain the main response characteristic that is used in this work. Mainly, the responses or the deformation in the longitudinal and transverse vibration are expressed by $\underline{u}_i$ where i represent either ps or ts. These subscripts are denoted to the analysis run on either the pre-fractal ps or the analysis run on the tessellates ts. This can be applied to the time symbols too. This would allow applying different time running on each space. More symbols are shown in Figure 1.5 and will be explained broadly in Chapter Three. Basically, this work is going to test the hypothesis of applying a vibration analysis on a porous structure represented by an IFS fractal. This is achieved by running two different analyses on two different spaces (fractal and tessellated) by using the same analysis method, which is in this case is the finite element method (FEM); then comparing the results in order to investigate the accuracy of the tessellated method in mimicking the fractal problems. In other words, a transport theory for fractals is introduced, which is used with a hole-fill mapping strategy, to facilitate the analysis of the transport problems on a tessellated continuum. Mainly, the TCM method enables well-known analytical and numerical continuum solutions to be immediately applied to solve problem on the pre-fractal space.
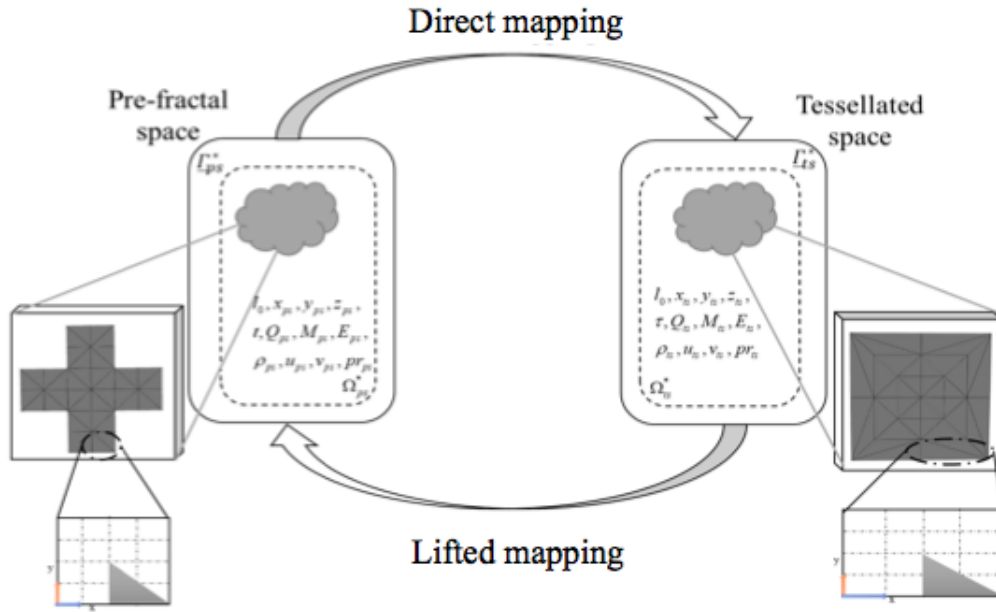
Figure 1.5: General mappings through both spaces.

1.4 Aim and objectives

The main aim of this study is to test the proposition of solving discontinuous domain problems such as a fractal as a structure in one-dimensional (1-D) and two-dimensional (2-D) spaces by mapping the problem into a continuous domain named as a tessellated space. This is accomplished through the following actions:

1. Establishing transport equations that link physics on the fractal to the tessellated in any dimensions of 1-D or 2-D.

2. Implementing the newly devolved method in creating the tessellated space and improving the work started in reference [11] for 1-D or 2-D application.

3. Investigating the possibility of using an isotropic and anisotropic scaling process in creating the tessellated space, for 1-D application.

4. Developing a Python code to build pre-fractal model and it is corresponding tessellated model automatically for 2-D model. Especially to ease

calculating the F-Function; and calculating then assigning the complex and local material properties.

5. Presenting complex material distribution matrices on different tessellated continuum spaces of non-product fractals with the aid of Python code in ABAQUS.

6. Testing the analytical solutions on both spaces (fractal and tessellated) to investigated the theory accuracy for 1-D and 2-D models.

7. Testing the numerical analysis of the fractal and the tessellated on 1-D and 2-D models.

8. Testing the finite element method (FEM) in performing different analysis such as static, frequency and dynamic on each model separately.

9. Expanding the validity of the proposed theory by testing different boundary conditions and vibrating excitations cases.

10. Investigate the possibility of using different pre-fractals as structures in this study, such as the Sierpinski Carpet and the Vicsek fractal.

1.5 Outline

The next chapters are presenting the following information

1. Chapter Two presents an extended historical background for vibration of structures, fractals and tessellated.

2. Chapter Three explains the main continuum equations that are employed in this work. Also listing the main steps of applying the TCM theory.

3. Chapter Four demonstrates the static analysis for the tested pre-fractal models in 1-D and 2-D spaces.

4. Chapter Five tests the dynamic analysis for 1-D pre-fractal models.

5. Chapter Six verifies the TCM theory for the dynamic analysis for 2-D pre-fractal models.

6. Chapter Seven lists the main conclusions and future works.

1.6   Publishing

- **Posters:**

    - Show Case University of Manchester, 2016.

    - MACE PGR Conference, 2017.

- **Conference Papers:**

    - 2-D Study on Free Vibration Analysis of Pre-fractal Structures Using Finite Element Method , MACE PGR Conference.

    - Tessellated continuum mechanics: forced vibration of cantor Dust-Like structures, Fourth International Conference on Mathematics and Computers in Sciences and in Industry (MCSI), 2017.

- **Journals Papers:**

    - A tessellated continuum approach: A Similitude Approach to Holey-Beam Vibration,Applied Mathematical modelling , 2018.

    - A tessellated continuum approach for the static analysis of perforated structures, Computers and Structures, 2019.

Literature Review

2.1   Introduction

This chapter introduces the background and the historical development of the following subjects: theory of plates; fractals; and tessellated. In more details, the main methodologies associated with the use of fractals in industry along with a brief introduction to each application. Most importantly, a brief description of the novel method called the Tessellated Continuum Mechanics (TCM) theory and its application in the literature is presented. This chapter ends with a summary of the main observations on the presented literature review about the subjects mentioned above.

2.2   Vibration analysis

Vibration analysis of industrial machinery has been around for many decades, but gained prominence with the introduction and widespread use of the personal computer. Vibration analysis refers to the process of measuring the vibration levels and frequencies of industrial machinery, and using that information to determine the 'health' of the machine, and its components; a very simple example is an industrial machine (such as a fan or pump) when it is operated, it generates vibration.

2.2.1 Applications perforated plates

The mechanical and dynamical behaviour for irregular perforated structures is crucial to be considered for optimisation purposes, due to the wide range of their applications in industry, as mentioned earlier in Chapter One. Again, the perforated plate is mostly used in nuclear reactors. There are several perforated structures, which provide both structural support and flow-passage of a coolant [16]. In the automotive industry, perforated plates are used in vehicle exhaust silencers, attenuators in jet engines [17]. Moreover, the applications of micro-perforated plates are well found in architecture and urban in Mandelson aeronautics and space industries for their well-known noise reduction property [18]; Thus perforated plates are also widely used in absorber design.

2.2.2 Theory of plate

Many scholars have developed the theory of plates. However, the exact solution is quite rare and only available for simple boundary conditions [19]. Therefore, the numerical methods are more widely recognised in this type of work. Most scholars are satisfied with using two-dimensional (2-D) Finite Element (FE) models to simulate the response of smart structures and avoid using the use of three-dimensional (3-D) models due to their complexity compared to the 2-D models with a comparable accuracy. Semi closed-form solutions of the dynamic response of plates were presented mainly for a few cases of boundary conditions, such as those of simple support at all four edges of plate (Navier-type solutions) or at parallel edges (Levy-type solutions) [20].

2.2.3 Theory of perforated plates

O 'Donnell in 1970 [21] introduced an astonishing idea of predicting the static deformation of perforated plates. The researcher introduced the using of equivalent elastic properties that make a solid plate's deflection identical to that of a whole continuous thick plate. This solution depends on using deflection efficiency $\zeta = G/G^*$, where G is the flexural rigidity of the plate, while $*$ is denoted for the equivalent plate and depends on the type of perforation. On the same hand, ligament efficiency r depends on the degree of the plate perforation and it is

defined by $r = p/d$; where p is the pitch and d is diameter of the holes. These outcomes are implemented in ASME in 2004, and have a limitations regarding the hole's shape and the distribution of the holes on an array of equilateral triangles, besides the holes thickness compared to the hole pitch as cited in reference [22]. The results is found to be taken under a static loading that will cover only the first mode. And for this reason later researchers had to redefine the material properties for the dynamic analysis as will be explained later.

Due to the difficulty of analysing this field, since 1976 researchers attempted to use numerical methods in dealing with these models. For example, Aksu and Ali. [23], in the same mentioned year succeeded in demonstrating the possibility of using 2-D finite difference method (FDM). The researchers used this method in computing the natural frequency and modal analysis behaviour of plates with rectangular cut-outs for the first time in the literature. The results showed that the natural frequencies were lower than the experimental data. Later on, in 1988, the first numerical and experimental validations to the calculations of the dynamic structural response were investigated by Choi [24]. This solution was found to be inaccurate because it used the concept of equivalent solid material properties where a static approach is used to solve a dynamic problem. Later, the researcher tested different perforated plates. For example, in 1996, specific parameters that define the geometry of the holes were introduced to provide a better understanding of the effect of one hole on the natural frequencies of perforated plates as in Boay [25], where they presented a parametric study on a composite perforated plate by changing the hole diameters and boundary conditions to find their effects on the natural frequencies and mode shapes. Another researcher in the same year compared the tensile behaviour between the numerical and experimental results of the shadow mask[1] by Baik et al. [26] where they obtained good results by FEM. On the other hand, some researchers used a model-updating technique to improve the FEM analysis in car exhaust [27]. These methods are not practical for a complicated structure. Besides, this approach is considered to be time-consuming, because of the necessity of designing and manufacturing new experimental specimens for each case.

Unfortunately, researchers found that the accuracy of the equivalent material

---

[1]shadow mask: is a technology of manufacturing the Cathode Ray Tube (CRT) television and computer screen display.

properties is less than the real case. In 1997, Kaap et al. [28] found that the modal frequencies based upon equivalent static material properties give results less than those obtained from modal frequencies with real material properties by using FE methods.

Some alternative methods are used nowadays, such as in Kalita and Haldar [29], where the authors studied the dynamical characteristics of thick and thin rectangular plates with central cut-outs by incorporating a first-order shear deformation theory (FSDT) in the FE method on the frequency response. The non-dimensional frequency parameters for plates of various aspect ratio, boundary conditions, and thickness ratio were computed.

Jhung in 2006 [30] used modal analysis to propose equations to calculate Young's moduli in a perforated plate with a square penetration. Most recently, researchers are studying more complicated configurations such as considering the hydro-elastic water impact of a perforated plate by using the commercial explicit finite element code LS-DYNA [31]. Furthermore, all the previously discussed work only tests uniform hole scattering patterns. Besides this, the listed works above were limited to boundary condition such as free, clamped, and simply supported.

2.3   Fractals

Fractals are constructed by two different methods. A lot of complex geometries are represented using fractals, but their uses in practical analysis is laid with lots of difficulties. The reason behind this is the lack of meaningful measures of higher iteration fractals, where traditional dimension of length, area, and volume are undefined because of non-integer Hausdorff fractal dimensions[2] [32]. This will affect defining the traditional physical quantities such as fluxes (rates per unit area) and densities (mass per unit volume). Attempts to overcome these difficulties can be found in the literature [33]. One possible method to avoid the problem altogether is to use pre-fractals, which are explained in detail in the following sections:

[2]Hausdorff fractal dimensions is a measure of roughness and/or chaos that was first introduced in 1918 by mathematician Felix Hausdorff, where the number zero represents a single point; 1 represents a line; 2 represent a square; and finally a cube is represented by number 3

2.3.1 Background

In physical problems, fractal geometry is not possible to use, as has been mentioned earlier in Section 2.3. This is because that the traditional definitions of stress, pressure, and strain become non-quantifiable on these spaces. So, it better to work with pre-fractals, where these quantities are definable. This can be rephrase as pre-fractal represents a closer approximation to reality than the fractal itself. Moreover, fractals are generated by recursion process. Infinite sequences of pre-fractal recursion can generated a fractal, while choosing the limits of this iteration is following the researcher's insight.

An alternative perspective to view pre-fractal is in like viewing other geometric finite element objects such as cylinders, spheres, cuboids, etc. Although the fact that these models are not appear in real physical space but still are used to fill the engineering analysed models. The application of fractal geometry from mathematical perspective to a physical fractals can be found in the references [34] and [35]. It is necessary to recognise that the standard definition of stress and strain is not defined on a fractal. This led to use fractional derivatives [36]. Although this science is consider new compared to the other branch of mathematics, where it used for the first time in 1695, there is still no united definition for fractal calculus but the Riemann one [37]. Other definitions to fractional derivatives [38], but still give rise to zero for a constant function. Again using pre-fractals to replace the analysis on fractal is can be found in [39]. This is enabled using the governing equations in describing the standard physical quantities which are quantifiable on pre-fractal space. Some researchers [35] established a general framework for fractal mechanics. All what is mentioned earlier are showing the need to the TCM methodology to be particularly useful in obtaining classical solutions. The methodology presented in this project is founded on small defection theory and modal analysis.

Some of the interesting research in the filed is testing the acoustics damping properties for Peano-fractal where the results proved that this geometry has a better damping characteristics than the current used models [40]. A dynamic analysis is investigated for Von koch fractal as a CF beam [41] with ignoring the damping and the external force. This is accomplished by using the transfer law to find the elasticity and the mass. Some researchers have used fractals in the

description and testing methods to quantify different types of data in calculus, such as quantifying the area-restricted searching (ARS) for a prey searching predator animals, for understanding animals' critical habitat in searching for prey and foraging specialisation [42].

2.3.2   Industrial applications

Fractals can be found almost everywhere and in all areas of science. This section introduces a short list of the main areas where scientists have tested the beauty and the efficiency of applying pre-fractals in industry:

Salim and Ali, in 2011 [43] used Peano-fractal type second iteration in designing a new dual-band internal printed monopole antenna. This design provided more compact design than the traditional one with the same efficiency. Furthermore, pre-fractals have also been used in the observation of a material microstructure, see Ozaki and Nishigori, in 1988 [44] (see Figure 2.1). Designing a more efficient radiator is presented by Rozanova et al. [45], in 2012, who found that using irregular shapes for heat diffusers allowed them to increase heat transfer, but the efficiency decreased with time. Figure 2.2 shows the pre-fractal shape used in Rozanova's study, which is a type of the Peano-fractal. This work showed that radiators with irregular surfaces permit an increase in the cooling of pulsed heat sources. In the end, different work has been performed by Blyth and Pozrikidis [10], in 2003, to improve the 2-D solutions of a heat conduction equation of irregular surfaces of Von Koch pre-fractals, which are similar to a real snowflake shape.

Lastly, in 2016, [46] researchers found that fractal zone plates offer much improvement in performance when it comes to chromatic aberration and depth of field over Fresnel lenses. A zone plate consists of a set of radially symmetric rings, known as Fresnel zone plates (FZP), which alternate between opaque and transparent. Light hitting the zone plate will diffract around the opaque zones. The zones can be spaced so that the diffracted light constructively interferes at the desired focus, creating an image (see Figure 2.3).
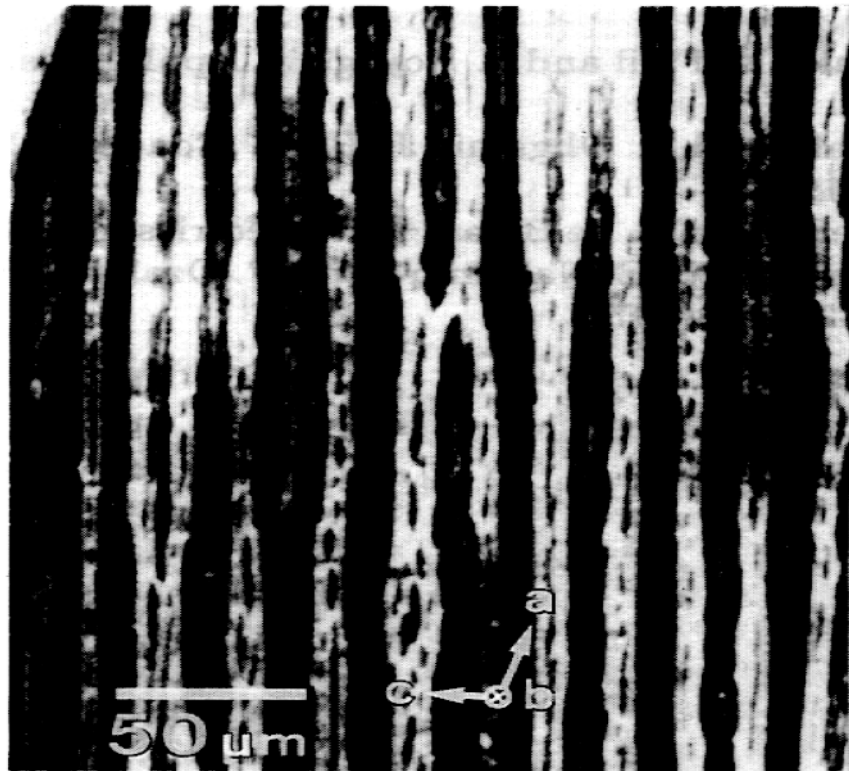
Figure 2.1: SEI (secondary electron images) observed on the TGS plate [44].
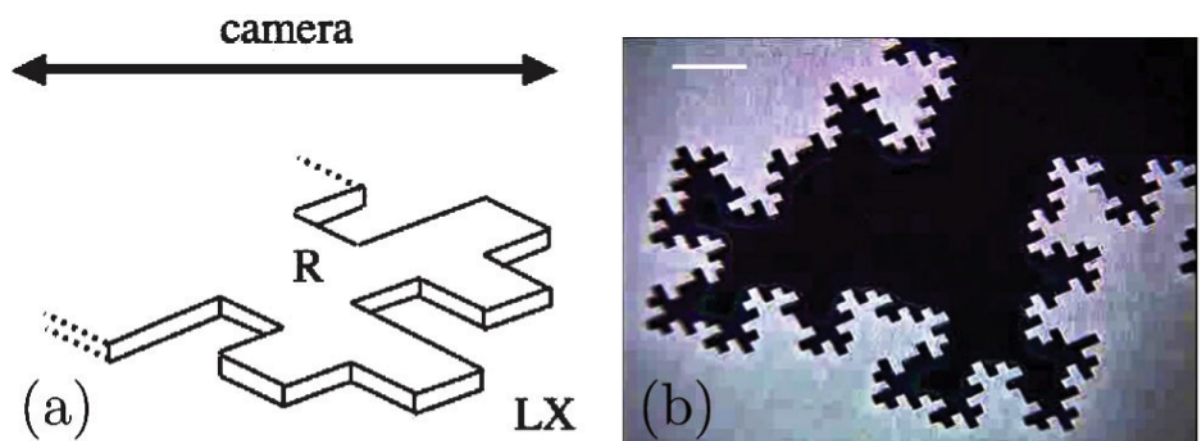
Figure 2.2: Experimental visualisation of heat propagation in 2-D radiator [45].
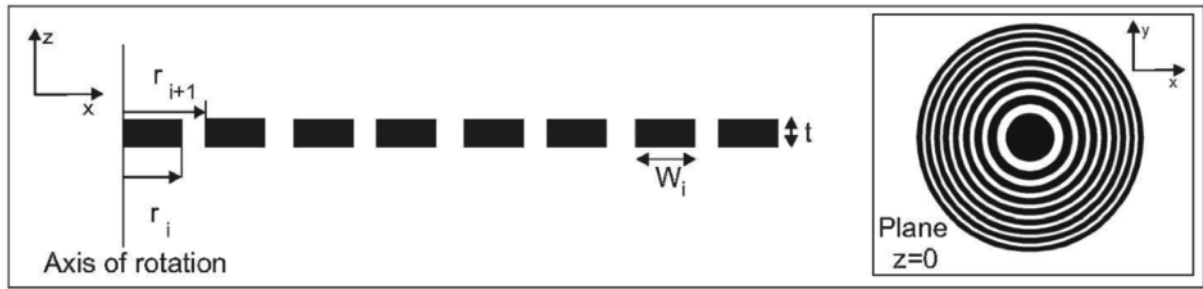
Figure 2.3: Schematic section diagram of the generation for a Fresnel zone plate [46].

2.3.3 Pre-fractal applications in mechanics

Some of the work that can be related to the pre-fractal in solid mechanics is that by Katlia and Haldar in 2015 [29]. A 2-D plate with a central cut-out can be considered as the first pre-fractal structure. The researchers used a nine-node isoperimetric plate element[3] in conjunction with first-order shear deformation theory[4] for free vibration analysis of rectangular plates. More extensive study on thin and thick plates including a Sierpinski Carpet of the first set as structure by considering different aspect ratio was performed. The researcher found that rotary inertia has a significant effect on thick plate analysis, while this effect can be ignored in a thin plate. Moreover, increasing the thickness ratio faces a decrease in frequency. Besides this, when the researchers increased the cut-out area, they found that it affected the fundamental frequency and forced it to increase, too. Finally, the natural frequency is lowest when an edge is kept free, followed by a simply supported edge and at a maximum for a clamped edge, i.e. natural frequencies will increase if constraints at the boundary are also increased. Due to the fact that Euclidean space deals with regular geometries and it is not suited for describing irregular objects such as those in nature, where stochastic models[5] are taken into account, Tarasov in 2005 [7] provided an alternative approach to describe fractals by using the concept of fractional integration to represent the mass of a fractal structure. These integrals were used to describe

---

[3]Isoperimetric structure having equal perimeters, this term is used particularly for geometrical figures

[4]mainly this theory implies a linear displacement variation through the thickness

[5] Stochastic model is a tool for determine probability distributions of potential outcomes by qualify a random variation in one or more inputs.

the dynamical rules in the fractal media. This led to a better description of the physics in fractal media; the author suggested that fractal dimension can be best calculated by the box-counting method[6]. Moreover, he considered a fractional generalisation of the Navier-Stokes[7] and Euler-Bernoulli equations by considering sound waves in fractal structures.

Furthermore, Starzeski [47] derived a formulation of the second law of thermo-dynamics for mass density media, which has a fractal structure. The derivation hinges on the concept of internal (kinematic) variables and internal stresses, as well as the split of the total stress into its quasi-conservative and dissipative components. The dissipation function is recognised to be functional in fractional-type rates of strain and internal variables. Postulating the thermodynamic orthogonality on any length scale allowed derivation of constitutive laws of elastic-dissipative fractal media involving generalised derivatives of strain and stress [48]. They tested some basic methods in thermodynamics, some of which were found not to match their results. They ended with an note that Ziegler's electro-mechanics is very suitable for creating a random media precisely, which is an approach that scale-dependent homogenisation of elastic/dissipative media, because it enable an elastic dissipative of a media by allowing a scale-dependent homogenisation this is the core of the Hill condition, where there are two approaches for solutions, the first is either by considering the stress and strain are the same or considering the energy / power is equivalence between the smooth continuum and the heterogeneous. Another contracting note is found, which is thermo-mechanics of Truesdell's is not follow the Hill condition. This is because that the stress has the main focus compared to the energy .

Butera and Paola, in 2014 [9] were able to fill the gap between fractals and fractional calculus, based on the relationship established between power laws and fractal geometries. They tested their theory of a viscous fluid seeping through a porous medium that they modelled as a fractal-shaped hollowed brick. Fractal theory in the vibration field is generally found in literature reviews through its implementation in condition monitoring for milling tool wear [49-52]. All the

---

[6]box-counting method is used for gathering data or analysing complex patterns by breaking them into smaller dataset or object. Then analysing the pieces at each smaller scale. This method can be represented by the zooming in or out the studied models.

[7]Navier-Stokes method describes the motion of viscous fluid substances by applying the second law of Isaac Newton to fluid in motion.

listed researches are describing the complexity of running the analysis on the pre-fractal space. And the only method used to analyses geometries with the same shapes as the pre-fractal has been implemented by the FEM and the FDM and presented for simple cases only.

2.4   Tessellation

Fractals allow the representation of complex self-similar geometries, but their application is found with difficulties, which stand from an inability to define traditionally derived physical quantities such as length to stress. Due to the wide range of pre-fractal's application, this project is focusing on such structures. In particular, this project is interested in driving a general transport approach for pre-fractals. This is completed by using a specific type of perforated plates that can rearranged into a continuum one by utilising a hole-fill map concept. The hole-fill maps is a part of the fractal construction process.
The following section gives explanations of the novel TCM approach and its successful development steps through the literature review:

2.4.1   Introduction

This project is based on replacing analysis of fractal structures by solving the problems on the tessellation. Employing the TCM approach in predicting the static and dynamic response of a complex perforated plate would overcome the need to calculate the equivalent elastic properties (at least for dynamic analysis). Quantities of singular interest in a vibrating system are displacement, momentum, velocity, mechanical energy in the form of kinetic and strain energy, time, and density. These must be linked between the pre-fractal and the tessellated space. The derivatives of these links/rules are going to be explained in more detail in Chapter Three.

2.4.2   Practical implementations of tessellation

The first work discussing the possibility of solving problems in the pre-fractal domain was published in 2011 by Davey and Rasgado [15]. This work covered

the possibility of calculating the analytical solution of static and dynamic analysis in a 1-D beam structure as pre-fractal. The results were remarkable when tested for two different vibration conditions (longitudinal and lateral). Idealised material properties were used. A symbol of the presented results are introduced in Figure 2.4. In this concept, each region on the pre-fractals is matched with contiguous regions on the continuum, by matching the strain and kinetic energy on both regions. This paper is considered to be the first work to point to the possibility of using the tessellated analysis but did not explain it clearly.

Later on, in 2013, Davey and Prosser, [11] tested the TCM theory by determining analytical solutions for conductive heat transfer problems through
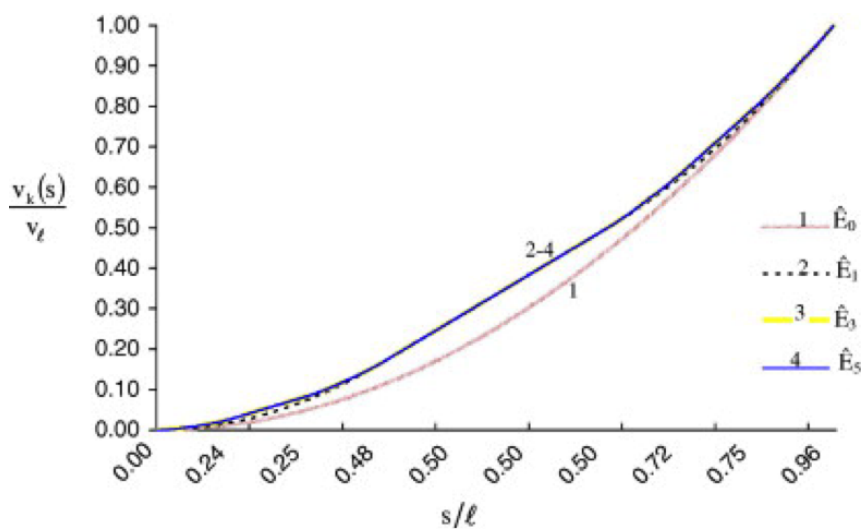
Figure 2.4: Truncated Fourier representation of initial beam displacement on $\hat{E}_k$, where $k = 0, 1, 3$, and 5 [15].

mining the analytical solutions for conductive heat transfer problems through a binary composite consisting of two isotropic materials with extreme material properties. The results showed that it is possible to determine finite temperature and heat transfer rates on pre-fractal dust for a two-phase moving boundary problem. Moreover, they established a methodology for determining the analytical heat transfer in temperature terms on fractal product dust. In this paper, the concept of an equivalent continuum solution is established more clearly, where the numbers of regions on the pre-fractal are matched with adjacent regions on the continuum so that energy can be equally transferred between the regions. Moreover, the transient behaviour is expressed in Figure 2.5 by using Fourier series (Fs) and FE. Moreover, another pre-fractal structure is tested, such as a

Cantor-dust, see Figure 2.6.

Further investigation was made by Davey et al. in 2015 [53], where more
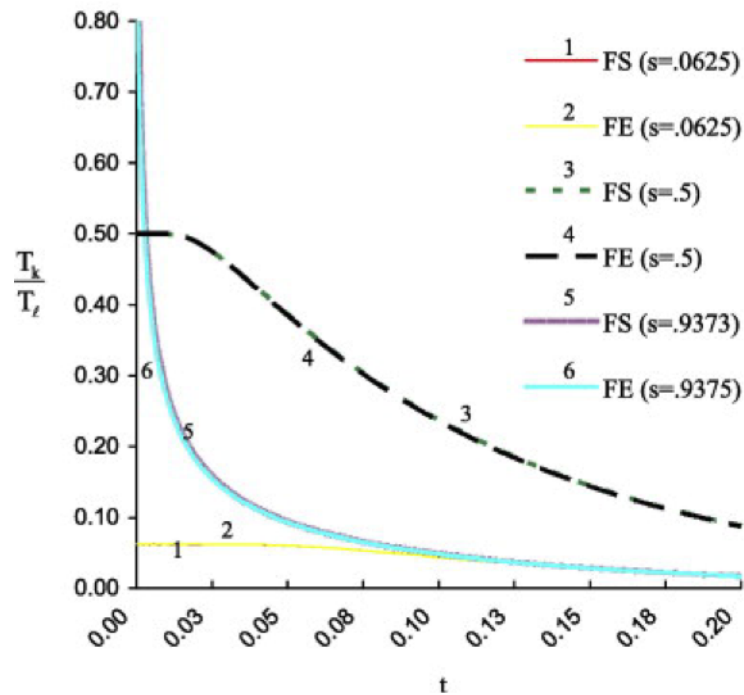
Figure 2.5: Temporal temperature response by Fourier series (Fs) and FE at different positions along the rod for $\hat{E}_4$ [11].
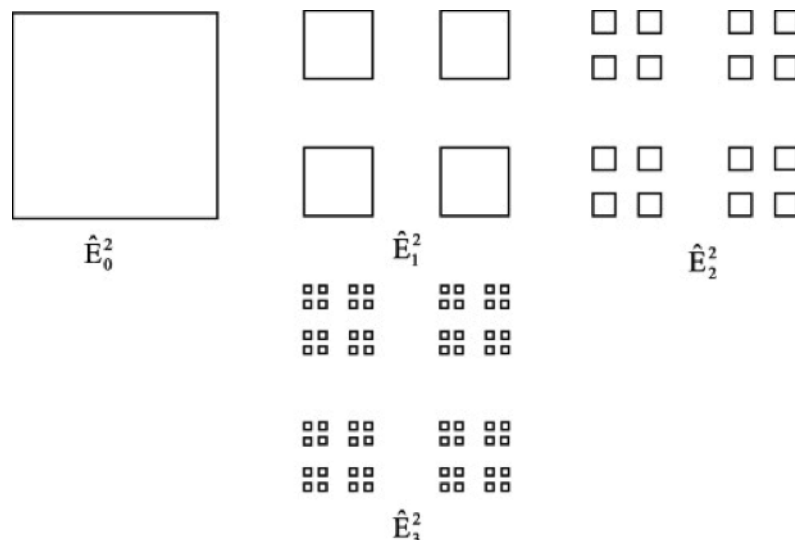
Figure 2.6: Pre-fractals of different $\hat{E}_k$ type Cantor Dust product [11].

complicated pre-fractal shapes such as Sierpinski gasket, Sierpinski Carpet and

(a) Pre-fractals

(b) Continuum
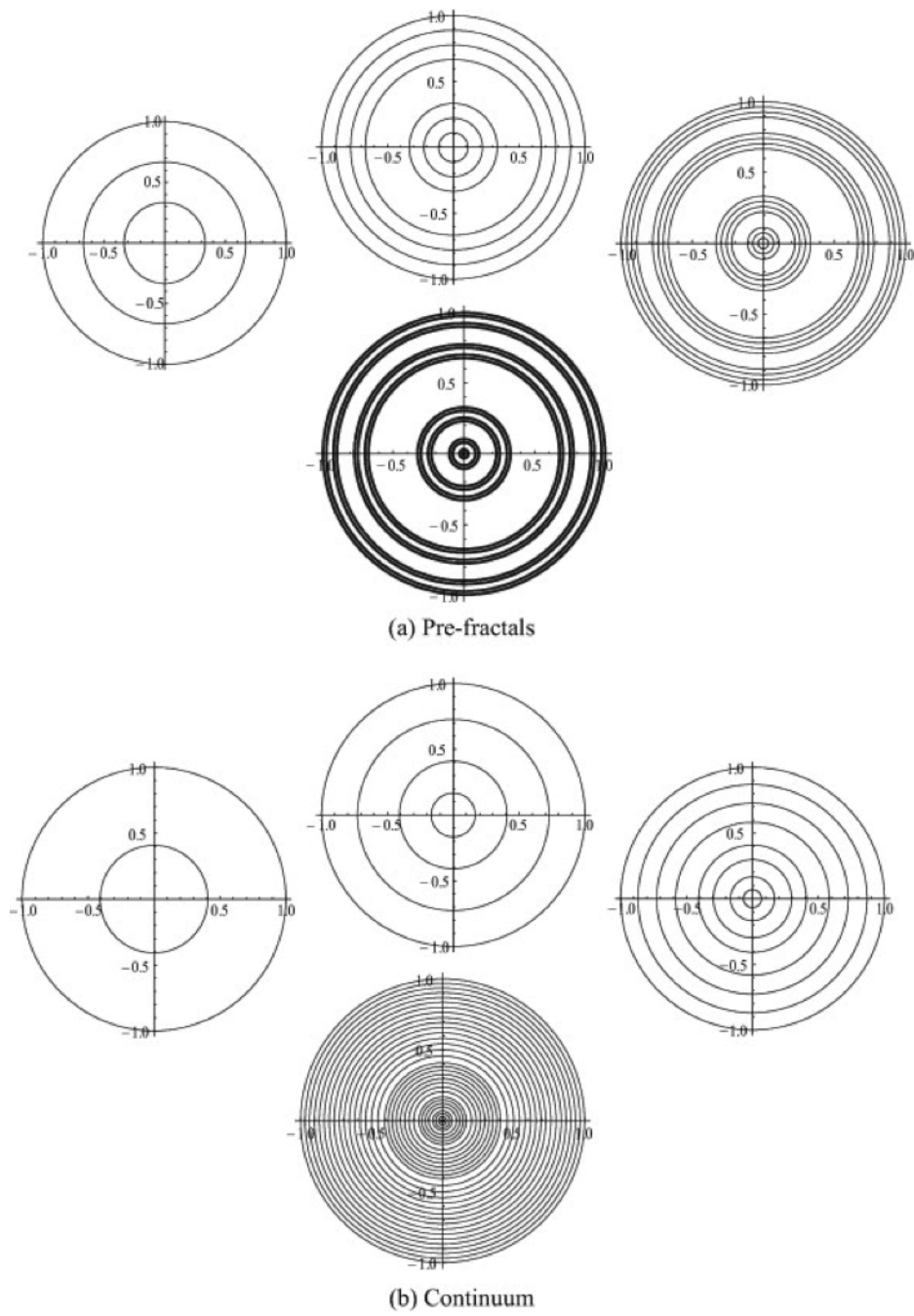
Figure 2.7: Rotated Cantor-dust pre-fractals and their corresponding continua [53].

Rotated Cantor-Dust, see Figure 2.7, were studied. The authors introduced a novel procedure to create hole-fill maps, which provides a direct way to generate the corresponding tessellated structure from its pre-fractal counterpart. The tessellated continuum is constructed in a process that essentially mirrors the pre-fractal construction process itself. They suggested two methods for hole-fill maps. The first is by using function compositions. The second is by linking the elements of a fractal with the corresponding elements on the tessellated continua by using the formula of function gradient (as will be discussed in detail in Chapter Three). For analytical analysis, the former approach is more suitable, since the requirement for the precise form of the governing partial differential equations can be elegantly established using the hole-fill maps and the integral transport equations. However, the weighted forms in the numerical analysis for the transport equations can be established and immediately applied using the second approach. Besides, they have presented the transport equation to link the physical properties on fractal to tessellation in both spaces. However, the authors had some restriction regarding choosing the fluid conductivity and the inability of their model to represent temperature differences perpendicular to the direction of the flow.

Davey et al., in 2016 [54], proposed a form of TCM theory coupled with the Galerkin finite element method to test the analysis of heat transfer on cellular structures. These structures are pre-fractals with increasing complexity. The results showed that the suggested method gave high accuracy convergence, but it required high heat transfer coefficients. The researchers also improved the hole-fill map equations and made them finer, see Figure 2.8 compared to the analysis run in reference [11]. The authors also found that the results were significantly improved.

Another approach is implemented by Jiang et al., in 2016 [55], where they tested the possibility of applying a discontinuity network (DN) with the Galerkin finite elements in the tessellated space. The discontinuity network is about creating a network of lines/surfaces where discontinuous behaviour is possible. The discontinuity network can be simultaneously established during the formation of the fractal and associated tessellation, resulting in an elegant procedure controlled through a relatively small number of maps. The physics of

(i) $\hat{T}_3$ with 6 tiles on $\hat{E}_0$

(ii) $\hat{E}_3$ with 6 tiles on $\hat{E}_0$

(iii) $\hat{T}_3$ with 18 tiles on $\hat{E}_0$

(iv) $\hat{E}_3$ with 18 tiles on $\hat{E}_0$

(v) $\hat{T}_3$ with 162 tiles on $\hat{E}_0$

(vi) $\hat{E}_3$ with 162 tiles on $\hat{E}_0$
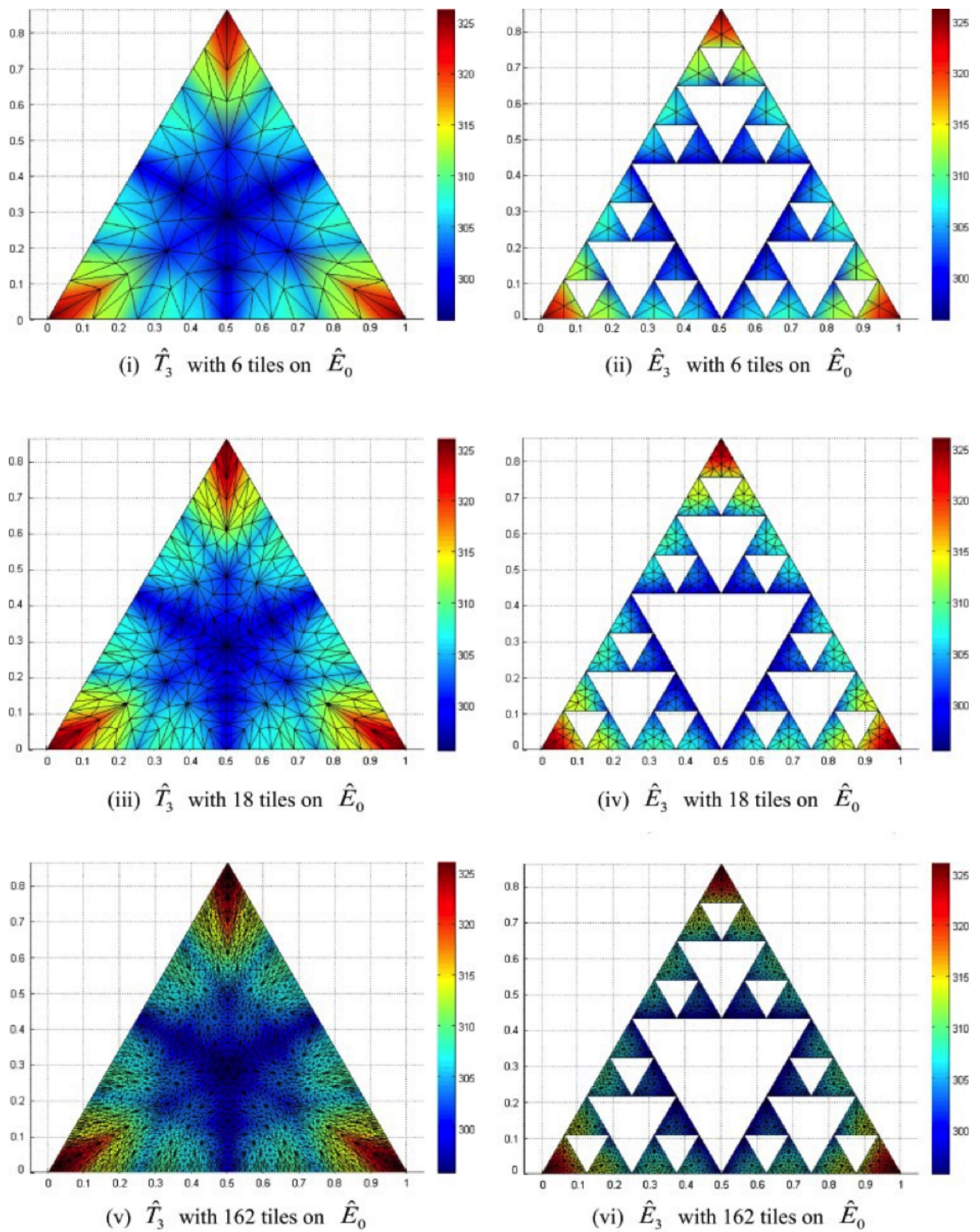
Figure 2.8: University of Manchester FE code represent the contour plot for temperature on $\hat{E}_3$ and $\hat{T}_3$ with different meshes [54].

the tessellations/pre-fractals is represented using weighted transport equations, which can be formulated directly without recourse to partial differential equations (PDEs). These techniques will be discussed in detail later in section 3.6. In parallel with the development of the tessellated theory, a related activity concerned with scaling has appeared in the open literature. The scaling work is founded on the idea that scaling can be achieved through the expansion/contraction of space itself. The first application of the concept was in metal-forming processes [56-58]. More recently the same method has been validated in bio-mechanical experimentation under isotropic scaling [59] and in the scaling of the powder compaction process [60]. More importantly the rule of finite similitude is found in [61].

2.5 Summary

The principal points found in the literature review are set out in brief below:

1. The only types of perforated plates that are studied in the literature are uniform perforated plates with simple shapes of holes (such as square, and circle).

2. Researchers typically use equivalent plate properties to investigate the static and dynamic plate behaviour, and this method has shown a deviation from the experimental results.

3. Using a model-updating technique to predict the dynamical elasticity of a perforated plate is an impractical approach and it is time-consuming.

4. Fractal geometry is an efficient tool to represent the surfaces or bodies that the classical method failed to represent.

5. Researchers have extended the capability of pre-fractal science to not only presenting shapes of objects but also using it as models in physical analysis.

6. Different types of pre-fractal were used in the literature to represent the physical behaviour of systems.

7. The governing equations are much simplified when using pre-fractals rather than using fractal where the solution are simplified to some extent the analysis.

8. One of the earliest papers that deals with pre-fractal solution as a continuum is found to ignore the discontinuity in lateral deflection in beams as in reference [15] where it deals with it as continuous.

9. A mathematical approach began to arise in fractal analysis in 2013, which is the TCM method.

10. Some limitations regarding the TCM were raised in reference [53], where the researcher had to be restricted in using a particular fluid conductivity.

11. A more developed hole-filling map technique is found in reference [15] for the TCM.

12. The idea of the discontinuity network (DN) in TCM is first implemented in reference [50] for matching the physics on both pre-fractal and tessellated spaces.

13. Since 2013 and till the current time the TCM theory has been tested and developed in different aspects such as in references [11, 53-61].

The gaps that are going to be tested in this work are in points 1,5, 8 and 12, 9, 10, and 13.

Tessellated Theory in Continuum Mechanics

3.1 Introduction

The transport method has proven its capability in matching the physics of complex structures as presented in [11, 15, 53-61] and as stated in the literature review. The general laws of physics are illustrated extensively in Section 3.2, which introduces the Finite Similitude method (FS). This method is founded on the idea of proportional transport equations representing the governing physics in the pre-fractal and tessellated spaces. The transport form of the governing equations is ideal for representing the discontinuous physics preserve in pre-fractal geometries and to capture all conservative and non-conservative physical laws.

Defining the tessellated structure in more specific mathematical forms and demonstrates the generation of the principal rules of connecting both spaces (pre-fractal and tessellated) are illustrated in this chapter. Conveniently, and efficiently, it is possible for both the pre-fractal and the tessellation aspects to be generated using a recursive method. The derivative of the main scalar constants are briefed, while a verification to the theory by linking the strain energy and calculating one of the most critical aspects in this work which is by finding the link between the elasticities are presented.

The following sections are all related in explaining the general headlines of the developed theory from previous works. It is necessary to present the theoretical

background in such method/style because in each chapter there will be a fill separated explanation to how apply the general theory (listed here) to on the studied problems according to the analysis type (the project work on the theoretical section are explained in the following chapters).

The main theory concepts are presented in Sections 3.3, and 3.4 which are concerned with explaining the hole-fill maps, the linear mapping function for wave theory, and the discontinuity network (DN) on the tessellated space. Finally, Section 3.5 is presenting the general theme of implementing the TCM theory in 1-D and 2-D applications.

3.2 Background theory

To perform analysis on discontinuous pre-fractal-like physical structures, a partial non-integral derivative is invariably needed. The solutions of such problems are implemented with vast difficulty, and the connection to physical systems is presently not fully understood. In an attempt to bypass these practical and conceptual difficulties, the tessellated continuum method was introduced. The approach involves the creation of a tessellated structure whose elements are in one-to-one correspondence with elements on the pre-fractal representing the physical perforated geometry. Both pre-fractals and tessellations are created recursively, and the map that relates their elements is termed as a hole-fill map because it has the function of closing holes when applied to the pre-fractal. Finite similitude [56] and [61] is used to relate the physics in corresponding spaces occupied by different spaces let assumed in this case to be tessellated and pre-fractal elements. Finite similitude exists when spatial transformations are linear, which can readily be achieved with the use of simple spatial elements (line, triangles, tetrahedrons etc.). Figure 1.5 illustrates how to relate the pre-fractal and tessellated spaces. Two basic maps are needed; a direct map (the hole-fill map) and its inverse, which serves to lift results from the tessellation to the pre-fractal. The tessellated space being continuous permits classical analysis and numerical tools such as the finite element method to be applied. The tessellations and pre-fractal are separately created by means of iterated function systems (IFS) but involve the same number of contraction and expansion maps for the

pre-fractal and tessellation [53]. The tiles on the tessellation can also double up as a finite element mesh in any numerical analysis. The notation representing the pre-fractal structure is $\hat{E}_k$, where k is the number of iterations used to create the pre-fractal using an iterated function system. Similarly, to generate the tessellation $\hat{T}_k$ the exact same numbers of expansion maps are involved. The hole-fill map can be formed directly by identifying corresponding elements in pre-fractals and tessellations or indirectly by means of function composition of the contraction and expansion maps and their inverses. The latter approach is more amenable to numerical analysis. Figure 3.1 illustrates the pre-fractal Cantor set and the corresponding tessellated structures, while Figure 3.2 to Figure 3.4 show the Sierpinski Carpet for different complexity; while Figure 3.5 to Figure 3.7 present the Vicsek fractal with their corresponding tessellated models. To accommodate discontinuous physics pervasive to pre-fractal geometries, it is advantageous to use weak forms of the governing equations. To this end the weak-continuum equation [62]:

$$\frac{D^*}{D^*t}\int_{\Omega^*}\rho\,\psi dV^* + \int_{\Gamma^*}\rho\,\psi(\underline{v}-\underline{v}^*)\cdot\underline{n}d\Gamma^* = -\int_{\Gamma^*}J^{\psi}\cdot\underline{n}d\Gamma^* + \int_{\Omega^*}\rho b^*dV^* \quad (3.1)$$

It is sufficiently generic to capture all conservative and non-conservative physical laws.

Here Ω^* is a control volume (CV) in the form of a continuous open set of points and surrounded by an orientable boundary Γ^*. Moreover, ψ is a specific field variable; ρ is material density; while $\underline{v}$ is the material velocity; $\underline{v}^*$ is the CV velocity; $\underline{n}$ is an outward pointing unit normal vector, J^{ψ} is a source term and b^* is a flux. The time derivative used in Equation (3.1) is connected to the CV velocity $\underline{v}^*$ through the identity $D^*/Dt^* = \partial/\partial t^* = \underline{v}^*\cdot\nabla$ [63], where ∇ is the traditional gradient operator. To develop the tessellated space, it is important to explain the transport equation on both spaces separately. In more details, the five transport equations on the pre-fractal space of concern here are those for space, mass, momentum, movement and energy. Explicitly stated the transport equations are:

$$\frac{D^*}{D^*t_{ps}}\int_{\Omega_{ps}^*}\rho_{ps}\psi_{ps}dV_{ps}^* + \int_{\Gamma_{ps}^*}\underline{v}_{ps}^*\cdot\underline{n}_{ps}d\Gamma_{ps}^* = 0 \quad (3.2)$$
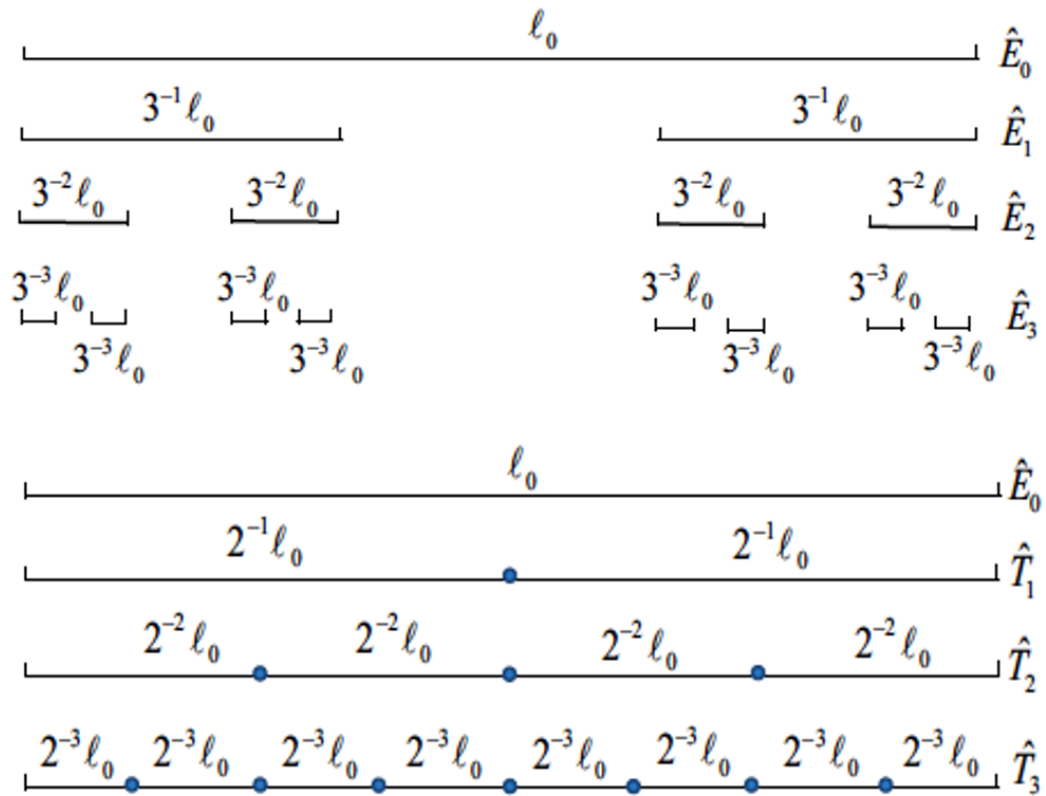
Figure 3.1: The Cantor set of pre-fractal $\hat{E}_k$ and its corresponding Tessellated $\hat{T}_k$ structure in x, y [11].
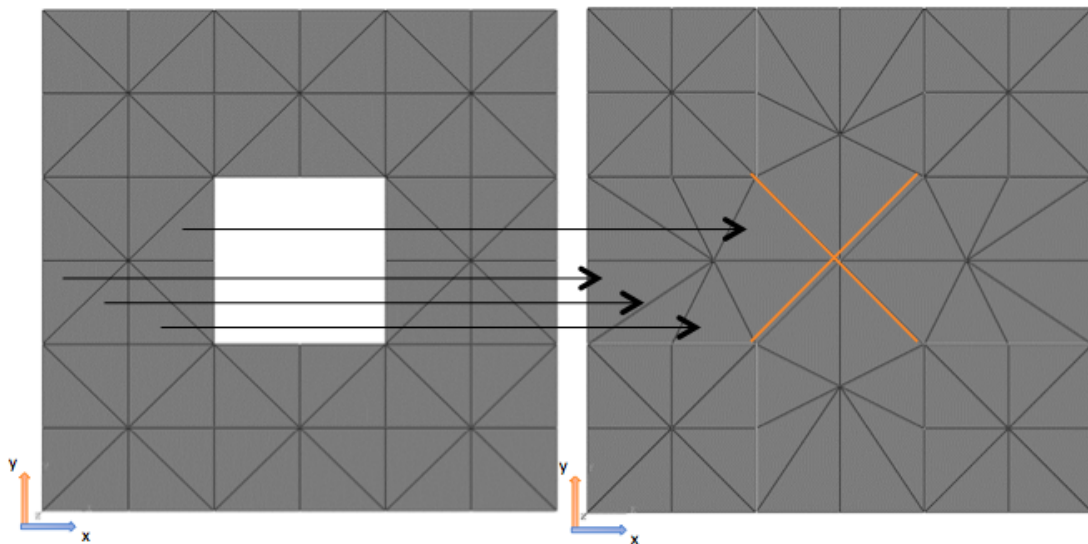
Figure 3.2: Sierpinski Carpet $\hat{E}_1$ and its corresponding Tessellated $\hat{T}_1$ structure with the discontinuity networks.
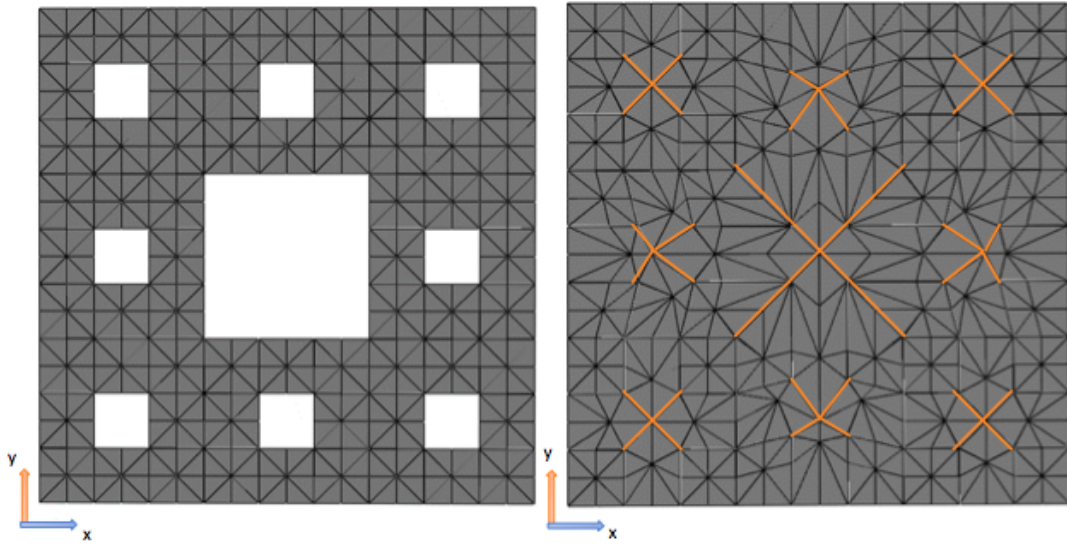
Figure 3.3: Sierpinski Carpet $\hat{E}_2$ and its corresponding Tessellated $\hat{T}_2$ structure with the discontinuity networks.
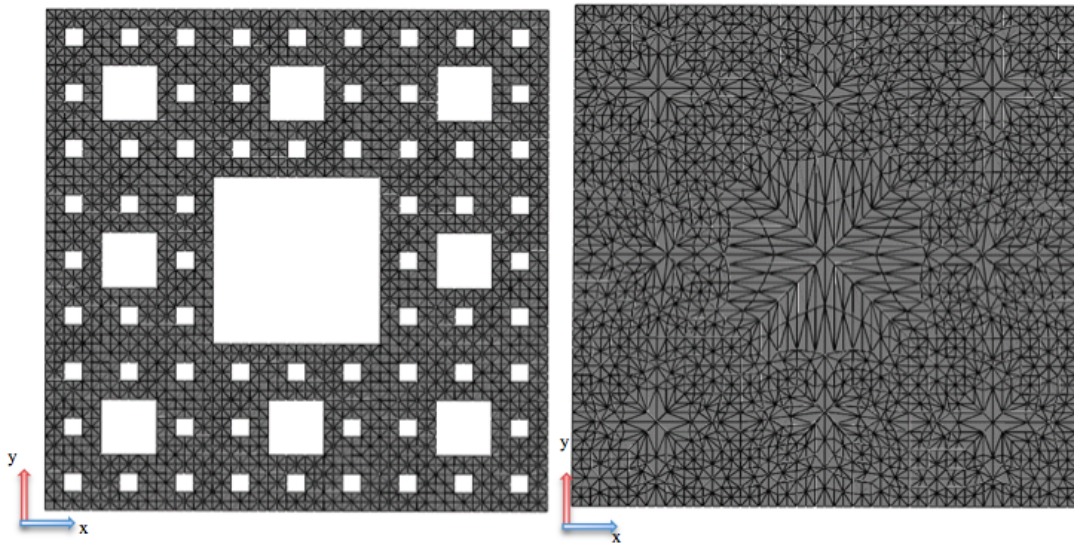
Figure 3.4: Sierpinski Carpet $\hat{E}_3$ and its corresponding Tessellated $\hat{T}_3$ structure with the discontinuity networks.
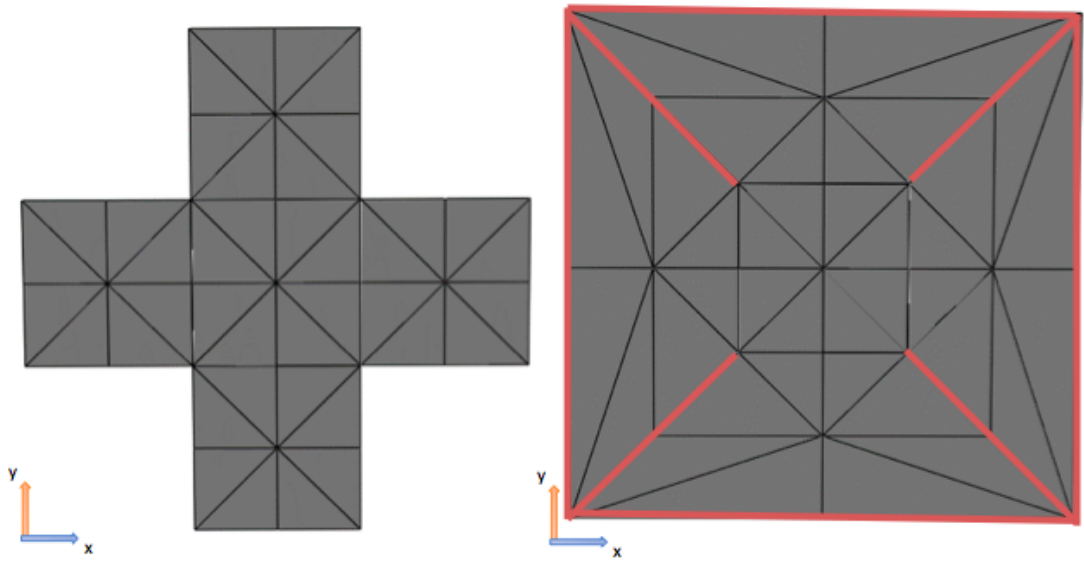
Figure 3.5: Vicsek pre-fractal $\hat{E}_1$ and it's corresponding tessellated structures $\hat{T}_1$ with the discontinuity networks.
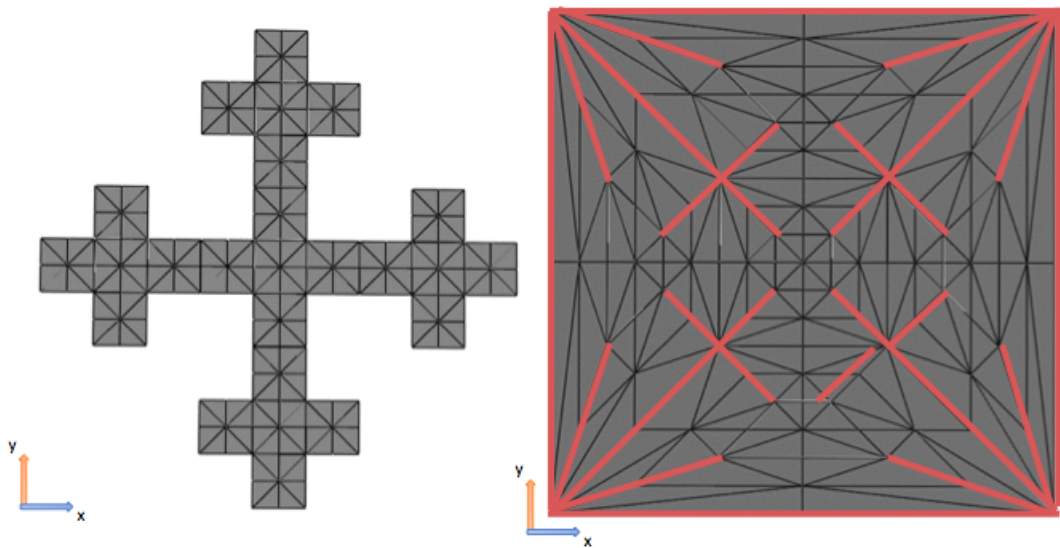
Figure 3.6: Vicsek pre-fractal $\hat{E}_2$ and it's corresponding tessellated structures $\hat{T}_2$ with the discontinuity networks.
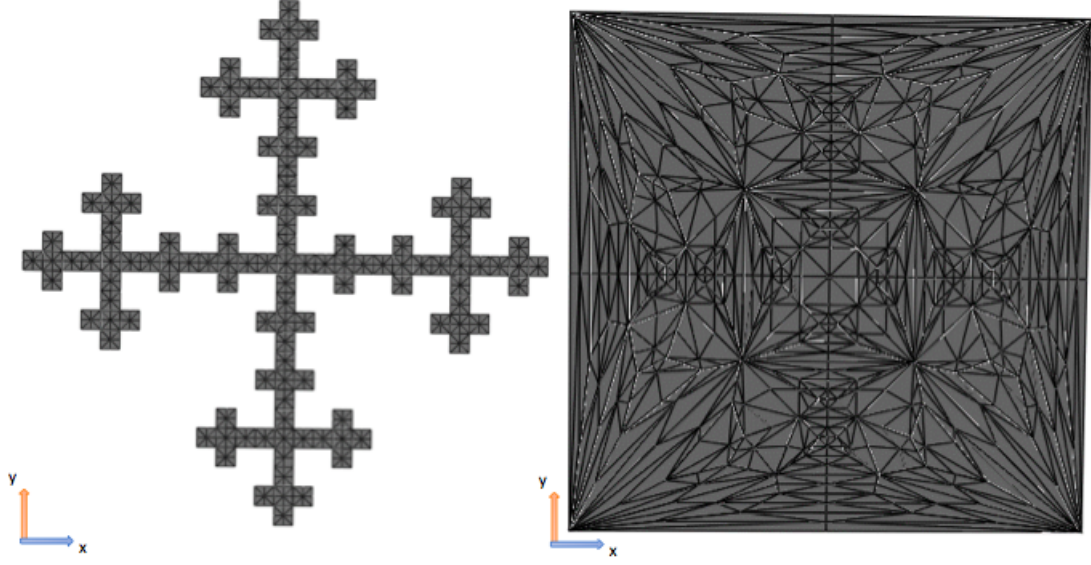
Figure 3.7: Vicsek pre-fractal $\hat{E}_3$ and it's corresponding tessellated structures $\hat{T}_3$ with the discontinuity networks.

$$\frac{D^*}{D^*t_{ps}} \int_{\Omega^*_{ps}} \rho_{ps} dV^*_{ps} + \int_{\Gamma^*_{ps}} \rho_{ps}(\underline{v}_{ps} - \underline{v}^*_{ps}) \cdot \underline{n}_{ps} d\Gamma^*_{ps} = 0 \tag{3.3}$$

$$\frac{D^*}{D^*t_{ps}} \int_{\Omega^*_{ps}} \rho_{ps}\underline{v}_{ps} dV^*_{ps} + \int_{\Gamma^*_{ps}} \rho_{ps}\underline{v}_{ps}(\underline{v}_{ps} - \underline{v}^*_{ps}) \cdot \underline{n}_{ps} d\Gamma^*_{ps} =$$

$$- \int_{\Gamma^*_{ps}} \underline{\underline{\sigma}}_{ps} \otimes \underline{n}_{ps} d\Gamma^*_{ps} + \int_{\Omega^*_{ps}} \rho_{ps} b^*_{ps} dV^*_{ps} \tag{3.4}$$

$$\frac{D^*}{D^*t_{ps}} \int_{\Omega^*_{ps}} \rho_{ps}\underline{u}_{ps} dV^*_{ps} + \int_{\Gamma^*_{ps}} \rho_{ps}\underline{u}_{ps}(\underline{v}_{ps} - \underline{v}^*_{ps}) \cdot \underline{n}_{ps} d\Gamma^*_{ps} =$$

$$- \int_{\Omega^*_{ps}} \rho_{ps}\underline{v}_{ps} dV^*_{ps} \tag{3.5}$$

$$\frac{D^*}{D^*t_{ps}} \int_{\Omega^*_{ps}} \rho_{ps}e_{ps} dV^*_{ps} + \int_{\Gamma^*} \rho_{ps}e_{ps}(\underline{v}_{ps} - \underline{v}^*_{ps}) \cdot \underline{n}_{ps} d\Gamma^*_{ps} =$$

$$- \int_{\Gamma^*_{ps}} \underline{v}_{ps}\underline{\underline{\sigma}}_{ps} \otimes \underline{n}_{ps} d\Gamma^*_{ps} + \int_{\Omega^*_{ps}} \rho_{ps}\underline{v}_{ps} dV^*_{ps} \tag{3.6}$$

where $\underline{u}$ is displacement; $\underline{\underline{\sigma}}$ is the Cauchy stress tensor [64]; $e = \upsilon + 0.5v \cdot v$ where υ is the specific internal energy. On the other hand, the equation on the tessellated space can be represented by the following equations:

$$\frac{D^*}{D^*t_{ts}} \int_{\Omega^*_{ts}} \rho_{ts} \psi_{ts} dV^*_{ts} + \int_{\Gamma^*_{ts}} \underline{v}^*_{ts} \cdot \underline{n}_{ts} d\Gamma^*_{ts} = 0 \tag{3.7}$$

56

$$\frac{D^*}{D^*t_{ts}} \int_{\Omega_{ts}^*} \rho_{ts} dV_{ts}^* + \int_{\Gamma_{ts}^*} \rho_{ts}(\underline{v}_{ts} - \underline{v}_{ts}^*) \cdot \underline{n}_{ts} d\Gamma_{ts}^* = 0 \tag{3.8}$$

$$\frac{D^*}{D^*t_{ts}} \int_{\Omega_{ts}^*} \rho_{ts}\underline{v}_{ts} dV_{ts}^* + \int_{\Gamma_{ts}^*} \rho_{ts}\underline{v}_{ts}(\underline{v}_{ts} - \underline{v}_{ts}^*) \cdot \underline{n}_{ts} d\Gamma_{ts}^* =$$

$$- \int_{\Gamma_{ts}^*} \sigma_{ts} \otimes \underline{n}_{ts} d\Gamma_{ts}^* + \int_{\Omega_{ts}^*} \rho_{ts}b_{ts}^* dV_{ts}^* \tag{3.9}$$

$$\frac{D^*}{D^*t_{ts}} \int_{\Omega_{ts}^*} \rho_{ts}\underline{u}_{ts} dV_{ts}^* + \int_{\Gamma_{ts}^*} \rho_{ts}\underline{u}_{ts}(\underline{v}_{ts} - \underline{v}_{ts}^*) \cdot \underline{n}_{ts} d\Gamma_{ts}^* =$$

$$- \int_{\Omega_{ts}^*} \rho_{ts}\underline{v}_{ts} dV_{ts}^* \tag{3.10}$$

$$\frac{D^*}{D^*t_{ts}} \int_{\Omega_{ts}^*} \rho_{ts}e_{ts} dV_{ts}^* + \int_{\Gamma_{ts}^*} \rho_{ts}e_{ts}(\underline{v}_{ts} - \underline{v}_{ts}^*) \cdot \underline{n}_{ts} d\Gamma_{ts}^* =$$

$$- \int_{\Gamma_{ts}^*} \underline{v}_{ts}\sigma_{ts} \otimes \underline{n}_{ts} d\Gamma_{ts}^* + \int_{\Omega_{ts}^*} \rho_{ts}\underline{v}_{ts} dV_{ts}^* \tag{3.11}$$

Again all these equations are applied to both pre-fractal and tessellated spaces separately. The subscripts *ps* and *ts* are used to identify pre-fractal and tessellated spaces, respectively. Although Equation (3.2) to (3.11) can be applied to Ω_{ps}^* and Ω_{ts}^* there presently exists no relationship between the physics in the two spaces, yet.

3.3 The Hole-fill maps

The theory developed in this work are not clear towards the finite similitude approach and if it can be applied on the whole physical space or some portion of it. This abstraction is crystallised in this section where similitude is restricted between portions of the physical space and tiles in a tessellation. By forming a tessellation, i.e. a collection of tiles, finite similitude can be established between the selected region in the physical space and the tessellation. The physical space are formed by using the pure IFS function listed in Appendix A [65]. In the same manner, the tessellated space is created by using the IFS for fractals with the hole-filing maps.

Going through the procedure of constructing the pre-fractal and its corresponding tessellated structure is essential because constructing the hole-fill map techniques

will be iterated in a similar method. Application of tessellated continuum mechanics to plate vibration involves the representation of the plate by a pre-fractal $\hat{E}_k$. The physics on $\hat{E}_k$ is transferred to a tessellation $\hat{T}_k$ and represented exactly at least down to the smallest element/domain considered. The construction of $\hat{E}_k$ involves the recursive application (k times) of a relatively small number of contraction maps S_i and the procedure is referred to as an IFS [5]. The recursive procedure starting from an initial domain $\hat{E}_o$ is described by the relationship $\hat{E}_k = \bigcup_{i=1} S_i(\hat{E}_{k-1})$. An initial tessellation is placed on $\hat{E}_o$ and has two functions, i.e. to form a kernel for the final mesh and to provide a mechanism for producing what is termed a hole-fill map. Prior to discussing these aspects however, it is necessary to understand how a tessellation is produced. This involves a process almost identical to that used for pre-fractal formation, i.e. starting from $\hat{T}_o = \hat{E}_o$ (again ensconced with the same initial tessellation) the recursive relationship $\hat{T}_k = \bigcup_{i=1} P_i(\hat{T}_{k-1})$ is applied. In this case, however, P_i are affine expansion maps and by design, an identical number of expansion and contraction maps are employed. As a consequence, the number of tiles in the tessellation $\hat{T}_k$ is identical to the number of pre-fractal elements in $\hat{T}_k$. In this way, a one-to-one correspondence is made between tiles and pre-fractal elements, which means that vibration analysis results performed on a tessellation. $\hat{T}_k$ can be lifted and returned to the corresponding pre-fractal $\hat{E}_k$.

Typical tessellations for some classical fractals are depicted in Figure 3.1 with affine contraction. In this figure the pre-fractal are constructed from one contracting maps that will form its whole geometry. This geometry mapping is presented by the following equation $S = (1/3)^k$. On the other hand, the hole filling maps that created the tessellated geometry for the Cantor set type of pre-fractal are equal to $P = (1/2)^k$ and the relation between the models is presented by the F-Function, which is equal to $F = (3/2)^k$.

For 2-D models, the initial domain $\hat{E}_1$ has eight tiles for the pre-fractals in Figure 3.2 and eight for those in the tessellated structure of $\hat{T}_1$, and each tile is purposely triangular. The creation of pre-fractals and tessellations is achieved independently using the recursive application of maps given in Appendix A for the pre-fractal. A hole-fill map has the function of closing holes and producing the corresponding tessellation. The independent creation of pre-fractals and tiles

means that triangular elements in each domain is a one-to-one relationship. This relationship is shown explicitly in Figure 3.2 by means of arrows connecting selection of tiles in each domain. A hole-fill map for a tile is a linear relationship which maps element from a pre-fractal domain into a different element in the tessellated space; the map is linear as a consequence of the triangular fields involved. The definition of F is achievable with the concept of a hole-fill map introduced in reference [53] advanced by Davey et al. [54]. Basically, the hole-fill map is a geometrical linear scaling procedure that is used to close the holes in the pre-fractal space and mirror it to create the tessellated space. In the hypothetical space, this procedure is used to stitch the structure, makes it continuous, and defines its characteristics. All this can be done by using linear scaling constant value, but it also could be done by using different linear scaling values for different parts in the same structure. The only case that is tested here is the constant scaling function known as local mapping. In general, the coordinates/length on the pre-fractal is expressed by x_{ps} and it is $x_{ps} \in \hat{E}_k$, while the tessellated coordinate is defined by x_{ts} which is represented by $x_{ts} \in \hat{T}_k \subset \hat{E}_k$. On the other hand, the relation between the coordinates of both spaces is represented by $x_{ts} : \hat{E}_o = \hat{E}_k \bigcup (\hat{E}_o / \hat{E}_k) \to \hat{T}_k$, and this is what we call it the local hole filling maps. These maps are a continuous, surjective but not injective function. Due to the fact that the Cantor set is a theoretical structure, the authors found that the best method to close the holes is to maintain the same initial length in 1-D and 2-D problems, which is (ℓ_o) that created the pre-fractal by using the iteration function system (IFS); and use equivalent values for the local scaling; then by using a Nanson's identity ($dV_{ts}^* = JdV_{ps}^*$ and $d\Gamma_{ps}^* = Jd\Gamma_{ts}^* \cdot F^{-1}$ [66]) for 1-D and 2-D models, for more details see the following section:

3.3.1   Linear mapping function

The core of continuum mechanics is displacement and deformation. Furthermore, the centre of this core is the deformation gradient. The deformation gradient illustrates the type of deformation that is applied to the objects. In general, there are two main types of deformations the rigid body translation and rotations or combinations of both. This is the main principle that is used to describe any process in physics at any time of that process. By following the same principle,

the direct relationship between the references can be created. And to give a better demonstration to this process, the following example is showing how the linear link is created. A vector X is used to define the coordinates of the undeformed reference, and x is a vector that is used to define the coordinates of the deformed reference. The deformation gradient denoted by $F_{x_{ts}^*}^{x_{ps}^*}$, is considered as the derivative of each element of the distorted vector with respect x to the undistorted vector X, where $x = x(X)$. So for the models in 1-D to find the geometrical relation that relates both spaces, the scaling function is simply expressed by [66]:

$$\mid F_{x_{ts}^*}^{x_{ps}^*} \mid = \frac{\partial x_i}{\partial X_j} = \frac{\ell_{ts}}{\ell_{ps}} = (\frac{\ell_o/2}{\ell_o/3})^k \tag{3.12}$$

On the other hand, the F-function for a 2-D function is created by relating the geometry of any two sides of the linear, triangular shapes through using the same concept of the Nanson's identities. Due to the complexity of the 2-D structure, this procedure is repeated for all the local initial meshes of the interested models. For this reason, a Python code is used for this task, see Appendix C. From these transportations, we can create the linear mapping tensor function $\mid F_{x^*}^{s^*} \mid$ that controls the geometry [66]: Thus

$$\mid F_{x_{ts}^*}^{x_{ps}^*} \mid = \frac{\partial x_i}{\partial X_j} = \begin{bmatrix} \frac{\partial x_1}{\partial X_1} & \frac{\partial x_1}{\partial X_2} & \frac{\partial x_1}{\partial X_3} \\ \frac{\partial x_2}{\partial X_1} & \frac{\partial x_2}{\partial X_2} & \frac{\partial x_2}{\partial X_3} \\ \frac{\partial x_3}{\partial X_1} & \frac{\partial x_3}{\partial X_2} & \frac{\partial x_3}{\partial X_3} \end{bmatrix} \tag{3.13}$$

Alternatively, Equation (3.13) must be translated into Python code to find the exact values of the second order matrix of size (3×3). This is illustrated in more details in Appendix C. The deformation gradient is found to be the link that relates details on the pre-fractal space with its corresponding trials on the tessellated space.

3.4   The Discontinuity Network (DN)

An another aspect also discussed in reference [55] is the concept of discontinuity networks (DN) mathematically denoted by D_k. A tessellation is absent of holes but a hole-fill map applied to a pre-fractal closes the holes, so the internal boundaries of the closed holes that form the tessellation are applied to the DN.

These boundaries are termed as a discontinuity network and like $\hat{E}_k$ and $\hat{T}_k$ a discontinuity network D_k is created recursively and satisfies $D_k = D_1 \bigcup_{i=1} P_i(D_{k-1})$ for $k \geq 2$. The DN are also labelled in 2-D models as in Figure 3.2 to Figure 3.7 by the red lines. Implementing the DN on a 1-D structure is essential to link the structure in 1-D for pre-fractal type a Cantor set (see Figure 3.1), where this is not a physical structure. For this reason, it needed a sort of connection. These connections are in the form of a linear equation. These equations are also needed to be mapped into the tessellated space. More information on the scaling procedure can be found in the next Chapters. Finally, the ability to create pre-fractals, tessellations and discontinuity networks recursively is an attractive feature.

3.5 Procedural considerations

This section is concerned with listing the main procedure for initiating, testing and verifying the Tessellated Continuum Mechanics (TCM) approach. This is achieved through the direct application of mechanics principles to physical structures represented by pre-fractals and on contrasting with results from the tessellated approach. Verification is first performed on a 1-D structure represented by pre-fractals for the Cantor Set. Testing a 1-D structure is beneficial as its simplicity enables the theory to be readily understood and appreciated which would not be the case for more complex structures. Presented in brief, the procedural steps for implementation of the tessellated approach with an outline of the TCM method are as follow.

3.5.1 Step 1: Tessellation formation

Recall from Section 2 that although pre-fractals and tessellations are created independently using iterated function schemes (IFS) the contraction maps involved in the tessellations are constructed to close holes on the pre-fractal $\hat{E}_1 = \bigcup_1 S_i(\hat{E}_o)$ [67]. This involves placing an initial triangular mesh on the tessellation on $\hat{E}_o = \hat{T}_o$ followed by forming $\hat{E}_1 = \bigcup_1 S_i(\hat{E}_o)$, which includes a scaled replica of the initial tessellation on each pre-fractal element of $\hat{E}_1$, i.e. on $S_i(\hat{E}_o)$. The initial mesh on $\hat{E}_o = \hat{T}_o$ although not unique, which can also be used as a means

of mesh refinement in any finite element analysis, must have sufficient elements to enable holes to be closed on $\hat{E}_1$ to form $\hat{T}_1$. The procedure is illustrated in Figure 3.2 and can be imagined to involve the morphing of $\hat{E}_1$ into $\hat{T}_1$ by means of tile distortion where selected triangular tiles are stretched linearly in order to close the holes in $\hat{E}_1$. Once $\hat{T}_1$ is established and recognising that the number of tiles on S_i and P_i are identical it is then possible to form the maps to satisfy the relationship $\hat{T}_1 = \bigcup_i P_i(\hat{T}_o)$. Note that each contraction map P_i is formed by a collection of linear sub-maps each designed to map a tile in $\hat{T}_o$ to a corresponding tile in $\hat{T}_1$. Once the maps P_i are known it is then a matter of simple recursion to create $\hat{T}_k$, see Appendix A.

3.5.2 Step 2: Direct mapping

Once $\hat{E}_k$ and $\hat{T}_k$ are known and appreciating that each has the exact same number of linear tiles it becomes possible to form the hole-fill map. As mentioned in Section 3.3 for numerical work, a direct procedure of identifying corresponding elements in $\hat{E}_k$ and $\hat{T}_k$ is preferred. For any two corresponding elements, a linear map taking points between them can be readily obtained. Under the finite similitude theory, a map taking points in an element in $\hat{E}_k$ to a corresponding element in $\hat{T}_k$ is viewed as space distortion. Invariably elements in $\hat{T}_k$ are bigger or equal to corresponding elements in $\hat{E}_k$, so the imagined distortion process is one of local piecewise expansion. A spatial increment in the physical space (where the pre-fractal resides) is related to an increment in the tessellated space (where the tessellation resides) by the relationship $dx_{ts} = F_{x_{ts}^*}^{x_{ps}^*} \cdot dx_{ps}$ [66], where $F_{x_{ts}^*}^{x_{ps}^*}$ is the hole-fill map and plays a pivotal role in the similitude theory as discussed in Section 3.3.

3.5.3 Step 3: Material properties

This section will be discussed separately in each chapter according to the type of analysis. But an overall view can be briefed here. The theory outlined in Section 3.2 incorporates a number of scaling parameters that must be set prior to application of the method, i.e. $\alpha^\rho, \alpha^u, \alpha^v$ and α^e but this has not been possible to be discussed yet. However, some of these constants are either dependent

or independent values. The tessellated approach has a peculiar advantage in that analysis results for the physical space (where the pre-fractal resides) is invariable of principal interest in any investigation. This means that the obtained results/ response on the tessellation space are only use as a tool that have no physical meaning at all but lead to the correct results once it is been lifted into the pre-fractal space. This means that the scaling parameters α^ρ, α^u and α^v can be set to any arbitrary value without affecting the results in the physical space. This can be contrasted against the typical setting for the finite-similitude theory applied to scaled experimentation; in this case results in the physical and scaled experiment have significance and constrain the parameters involved. Although the parameters α^u and α^v can be arbitrary, it is of interest to select these to imbue the tessellated space with physical attributes. Note here that the hole-fill map $F_{x_{ts}^*}^{x_{ps}^*}$ varies spatially in a piecewise manner and consequentially, in general, due to the fact that those constants mainly depend on the hole-fill maps. These scalars can also take up different values on each tile in a tessellation. A slightly more common alternative when dealing with fractals is mass conservation, since mass is matched with tessellation, which in this case applies to the whole tessellation. These choices control the α^ρ, which have a consequential impact on the choices for the other parameters, if similitude is to be enforced, which means α^ρ takes up the values J or 1, where $J = |F|$. A feature of the finite similitude is the matching of important material properties and Young's modulus and Poisson ratio play a critical part in plate deformation [68] and the relationship (check the next chapters to drive the constant scale) [69]:

$$C_{ts}^{ijnp} = \alpha^u \alpha^{-v} \alpha^{-\rho} h \beta^{-2} J^{-1} F_k^i F_l^j C_{ps}^{klrw} F_r^n F_w^p \qquad (3.14)$$

where C_{ts}^{ijnp} is the fourth order stiffness tensor [70]. This equation is arises from the energy equation as will be discussed later; α^i where $i = u, v, \rho$ is a constant scaling factor; F is the second order scaling tensor.

3.5.4   Step 4: Boundary conditions

In order to perform an analysis on the tessellated plate, it is necessary to apply the appropriate boundary conditions. The boundary conditions are those on

the pre-fractal but transferred to the tessellation under the scaling identities. Displacement is transferred under a specific relationship $\underline{u}_{ps}$, where for example a fixed boundary displacement constraint on a pre-fractal immediately transfers as a fixed displacement constraint on the tessellation. Similarly for stress (i.e. $\underline{\underline{\sigma}}_{ps}$), which confirms that free-stress boundary conditions match in each space. This is particularly pertinent for holes, which are stress-free in the physical space and must, therefore, remain stress-free in the tessellated space despite no gaps appearing at element edges in a tessellation.

3.5.5 Step 5: Analysis and post-processing

Following the creation of a tessellated structure and following application of the same boundary conditions (which can involve free stress on some inner element edges) it is a simple matter to run a traditional finite element analysis. All fields on a tessellation can subsequently be lifted back to the pre-fractal using the reverse-scaling identities, and more details will be provided later.

Chapter 4

Static Analysis of TCM

4.1 Introduction

This chapter is concerned with testing the Tessellated Continuum Mechanics (TCM) method in a 1-D and 2-D fractal as a holey-structure in static analysis. This is accomplished by demonstrating how the TCM approach can be applied to achieve very precise predictions of a pre-fractal-beam and pre-fractal-holey-plate response. This work involves the construction of the pre-fractal holey structure and its corresponding tessellated structure. Relating the pre-fractal structure to its corresponding tessellated structure as it is shown to be possible for static analysis in this chapter. This approach enables well known analytical and numerical approaches to be lifted from continuous beams to be applied in any corresponding pre-fractal beam. The analysis is based on matching physics on locally scaled spaces and investigating the effect of applying different scaling functions to create the tessellated continuum; isotropic and anisotropic scaling options are considered here.

This chapter is divided into: An introduction to the fundamental concept of the TCM theory for the static analysis is presented in Section 4.2. Then in sections 4.3 and 4.5 the main aspects of the theory are derived. Finite element (FE) analysis on 1-D structures is demonstrated in Section 4.6, while section 4.7 is concerned with the 2-D numerical analysis. Mainly this Chapter is focused in investigating the static analysis. Besides, isotropic and anisotropic scaling procedures to create a non-physical space (tessellated) is indicated. These structures are tested only by static analysis for 1-D and 2-D models. In the static

analysis perception, the structure will endure different types of excitation, then the beam's deformation is examined by means of displacement and displacement gradient.

4.2 Finite similitude: theoretical background in statics

The concept of finite similitude has appeared in the recent literature [56] and is concerned with the matching of continuum physics in two spaces. With this approach one of the spaces (the trial space) can be viewed as a distorted version of the physical space making it particularly useful for scaled experimentation. Finite similitude applies to the whole region of space, so it is not immediately transferable to tessellated continuum mechanics. However, the existence of a hole-fill map raises the possibility that the physics on pre-fractals and tessellations can be related through the mechanism of local space distortion. Each element in a pre-fractal is related in a one-to-one correspondence to an element in a tessellation (see Section 3.3) and therefore the physics between the two corresponding elements can in principle be matched locally according to the rules of finite similitude theory. The theory requires that the space-distortion map is an affine map and indeed this is the case here for the hole-fill map as confirmed by Equation (3.12). Since finite similitude is concerned with regions of space it naturally gives rise to the control volume concept. Finite similitude for tessellated continuum mechanics is therefore founded on the idea of proportional transport equations representing the governing physics in pre-fractal and tessellated elements. The transport form of the governing equations is suitable also for representing the discontinuous physics pervasive to pre-fractal and tessellated geometries and for the capture of all conservative and non-conservative physical laws. The focus in this chapter, being on the static behaviour of continuum mechanical structures, can be described by equations of the type:

$$-\int_{\Gamma_i^*} \underline{J}_i^{\psi} \cdot \underline{n}_i d\Gamma_i^* + \int_{\Omega_i^*} \rho_i b_i^{\psi} dV_i^* = 0 \qquad (4.1)$$

where Ω_i^* is a control volume (CV) in the form of a continuous open set of points surrounded by an orientable boundary Γ_i^* and the subscript i refers to the ith

element (either pre-fractal or tessellation). Furthermore, ψ is a field variable, ρ is material density, $\underline{n}_i$ is a unit normal vector pointing outward, b_i^{ψ} is a source term and $\underline{J}_i \cdot \underline{n}_i$ is a flux.

Equation (4.1) is a general form that can be used to capture the conservative and non-conservative quasi-static processes, which are assumed to be applicable on both spaces. It is convenient to drop the subscript i from Equation (4.1) at this point and relate two arbitrary corresponding elements in the pre-fractal and tessellation by the differential $dx_{ts} = F_{x_{ts}^*}^{x_{ps}^*} \cdot dx_{ps}$ [66]. Here also the subscripts ps and ts denote pre-fractal and tessellated spaces, respectively and $F_{x_{ts}^*}^{x_{ps}^*}$ is the hole-fill map that is fully described in Section 3.3, with all subscripts dropped for convenience and clarity. The relationship $dx_{ts} = F \cdot dx_{ps}$ enables Nanson's identities [71] to be applied to relate incremental volumes and areas, i.e. $d\underline{V}_{ts}^* = Jd\underline{V}_{ps}^*$ and $d\underline{\Gamma}_{ts}^* = Jd\underline{\Gamma}_{ps}^* \cdot F^{-1}$ where $J = det(F)$, $d\underline{\Gamma}_{ts}^* = \underline{n}_{ts}d\Gamma_{ts}^*$ and $d\underline{\Gamma}_{ps}^* = \underline{n}_{ps}d\Gamma_{ps}^*$. Armed with these identities Equation (4.1) provides three equations, as:

$$-\int_{\Gamma_{ps}^*} \underline{J}_{ps}^{\psi} \cdot \underline{n}_{ps}d\Gamma_{ps}^* + \int_{\Omega_{ps}^*} \rho_{ps}b_{ps}^{\psi}dV_{ps}^* = 0 \tag{4.2}$$

$$-\int_{\Gamma_{ts}^*} \underline{J}_{ts}^{\psi} \cdot \underline{n}_{ts}d\Gamma_{ts}^* + \int_{\Omega_{ts}^*} \rho_{ts}b_{ts}^{\psi}dV_{ts}^* = 0 \tag{4.3}$$

$$-\int_{\Gamma_{ps}^*} (F^{-1} \cdot \underline{J}_{ts}^{\psi}) \cdot \underline{n}_{ps}d\Gamma_{ps}^* + \int_{\Omega_{ps}^*} \rho_{ts}b_{ts}^{\psi}JdV_{ps}^* = 0 \tag{4.4}$$

where on multiplication of the last equation with $\alpha^{\psi} > 0$ (since seeking proportional physics) and contrasting with the first provides the general scaling relationships

$$\rho_{ps}\underline{b}_{ps}^{\psi} = \alpha^{\psi}J\rho_{ts}\underline{b}_{ts}^{\psi} \tag{4.5}$$

and

$$\underline{J}_{ps}^{\psi} = \alpha^{\psi}JF^{-1}\underline{J}_{ts}^{\psi} \tag{4.6}$$

or alternatively for vector equations

$$\rho_{ps}\underline{b}_{ps}^{\psi} = \alpha^{\psi}J\rho_{ts}G^{\psi} \cdot \underline{b}_{ts}^{\psi} \tag{4.7}$$

and

$$\underline{J}_{ps}^{\psi} = \alpha^{\psi}JG^{\psi} \cdot \underline{J}_{ts}^{\psi} \cdot F^{-T} \tag{4.8}$$

where G^Ψ is an invertible scaling matrix.

It should be noted that non-degeneracy of the inner product facilitates the absence of the unit normal $\underline{n}_{ps}$ from Equations (4.6) and (4.8) (since $\underline{n}_{ps}$ can point in any direction) and symmetry of the tensor ($\underline{J}^\Psi_{ps}$ and $\underline{J}^\Psi_{ts}$) immediately infers that G is a function of F with scaling accounted for by α^Ψ in Equation (4.8).

4.3   Mechanical relationships

This section is concerned with the practical implementation of the general scaling equation theory presented in the previous Section. This involves the application of particular equations pertinent to elasto-static problems. Consider first mass conservation, which in the two spaces means that M_{ps} and M_{ts} are constant where

$$M_{ps} = \int \rho_{ps} dV^*_{ps}, M_{ts} = \int \rho_{ts} dV^*_{ts} \tag{4.9}$$

which on the substitution of the Nanson identity $dV^*_{ts} = J dV^*_{ps}$ and multiplication by a scalar $\alpha^\rho > 0$ (giving $M_{ps} = \alpha^\rho M_{ts}$), provides the relationship:

$$\rho_{ps} = \alpha^\rho J \rho_{ts} \tag{4.10}$$

which ensures mass in the two spaces is proportional, where α^ρ is called the density scaling factor. Consider further momentum conservation which being a vector equation means that Equations (4.7) and (4.8) are applicable with $G^\Psi = F^{-1}$, which provides the stress tensor identity

$$\underline{\underline{\sigma}}_{ps} = \alpha^\nu J F^{-1} \cdot \underline{\underline{\sigma}}_{ts} \cdot F^{-T} \tag{4.11}$$

where, as mentioned above, because of symmetric considerations $G^\Psi = F^{-1}$, and body forces are related by $\rho_{ps}\underline{b}^\Psi_{ps} = \alpha^\nu J \rho_{ts} F^{-1} \cdot \underline{b}^\Psi_{ts}$ or in view of Equation (4.10) this reduces to $\alpha^\rho \underline{b}_{ps} = \alpha^\nu F^{-1} \cdot \underline{b}^\Psi_{ts}$.

Consider further movement, which was defined by Davey et al. [56], which in the two spaces means that $\underline{M}_{ps}$ and $\underline{M}_{ts}$ are constant where

$$\underline{M}_{ps} = \int_{\Omega^*_{ps}} \rho_{ps}\underline{u}_{ps} dV^*_{ps}, \underline{M}_{ts} = \int_{\Omega^*_{ps}} \rho_{ts}\underline{u}_{ts} dV^*_{ts} \tag{4.12}$$

which on the substitution of Nanson's identity ($dV_{ts}^* = JdV_{ps}^*$) and multiplication by scalar $\alpha^u F^{-1}$ (giving $\underline{M}_{ps} = \alpha^u F^{-1} \underline{M}_{ts}$), provides the relationship

$$\rho_{ps}\underline{u}_{ps} = \alpha^u J \rho_{ts} F^{-1} \cdot \underline{u}_{ts} \qquad (4.13)$$

but in view of Equation (4.10) reduces to $\alpha^\rho \underline{u}_{ps} = \alpha^u F^{-1} \cdot \underline{u}_{ts}$, where the choice $G^\psi = F^{-1}$ follows from the relationship $dx_{ts} = F \cdot dx_{ps}$.

The final equation of interest is energy and for elasto-statics, strain energy is of principal interest and in a control volume setting in the two spaces means that N_{ps} and N_{ts} are constant where

$$N_{ps} = \frac{1}{2} \int_{\Omega_{ps}^*} \underline{\underline{\sigma}}_{ps} : \underline{\underline{\varepsilon}}_{ps} dV_{ps}^*, N_{ts} = \frac{1}{2} \int_{\Omega_{ts}^*} \underline{\underline{\sigma}}_{ts} : \underline{\underline{\varepsilon}}_{ts} dV_{ts}^* \qquad (4.14)$$

where $\underline{\underline{\varepsilon}}$ is a strain tensor and again on the substitution of Nanson's identity $dV_{ts}^* = JdV_{ps}^*$ and multiplication by a scalar $\alpha^e > 0$ (giving $\underline{N}_{ps} = \alpha^e \underline{N}_{ts}$), provides the relationship

$$\underline{\underline{\sigma}}_{ps} : \underline{\underline{\varepsilon}}_{ps} = \alpha^e J \underline{\underline{\sigma}}_{ts} : \underline{\underline{\varepsilon}}_{ts} \qquad (4.15)$$

Thus, relationships between the tessellated and fractal spaces have been established for density, stress, displacement, force and strain energy but in order to form a closed system of equations, a constitutive law is required relating stress to strain.

4.4   Strain and constitutive relationships

The work here is limited to small deflection theory, so strain in the pre-fractal and tessellated spaces is the symmetric part of $(\partial u_i / \partial x^j)_{ps}$ and $(\partial u_i / \partial x^j)_{ts}$, respectively. A certain degree of care is required with regard to the position of subscripts and superscripts as distortion of space can lead to non-orthogonal coordinate systems. Therefore, in line with convention, upper scripts (superscripts) are termed contravariant with lower scripts (subscripts) being covariant. (Both vectors are used to give a different physical presentation to a physical quantity, for example stress must use the contravariant component while the strain uses the covariant component) The coordinate functions, displacement vectors and stress tensors introduced in Section 4.3 are all contravariant. Thus in suffix terms $dx_{ts} = F \cdot dx_{ps}$,

$\alpha^v J\underline{\underline{\sigma}}_{ts} = F \cdot \underline{\underline{\sigma}}_{ps} \cdot F^{-T}$ and $\alpha^u \underline{u}_{ts} = \alpha^\rho F \cdot \underline{u}_{ps}$, which are derivable from Equations (4.10), (4.11) and (4.13), are $dx_{ts}^i = F_j^i dx_{ps}^j$, $\alpha^v J\underline{\underline{\sigma}}_{ts}^{ij} = F_m^i \cdot \underline{\underline{\sigma}}_{ps}^{ml} \cdot F_l^j$ and $\alpha^u \underline{u}_{ts}^i = \alpha^\rho F_j^i \cdot \underline{u}_{ps}^j$. Strain however (i.e. $(\varepsilon_{ij})_{ps}$ and $(\varepsilon_{ij})_{ts}$) is required to be conjugate to stress and consequently must be covariant (since stress is contravariant) and hence the reason for the subscripts but note also that this requires the use of a covariant component of displacement with a subscript. Note further that the derivatives $\partial/\partial x_{ps}^j$ and $\partial/\partial x_{ts}^j$ are contravariant and are related via the chain rule $\partial/\partial x_{ps}^j = F_j^i \partial/\partial x_{ts}^j$ in view of the expression $dx_{ts}^i = F_j^i dx_{ps}^j$. It can be readily be deduced from $\alpha^u \underline{u}_{ts}^i = \alpha^\rho F_j^i \cdot \underline{u}_{ps}^j$ that similarly covector coefficients for displacement are related via $\alpha^\rho \underline{u}_{i,ps} = \alpha^u \beta^{-1} F_i^j \cdot \underline{u}_{j,ts}$, where $J = \beta^3$. To show this consider first the application of the chain rule $\partial/\partial x_{ps}^j = F_j^i \partial/\partial x_{ts}^i$, which gives $\alpha^\rho \partial u_{i,ps}/\partial x_{ps}^j = \alpha^u \beta^{-1} F_j^m F_l^k \partial u_{k,ts}/\partial x_{ts}^m$. Note further that Equation (4.15) in suffix notation gives:

$$\underline{\underline{\sigma}}_{ps} : \underline{\underline{\varepsilon}}_{ps} = (\underline{\underline{\sigma}}^{ij} : \underline{\underline{\varepsilon}}_{ij})_{ps} = \underline{\underline{\sigma}}_{ps}^{ij} \frac{\partial u_{ips}}{\partial x_{ps}^j} = \alpha^e J (\underline{\underline{\sigma}} : \underline{\underline{\varepsilon}})_{ps} =$$

$$\alpha^e J (\underline{\underline{\sigma}}^{ij} \underline{\underline{\varepsilon}}_{ij})_{ts} = \alpha^e J \underline{\underline{\sigma}}_{ts}^{ij} \frac{\partial u_{its}}{\partial x_{ts}^j} \tag{4.16}$$

which on substitution of $\underline{\underline{\sigma}}_{ps}^{ij} = \alpha^v J F_m^{-i} \underline{\underline{\sigma}}_{ts}^{ml} F_l^{-j}$ and $\alpha^\rho \partial u_{ips}/\partial x_{ps}^j = \beta^{-1} \alpha^u F_j^m F_i^k$ x $\partial u_{kts}/\partial x_{ts}^m$ into the left hand side gives:

$$\underline{\underline{\sigma}}_{ps}^{ij} \frac{\partial u_{ips}}{\partial x_{ps}^j} = \alpha^{-\rho} \alpha^v \alpha^u \beta^{-1} J (F_m^{-i} \underline{\underline{\sigma}}_{ts}^{ml} F_l^{-j}) (F_j^n F_i^k \frac{\partial u_{kts}}{\partial x_{ts}^n})$$

$$= \alpha^{-\rho} \alpha^v \alpha^u \beta^{-1} J (F_i^k F_m^{-i}) (F_j^n F_l^{-j}) \underline{\underline{\sigma}}_{ts}^{ml} \frac{\partial u_{kts}}{\partial x_{ts}^n} = \alpha^{-\rho} \alpha^v \alpha^u \beta^{-1} J (\delta_m^k) (\delta_l^n)$$

$$\underline{\underline{\sigma}}_{ts}^{ml} \frac{\partial u_{kts}}{\partial x_{ts}^n} = \alpha^{-\rho} \alpha^v \alpha^u \beta^{-1} J \underline{\underline{\sigma}}_{ts}^{ml} \frac{\partial u_{mts}}{\partial x_{ts}^l} \tag{4.17}$$

which matches the right hand side of Equation (4.16) on setting $\alpha^e = \alpha^{-\rho} \alpha^v \alpha^u \beta^{-1}$.

4.5 Constitutive relationships in both spaces

The scaling relationships considered thus far make no recourse to constitutive laws (although Equations (4.11) and (4.15) provide some constraint) and also

only connect a single triangular tile in a tessellation to a corresponding triangular element in the pre-fractal. To proceed further, it is necessary to find a general elasticity relationship that applies in the tessellated space. The relationship between stress and strain in the physical space is assumed linear and takes the form $\underline{\underline{\sigma}}_{ps} = \underline{\underline{\underline{C}}}_{ps}\underline{\underline{\varepsilon}}_{ps}$, where $\underline{\underline{\underline{C}}}_{ps}$ is the fourth-order stiffness tensor. In suffix notation, this relationship is of the form $\sigma_{ps}^{ij} = C_{ps} : \varepsilon_{ps,km}$ [70], where for an isotropic material (see reference [68]),

$$C_{ps}^{ijkm} = K g_{ps}^{ij} g_{ps}^{km} + \mu (g_{ps}^{ik} g_{ps}^{jm} + g_{ps}^{im} g_{ps}^{jk} - \frac{2}{3} g_{ps}^{ij} g_{ps}^{km}) \quad (4.18)$$

where K and μ are the bulk and shear modulus, which in terms of Poisson's ratio v, Young's modulus E are related by the identities $3K = E/(1-2v)$ and $2\mu = E/(1+v)$).

The symbol g_{ps}^{ij} appearing in Equation (4.18) is a 2nd-order metric tensor [71], which for an orthogonal coordinate system equates to the Kroneckal delta symbol δ^{ij}. The metric tensor is symmetric (i.e. $g_{ps}^{ij} = g_{ps}^{ji}$) and it can be seen on inspection of Equation (4.18) that the stiffness tensor is also symmetric in the following sense: $C_{ps}^{ijkm} = C_{ps}^{jikm} = C_{ps}^{ijmk} = C_{ps}^{kmij}$ [69]. With the constitutive behaviour defined on the physical space, it is now possible through the scaling identities to determine the required law for the tessellated space. This involves the substitution of the relationships $\sigma_{ps}^{ij} = C_{ps}^{ijkm}\varepsilon_{ps,km}$ and $\alpha^\rho \partial u_{i,ps}/\partial x_{ps}^j = \alpha^u \beta^{-1} F_j^m F_l^k \partial u_{k,ts}/\partial x_{ts}^m$ into $\alpha^v J \sigma_{ts}^{ij} = F_m^i \sigma_{ps}^{ml} F_l^j$ to give:

$$\sigma_{ts}^{pq} = \alpha^{-v} J^{-1} F_i^p \sigma_{ps}^{ij} F_j^q = \alpha^{-v} J^{-1} F_i^p (C_{ps}^{ijkm}\varepsilon_{ps,km}) F_j^q =$$

$$\alpha^{-v} J^{-1} F_i^p (C_{ps}^{ijkm}\frac{\partial u_{kps}}{\partial x_{ps}^m}) F_j^q = \alpha^{-v} J^{-1} F_i^p (C_{ps}^{ijkm}\alpha^{-\rho}\alpha^u \beta^{-1} F_m^l F_k^n)\frac{\partial u_{lts}}{\partial x_{ts}^n} F_j^q =$$

$$(\alpha^{-v} J^{-1} F_i^p F_j^q \alpha^{-\rho}\alpha^u \beta^{-1} C_{ps}^{ijkm} F_m^l F_k^n)\frac{\partial u_{lts}}{\partial x_{ts}^n} = C_{ts}^{pqnl}\frac{\partial u_{lts}}{\partial x_{ts}^n} = C_{ts}^{pqnl}\varepsilon_{ts,nl} \quad (4.19)$$

where it can be deduced that C_{ts}^{pqnl} possesses the same symmetric properties associated with C_{ps}^{ijkm} alluded to above.

4.6 Case Studies in 1-D

It is of interest to examine the TCM theory application in a 1-D setting as this reduces the relative complexity of the theory and allows both numerical

and analytical investigations to be investigated. The pre-fractals considered are those applied in the construction of the classical Cantor set fractal. One of the difficulties with holey 1-D constructions is that they do not form load-bearing structures and consequentially can not withstand load. To rectify this rigid elements are assumed to occupy the holes in the pre-fractals. Although somewhat artificial this assumption is particularly convenient for the tessellation as it immediately means slopes match for elements in the discontinuity network (see Figure 3.1). The 1-D models are built according to the procedure outlined in Section 3.5. The material properties along with geometrical features of the pre-fractal and tessellated models used in this study are depicted in Table 4.1. Both the pre-fractal and tessellated geometry are created by the application of contraction maps given in Section 3.3. Three levels of complexity are tested with analysis for the pre-fractals $\hat{E}_1$, $\hat{E}_2$ and $\hat{E}_3$ performed on the tessellations $\hat{T}_1$, $\hat{T}_2$ and $\hat{T}_3$ identified in Table 4.1 under the headings $k = 1, 2$ and 3. In addition, isotropic and anisotropic scaling is tested, distinguished by their hole-fill maps, which are:

$$
F_k = \beta_k \begin{bmatrix} 1 & 0 & 0 \\ 0 & 1 & 0 \\ 0 & 0 & 1 \end{bmatrix}, F_k = \begin{bmatrix} \beta_k & 0 & 0 \\ 0 & 1 & 0 \\ 0 & 0 & \beta_k \end{bmatrix}, F_k = \begin{bmatrix} \beta_k & 0 & 0 \\ 0 & \beta_k^{0.5} & 0 \\ 0 & 0 & \beta_k^2 \end{bmatrix} \tag{4.20}
$$

where $\beta_k = (3/2)^k$ and F_k is the hole-fill map connecting $\hat{E}_k$ to $\hat{T}_k$.

The hole-fill maps in Equation (4.20) are uniform and when applied to $\hat{E}_k$ have the effect of closing the holes whilst at same time maintaining the overall initial length of the structure. The material properties for the tessellation are determined using Equations (4.10) and (3.14) or (4.19), which are presented in Table 4.1 along with associated properties for the pre-fractal. The scaling factors α^ρ, α^u and α^v affect the predictions on the pre-fractals and are listed in Table 4.1 and Table 4.2.

All numerical analysis performed is done with commercial FE software ABAQUS (version 6.13), using a linear beam elements type B32 [72] for both pre-fractal and tessellated structures.

Table 4.1: Material properties and dimensions for 1-D pre-fractal and isotropic scaling tessellated cases.

k		1	2	3
Scalar Constant	α^u	1.000	1.000	1.000
	α^v	1.500	2.25	3.375
	h	1.000	1.000	1.000
Pre-fractal	L_{ps} (m)	0.3333	0.1111	0.0370
	ρ_{ps} (kg/m^3)	1.000	1.000	1.000
	E_{ps} (kg/m^2)	1.000	1.000	1.000
Tessellated	L_{ts} (m)	0.5000	0.2500	0.1250
	ρ_{ts} (kg/m^3)	0.2700	0.0878	0.0026
	E_{ts} (kg/m^2)	0.6666	0.4444	0.2963

Table 4.2: Material properties and dimensions for 1-D pre-fractal and anisotropic tessellated scaling cases.

Properties		Case 1	Case 2
Pre-fractal	L_{ps} (m)	0.037	0.037
Scalar Constant	α^ρ	1.000	1.000
	α^u	3.375	11.39069
	α^v	3.375	11.39069
	h	1.000	1.000
Tessellated	L_{ts} (m)	0.125	0.125
	W_{ts} (m)	0.02	0.037
	Th_{ts} (m)	0.06750	0.228
	ρ_{ts} (kg/m^3)	0.088	0.0142
	E_{11} (N/m^2)	8.64976	18.076
	E_{22} (N/m^2)	0.759375	1.789
	E_{33} (N/m^2)	1.120	1.500
	G_{11} (N/m^2)	1.28145	2.587
	G_{12} (N/m^2)	49.2631	57.246
	G_{23} (N/m^2)	14.5965	16.586

4.6.1 Analytical verification

In order to test the efficiency of the ABAQUS numerical model, comparison is made against a general analytical derived solution for $\hat{E}_k$ with $\beta_k = (3/2)^k$. A Bernoulli cantilever beam (i.e. a beam with clamped-free (CF) boundary conditions) is considered with a lateral load of magnitude applied to the free end. The equivalent tessellated model is correspondingly a CF beam, but in this case, the covariant displacement is required to satisfy the relationship $\alpha^p \underline{u}_{ps} = \alpha^u F^{-1} \cdot \underline{u}_{ts}$, which for $\alpha^p = \alpha^u = 1$ and with $F = F^k$ taking any of the forms in Equation (4.20) gives $w_{ps} = \beta F_{33}^{-1} w_{ts}$ for lateral displacement in the z-direction, where $F_{33} = \beta_k$ or $F_{33} = \beta_k^2$. Both beams are presented in Figure 4.1 on $\hat{E}_1$ for the pre-fractal and on $\hat{T}_1$ for the tessellation with the material properties presented in Table 4.1.

Each Cantor set structure $\hat{E}_k$ consists of 2^k deformable parts of equal length and for $k > 1$ includes $2^k - 1$ rigid segments (holes) as depicted in Figure 3.1. Enumerating nodes from left to right (starting from $i = 1$) results in a segment placed between coordinates x^i_{ps} and x^{i+1}_{ps} being rigid for even i and deformable if i is odd. The Bernoulli cantilever beam requires a solution to $w''_{ps} = M_{x,ps}/E_{ps}I_{ps}$, where $M_{x,ps} = Q_{ps}(\ell_o - x_{ps})$, E_{ps} is Young's modulus, I_{ps} is the second moment of area and ℓ_o is the beam length. Thus deformation in any deformable segment is a cubic polynomial and takes the general form [71]:

$$w_{ps}(\hat{x}_{ps}) = \frac{Q_{ps}\ell_o^3}{E_{ps}I_{ps}}\left(\frac{(\hat{x}_{ps} - \hat{x}^i_{ps})^2}{2} - \frac{(\hat{x}_{ps} - \hat{x}^i_{ps})^3}{6}\right) + \frac{dw_{ps}}{d\hat{x}_{ps}}\Big|_{x^i_{ps}}(\hat{x}_{ps} - \hat{x}^i_{ps}) + w_{ps}\big|_{x^i_{ps}}$$

(4.21)

where $\hat{x}_{ps} = x_{ps}/l_o$ and $x^i_{ps} \leq x_{ps} \leq x^{i+1}_{ps}$. A rigid element satisfies the equation $w''_{ps} = 0$ and takes the form

$$w_{ps}(\hat{x}_{ps}) = \frac{dw_{ps}}{d\hat{x}_{ps}}\Big|_{x^i_{ps}}(\hat{x}_{ps} - \hat{x}^i_{ps}) + w_{ps}\big|_{x^i_{ps}} \qquad (4.22)$$

which is readily obtained from Equation (4.21) in the limit $E_{ps} \to \infty$ (A sample of the analytical results is introduced in Appendix B for $k = 3$).

The presented solutions for the general model are shown in Figure 4.2. These solutions for displacement and slope for different pre-fractals are presented in Figure 4.3 and Figure 4.4. Included in the figures are ABAQUS predictions, which provide almost exact replication of the analytical output. An alternative

Figure 4.1: Pre-fractal and tessellated cantilever beams for $k = 1$.

Figure 4.2: Pre-fractal and tessellated cantilever beams for $k = 3$.

route to analytical solutions on $\hat{E}_k$ is via the similitude theory and the lifting of these from $\hat{T}_k$. This can be achieved by first determining the solution to $w''_{ts} = M_{x,ts}/E_{ts}I_{ts}$, where $M_{x,ts} = Q_{ts}(\ell_o - x_{ts})$, E_{ts} is the Young's modulus; I_{ts} is the second moment of area and ℓ_o is the beam length. The tessellated beam is absent of rigid segments (as these appear as discontinuities) and the deformable segments are described by an equation similar in form to (4.21), i.e.

$$w_{ts}(\hat{x}_{ts}) = \frac{Q_{ts}\ell_o^3}{E_{ts}I_{ts}}\left(\frac{(\hat{x}_{ts} - \hat{x}_{ts}^i)^2}{2} - \frac{(\hat{x}_{ts} - \hat{x}_{ts}^i)^3}{6}\right) + \frac{dw_{ts}}{d\hat{x}_{ts}}\Big|_{x_{ts}^i}(\hat{x}_{ts} - \hat{x}_{ts}^i) + w_{ts}\Big|_{x_{ts}^i} \quad (4.23)$$

75

where $\hat{x}_{ts} = x_{ts}/l_o$ and $x_{ts}^i \leq x_{ts} \leq x_{ts}^{i+1}$.

The lifting of Equation (4.21) to arrive at Equation (4.23) is achieved on substitution of the following maps and identities: $Q_{ts} = \alpha^{-v}F_{33}Q_{ps} = \beta^{-1}F_{33}Q_{ps}$, $I_{ts} = F_{22}F_{33}^3 I_{ps}$, $\hat{x}_{ts} - \hat{x}_{ts}^i$, $\hat{x}_{ps} - \hat{x}_{ps}^i$, $w_{ts} = \beta F_{33}^{-1}w_{ps}$, and from Equation (3.14) $E_{ts} = \beta^{-2}J^{-1}F_{11}^4 E_{ps} = \beta^{-2}F_{11}^3 F_{22}^{-1}F_{33}^{-1}E_{ps}$, since $J = \beta^3 = F_{11}F_{22}F_{33}$.

An alternative approach to confirm Equation (4.21) and (4.19) or (3.14) are related is directly form the governing equation $w_{ts}^{''} = M_{x,ts}/E_{ts}I_{ts}$ and $w_{ps}^{''} = M_{x,ps}/E_{ps}I_{ps}$, which on substitution of pertinent identities takes the form [73]:

$$\frac{d^2 w_{ts}}{dx_{ts}^2} = \frac{\beta}{F_{11}^2 F_{33}} \frac{d^2 w_{ps}}{dx_{ps}^2} =$$

$$\frac{M_{x,ts}}{E_{ts}I_{ts}} = \frac{\beta^{-1}F_{11}F_{33}M_{x,ps}}{(\beta^{-2}F_{11}^3 F_{22}^{-1}F_{33}^{-1}E_{ps})(F_{22}F_{33}^3 I_{ps})} = \frac{\beta}{F_{11}^2 F_{33}} \frac{M_{x,ps}}{E_{ps}I_{ps}} \qquad (4.24)$$

where use is made of the identity $M_{x,ts} = \beta^{-1}F_{11}F_{33}M_{x,ps}$ [74], which confirms that with similitude the solution to $w_{ts}^{''} = M_{x,ts}/E_{ts}I_{ts}$ is also a solution to $w_{ps}^{''} = M_{x,ps}/E_{ps}I_{ps}$ and vice versa.

ABAQUS results for the tessellation for different values of k are depicted in Figure 4.5 and Figure 4.6. It is clear from the figures (including Figure 4.3 and Figure 4.4) that very precise predictions are achievable with ABAQUS on both pre-fractals and tessellations. Now that the tessellated approach has been confirmed analytically for a simple cantilever beam and the accuracy of the ABAQUS models confirmed it remains to test the lifting process for both isotropic and anisotropic cases in Equation (4.21).

4.6.2 Isotropic lifting process

The beam depicted in Figure 4.2 is reanalysed numerically for isotropic scaling to test the lifting of results. The results on a pre-fractal can be obtained by two independent routes, i.e. by means of direct analysis and indirectly by lifting results from the tessellation. The lifting process is of principal interest here to illustrate how it is possible to achieve results of high accuracy on a continuum. However, the fact that two routes of analysis are possible provides a direct means for checking accuracy even when analytical solutions are unavailable although in this particular instance these are presented in Figure 4.7 and Figure 4.8. The
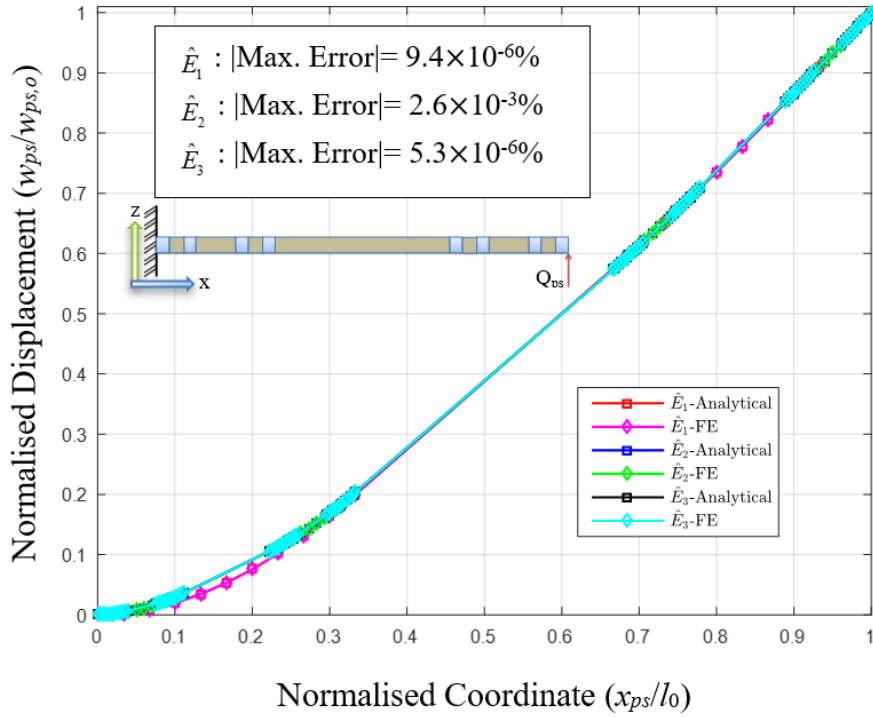
Figure 4.3: Analytical and FE predictions of deflection on different pre-fractal cantilevers
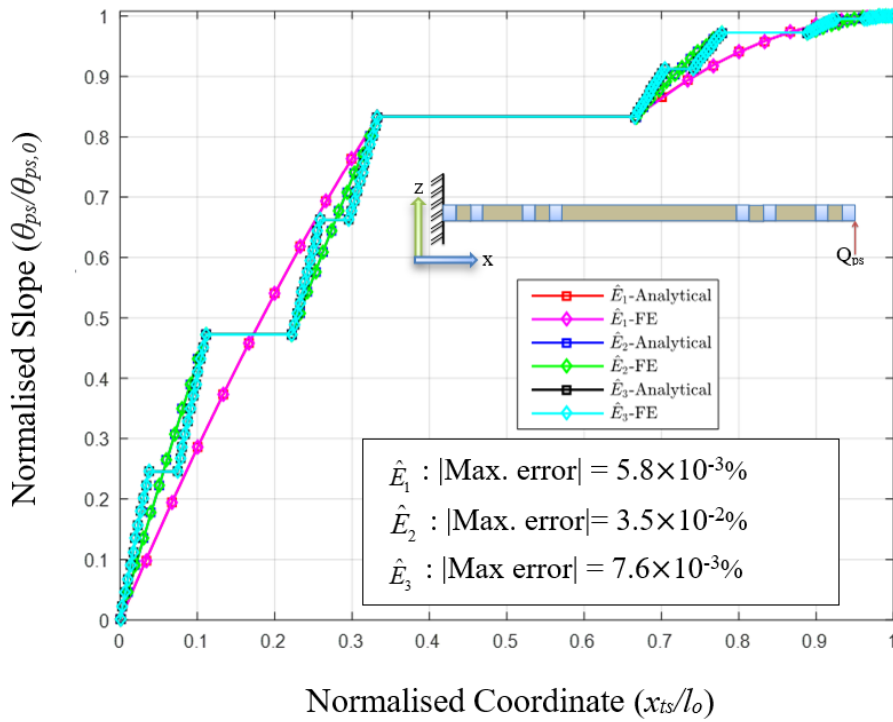
Figure 4.4: Analytical and FE predictions of slope on different Cantor pre-fractal cantilevers.
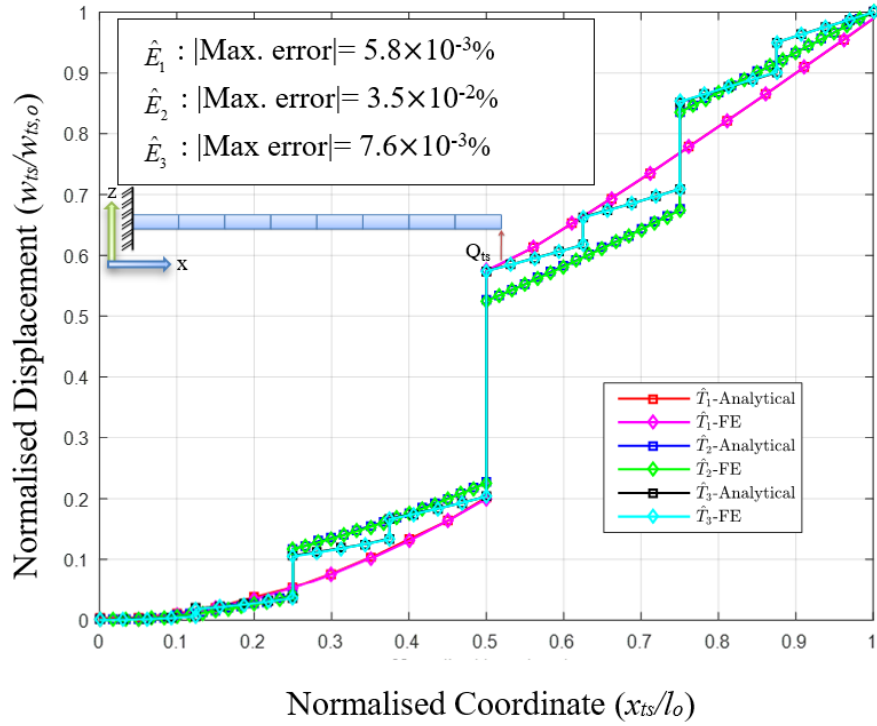
Figure 4.5: Analytical and FE predictions of deflection on different Cantor tessellated cantilevers.
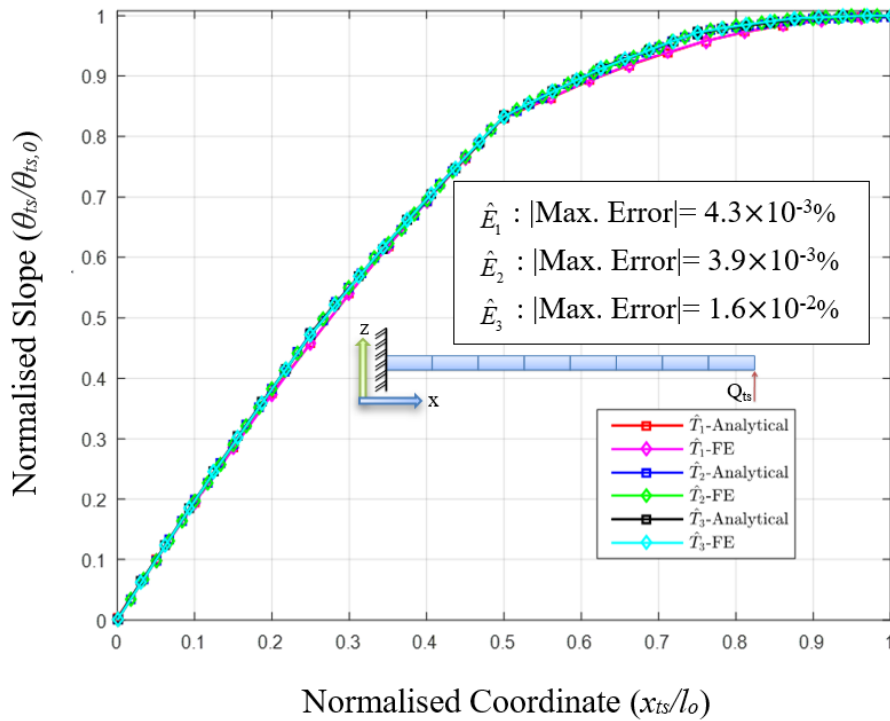
Figure 4.6: Analytical and FE predictions of slope on different tessellated cantilevers.
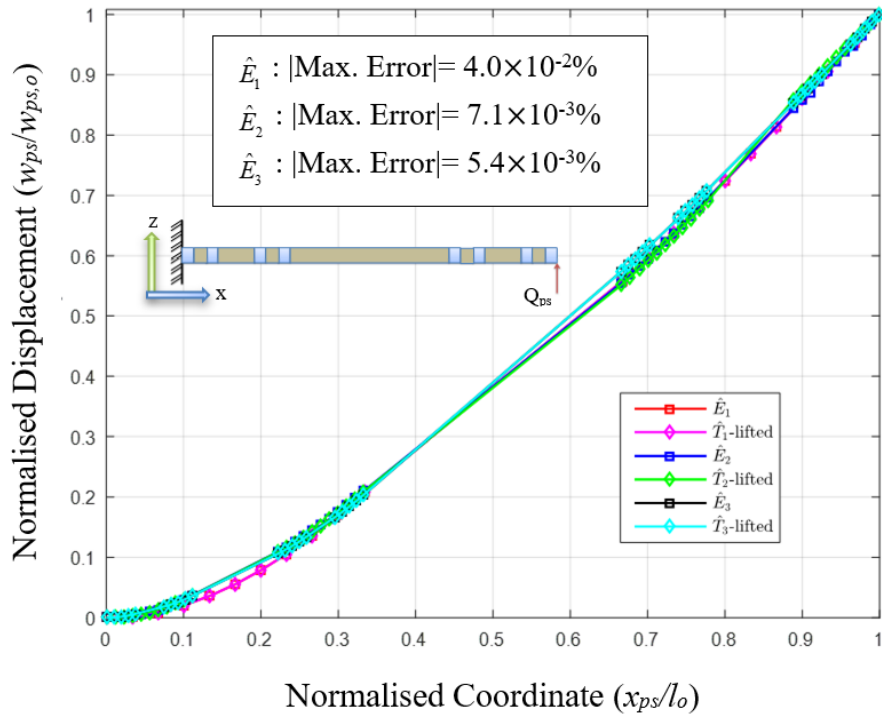
Figure 4.7: Direct numerical and lifted tessellated deflections for cantilever pre-fractals.
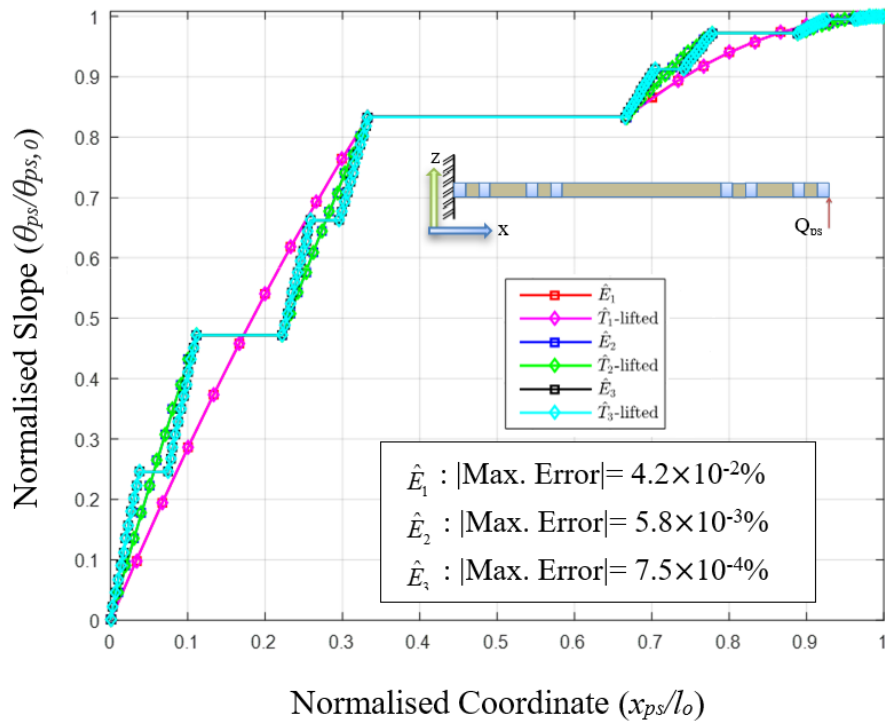
Figure 4.8: Direct numerical and lifted tessellated slope predictions for cantilever pre-fractals.

79

lifted and direct numerical predictions are provided in Figure 4.7 and Figure 4.8 on $\hat{E}_k$ for $k = 1 : 3$. Note from Figure 4.7 and Figure 4.8 that the maximum absolute errors involved are extremely small but it is important to appreciate that numerical predictions are being contrasted against numerical predictions. Thus, some care is required here because with similitude, and with the same number of elements employed in both analyses, extremely small errors are anticipated yet absolute errors can with a coarse mesh remain large [75]. The results of Figure 4.7 and Figure 4.8 confirm that absolute errors are small in this case also. The tests confirm the equivalence of the direct and the tessellated approach.

4.6.3   Anisotropic lifting process

This section is concerned with anisotropic scaling of pre-fractal elements for the formation of a tessellation for the determination of lateral beam deformation of the CC beam depicted in Figure 4.2. The beam is loaded by an off-centre, point load located at the left edge of the central rigid segment (hole). Note that the central rigid segment (hole) is present for all $\hat{E}_k$ for all $k \geq 1$, so the load-point position does not change with k. The two anisotropic hole-fill maps presented in Equation (4.20) are applied. The tests are designed to illustrate that anisotropic scaling is permissible and that predicted results on the pre-fractals (lifted from a tessellation) do not depend on the form of the hole-fill map. The material properties of the pre-fractal are identical to those used in Sections 4.6.1 and 4.6.2 and details are provided in Table 4.2. Note that Young's modulus is for convenience set to unity for the pre-fractal material since dimensionless outputs are of principal interest. The density and elastic properties for the tessellated material are determined using Equations (4.10) and (3.14), respectively and are recorded in Table 4.2. The predictions for the tessellated beams on $\hat{T}_3$ are presented in Figure 4.9 and Figure 4.10. It is apparent on examination of the figures that both beams provide near identical outputs despite having different widths and heights. Recall that each tessellated beam is created on application of the anisotropic scaling maps in Equation (4.20) to the pre-fractal elements, which has the effect of producing different lateral dimensions. The reason for the near identical results in Figure 4.11 and Figure 4.12 is not because displacements are identical but as a consequence of the dimensionless coordinates used on the

axes of these figures. The displacement and slope of the pre-fractal CC beam on $\hat{E}_3$ can be found in Figure 4.13 and Figure 4.14. Observe that three methods of prediction are presented, i.e. the direct method, and the two lifted tessellated results obtained on employing the two anisotropic maps in Equation (4.21). All methods provide consistent results to very high accuracy and the source of error can be associated with rounding errors in the numerical calculations. For consistency the number of finite elements used in each deformable pre-fractal segment (and tile) was set equal to 10 as this was found to provide good accuracy. This number or elements was applied for the entire numerical analysis of the beam structures.
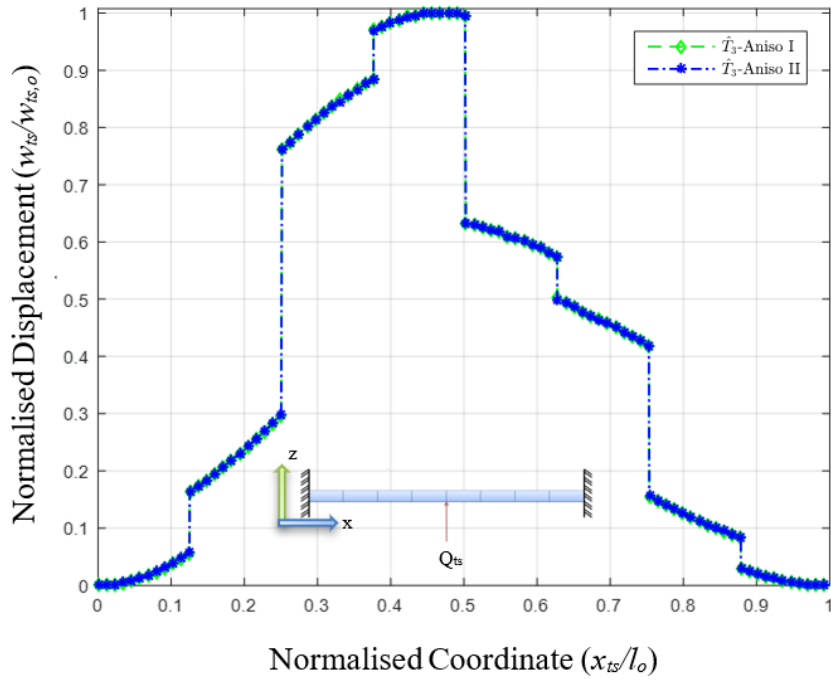
Figure 4.9: FE prediction of deflection on the tessellated CC beam $\hat{E}_3$.
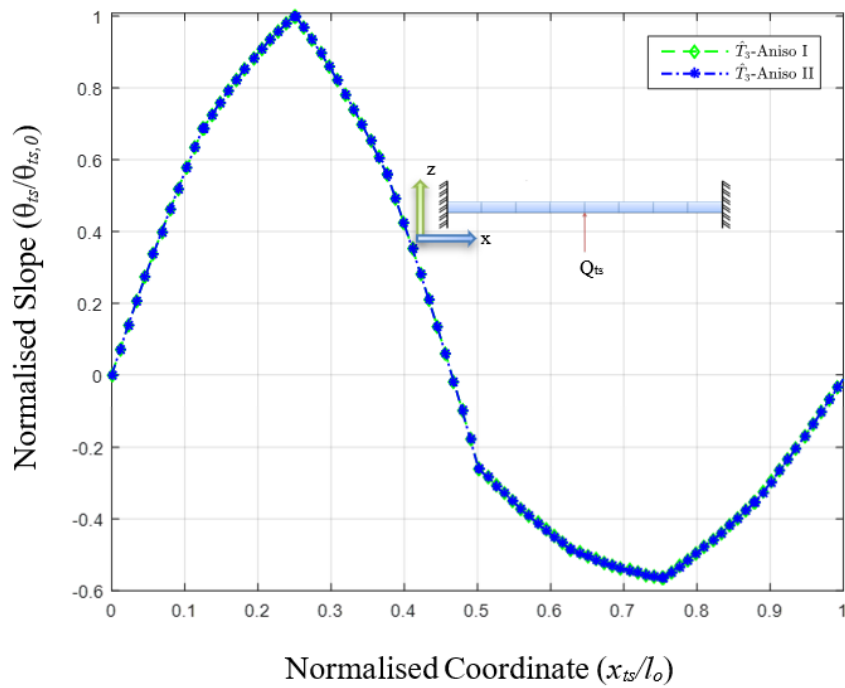
Figure 4.10: FE prediction of slope on the tessellated CC beam $\hat{T}_3$.
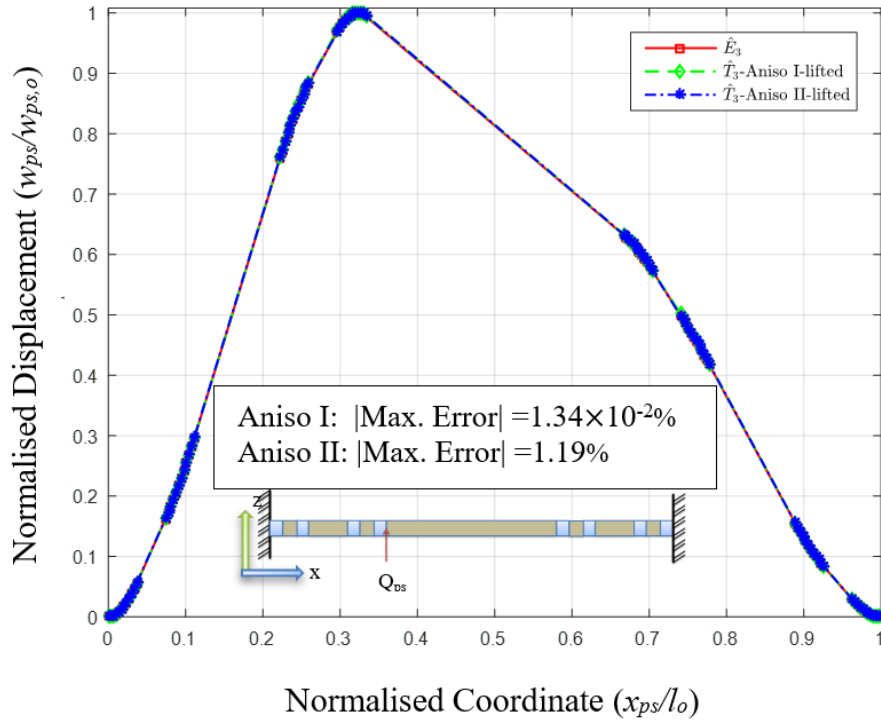
Figure 4.11: Direct numerical and lifted tessellated deflection for the pre-fractal CC beam $\hat{E}_3$.
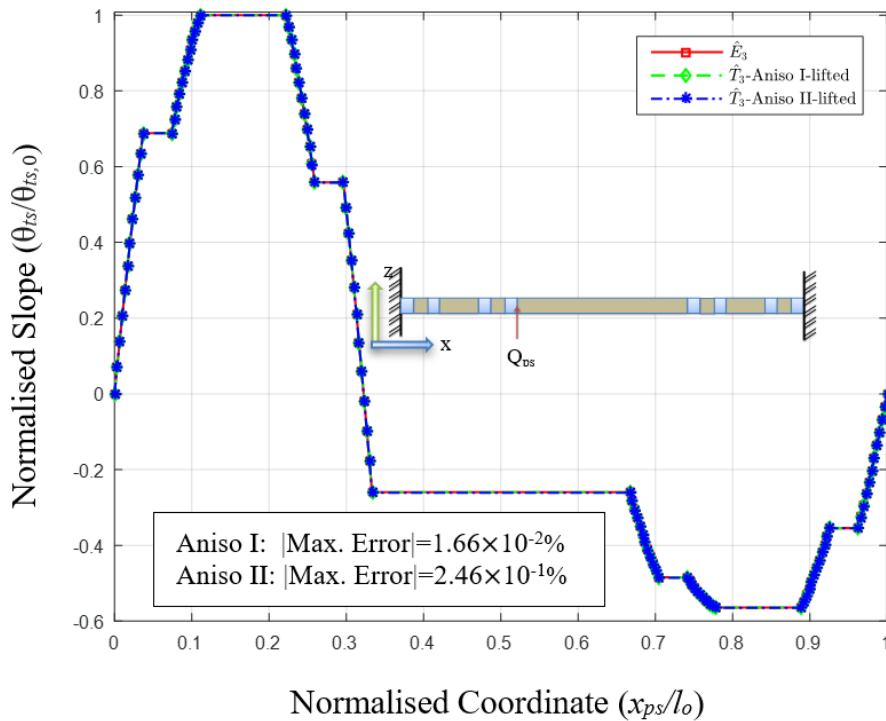
Figure 4.12: Direct numerical and lifted tessellated slope for the pre-fractal CC beam $\hat{E}_3$.

4.7   Case Studies in 2-D

The main focus of this work is the analysis of 2-D pre-fractal plate structures since these are found in engineering applications as discussed in the introduction. The pre-fractals analysed here are employed in the construction of two well-known traditional fractals, i.e. the Sierpinski Carpet and Vicsek fractal. Unlike the 1-D models considered in Section 4.6 there is no need for the employment of artificial rigid elements since holey plates are load-bearing structures. Three different levels of complexity are analysed with the meshes employed in the analysis of the Sierpinski carpet found in Figure 3.2, Figure 3.3 and Figure 3.4 for both pre-fractals and tessellations. Figure 3.5, Figure 3.6 and Figure 3.7 illustrated the Vicsek fractal for the first three complexities. Material properties and dimensions are presented in Table 4.3, with both the Sierpinski and Vicsek sharing the same material properties and overall dimensions. It is important to appreciate that the meshes depicted in these figures are generated as part of the recursive procedure for the generation of pre-fractals and tessellations. In this case an initial tessellation consisting of eight elements was placed on $\hat{E}_o$ and $\hat{T}_o$. The number of elements on $\hat{E}_1$ and $\hat{T}_1$ is correspondingly equal to the number of elements on $\hat{E}_o$ multiplied by the number of contraction maps used in the IFS, which for the Sierpinski carpet is eight. The numbers of elements employed in the analysis of both the Sierpinski and Vicsek pre-fractals are given in Table 4.4. The contraction maps employed are listed in Appendix A for the Sierpinski Carpet and Vicsek fractal, respectively. Likewise the contraction maps used to create corresponding tessellated models for both structures are also provided in Appendix A. Note that both pre-fractals and tessellations involve the same number of contraction maps.   The hole-fill maps for the 2-D plates generally involve off-diagonal terms to account for shear and take the form [66]:

$$F_k = \beta_k \begin{bmatrix} \beta_{k,11} & \beta_{k,12} & 0 \\ \beta_{k,21} & \beta_{k,22} & 0 \\ 0 & 0 & 1 \end{bmatrix} \tag{4.25}$$

where unlike the 1-D cases considered in Section 4.6, F_k is seldom uniform as hole-filling is not a spatially uniform process.

The determination of the hole-fill maps is achieved using the object-oriented

Table 4.3: Material properties and dimensions for the 2-D pre-fractal models.

Properties	Values
Length (m)	0.900
Width (m)	0.900
Thickness (m)	0.010
Density (kg/m^3)	2698.8
Elasticity (GN/m^2)	68.900
Poisson's ratio	0.300

Table 4.4: Number of elements on pre-fractal and tessellated for the 2-D models.

Structure Type	$k = 1$	$k = 2$	$k = 3$
Sierpinski Carpet	64	512	4096
Vicsek fractal	40	200	1000

programming language Python, which facilitates the transfer of data to the ABAQUS software (check Appendix C for more information about how to implement this code to create the 2-D models). Unlike the 1-D analysis analytical solutions are unavailable, so the tessellated lifted solutions are contrasted against direct numerical analysis performed in the commercial FE software ABAQUS. Shell elements of type SR8 [72] are used to model the structures in both the tessellated and pre-fractal spaces.

4.7.1 Numerical verification of Sierpinski Carpet

The Sierpinski Carpet pre-fractals presented in Figure 3.2, Figure 3.3 and Figure 3.4 are considered as holey-plates with CCCC boundary conditions subject to lateral pressure of magnitude R_{ps}. The corresponding tessellated structure possesses identical boundary conditions but a pressure of magnitude R_{ts}, which varies over the surface of the tessellation determined by Equation (4.11) with F substituted by F_k of Equation (4.25). Although the density of the plate plays no significant part in the static analysis it is nonetheless determined using Equation (4.10). Equation (3.14) plays a critical role in determining the elastic properties of the tiles in the tessellation. The distributions of the normal values of Young's

moduli on the tessellation, as determined by Equation (4.11), are presented in Figure 4.13 to Figure 4.17. The figure reveals just how geometric complexity from a pre-fractal is transferred into material complexity on a tessellation. Structural responses of the plates are calculated numerically by using ABAQUS (version 6.13) and SR8 shell elements were found to give the best results on both pre-fractal and tessellated spaces. Although a uniform pressure is applied on the pre-fractal plate the pressure over the tessellated plate as calculated using Equation (4.11) takes on a more complex pattern as apparent on examination of Figure 4.14. Confirmation of the validity of the approach is achieved by comparing of the results between the pre-fractal responses in terms of lateral deformation contrasted to the lifted response from the tessellated plate. These results are presented in Figure 4.15 and Figure 4.16, where the lifted results are almost identical to the direct pre-fractal predictions within the bounds of rounding errors in the numerical calculations. An overall picture of the lateral behaviour of the tessellated and pre-fractal plates is presented in Figure 4.17.

4.7.2   Processing time analysis on Sierpinski Carpet

Although the prime focus of the work is to determine whether it is possible to analysis holey-plates to high accuracy it is interest to investigate the extent of processing and computing time discrepancies between the two approaches. The processing times required to build the pre-fractals and corresponding tessellations are presented in Figure 4.18. Not too unexpectedly processing time for model construction for the tessellated structures is slightly longer than the direct approach due to the time required determining the element stiffness matrices. Note however that corresponding pre-fractals and tessellations have identical numbers of unknowns and equations [75].

4.7.3   Numerical Verification of Vicsek fractal

The Vicsek pre-fractals presented in Figure 3.5 to Figure 3.7 are selected to provide a significant challenge for the tessellated approach. These pre-fractals are significantly different in form from a continuous square plate structure and
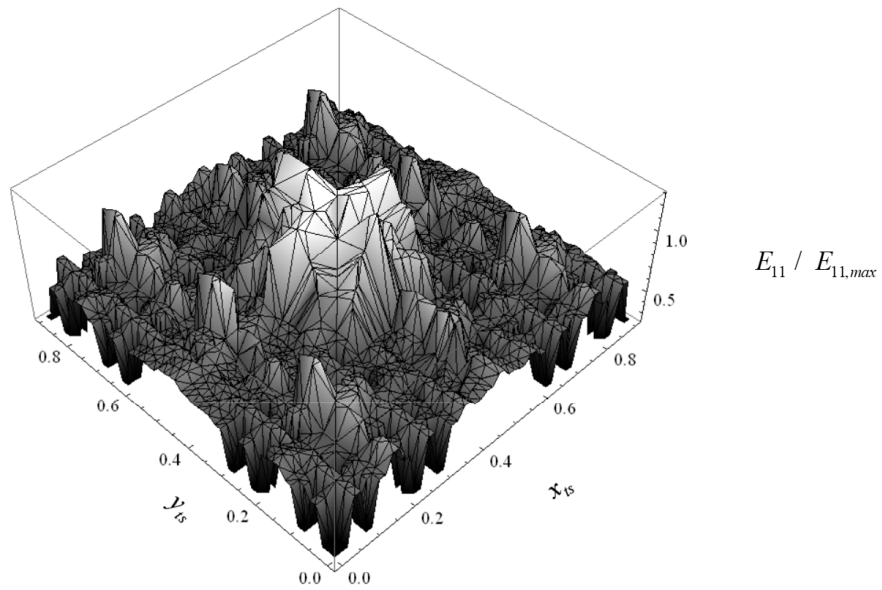
Figure 4.13: Normalised Young's moduli for $E_{11}/E_{11,max}$ on Sierpinski Carpet tessellation $\hat{T}_3$.
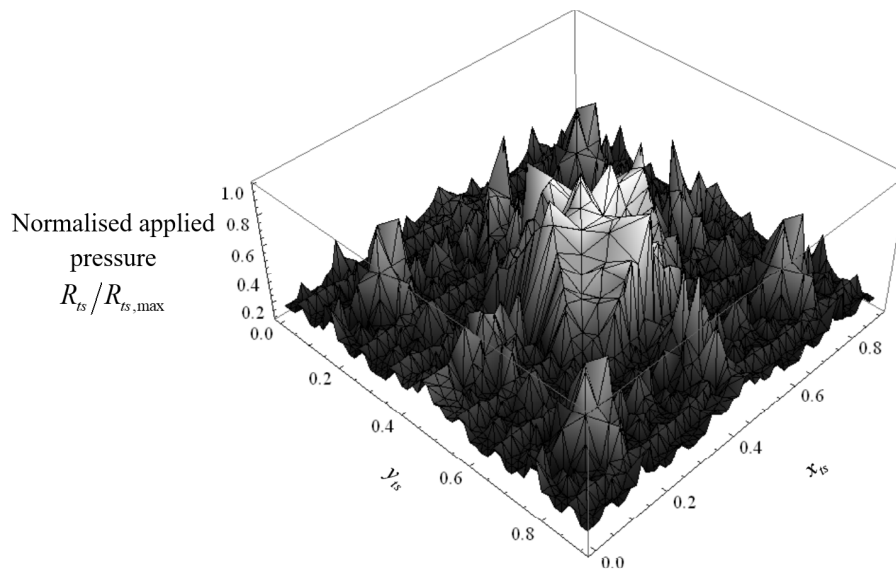
Figure 4.14: Normalised pressure distribution for $R_{ts}/R_{ts,max}$ on Sierpinski Carpet tessellation $\hat{T}_3$.
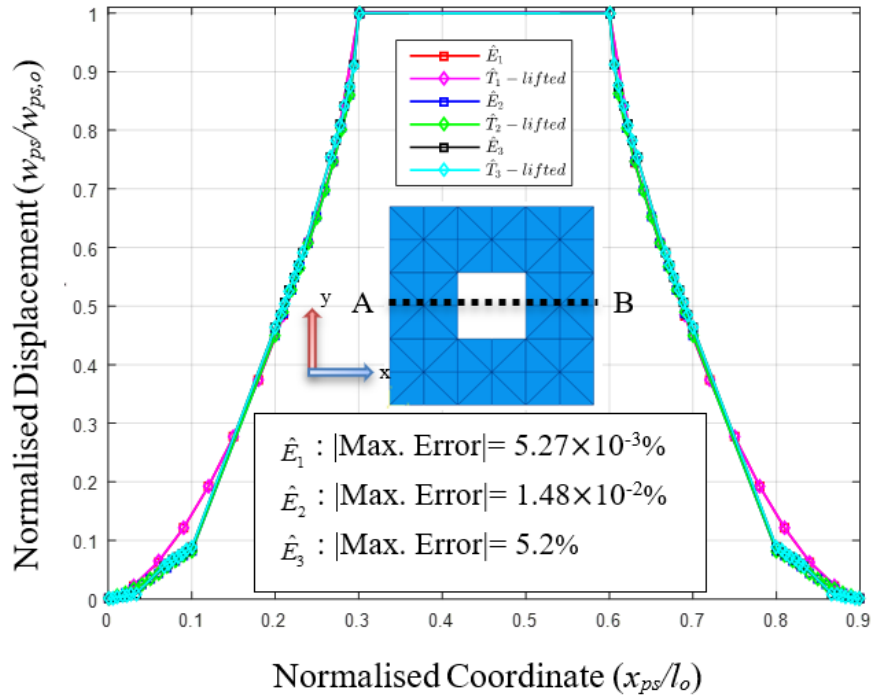
Figure 4.1 5 Direct numerical and lifted tessellated deflection for the Sierpinski carpet pre-fractal CCCC plate subjected to pressure loading.
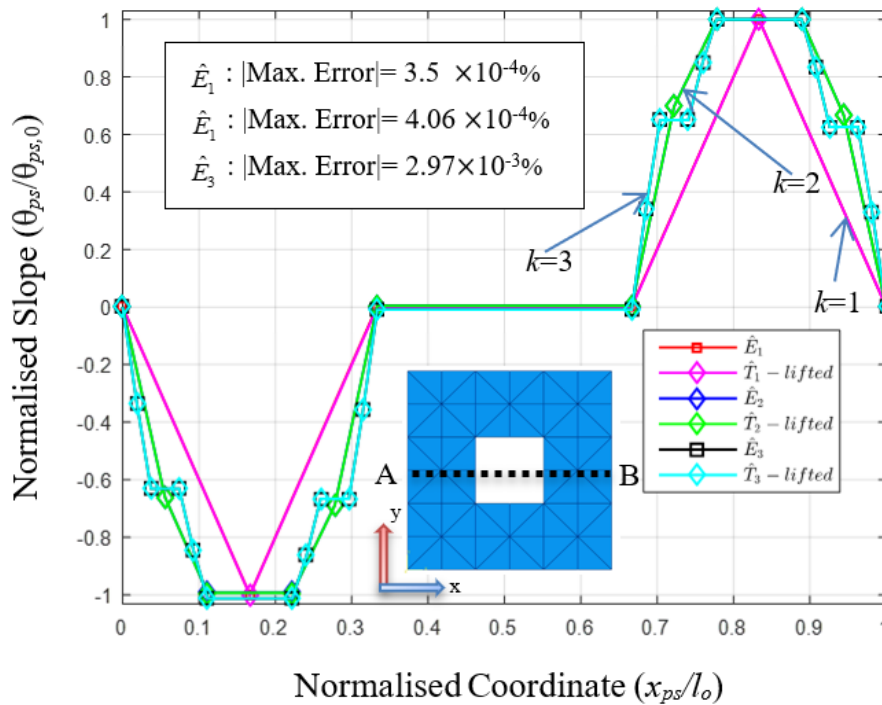
Figure 4.16 Direct numerical and lifted tessellated slope ($\theta_{ps} = \partial w_{ps}/\partial x_{ps}$) for the Sierpinski carpet pre-fractal CCCC plate subjected to pressure loading.

(a) Normalised lateral displacement (w_{ps}) in $\hat{E}_3$

(b) Normalised lateral displacement (w_{ts}) in $\hat{T}_3$

(c) Normalised slope ($\partial w_{ps} / \partial x_{ps}$) in $\hat{E}_3$

(d) Normalised Slope ($\partial w_{ts} / \partial x_{ts}$) in $\hat{T}_3$
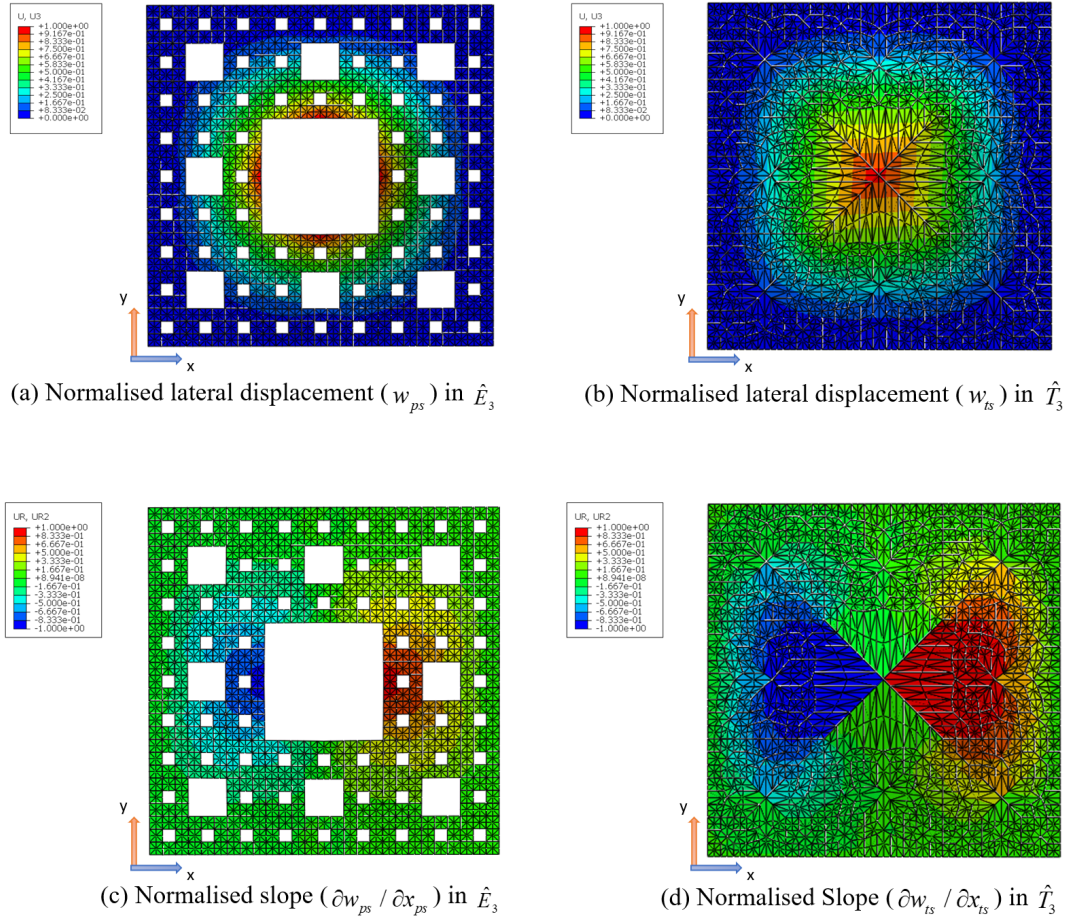
Figure 4.17: Overall response of CCCC plates $\hat{E}_3$ and $\hat{T}_3$ for the Sierpinski Carpet subjected to pressure loading.

at first glance it might be considered impractical if not impossible to analyse these types of structure on a square plate. However, the tessellated approach is able to achieve this to very high accuracy. The meshes used in the analysis are depicted in Figure 3.5 to Figure 3.7, which are generated by the recursive process with again an initial tessellation of 8 tiles on $\hat{E}_o$ and $\hat{T}_o$. Note the severity of the skewed elements that appear on the tessellations. Numerical issues typically associated with skewed elements do not arise with the tessellated approach because skewness and deviation in material properties counteract each other to represent the behaviour on the pre-fractals. Both the pre-fractals and tessellation are under CCCC boundary conditions although only the four outermost edges of the pre-fractals are clamped. A displacement boundary condition has been applied on the centre of each model of arbitrary magnitude. Contour plots for
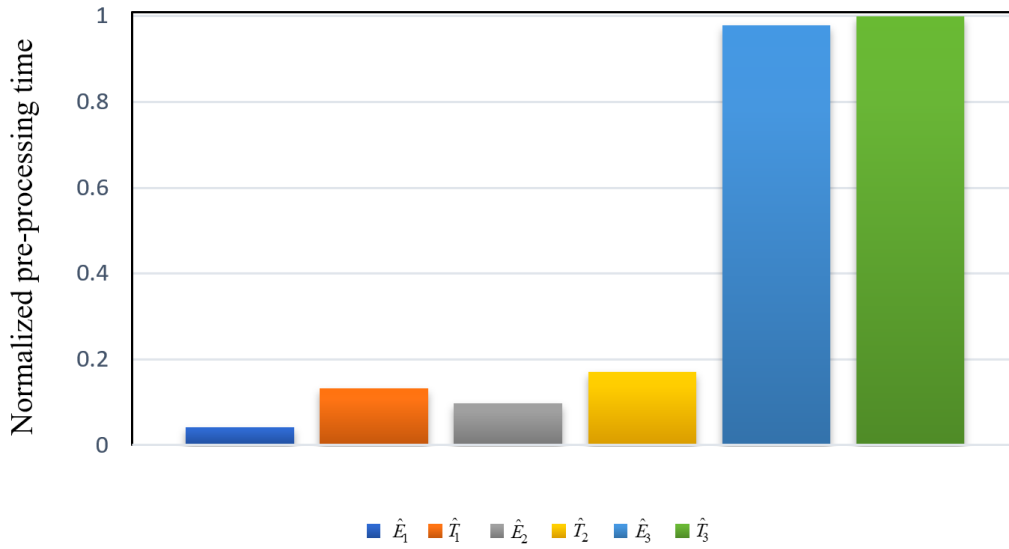
Figure 4.18: Normalised computational requirements for building pre-fractal and tessellation models.

pre-fractal structure $\hat{E}_3$ with its corresponding tessellation $\hat{T}_3$, are represented in Figure 4.19 for lateral deformation and slope. The structures' deformations are captured in Figure 4.20 and Figure 4.21 in terms of out of plane deformation and slope. It is evident from these figures that high accuracy is achievable with the tessellated approach. Note that the contour plot in the tessellated space (Figure 4.19) has similarities with contours on the associated pre-fractals, since the latter is obtained by the lifting process. However, recall that the out-of-plane displacement suffers no scaling so pre-fractals and tessellations have near-identical values on corresponding elements.
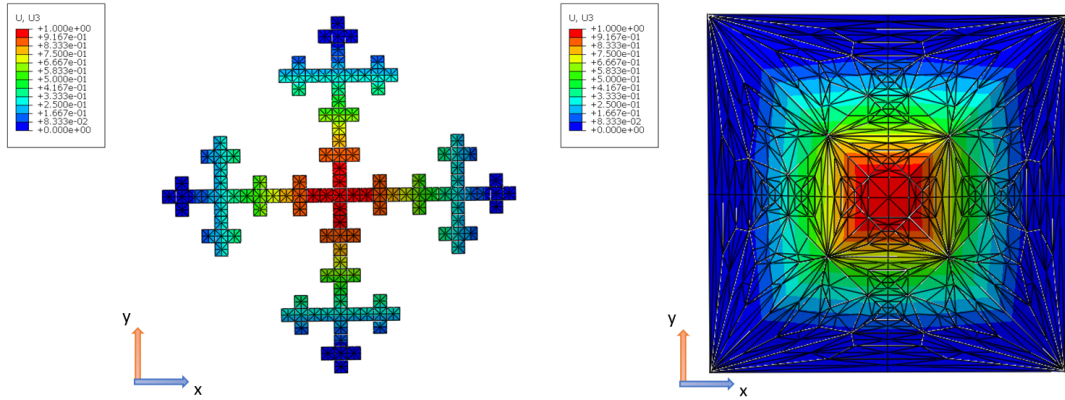
(a) Normalised lateral displacement (w_{ts}) in $\hat{E}_3$

(b) Normalised lateral displacement (w_{ts}) in $\hat{T}_3$
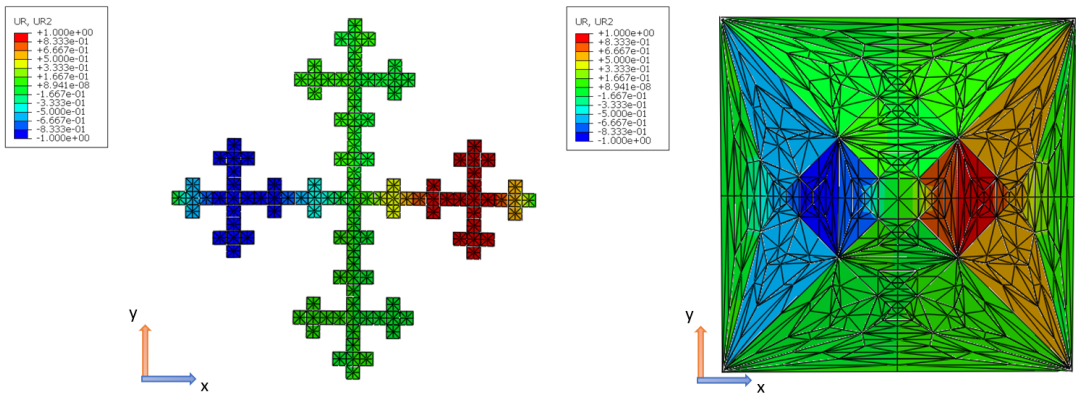
(c) Normalised slope ($\partial w_{ps} / \partial x_{ps}$) in $\hat{E}_3$

(d) Normalised Slope ($\partial w_{ts} / \partial x_{ts}$) in $\hat{T}_3$

Figure 4.19: Overall response of CCCC plates $\hat{E}_3$ and $\hat{T}_3$ for the Vicsek fractal subjected to a centrally loaded deflection.
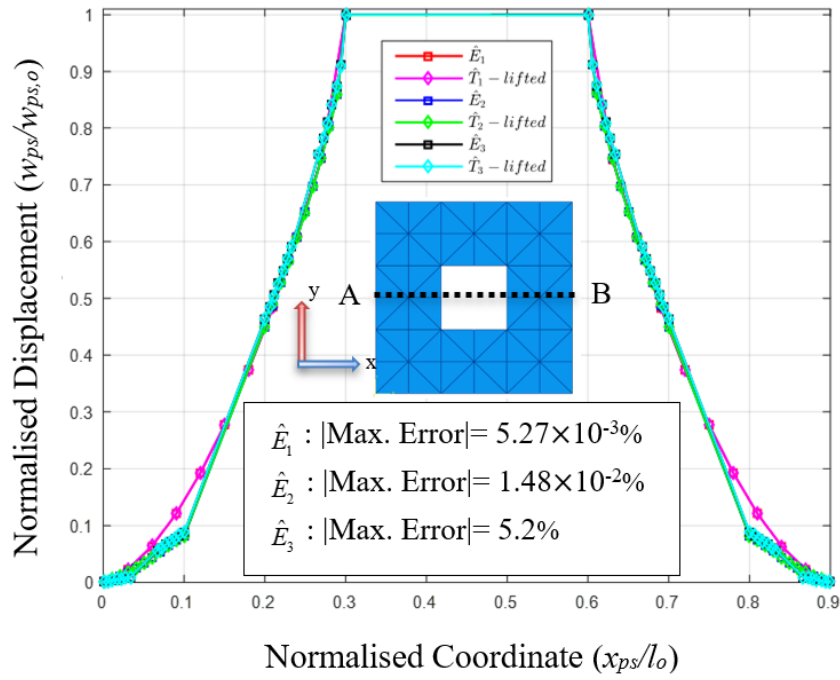
Figure 4.20: Displacement (w_{ps}) on the CCCC tessellated Vicsek plate subjected to a centrally loaded deflection.
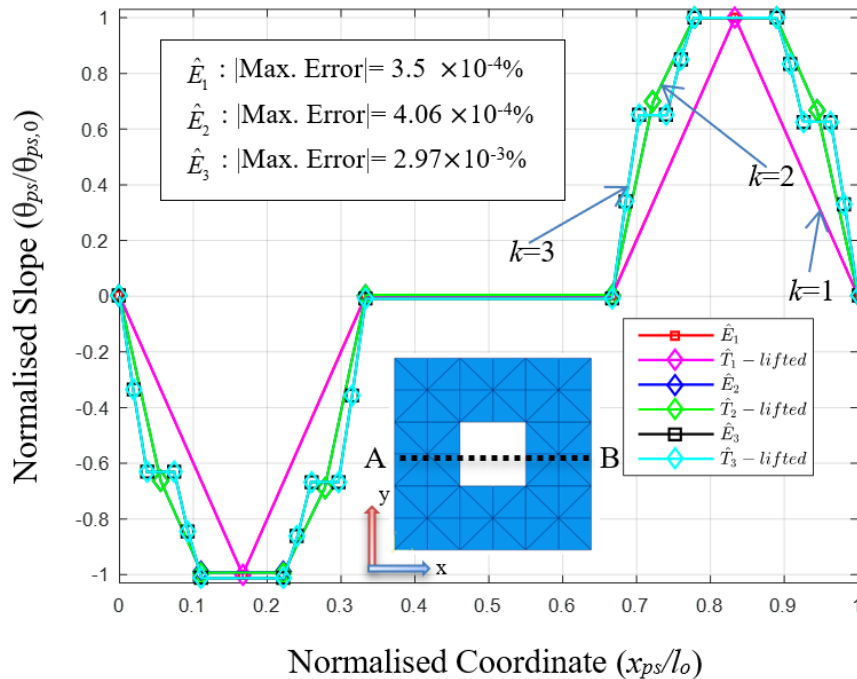
Figure 4.21: Slope ($\theta_{ps} = \partial w_{ps}/\partial x_{ps}$) on the CCCC tessellated Vicsek plates subjected to a centrally loaded deflection.

4.8   Summary

The main points found in this chapter can be briefed as follow:

1. Implement the transport equations which include using the conserved continuum laws on the pre-fractal space for 1-D and 2-D are achieved in this chapter.

2. The TCM theory has successfully presented 1-D and 2-D pre-fractal models statically with negligible error.

3. The TCM theory is found completely able to represent two different boundary conditions for the 1-D models in isotropic and anisotropic scaled models, see Figures 4.9 to 4.14.

4. The TCM theory is found to control the mesh distribution on the 2-D studied models, while it has no effect once and for all at the 1-D models.

5. The DN can be seen clearly in the lateral displacement in shape of jumps while for the slope response has no effect see Figures 4.11 and 4.12.

6. Time required to built the tessellated model by Python are found to be a little higher compared with the time required to build the same pre-fractal models although the differences disappears while building higher order models, see Figure 4.22.

7. The TCM theory has proven its ability in duplicating extreme models geometries such as the Vicsek fractal with a very high accuracy as in Figures 4.23.

8. An interesting observation can be made from the analysis run on the 2-D models, which is the mesh sensitivity towards the lower studied models (k), where the accuracy has been reduced. This effect is improved when testing higher models (k).

Chapter 5

Dynamic 1-D Analysis of TCM

5.1 Introduction

This chapter is concerned with the development and application of tessellated continuum mechanics for the dynamic analysis of holey-structural vibration problems. There presently exists no means of performing vibration analysis of holey structures represented in literature as pre-fractals in a continuum. This chapter demonstrates how the tessellated approach can be applied to achieve very precise predictions for holey-pre-fractal structure with a special concentration on applying the theory to 1-D models as a case study. The next chapter is devoted in applying the theory developed in this chapter to 2-D models. Tessellated continuum mechanics involves the creation of pre-fractal holey structures and corresponding tessellated continua with contraction maps. The recursive application of contraction maps for the creation of the structure and tessellation provides for the efficient creation and linking of holey structures to continua. Relating the behaviour of holey structures to tessellated continua is shown to be possible in this work for classical beam theory. The approach enables known analytical and numerical approaches to be lifted from continuous beams to any corresponding fractal beam. The theory is founded on matching physics on locally scaled spaces and investigated in this work is the effect of applying different scaling factors to create the tessellated continuum; isotropic and anisotropic scaling options are investigated. The tessellated approach is tested in this chapter for vibration analysis on pre-fractals for the well-known pre-fractal of the Cantor set. Two different modes of vibration along with the effects of using different boundary

conditions and excitation options are examined. To cater for discontinuous physics, discontinuity networks are incorporated providing good results for the cases studied. High accuracy is reported in this work along with measurable vibratory responses on fractal arrangements, along with finite measures of transient structural response and energy. The background theory underpinning all the main general concepts of the tessellated approach is presented in Section 5.2. Section 5.3 introduces the finite similitude concept, which contrasts the physics on two moving control volumes. The impact of small deflection theory is also examined along with its effect on constitutive laws in Section 5.4. Section 5.5 presents the covariant and contravariant definitions of objects in space. While the most significant part is Section 5.6 where the scaling constitutive relation are listed. The basic presentation of the main concept are briefed in Section 5.7. Analytical study and numerical studies are verified in Section 5.8. This chapter is ending with a conclusion in Section 5.9.

5.2   Background theory for dynamic analysis

Pre-fractals and tessellations are created recursively, and the map that relates elements is termed a hole-fill map because it has the function of closing holes when applied to the pre-fractal (as described in Chapter Three, Section 3). Finite similitude [56] is used to relate the physics in corresponding spaces occupied by tessellated and pre-fractal elements. Finite similitude exists when spatial transformations are linear, which can readily be achieved with the use of simple spatial elements (line, triangles, tetrahedrons etc.). Figure 1.5 illustrates how to relate the pre-fractal and tessellated spaces by general mappings. Two basics maps are needed; a direct map (the hole-fill map) and its inverse, which serves to lift results from the tessellation to the pre-fractal. The tessellated space being continuous permits classical analysis and numerical tools such as the finite element method can be applied. The tessellations and pre-fractal are created separately by means of iterated function systems (IFS) but involve the exact same number of contraction and expansion maps for the pre-fractal and tessellation, respectively [2]. The tiles on the tessellation can also double up as a finite element mesh in any numerical analysis. The notation representing the pre-

fractal structure is $\hat{E}_k$, where k is the number of iterations used to create the pre-fractal using an iterated function system [67]. Similarly, to generate the tessellation $\hat{T}_k$ the exact same number of expansion maps are involved. The hole-fill map can be formed directed by identifying corresponding elements in pre-fractals and tessellations or indirectly by means of function composition of the contraction maps and their inverses. The former approach is more amenable to numerical analysis. Figure 3.1 illustrates the pre-fractal Cantor set and its corresponding tessellated structures. To accommodate discontinuous physics pervasive to pre-fractal geometries, it is advantageous to use weak forms of the governing equations. To this end the weak-continuum equation as in Equation (3.1) is sufficiently generic to capture all conservative and non-conservative physical laws.

5.3 Continuum mechanics in two spaces

This section reintroduces the governing equations pertinent to continuum mechanics and hence beam-vibration. A general approach is taken at this stage to satisfy the requirements of finite similitude, which unlike other approaches, applies to the whole of continuum mechanics to establish the required scaling identities. Consider then the nine transport equations pertinent to vibration and similitude, which constrain the behaviour of volume, mass, momentum, movement (see reference [76]) and energy; and explicitly take the form of the equations stated in Chapter Three. Those equations can be used to describe the physics on both pre-fractal control volumes as in Equations (3.2 to 3.6) and tessellated control volumes as in Equations (3.7 to 3.11).
Again all these equations are applied to both pre-fractal and tessellated spaces separately. Although Equations (3.2) to (3.11) are applied to Ω_{ps}^* and Ω_{ts}^* there presently exists no connection between the physics in the two spaces for dynamic analysis. To establish a link, it is first necessary to link both time and space through two separate maps (for non-relativistic physics). The spatial map takes a point $x_{ps}^* \in \Omega_{ps}^*$ and relates it to a point $x_{ts}^* \in \Omega_{ts}^*$, whilst a temporal map relates timescales t_{ps} and t_{ts}. In differential form, these two maps for synchronised control volumes (see reference [76] for details) $dx_{ts}^* = F \cdot dx_{ps}^*$ [66] and

$dt_{ps} = hdt_{ts}$, where h is a positive scalar and F can be viewed as a spatial deformation gradient with components $F_j^i = \partial x_{ts}^{i*}/\partial x_{ps}^{j*}$. It is essential to appreciate that the map $x_{ts}^*(x_{ps}^*)$ defines a relationship between points in control volumes and does not at this stage relate material points in pre-fractals and tessellations. The assumed existence of F enables relationships between elemental volumes and areas through Nanson's identities $d\underline{V}_{ts}^* = Jd\underline{V}_{ps}^*$ and $d\underline{\Gamma}_{ts}^* = Jd\underline{\Gamma}_{ps}^* \cdot F^{-1}$ [76], where $J = det|F|$, with the control volumes Ω_{ps}^* and Ω_{ts}^*, the temporal relationship $dt_{ps} = hdt_{ts}$ along with Nanson's identities, Equation (3.1) adopts five forms (similarly for Equations (3.2) to (3.6)), i.e.

$$\frac{D^*}{D^*t_{ps}} \int_{\Omega_{ps}^*} \rho_{ps}\psi_{ps}dV_{ps}^* + \int_{\Gamma_{ps}^*} \rho_{ps}\psi_{ps}(\underline{v}_{ps} - \underline{v}_{ps}^*) \cdot \underline{n}_{ps}d\Gamma_{ps}^* =$$

$$-\int_{\Gamma_{ps}^*} \underline{J}_{ps}^\psi \cdot \underline{n}_{ps}d\Gamma_{ps}^* + \int_{\Omega_{ps}^*} \rho_{ps}\underline{b}_{ps}^*dV_{ps}^* \tag{5.1}$$

and

$$\frac{D^*}{D^*t_{ts}} \int_{\Omega_{ts}^*} \rho_{ts}\psi_{ts}dV_{ts}^* + \int_{\Gamma_{ts}^*} \rho_{ts}\psi_{ts}(\underline{v}_{ts} - \underline{v}_{ts}^*) \cdot \underline{n}_{ts}d\Gamma_{ts}^* =$$

$$-\int_{\Gamma_{ts}^*} \underline{J}_{ts}^\psi \cdot \underline{n}_{ts}d\Gamma_{ts}^* + \int_{\Omega_{ts}^*} \rho_{ts}\underline{b}_{ts}^*dV_{ts}^* \tag{5.2}$$

moreover, on applying $d\underline{V}_{ts}^* = Jd\underline{V}_{ps}^*$, $d\underline{\Gamma}_{ts}^* = Jd\underline{\Gamma}_{ps}^* \cdot F^{-1}$, and $dt_{ps} = hdt_{ts}$ to Equation (5.2) gives

$$\frac{D^*}{D^*t_{ps}} \int_{\Omega_{ps}^*} \rho_{ts}J\psi_{ts}dV_{ps}^* + \int_{\Gamma_{ps}^*} \rho_{ts}h^{-1}J\psi_{ts}(F^{-1} \cdot (\underline{v}_{ts} - \underline{v}_{ts}^*)) \cdot \underline{n}_{ps}d\Gamma_{ps}^* =$$

$$-\int_{\Gamma_{ps}^*} h^{-1}J\underline{J}_{ts}^\psi \cdot (F^{-T} \cdot \underline{n}_{ts})d\Gamma_{ps}^* + \int_{\Omega_{ps}^*} h^{-1}\rho_{ts}\underline{b}_{ts}^*dV_{ps}^* \tag{5.3}$$

The contrasting of Equations (5.1) and (5.3) provides a means for comparing the physics in each space.

5.4   Small deflection Similitude

The identities provided by Equations (5.3) must be satisfied for all Equations (3.2) to (3.11). This procedure was first performed in reference [77], so it serves no purpose to repeat this here. However, with the assumption of small deflection theory a simplification occurs in $(\underline{v}_{ts} - \underline{v}_{ts}^*) = hF(\underline{v}_{ps} - \underline{v}_{ps}^*)$ [76]. This

equation reduces to $\underline{v}_{ts}^* = hF^{-1}\underline{v}_{ps}^*$ (see Table 5.1) as a consequence of the loss of the material convection terms from Equations (3.3) to (3.11). The governing transport equation for solid mechanics reduces to

$$\frac{D^*}{D^*t}\int_{\Omega^*}\rho\psi dV^* - \int_{\Gamma^*}\rho\psi\underline{v}^*\cdot\underline{n}d\Gamma^* = -\int_{\Gamma^*}\underline{J}^{\psi}\cdot\underline{n}d\Gamma^* + \int_{\Omega^*}\rho b^* dV^* \qquad (5.4)$$

which applies approximately for the case $\underline{v} = 0$. The key to Similitude is the successful application of Equation (5.1) and (5.3) to each of the transport equations pertinent to continuum mechanics [48]. This is illustrated in Table 5.1.

5.4.1 Volume Similitude

The following two equations must match for volume Similitude:

$$\frac{D^*}{D^*t_{ps}}\int_{\Omega_{ps}^*} dV_{ps}^* - \int_{\Gamma_{ps}^*}\underline{v}_{ps}^*\cdot\underline{n}_{ps}d\Gamma^* = 0 \qquad (5.5)$$

$$\frac{D^*}{D^*t_{ps}}\int_{\Omega_{ps}^*}\alpha J dV_{ps}^* - \int_{\Gamma_{ps}^*}\alpha h^{-1}J(F^{-1}\cdot\underline{v}_{ts}^{*})\cdot\underline{n}_{ps}d\Gamma_{ps}^* = 0 \qquad (5.6)$$

which are Equation (5.1) and Equation (5.3) multiplied by α, with $\psi = \rho^{-1}$, $J^{\psi} = 0$ and $b = 0$.

It is evident that these two equations are equal if and only if their corresponding integrands match, i.e. $\alpha J = 1$ and $\underline{v}_{ps}^* = \alpha h^{-1}J(F^{-1}\cdot\underline{v}_{ts}^*)$, where this latter equation reduces to

$$\underline{v}_{ts}^* = hF\underline{v}_{ps}^* \qquad (5.7)$$

Note that condition $\alpha J = 1$ confirms that J can take up any value since α is arbitrary, and $\underline{v}_{ts}^* = hF\underline{v}_{ps}^*$ reveals that motion of a control volume in one space is not too surprisingly connected to the motion in another.

5.4.2 Mass Similitude

The following two equations must match for mass Similitude:

$$\frac{D^*}{D^*t_{ps}}\int_{\Omega_{ps}^*}\rho_{ps}dV_{ps}^* - \int_{\Gamma_{ps}^*}\rho_{ps}\underline{v}_{ps}^*\cdot\underline{n}_{ps}d\Gamma_{ps}^* = 0 \qquad (5.8)$$

$$\frac{D^*}{D^*t_{ps}}\int_{\Omega_{ps}^*}\alpha^{\rho}J\rho_{ts}dV_{ps}^* - \int_{\Gamma_{ps}^*}\alpha^{\rho}\rho_{ts}h^{-1}J(F^{-1}\cdot\underline{v}_{ts}^*)\cdot\underline{n}_{ps}d\Gamma_{ps}^* = 0 \qquad (5.9)$$

Table 5.1: Finite Similitude identities.

Transport Equation	Physical field $\underline{\Psi}$	Flux $\underline{J}$	Source b	Scalar identity	Similitude Equation
Volume	ρ^{-1}	0	0	$\alpha = J^{-1}$	$\underline{v}^*_{ts} = hF \cdot \underline{v}^*_{ps}$
Mass	1	0	0	$\alpha^\rho = \dfrac{1}{J^{-1}}$	$\rho_{ps} = \alpha^{rho}\,\rho_{ts}J$
Momentum	$\underline{v}$	$-\underline{\underline{\sigma}}$	$\underline{b}$	$\alpha^v = h^{-1}\alpha^u$	$\alpha^v \underline{v}_{ts} = \alpha^\rho F \cdot \underline{v}_{ps}$ $\underline{\underline{\sigma}}_{ps} = \alpha^v h^{-1} J F^{-1} \cdot \underline{\underline{\sigma}}_{ts} \cdot F^{-T}$
Movement	$\underline{u}$	0	$\underline{v}$	$\alpha^u = h\alpha^v$	$\alpha^u \underline{u}_{ts} = \alpha^\rho F \cdot \underline{u}_{ps}$
Energy	$e = u + \tfrac{1}{2}\underline{v}\cdot\underline{v}$	$-\underline{v}\cdot\underline{\underline{\sigma}}$	$\underline{b}\cdot\underline{v}$	$\alpha^e \cdot \alpha^\rho = (\beta^{-1}\alpha^v)^2$	$(\alpha^v)^2 \underline{v}_{ts}\cdot\underline{v}_{ts} = (\alpha^\rho)^2 \underline{v}_{ps}\cdot F^T\cdot F\cdot\underline{v}_{ps}$

which are Equation (5.1) and Equation (5.3) multiplied by α^ρ, with $\psi = 1$, $\underline{J}^\rho = 0$ and $b^\rho = 0$.

These two equations are equal if and only if their corresponding integrands match, i.e. $\alpha^\rho \rho_{ts} J = \rho_{ps}$ and $\underline{v}^*_{ps}\rho_{ps} = \alpha^\rho \rho_{ts} h^{-1} J (F^{-1} \cdot \underline{v}^*_{ts})$, where this latter equation is now automatically satisfied by the identity $\underline{v}^*_{ts} = hF\underline{v}^*_{ps}$ obtained with volume Similitude. The field identity

$$\rho_{ps} = \alpha^\rho J \rho_{ts} \tag{5.10}$$

provides a means of matching densities by the appropriate selection of the scalar α^ρ.

5.4.3 Momentum Similitude

The following two equations must match for momentum Similitude:

$$\frac{D^*}{D^* t_{ps}} \int_{\Omega^*_{ps}} \rho_{ps}\underline{v}_{ps} dV^*_{ps} - \int_{\Gamma^*_{ps}} \rho_{ps}\underline{v}_{ps}(\underline{v}^*_{ps} \cdot \underline{n}_{ps}) d\Gamma^*_{ps} =$$

$$- \int_{\Gamma^*_{ps}} \underline{\underline{\sigma}}_{ps} \cdot \underline{n}_{ps} d\Gamma^*_{ps} + \int_{\Omega^*_{ps}} \rho_{ps}\underline{b}^*_{ps} dV^*_{ps} \tag{5.11}$$

$$\frac{D^*}{D^* t_{ps}} \int_{\Omega^*_{ps}} \alpha^v \rho_{ts} JF^{-1} \cdot \underline{v}_{ts} dV^*_{ps} - \int_{\Gamma^*_{ps}} \alpha^v \rho_{ts} h^{-1} JF^{-1} \cdot \underline{v}_{ts}(F^{-1}\underline{v}^*_{ts}) \cdot \underline{n}_{ps} d\Gamma^*_{ps} =$$

$$- \int_{\Gamma^*_{ps}} \alpha^v Jh^{-1}(F^{-1} \cdot \underline{\underline{\sigma}}_{ts} \cdot F^{-T}) \cdot \underline{n}_{ps} d\Gamma^*_{ps} + \int_{\Omega^*_{ps}} \rho_{ts}\alpha^v Jh^{-1}F^{-1} \cdot \underline{b}^*_{ts} dV^*_{ps} \tag{5.12}$$

which are Equation (5.1) and Equation (5.3) multiplied by $\alpha^v F^{-1}$, with $\psi = \underline{v}$ „$\underline{J}^\psi = -\underline{\underline{\sigma}}$ and $b^\psi = \underline{b}$.

Following the identical approach to volume and mass, it is evident that these two equations are equal if and only if their corresponding integrands match. The first integrand on the left-hand side of Equation (5.11) and Equation (5.12) gives $\alpha^v \rho_{ts} JF^{-1} \cdot \underline{v}_{ts} = \rho_{ts}\underline{v}_{ps}$, which reduces to

$$\alpha^v \underline{v}_{ts} = \alpha^\rho F \cdot \underline{v}_{ps} \tag{5.13}$$

on substitution of $\rho_{ps} = \alpha^\rho J\rho_{ts}$.

The second integrand is automatically by Equation (5.18) and $\underline{v}^*_{ts} = hF \cdot \underline{v}^*_{ps}$, whilst the third provides the identity

$$\underline{\underline{\sigma}}_{ps} = \alpha^v h^{-1} JF^{-1} \cdot \underline{\underline{\sigma}}_{ts} \cdot F^{-T} \tag{5.14}$$

which as required provides an identity for symmetric tensors.

The forth integrand in Equation (5.11) and Equation(5.12) provides the identity $\rho_{ps}\underline{b}_{ps} = \rho_{ts}\alpha^v Jh^{-1}F^{-1}\cdot\underline{b}_{ts}$ but on substitution of $\rho_{ps} = \alpha^\rho J\rho_{ts}$ gives

$$\alpha^\rho \underline{b}_{ps} = \alpha^v h^{-1}F^{-1}\cdot\underline{b}_{ts} \tag{5.15}$$

providing a relationship for body forces in the two spaces.

5.4.4 Movement Similitude

The following two equations must match for movement Similitude:

$$\frac{D^*}{D^*t_{ps}}\int_{\Omega^*_{ps}}\rho_{ps}\underline{u}_{ps}dV^*_{ps} - \int_{\Gamma^*_{ps}}\rho_{ps}\underline{u}_{ps}(\underline{v}^*_{ps}\cdot\underline{n}_{ps})d\Gamma^*_{ps} = \int_{\Omega^*_{ps}}\rho_{ps}\underline{v}^*_{ps}dV^*_{ps} \tag{5.16}$$

$$\frac{D^*}{D^*t_{ps}}\int_{\Omega^*_{ps}}\alpha^u\rho_{ts}JF^{-1}\cdot\underline{u}_{ts}dV^*_{ps} - \int_{\Gamma^*_{ps}}\alpha^u\rho_{ts}h^{-1}JF^{-1}\cdot\underline{u}_{ts}(F^{-1}\underline{v}^*_{ts})\cdot\underline{n}_{ps}d\Gamma^*_{ps} =$$

$$\int_{\Omega^*_{ps}}\rho_{ts}\alpha^u JF^{-1}h^{-1}\cdot\underline{v}^*_{ts}dV^*_{ps} \tag{5.17}$$

which are Equation (5.1) and Equation (5.3) multiplied by $\alpha^v F^{-1}$, with $\psi = \underline{u}$, $\underline{J}^v = 0$ and $b^\psi = \underline{v}$.

Similarly to momentum these two equations are equal if and only if their corresponding integrands match. The first integrand on the left-hand side of Equation (5.16) and Equation (5.17) gives $\alpha^u\rho_{ts}JF^{-1}\cdot\underline{u}_{ts} = \rho_{ps}\underline{u}_{ps}$, which reduces to

$$\alpha^u\underline{u}_{ts} = \alpha^\rho F\cdot\underline{u}_{ps} \tag{5.18}$$

on substitution of $\rho_{ps} = \alpha^\rho J\cdot\rho_{ts}$.

The second integrand is automatically by substituting of Equation (5.13) and $\underline{v}^*_{ts} = hF\underline{v}^*_{ps}$, whilst the forth (the third being identical zero) gives $\underline{v}^*_{ps}\rho_{ps} = \rho_{ps}\alpha^u h^{-1}JF^{-1}\underline{v}^*_{ts}$, which reduces to

$$\underline{v}^*_{ps} = \alpha^{-\rho}\alpha^u h^{-1}JF^{-1}\cdot\underline{v}^*_{ts} \tag{5.19}$$

on substitution of $\alpha^\rho\rho_{ts}J = \rho_{ps}$.

Comparison of Equations (5.18) and (5.13) reveals that the scalars α^u and α^v must be related by the identity $\alpha^u = h\alpha^v$. This relationship arises from the

connection that velocity has with displacement being equal the rate of change of displacement. Differentiation of Equation (5.16) and Equation (5.17) with respect to time must provide Equations (5.13) and (5.18) but note account must be made of the different time scales, i.e. $dt_{ps} = hdt_{ts}$ so that $\alpha^u D\underline{u}_{ts}/Dt_{ts} = \alpha^\rho hF \cdot D\underline{u}_{ps}/Dt_{ps}$.

5.4.5 Energy Similitude

The following two equations must match for energy similitude:

$$\frac{D^*}{D^* t_{ps}} \int_{\Omega_{ps}^*} \rho_{ps} e_{ps} dV_{ps}^* - \int_{\Gamma_{ps}^*} \rho_{ps} e_{ps} (\underline{v}_{ps}^* \cdot \underline{n}_{ps}) d\Gamma_{ps}^* =$$

$$\int_{\Omega_{ps}^*} \underline{n}_{ps} \cdot \underline{\underline{\sigma}}_{ps} \cdot \underline{v}_{ps} dV_{ps}^* + \int_{\Omega_{ps}^*} \rho_{ps} \underline{b}_{ps} \cdot \underline{n}_{ps} dV_{ps}^* \qquad (5.20)$$

$$\frac{D^*}{D^* t_{ps}} \int_{\Omega_{ps}^*} \alpha^e \rho_{ts} J e_{ts} dV_{ps}^* - \int_{\Gamma_{ps}^*} \alpha^e \rho_{ts} h^{-1} J e_{ts} (F^{-1} \cdot \underline{v}_{ts}^*) \cdot \underline{n}_{ps} d\Gamma_{ps}^* =$$

$$- \int_{\Gamma_{ps}^*} \alpha^e J h^{-1} (F^{-T} \cdot \underline{n}_{ps}) \cdot (\underline{\underline{\sigma}}_{ts} \cdot \underline{v}_{ts}) d\Gamma_{ps}^* + \int_{\Omega_{ps}^*} \rho_{ts} \alpha^v J h^{-1} \underline{b}_{ts} \cdot \underline{v}_{ts} dV_{ps}^* \quad (5.21)$$

which are Equation (5.1) and Equation (5.3) multiplied by α^e, with $\psi = e$, $\underline{J}^\psi = -\underline{\underline{\sigma}} \cdot \underline{v}$ and $b^e = \underline{b} \cdot \underline{v}$, where $e = \frac{1}{2}\underline{v} \cdot \underline{v}$ [78].

Equation (5.20) and Equation (5.21) provides a description for mechanical energy in the two domains and as such does not provide any additional constraint over and above the momentum equations but is useful nonetheless. It follows the previous case where the two equations in Equation (5.20) and Equation (5.21) are equal if and only if their corresponding integrands match. The first integrand on the left-hand side of Equation (5.20) and Equation (5.21) gives $\alpha^e \rho_{ts} J e_{ts} = \rho_{ps} e_{ps}$, which reduces to

$$\alpha^e \underline{v}_{ts} \cdot \underline{v}_{ts} = \alpha^\rho \underline{v}_{ps} \cdot \underline{v}_{ps}. \qquad (5.22)$$

on substitution of $\rho_{ps} = \alpha^\rho J \rho_{ts}$, which appears to be false on consideration of the identity $\alpha^v \underline{v}_{ts} = \alpha^\rho F \cdot \underline{v}_{ps}$, which provides the identity

$$(\alpha^v)^2 \underline{v}_{ts} \cdot \underline{v}_{ts} = (\alpha^\rho)^2 (F \cdot \underline{v}_{ps}) \cdot (F \cdot \underline{v}_{ps}) = (\alpha^\rho)^2 \underline{v}_{ps} \cdot (F^T \cdot F) \underline{v}_{ps} \qquad (5.23)$$

This indicates, that an alternative viewpoint is required if the energy equations are be matched. It is prudent at this point to consider first contravariant and covariant terms prior to returning to energy similitude.

5.5 Space deformation versus coordinate transformation

Equation (5.23) at first sight provides a halt to the similitude process but is in fact revealing an underlying phenomenon with space scaling, i.e. an attached coordinate system within the distorted space will itself distort. A consequence of skewing the coordinate system is a change in the metric [76], which is revealed in Equation (5.23). Transport equations are coordinate independent however but implicit in the application of Newtonian physics is inertial coordinate frames. Note that all the transport equations (apart from energy presently) involve terms that do not explicitly involve the metric, i.e. terms of the form $\underline{v}^* \cdot \underline{n}$ and $\underline{J}^\Psi \cdot \underline{n}$, which in suffix notation are $v^{*i}n_i$ and $J^{\Psi i}n_i$, respectively and consequently do not explicitly invoke the underlying metric. It is apparent therefore for similitude of the energy equation it is necessary to ensure that the metric does not make an appearance. This is achieved with kinetic energy and Equation (5.22) by the identity

$$\alpha^e \underline{v}_{ts} \cdot \underline{v}_{ts} = \alpha^e v^i_{ts} \cdot v_{tsi} = \alpha^\rho \underline{v}_{ps} \cdot \underline{v}_{ps} = \alpha^\rho v^i_{ps} \cdot v_{psi} \tag{5.24}$$

with no appearance of the coordinate-system metrics.

The incorporation of covariant terms in the definition of kinetic energy (lower index) adds a degree of flexibility and circumvents the difficultly associated with Equation (5.24). To see this consider the substitution of the identity $\alpha^v \underline{v}_{ts} = \alpha^\rho F \cdot \underline{v}_{ps}$ (i.e. $\alpha^v (F^{-1})^i_j \underline{v}^j_{ts} = \alpha^\rho v^i_{ps}$) into Equation (5.24) and assume for definiteness that an orthonormal frame is adopted in the physical space so that $v_{ps,i} = \delta_{ij} v^j_{ps}$ [61]. Consequently

$$(\alpha^\rho)^2 v^i_{ps} \cdot v_{ps,i} = (\alpha^\rho)^2 v^i_{ps} \delta_{ij} v^j_{ps} = (\alpha^\rho)^2 v^i_{ps} \cdot v^i_{ps} = (\alpha^v)^2 v^j_{ts} (F^{-1})^i_j (F^{-1})^i_k v^k_{ts} \tag{5.25}$$

but similarly

$$\alpha^\rho \alpha^e \underline{v}_{ts} \cdot \underline{v}_{ts} = \alpha^\rho \alpha^e v^j_{ts} v_{tsj} = \alpha^\rho \alpha^e v^j_{ts} G_{jk} v^k_{ts} \tag{5.26}$$

where G_{jk} is some scalar multiple of the metric for the tessellated space and according to Equation (5.23) this equation must match Equation (5.24). Bearing in mind that the coordinate system metric has no connection to the

scalars, which suggests that $\alpha^p \alpha^e = (\alpha^v)^2$ and $G_{jk} = (F^{-1})^i_j (F^{-1})^i_k$ or $G = F^{-T} \cdot F^{-1}$ as revealed in Equation (5.22). However, it is particularly convenient for the metric to satisfy $|G| = 1$ as this ensures according to the Piola formula ($dV_{ts} = (|\underline{G}|/|\underline{g}|)^{0.5} J dV_{ps}$) [76], that Nanson's identity remains applicable (i.e. $dV_{ts} = J dV_{ps}$) since $|\underline{g}| = |\underline{G}| = 1$, where in this case $\underline{g} = \underline{I}$ and $J = det|F|$. It is convenient at this point to define the linear scalar β to satisfy $\beta^D = J = |F|$, where D is the topological dimension (typically $D = 3$) and set the metric equal to $G = \beta^2 F^{-T} \cdot F^{-1}$, which ensures $|G| = 1$ and consequently

$$\alpha^e \alpha^p = (\beta^{-1} \alpha^v)^2 \tag{5.27}$$

providing an additional relationship between the scalars.

Armed with a metric for the tessellated space it is now possible to confirm similitude for the energy transport equation. Recall that similitude for energy meant the matching of the corresponding integrands in Equation (5.20) and Equation (5.21) and presently with the correct interpretation placed on Equation (5.23) it has been confirmed that the first integrand matches. The second integrand automatically matches with the matching of the first and the identity $\underline{v}^*_{ts} = hF \cdot \underline{v}^*_{ps}$. The third integrand provides

$$\underline{\underline{\sigma}}_{ps} \cdot \underline{v}_{ps} = \sigma^{ij}_{ps} \cdot v_{psj} = \alpha^e h^{-1} J (F^{-1} \underline{\underline{\sigma}}_{ts}) \cdot v_{ts} = \alpha^e h^{-1} J (F^{-1})^i_j \sigma^{jk}_{ts} \cdot v_{ts,k} \tag{5.28}$$

where it is recognised that a covariant representation of the velocities is required and since the metric is known it follows that $v_{tsk} = G_{kj} v^j_{ts}$ and consequently the contravariant identity $\alpha^v \underline{v}_{ts} = \alpha^p F \cdot \underline{v}_{ps}$ (which equals) $\alpha^v (\beta^2 F^{-T} \cdot F^{-1}) \cdot \underline{v}_{ts} = \alpha^p \beta^2 F^{-T} \cdot \underline{v}_{ps}$ transforms into the covariant form $\alpha^v \underline{v}_{ts} = \alpha^p \beta^2 F^{-T} \cdot \underline{v}_{ps}$ (or $\alpha^v F^T \cdot \underline{v}_{ts} = \alpha^p \beta^2 \underline{v}_{ps}$), which on substitution in Equation (5.28) gives

$$\underline{\underline{\sigma}}_{ps} \cdot \underline{v}_{ps} = \alpha^e h^{-1} J (F^{-1} \cdot \underline{\underline{\sigma}}_{ts} \cdot F^{-T}) \cdot (F^T \cdot \underline{v}_{ts}) =$$
$$(\alpha^v)^{-1} \alpha^p \beta^2 \alpha^e h^{-1} J (F^{-1} \cdot \underline{\underline{\sigma}}_{ts} \cdot F^{-T}) \cdot \underline{v}_{ts} \tag{5.29}$$

But observe that Equation (5.14) gives $\underline{\underline{\sigma}}_{ps} \cdot \underline{v}_{ps} = \alpha^v h^{-1} J (F^{-1} \cdot \underline{\underline{\sigma}}_{ts} \cdot F^{-T}) \cdot \underline{v}_{ps}$, which matches if $(\alpha^v)^{-1} \alpha^p \beta^2 \alpha^e = \alpha^v$ but this is simply Equation (5.27). The final requirement for energy similitude is the matching of the fourth integrand in Equation (5.20) and Equation (5.21), which provides

$$\rho_{ps} \underline{b}_{ps} \cdot \underline{v}_{ps} = \rho_{ts} \alpha^v J h^{-1} \underline{b}_{ts} \cdot \underline{v}_{ts} \tag{5.30}$$

where again it is recognised that a covariant description of velocity is involved. Incorporation of $\rho_{ps} = \alpha^\rho \rho_{ts} J$, $\alpha^\rho \underline{b}_{ps} = \alpha^v h^{-1} F^{-1} \cdot \underline{b}_{ts}$ and $\alpha^v F^T \cdot \underline{v}_{ts} = \alpha^\rho \beta^2 \cdot \underline{v}_{ps}$ into Equation (5.30) readily confirms, that with the correct interpretation, energy similitude is obtained.

5.6 Finite Similitude and constitutive scaling constants

The rules of similitude do not involve constitutive behaviour but these are required for closure of the governing transport equation and consequently the effect of scaling on these needs to be understood. Small deflection theory is assumed to apply and the strain tensors in the pre-fractal and tessellated spaces are represented by the symmetric part of $(\partial u_i / \partial x^j)_{ps}$ and $(\partial u_i / \partial x^j)_{ts}$, respectively. The constitutive behaviour is assumed to be linear elastic and captured in the physical space by the relationship $\sigma^{ij}_{ps} = C^{ijkm}_{ps} \varepsilon_{pskm}$, which in tensorial form is $\underline{\underline{\sigma}}_{ps} = \underline{\underline{\underline{C}}}_{ps} : \underline{\underline{\varepsilon}}_{ps}$. The fourth-order stiffness tensor [79] is represented in Equation (4.18).

Before proceeding it is convenient at this point to establish an identity for strain, which requires a covariant relationship for displacement. This is readily deduced from the covariant expression for velocity (i.e. $\alpha^v \underline{v}_{ts} = \alpha^\rho \beta^2 F^{-T} \cdot \underline{v}_{ps}$) which suggests $\alpha^u \underline{u}_{ts} = \alpha^\rho \beta^2 F^{-T} \cdot \underline{u}_{ps}$. More rigorously is the application of the metrics $G^{-1} = \beta^{-2} F \cdot F^T$ (or $(G^{-1})^{ij} = \beta^{-2} F^i_k F^j_k$) and I (or δ^{ij}) to Equation (5.18) (i.e. $\alpha^u \underline{u}_{ts} = \alpha^\rho F \cdot \underline{u}_{ps}$), which yields

$$\alpha^\rho u^i_{ps} = \alpha^\rho \delta^{ij} u_{psj} = \alpha^\rho u_{ps,i} = \alpha^u (F^{-1})^i_j u^j_{ts} = \alpha^u (F^{-1})^i_j G^{jk} u_{ts,k}$$

$$= \alpha^u \beta^{-2} (F^{-1})^i_j F^i_l F^k_l u_{tsk} = \alpha^u \beta^{-2} \delta^i_l F^k_l u_{tsk} = \alpha^u \beta^{-2} F^k_i u_{ts,k} \qquad (5.31)$$

which in vectorial terms returns as expected $\alpha^u \underline{u}_{ts} = \alpha^\rho \beta^2 F^{-T} \cdot \underline{u}_{ps}$.

In view of the differential relationship $dx_{ts} = F \cdot dx_{ps}$ (or $dx^i_{ts} = F^i_j dx^j_{ps}$) it follows from the chain rule that $\partial / \partial x^j_{ps} = F^m_j \partial / \partial x^m_{ts}$ and consequently applying this to $\alpha^{-u} u_{psi} = \alpha^{-\rho} \beta^{-2} F^k_i u_{ts,k}$ gives

$$\alpha^{-u} \partial u_{ps,i} / \partial x^j_{ps} = \alpha^{-\rho} \beta^{-2} F^k_i F^m_j \partial u_{ts,k} / \partial x^m_{ts} \qquad (5.32)$$

and in view of the identity $\sigma_{ts}^{ij} = C_{ps}^{ijkm}\varepsilon_{ps,km} = C_{ps}^{ijkm}(\partial u_{ps,k}/\partial x_{ps}^m)$ along with the stress identity $\sigma_{ts}^{ij} = \alpha^{-v}hJ^{-1}F_k^i\sigma_{ps}^{kl}F_l^j$ it follows that

$$\sigma_{ts}^{ij} = \alpha^{-v}hJ^{-1}F_k^iF_l^jC_{ps}^{klrw}\frac{\partial u_{psr}}{\partial x_{ps}^w} =$$

$$\alpha^u\alpha^{-v}\alpha^{-\rho}h\beta^{-2}J^{-1}F_k^iF_l^jC_{ps}^{klrw}F_r^nF_w^p\frac{\partial u_{ps,n}}{\partial x_{ps}^p} \qquad (5.33)$$

which is $\sigma_{ts}^{ij} = C_{ts}^{ijnp}\varepsilon_{ts,np}$, where [80]:

$$C_{ts}^{ijnp} = \alpha^u\alpha^{-v}\alpha^{-\rho}h\beta^{-2}J^{-1}F_k^iF_l^jC_{ps}^{klrw}F_r^nF_w^p \qquad (5.34)$$

confirming a linear-elastic orthotropic constitutive law for the tessellated material, and similar to the Equation (4.19) driven in the previous chapter.

For convenience all the similitude identities are tabulated in Table 5.2 where both contravariant and covariant identities are presented along with relationships between scaling factors.

Another way, to find the general scaling rules is by rewriting the scaling equation

Table 5.2: Scaling relationships for contravaiant and covariant components.

Physical Field	Contravariant Rules	Covariant Rules
ρ	$\rho_{ps} = \alpha^\rho J\rho_{ts}$	$\rho_{ps} = \alpha^\rho J\rho_{ts}$
$\underline{\underline{\sigma}}$	$\underline{\underline{\sigma}}_{ps} = \alpha^v h^{-1}JF^{-1}\cdot\underline{\underline{\sigma}}_{ts}\cdot F^{-T}$	—
$\underline{u}$	$\alpha^u\underline{u}_{ts} = \alpha^\rho F\cdot\underline{u}_{ps}$	$\alpha^u\underline{u}_{ts} = \alpha^\rho\beta^2F^{-T}\cdot\underline{u}_{ps}$
$\underline{v}$	$\alpha^v\underline{v}_{ts} = \alpha^\rho F\cdot\underline{v}_{ps}$	$\alpha^v\underline{v}_{ts} = \alpha^\rho\beta^2F^{-T}\cdot\underline{v}_{ps}$

in the following form from Equation (3.1). This gives rise to the identities [77]:

$$\rho_{ps}b_{ps}^\Psi = \alpha^\Psi h^{-1}J\rho_{ts}b_{ts}^\Psi$$

or

$$\rho_{ps}b_{ps}^\Psi = \alpha^\Psi h^{-1}J\rho_{ts}G^\Psi\cdot b_{ts}^\Psi \qquad (5.35)$$

$$\underline{J}_{ps}^\Psi = \alpha^\Psi h^{-1}JF^{-1}\cdot\underline{J}_{ts}^\Psi$$

or

$$\underline{J}_{ps}^\Psi = \alpha^\Psi h^{-1}JG^\Psi\cdot\underline{J}_{ts}^\Psi\cdot F^{-T} \qquad (5.36)$$

$$\rho_{ps}\psi_{ps} = \alpha^{\Psi}J\rho_{ts}\psi_{ts}$$

or

$$\rho_{ps}\psi_{ps} = \alpha^{\Psi}J\rho_{ts}G^{\Psi}\cdot\psi_{ts} \tag{5.37}$$

along with

$$(v_{ts} - v_{ts}^{*}) = hF\cdot(v_{ps} - v_{ps}^{*}) \tag{5.38}$$

5.7   Analytical studies

A particular advantage of the tessellated approach is that a known analytical solution on a continuum can be immediately lifted to the holey beam by means of Finite Similitude. The focus on beams reduces the relative complexity of the tessellated theory and allows both numerical and analytical investigations to be readily performed. The pre-fractals considered are restricted to the Cantor dust fractal and classical slender and thick beams are the focus of the analytical work. One of the difficulties with holey beam constructions is that they do not form load-bearing structures, which is rectified here by the insertion of rigid elements in places where the holes in the pre-fractals are located. This assumption is convenient albeit somewhat artificial as it has the advantage that slopes match for elements in the discontinuity network on a tessellation (see Figure 5.1). The geometrical features along with material properties of the pre-fractal and tessellated models used in this work are presented in Table 4.1. The contraction maps given in Section 3.3 are applied to create both the pre-fractal and tessellated geometry. A number of levels of complexity are tested with a particular focus on the pre-fractals $\hat{E}_1$, $\hat{E}_2$ and $\hat{E}_3$ with analysis performed on the tessellations $\hat{T}_1$, $\hat{T}_2$ and $\hat{T}_3$. Isotropic and anisotropic scaling is tested (similar to the previous chapter) distinguished by the following hole-fill maps as in Equation (4.20), and repeated here as:

$$F_k = \beta_k\begin{bmatrix}1 & 0 & 0 \\ 0 & 1 & 0 \\ 0 & 0 & 1\end{bmatrix}, F_k = \begin{bmatrix}\beta_k & 0 & 0 \\ 0 & 1 & 0 \\ 0 & 0 & \beta_k\end{bmatrix}, F_k = \begin{bmatrix}\beta_k & 0 & 0 \\ 0 & \beta_k^{0.5} & 0 \\ 0 & 0 & \beta_k^2\end{bmatrix} \tag{5.39}$$

where $\beta_k = (3/2)^k$ and F_k is the hole-fill map connecting $\hat{E}_k$ to $\hat{T}_k$.

The hole-fill maps in Equation (5.39) are uniform and when applied to $\hat{E}_k$ have
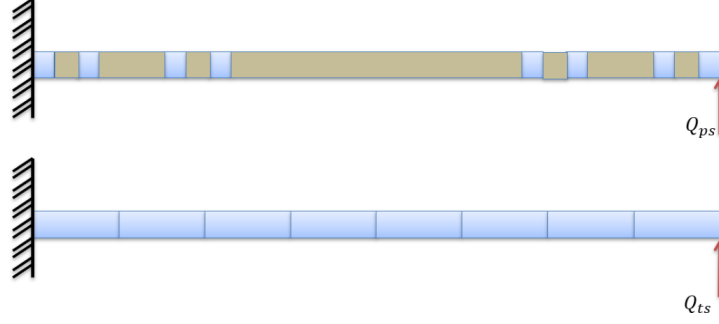
Figure 5.1: Pre-fractal Cantor set and tessellation with DN of the third set under lateral force excitation.

the effect of closing the holes whilst and applies a one-to-one correspondence between corresponding elements. The anisotropic geometrical features along with material properties of the pre-fractal and tessellated models used in this work are presented in Table 4.2. The focus here is principally on a beam model of length ℓ_o with k set equal to 3, consisting of 8 deformable segments of a length $L_{ps} = \ell_o/3^3$. The pre-fractal beam has seven holes of different lengths, i.e. four of length $\ell_o/3^3$, two of length $\ell_o/3^2$, and one of length $\ell_o/3$ (see Figure 5.1). The corresponding tessellated beam is a continuous structure that is consists of 8 tiles of length $L_{ts} = \ell_o/2^3$.

The analytical study performed here also serves the purpose of testing the numerical models founded on the commercial FE software ABAQUS (version 6.13). Linear beam elements of type B32 [72] are adopted for both pre-fractal and tessellated structures.

5.7.1 Thick beams temporal response

Thick beams provide the simplest system and two different beam systems are considered with one dominated by shear and negligible rotational inertia and the other dominated by bending and rotational inertia with negligible lateral inertia. The governing equations in the tessellated space for these two cases are [81]:

$$\rho_{ts}A_{ts}\frac{\partial^2 w_{ts}}{\partial t_{ts}^2} = K_{ts}G_{ts}A_{ts}\frac{\partial^2 w_{ts}}{\partial x_{ts}^2}$$

or

$$\frac{\partial^2 w_{ts}}{\partial t_{ts}^2} = c_{ts}^2 \frac{\partial^2 w_{ts}}{\partial x_{ts}^2} \tag{5.40}$$

and

$$\rho_{ts} \kappa_{ts} \frac{\partial^2 \theta_{ts}}{\partial t_{ts}^2} = E_{ts} \kappa_{ts} \frac{\partial^2 \theta_{ts}}{\partial x_{ts}^2}$$

or

$$\frac{\partial^2 \theta_{ts}}{\partial t_{ts}^2} = C_{ts}^2 \frac{\partial^2 \theta_{ts}}{\partial x_{ts}^2} \tag{5.41}$$

where $\theta = \partial w_{ts}/\partial x_{ts}$, $\kappa_{ts} = (I_{ts}/A_{ts})^{0.5}$, A_{ts} is cross sectional area, I_{ts} is second moment of area about the neutral axis, G_{ts} and E_{ts} are shear and Young's modulus, respectively.

The hyperbolic Equation (5.40) is arrived at in the limit $A_{ts} \to \infty$ (i.e. large cross sectional area) and similarly Equation (5.41) involves the limit $\kappa_{ts} \to \infty$ (i.e. large moment of inertia). The signal velocities in Equations (5.40) and (5.41) take the form $c_{ts} = (K_{ts}G_{ts}/\rho_{ts})^{0.5}$ and $C_{ts} = (E_{ts}/\rho_{ts})^{0.5}$. Equations (5.40) and (5.41) are separable and consequently when a beam (governed by one of these equations) is released from a stationary-deformed state it has an analytical solution of the form (for Equation (5.40)) [82]:

$$w_{ts}(x_{ts}, t_{ts}) = \sum_{m=1}^{\infty} b_m \cos(\omega_m t_{ts}) \sin(\frac{\omega_m}{c_{ts}} x_{ts}) \tag{5.42}$$

where m is equal to infinity, also the initial condition $\bar{w}(x_{ts})$ is representable by a Fourier series [83], arrived at by setting $t_{ts} = 0$, i.e.

$$\bar{w}_{ts}(x_{ts}) = w_{ts}(x_{ts}, 0) = \sum_{m=1}^{\infty} b_m \sin(\frac{\omega_m}{c_{ts}} x_{ts}) = \sum_{m=1}^{\infty} b_m \sin(\frac{(2m-1)\pi}{2} \hat{x}_{ts}) \tag{5.43}$$

with $\omega_m = \frac{(2m-1)\pi}{2\ell_o}$ [83] , $\hat{x}_{ts} = x_{ts}/\ell_o$ and Euler coefficients $b_m = 2 \int_0^{\ell_o} \bar{w}_{ts}(\hat{x}_{ts})$ $\sin(\frac{(2m-1)\pi}{2} \hat{x}_{ts}) d\hat{x}_{ts}$, and for the assumed initial deflection $\bar{w}_{ts}(\hat{x}_{ts}) = U_o \hat{x}_{ts}$ equals

$$b_m = (\frac{2U_o}{(2m-1)\pi})^2 [\sin(\frac{(2m-1)\pi}{2}) - \frac{(2m-1)\pi}{2} \cos(\frac{(2m-1)\pi}{2})] \tag{5.44}$$

It is important to appreciate that Equations (5.40) and (5.41) arise from the momentum equation with particular assumptions in force, so it is important to identity what is contravariant and what is covariant when relating these equations

to the physical space despite these being identical in an orthonormal frame. With this in mind the analytical solution on $\hat{E}_k$ can be immediately lifted from $\hat{T}_k$ (i.e. Equation (5.42)) via the Similitude theory as simply requires the application of the contravariant identity $w_{ps}(x_{ps}, t_{ps}) = \alpha^{-\rho} \alpha^u F_{33}^{-1} w_{ts}(\hat{x}_{ps}\ell_o, h^{-1} t_{ps})$, where $(\hat{x})_{ts} \rightarrow (\hat{x})_{ps}$ with $\hat{x}_{ts} = x_{ts}/\ell_o$ and $\hat{x}_{ps} = x_{ps}/\ell_o$.

An alternative means of checking the form of the solution in the physical space is by means of direct substitution of the appropriate identities into Equations (5.40) and (5.41). Note that $A_{ts} = F_{22}F_{33}A_{ps}$, and from Equation (5.34) it can be deduced that $E_{ts} = \alpha^{-\rho}\beta^{-2}h^2 J^{-1}F_{11}^4 E_{ps} = \alpha^{-\rho}\beta^{-2}h^2 F_{11}^3 F_{22}^{-1} F_{33}^{-1} E_{ps}$ and $G_{ts} = \alpha^{-\rho}\beta^{-2}h^2 J^{-1}F_{11}^2 F_{33}^2 G_{ps} = \alpha^{-\rho}\beta^{-2}h^2 F_{11}F_{22}^{-1}F_{33}G_{ps}$ since the Jacobian $J = \beta^3 = F_{11}F_{22}F_{33}$. Note in addition that the covariant form of displacement is required on the right-hand side of Equations (5.40) and (5.41), since this arises out of the constitutive equation, which from Table 5.2 is $\alpha^u \underline{u}_{ts} = \alpha^\rho \beta^2 F^{-T} \cdot \underline{u}_{ps}$ and consequently $\alpha^u w_{ts} = \alpha^\rho \beta^2 F_{33}^{-1} w_{ps}$, from which it can be deduced that $\alpha^u \theta_{ts} = \alpha^\rho \beta^2 F_{33}^{-1} F_{11}^{-1} \cdot \theta_{ps}$ (since $\theta_{ts} = \partial w_{ts}/\partial x_{ts}$). On the left-hand side of Equations (5.40) and (5.41) are contravariant displacement, which again form Table 5.2, and consequently $\alpha^u \underline{w}_{ts} = \alpha^\rho F_{33} w_{ps}$, $\alpha^u \underline{u}_{ts} = \alpha^\rho F \cdot \underline{u}_{ps}$ and $\alpha^u \theta_{ts} = \alpha^\rho F_{33}^{-1} F_{11} \cdot \theta_{ps}$ (arising out of $x_{ts}\theta_{ts} = -u_{ts}$). Armed with this information the left hand side of Equation (5.40) transforms in the following manner [84]

$$\rho_{ts}A_{ts}\frac{\partial^2 wts}{\partial t_{ts}^2} = (J^{-1}\alpha^{-\rho}\rho_{ps})(F_{22}F_{33}A_{ps})(\alpha^{-u}\alpha^\rho F_{33}h^2)\frac{\partial^2 w_{ps}}{\partial t_{ps}^2} =$$

$$\alpha^{-u}h^2\rho_{ps}A_{ps}F_{11}^{-1}F_{33}\frac{\partial^2 w_{ps}}{\partial t_{ps}^2} \qquad (5.45)$$

and similarly for the right hand side

$$K_{ts}G_{ts}A_{ts}\frac{\partial^2 w_{ts}}{\partial x_{ts}^2} =$$

$$K_{ps}(\alpha^{-\rho}\beta^{-2}J^{-1}h^2 F_{11}^2 F_{33}^2 G_{ps})(F_{22}F_{33}A_{ps})(\alpha^{-u}\alpha^\rho \beta^2 F_{11}^{-2}F_{33}^{-1})\frac{\partial^2 w_{ps}}{\partial x_{ps}^2} =$$

$$\alpha^{-u}h^2 K_{ps}A_{ps}G_{ps}F_{11}^{-1}F_{33}\frac{\partial^2 w_{ps}}{\partial x_{ps}^2} \qquad (5.46)$$

which on equating gives the expected equation in the physical space.

The clamped-free beam on $\hat{T}_3$ is subjected to an initial point shear load at the

free end of the beam; the load is released and the beam allowed to vibrate freely. The analytical solution on $\hat{T}_3$ for this behaviour is described by Equation (5.42) with coefficients provided by Equation (5.44) for the first three terms. The beam is initially displaced at its free end and released to vibrate freely (a numerical comparison between the pre-fractal and the tessellated behaviour are presented subsequently in Section 5.8). This response is recorded at the deforming point. In order to confirm the expected response, the analytical solution represented by Equation (5.42) is compared against results obtained from ABAQUS, employing beam elements of type B32 [72]. Despite increasing the cross-sectional area, the ABAQUS model suffers to a small extent from bending. This is reflected in the results shown in Figure 5.2, where although a perfect match is not obtained the agreement between analytical and numerical results is very good [75].
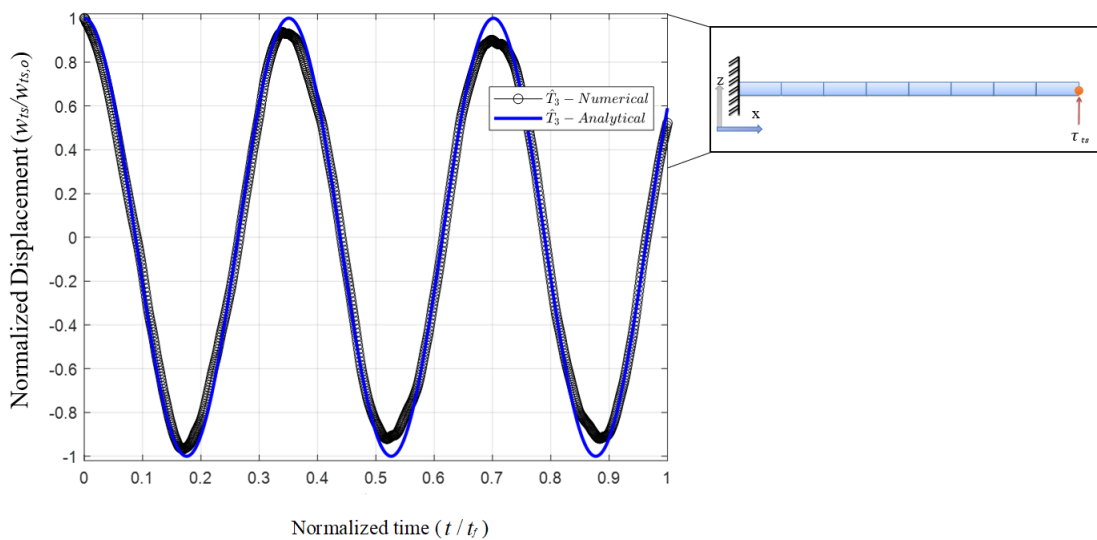
Figure 5.2: Transient lateral shear response for a thick beam on $\hat{T}_3$ measured at the free end.

5.7.2   Slender beams temporal response

Slender beams are dominated by bending and two equations of classical interest are the Euler-Bernoulli beam and the Rayleigh beam for uniform thickness and

no viscous damping, which take the form [82]:

$$\rho_{ts}A_{ts}\frac{\partial^2 w_{ts}}{\partial t_{ts}^2} = -\frac{\partial^2}{\partial x_{ts}^2}\left(E_{ts}I_{ts}\frac{\partial^2 w_{ts}}{\partial x_{ts}^2}\right) \tag{5.47}$$

$$\rho_{ts}A_{ts}\frac{\partial^2 w_{ts}}{\partial t_{ts}^2} - \frac{\partial}{\partial x_{ts}}\left(\rho_{ts}I_{ts}\frac{\partial^2 \theta}{\partial t_{ts}^2}\right) = -\frac{\partial^2}{\partial x_{ts}^2}\left(E_{ts}I_{ts}\frac{\partial^2 w_{ts}}{\partial x_{ts}^2}\right) \tag{5.48}$$

It is of interest to repeat the exercise in Section 5.7.1 to ascertain the form of the governing equations in the physical space. The first term on the left-hand side of Equations (5.47) and (5.48), is done above as in equation (5.40) and transforms as described by Equation (5.45). The right-hand side of Equation (5.47) requires the identity $I_{ts} = F_{22}F_{33}^3 I_{ps}$ and for a prismatic beam takes the form [75]

$$E_{ts}I_{ts}\frac{\partial^4 w_{ts}}{\partial x_{ts}^4} = (\alpha^{-\rho}\beta^{-2}h^2 F_{11}^3 F_{22}^{-1}F_{33}^{-1}E_{ps})(F_{22}F_{33}^3 I_{ps})(\alpha^{\rho}\alpha^{-u}\beta^2 F_{33}^{-1}F_{11}^{-4})\frac{\partial^4 w_{ps}}{\partial x_{ps}^4}$$

$$= \alpha^{-u}h^2 F_{11}^{-1}F_{33}E_{ps}I_{ps}\frac{\partial^4 w_{ps}}{\partial x_{ps}^4} \tag{5.49}$$

which on equating with Equation (5.45) provides the equation expected as the term $\alpha^{-u}h^2 F_{11}^{-1}F_{33}$ simply cancels from both sides.

Consider now the second term on the left-hand side of Equation (5.48) with insertion of the contravariant form $\alpha^u\theta_{ts} = \alpha^{\rho}F_{11}F_{33}^{-1}\theta_{ps}$ for a prismatic bar of invariant density gives

$$\rho_{ts}I_{ts}\frac{\partial^3 \theta_{ts}}{\partial x_{ts}\partial t_{ts}^2} = (J^{-1}\alpha^{-\rho}\rho_{ts})(F_{22}F_{33}^3 I_{ps})(F_{11}^{-1}h^2)(\alpha^{-u}\alpha^{\rho}F_{33}^{-1}F_{11})\frac{\partial^3 \theta_{ps}}{\partial x_{ps}\partial t_{ps}^2} =$$

$$\alpha^{-u}h^2 F_{11}^{-1}F_{33}\rho_{ps}I_{ps}\frac{\partial \theta_{ps}}{\partial x_{ps}\partial t_{ps}^2} \tag{5.50}$$

and since the other terms are common to Equation (5.49) it follows on division by $\alpha^{-u}h^2 F_{11}^{-1}F_{33}$ that the expected equation is returned.

Unlike the thick shear beam, solutions to Equations (5.47) and (5.48) on a tessellation has discontinuities present at the discontinuity network and as such standard analytical solutions are not available. However, for the sake of comparison it is possible to confine the behaviour of the tessellated beam to be continuous. This restriction has the effect of limiting the response of the pre-fractal with kinks appearing at the connections between rigid and pliable elements. Although

somewhat non-physical this limitation does allow for the application of analytical solutions and for the further testing of the theoretical constructs.

Consider then a pinned-pinned beam under a force applied at the centre of the span and in static equilibrium; the force is removed and the beam is allowed to vibrate freely. The analytical solution for this case is again described by Equation (5.42) but with wave number $(\omega/c_{ts})_m = (m\pi/\ell_o)$ [85], where in this case c_{ts} is the frequency-dependent bending wave propagation (phase) speed, which satisfies $c_{ts}^2 = (E_{ts}I_{ts}/\rho_{ts}A_{ts})^{0.5}\omega$. The material properties used in this section are for aluminium with density of 2698.8 (kg/m^3) and Young modulus of 68.9×10^9 (N/m^2) and a comparison between analytical and numerical frequencies values are presented in Table 5.3 with percentage error defined by $|\omega^{analytical} - \omega^{numerical}|/\omega^{analytical} \times 100\%$. The initial deflection of the beam $\bar{w}_{ts}(x_{ts})$ is equal to $\bar{w}_{ts}(\hat{x}_{ts}) = \frac{Q_{ts}l_o^3}{48E_{ts}I_{ts}}(3\hat{x}_{ts} - 4\hat{x}_{ts}^3)$ for $0 \geq \hat{x}_{ts} \geq \frac{1}{2}$ and $\bar{w}_{ts}(1 - \hat{x}_{ts})$ for $\frac{1}{2} \geq \hat{x}_{ts} \geq 1$; and consequently, the Euler coefficients obtained from $b_m = 2\int_0^1 \bar{w}_{ts}(\hat{x}_{ts})\sin(m\pi\hat{x}_{ts})d\hat{x}_{ts}$ are [81] or [83]

$$b_m = (\frac{Q_{ts}}{20m^3\pi^3 E_{ts}I_{ts}})((\frac{1}{2} - \frac{m^2\pi^2}{25})\cos(\frac{m\pi}{2})) \tag{5.51}$$

Finally, the analytical solution represented by Equation (5.42) is compared

Table 5.3: Differences in the natural frequencies: analytical vs numerical.

Mode n	Analytical ω_n^{ana} (rad/sec)	Numerical ω_n^{num} (rad/sec)	Error % $\|\frac{\omega_n^{ana} - \omega_n^{num}}{\omega_n^{ana}}\| \times 100\%$
1	46.17	46.15	0.04
2	184.70	184.40	0.16
3	415.59	414.02	0.37
4	738.83	733.89	0.66

with numerical results on produced by ABAQUS using beam elements type B32 [72]. The results are presented in Figure 5.3, where an almost perfect match is achieved.
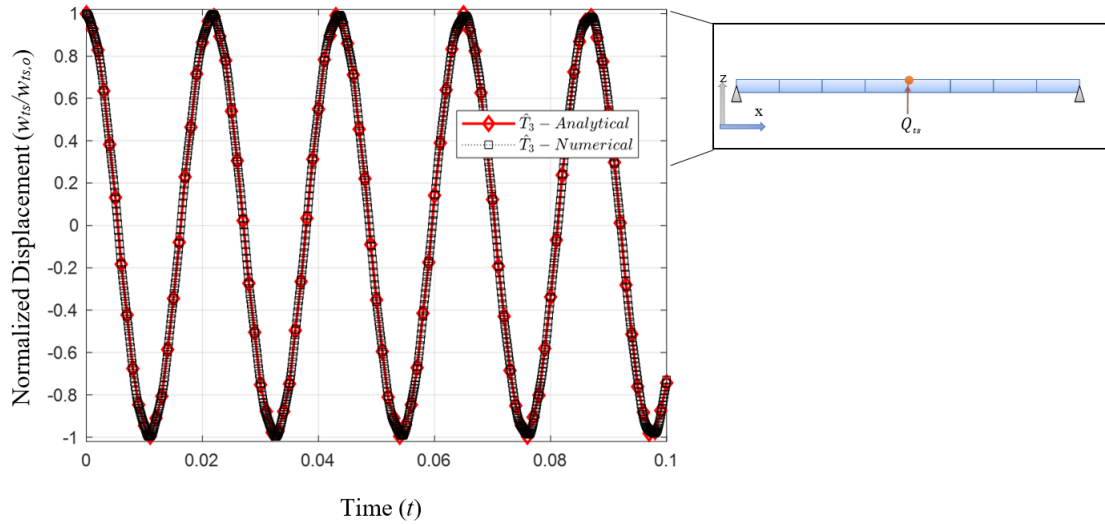
Figure 5.3: Transient lateral bending response for a slender beam on $\hat{T}_3$ measured at the mid point.

5.8 Numerical studies

This section is concerned with further testing tessellated continuum mechanics for beams involving both isotropic and anisotropic scaling along with changes in boundary and loading conditions. Both force and displacement loading are investigated in the dynamic analysis of the beams. The beam models considered in the physical space are formed from pre-fractals of the Cantor set of different levels of complexity as indicated by the index k, where k is set equal to 1, 2, or 3. As mentioned in Section 5.7, holey beams are not load bearing but are made so by the insertion of light rigid sections. This has the effect of introducing a discontinuity network into the corresponding tessellation as discussed in Section 3.4. This concept was first introduced by Jiang et al. [55] to extend the types of analysis that could be performed on tessellations although the work was limited to heat transfer problems. Although the approach allows discontinuities to appear at the edges of tiles in a tessellation, these are not arbitrary and are constrained by the physical behaviour of the pre-fractal. For holey beams the rigid-body motion of the connecting elements constrains the jump behaviour on a tessellation at a discontinuity so that slope matches across any jump. Unlike the analytical approach in Section 5.7, where known continuous solutions are

lifted to the pre-fractal the absence of such solutions means that it is necessary to lift projected numerical solutions from the tessellations. An example of the situation is presented in Figure 5.1 where a cantilever beam is subjected to a lateral load magnitude of Q_{ps} at its free end. The corresponding tessellated cantilever model is also presented in sub Figure 5.1 but in this case the loading conditions and constraints are set by the contravariant identities presented in Table 5.2. Introduced in section 5.4 are the rules for the creation of the tessellated model accounting for both its geometry and material behaviour, mirroring to a large extent the pre-fractal model. Unless otherwise stated the pre-fractal models are bestowed with the material properties and the dimensions (segment lengths) presented in Table 4.1.

Examined here is the application of isotropic and anisotropic scaling as dictated by the matrix (tensor) F, which is set equal to F_k in Equation (5.39) and consists of diagonal coefficients with $\beta = \beta_k = (3/2)^k$. Since the segments of any of the pre-fractals under consideration are equal in length it allows F to be uniformly applied over the whole beam, which is a convenient simplification. Isotropic scaling occurs when all the diagonal terms in F are equal and it has the effect of changing not only the length of any pre-fractal beam but also its thickness and height. This affects the second moment of area in the following manner $I_{ts} = \beta^4 I_{ps}$. Bearing in mind that hole-fill maps are expansive this invariably means that $\beta > 1$ (e.g. $\beta = (3/2)^k$) and consequently isotropic scaling contrasts the behaviours of beams of different cross sectional areas. However, a particular peculiarity of the scaling theory is that it also features anisotropic scaling and two such examples are provided in Equation (5.39). The middle example has the effect of leaving the height of the beam unchanged but alters the thickness and gives the relationship $I_{ts} = \beta^3 I_{ps}$. The last example in Equation (5.39) changes dimensions in a non-linear manner and provides the identity $I_{ts} = \beta^{13/2} I_{ps}$. It is evident that the scaling theory provides relationships between beams of different sizes and it is of some interest to investigate and test the concepts involved here. A manifestation of anisotropic scaling however is anisotropic material properties as revealed by Equation (5.34) and particular properties are found in Table 4.2. The numerical analysis presented here is performed with the commercial FE software package ABAQUS (version 6.13). Linear beam element type B32 [72]

is applied for analysis of beams in both pre-fractal and tessellated spaces. For consistency the number of finite elements used in each deformable pre-fractal segment (and tile) was set equal to 10 as this was found to provide converged results to high accuracy. This number or elements was applied for the entire numerical analysis of the beam structures with identical numbers of elements in corresponding pre-fractals and tessellations. Two analysis types are considered in both spaces, which are frequency and dynamic analysis. Although analytical results are not available for comparison the results in the physical space can be determined both directly and indirectly and therefore can be contrasted. The direct results are obtained with ABAQUS but do not involve the scaling theory whilst the lifted results are also obtained with ABAQUS but in this case the analysis is performed on the tessellation with tiles doubling up as elements. The aim here is to show that analysis on a continuum is possible for holey beams.

5.8.1 Frequency analysis

Determining natural frequencies and mode shapes is a good first step, since this can be done for both spaces and they underpin the characteristic behaviour of both pre-fractal and tessellated beams. Two cases are compared in this section for the purpose of initial verification of the tessellated approach. The models considered are two pre-fractal beams. The first is a built-in beam with $k = 1$ and the other a cantilever beam with $k = 2$. Material properties for both beams are listed in Table 4.1 with isotropic scaling applied in the scaling process. Although all frequencies can be determined numerically with ABAQUS the following formula [81, 85 and 86]

$$f_{i,ts} = \frac{\lambda_i^2}{2\pi L_{ts}^2}(\frac{E_{ts}I_{ts}}{\rho_{ts}A_{ts}})^{0.5} \tag{5.52}$$

provides a good approximation in the tessellated space, where λ_i is a dimensionless parameter whose value is dependent on the boundary conditions. Formula (5.52) has another form $f_{i,ps}$ in the physical space that is readily related through the mappings to confirm that $f_{i,ps}$ and $f_{i,ts}$ are algebraically connected. The frequencies and mode shapes obtained via ABAQUS are presented in Tables 5.4 to 5.7. Observe in those tables that the pre-fractal elements are linked by

means of rigid elements to provide a load bearing structure as mentioned above in Section 5.7. With $h = 1$ it is anticipated that the frequencies in the two spaces match; within the bounds of numerical accuracy the results in the tables confirm that this is indeed the case. The lowest accuracy in the natural frequencies is to equal 4.63×10^{-2} rad/sec at the first mode (with $k = 1$) and the least absolute relative error of 4.54×10^{-2} rad/sec occurs at the fourth mode (for $k = 2$).

Table 5.4: Differences in the natural frequencies for CC beam on $\hat{E}_1$ and $\hat{T}_1$.

Mode n	Physical-natural frequency $\omega^{num}_{n,ps}$(rad/sec)	Tessellated-natural frequency $\omega^{num}_{n,ts}$(rad/sec)	Absolute relative error $\left\lvert\frac{\omega^{num}_{n,ps} - \omega^{num}_{n,ts}}{\omega^{num}_{n,ps}}\right\rvert$
1	4.60×10^{-2}	4.82×10^{-2}	4.63×10^{-2}
2	7.39×10^{-2}	7.50×10^{-2}	1.42×10^{-2}
3	2.44×10^{-2}	2.55×10^{-2}	4.35×10^{-2}
4	2.79×10^{-2}	2.87×10^{-2}	2.91×10^{-2}

Furthermore, the frequency analysis is also repeated for the anisotropic scaling cases for the tessellated models. The two anisotropic scaling cases listed in Equation (5.39) are used to create tessellated geometries. A frequency analysis is run and the results are presented in Tables 5.8 and 5.9. This case study is run for pre-fractal of the third complexity under a boundary conditions of clamped-clamped represented by (CC). The material properties for the anisotropic cases are listed in Table 4.2. The natural frequencies are presented in Table 5.8, while the mode shapes are presented in Table 5.9. The maximum error is found for the second scaling case at the third mode shape with value of 0.282 relative error.

5.8.2 Free vibration analysis

In this section, the transient response of pre-fractal beams is tested by six different vibration analyses. Presented in Table 5.10 are the seven test cases considered to assess the tessellated theory. Different boundary conditions and excitation sources are applied along with isotropic and anisotropic scaling for the creation of the tessellated beams.

Table 5.5: Mode shapes for CC beam with isotropic scaling of $\hat{E}_1$.
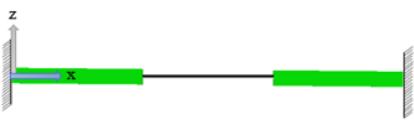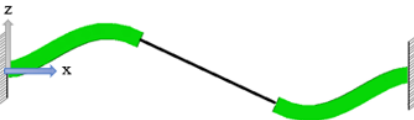
Mode number	Mode shape pre-fractal space	Mode shape tessellated space
-		
1	$\omega_{1,ps} = 4.60\text{x}10^{-02}\,rad\,/\,\sec$	$\omega_{1,ps} = 4.82\text{x}10^{-02}\,rad\,/\,\sec$
2	$\omega_{2,ps} == 7.39\text{x}10^{-2}\,rad\,/\,\sec$	$\omega_{2,ts} = 7.50\text{x}10^{-2}\,rad\,/\,\sec$
3	$\omega_{3,ps} = 2.44\text{x}10^{-2}\,rad\,/\,\sec$	$\omega_{3,ts} = 2.55\text{ x}10^{-2}\,rad\,/\,\sec$
4	$\omega_{4,ps} = 2.79\text{x}10^{-2}\,rad\,/\,\sec$	$\omega_{4,ts} = 2.87\text{x}10^{-2}\,rad\,/\,\sec$

Table 5.6: Differences in the natural frequencies for built in beam on $\hat{E}_2$ and $\hat{T}_2$.

Mode n	Physical-natural frequency $\omega_{n,ps}^{num}$ (rad/sec)	Tessellated-natural frequency $\omega_{n,ts}^{num}$ (rad/sec)	Absolute relative error $\left\lvert\frac{\omega_{n,ps}^{num}-\omega_{n,ts}^{num}}{\omega_{n,ps}^{num}}\right\rvert$
1	6.19×10^{-2}	5.90×10^{-2}	4.54×10^{-2}
2	5.43×10^{-2}	5.43×10^{-2}	1.22×10^{-4}
3	9.94×10^{-2}	9.55×10^{-2}	3.90×10^{-2}
4	4.77×10^{-2}	4.77×10^{-2}	4.61×10^{-4}

Table 5.7: Mode shapes for CF beam with isotropic scaling of $\hat{E}_2$.
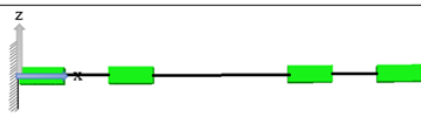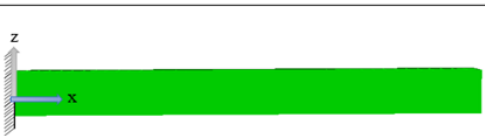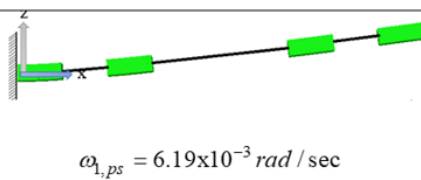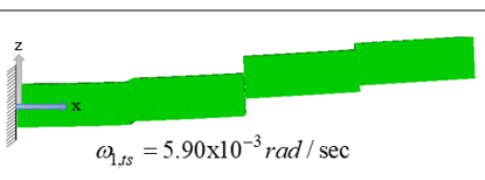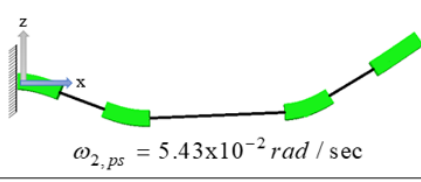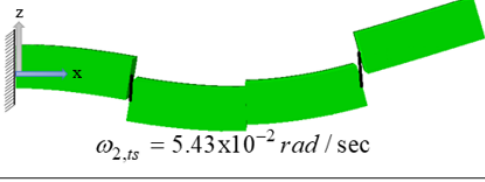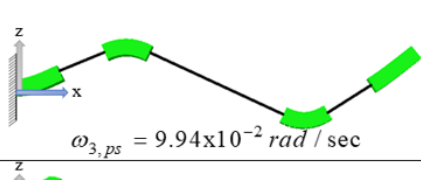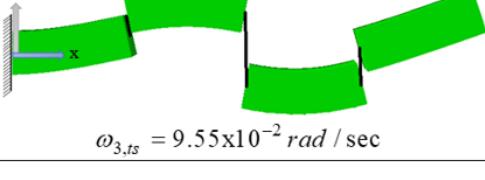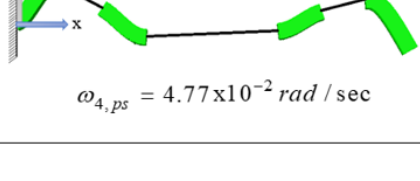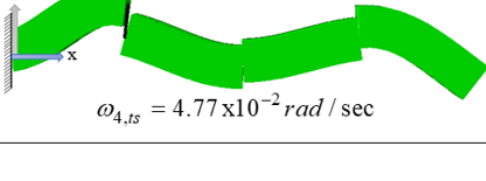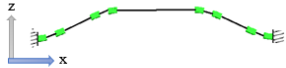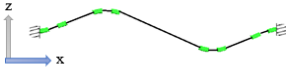
Mode number	Mode shape pre-fractal space	Mode shape tessellated space
-		
1	$\omega_{1,ps} = 6.19\text{x}10^{-3}\,rad/\sec$	$\omega_{1,ts} = 5.90\text{x}10^{-3}\,rad/\sec$
2	$\omega_{2,ps} = 5.43\text{x}10^{-2}\,rad/\sec$	$\omega_{2,ts} = 5.43\text{x}10^{-2}\,rad/\sec$
3	$\omega_{3,ps} = 9.94\text{x}10^{-2}\,rad/\sec$	$\omega_{3,ts} = 9.55\text{x}10^{-2}\,rad/\sec$
4	$\omega_{4,ps} = 4.77\text{x}10^{-2}\,rad/\sec$	$\omega_{4,ts} = 4.77\text{x}10^{-2}\,rad/\sec$

Table 5.8: Differences in the natural frequencies for CC beam with anisotropic scaling of $\hat{E}_3$.

Mode n	Physical natural frequency $\omega_{n,ps}^{num}$ (rad/sec)	Tessellated-Case I $\omega_{n,ts}^{num}$ (rad/sec)	Tessellated natural frequency-Case II $\omega_{n,ts}^{num}$ (rad/sec)	Absolute relative error - Case I $\left\lvert\frac{\omega_{n,ps}^{num}-\omega_{n,ts}^{num}}{\omega_{n,ps}^{num}}\right\rvert$	Absolute relative error - Case II $\left\lvert\frac{\omega_{n,ps}^{num}-\omega_{n,ts}^{num}}{\omega_{n,ps}^{num}}\right\rvert$
1	0.81×10^{-2}	0.82×10^{-2}	0.82×10^{-2}	0.61×10^{-2}	0.01×10^{-2}
2	1.45×10^{-1}	1.45×10^{-1}	1.44×10^{-1}	0.00×10^{-1}	0.01×10^{-1}
3	5.86×10^{-1}	5.67×10^{-1}	4.21×10^{-1}	3.12×10^{-1}	0.28×10^{-1}
4	6.18×10^{-1}	5.98×10^{-1}	4.48×10^{-1}	3.23×10^{-1}	0.27×10^{-1}

Table 5.9: Mode shapes for CC beam with anisotropic scaling of $\hat{E}_3$.

Mode number	Mode shape pre-fractal space	Mode shape tessellated space-Case I	Mode shape tessellated space-Case II
1	$\omega_{1,ps} = 0.818 \times 10^{-2}\, rad\,/\sec$	$\omega_{1,ts} = 0.8228 \times 10^{-2}\, rad\,/\sec$	$\omega_{1,ts} = 0.8235 \times 10^{-2}\, rad\,/\sec$
2	$\omega_{2,ps} = 14.50 \times 10^{-2}\, rad\,/\sec$	$\omega_{2,ts} = 14.50 \times 10^{-2}\, rad\,/\sec$	$\omega_{2,ts} = 14.40 \times 10^{-2}\, rad\,/\sec$
3	$\omega_{3,ps} = 58.60 \times 10^{-2}\, rad\,/\sec$	$\omega_{3,ts} = 56.77 \times 10^{-2}\, rad\,/\sec$	$\omega_{3,ts} = 42.08 \times 10^{-2}\, rad\,/\sec$
4	$\omega_{4,ps} = 61.80 \times 10^{-2}\, rad\,/\sec$	$\omega_{4,ts} = 59.80 \times 10^{-2}\, rad\,/\sec$	$\omega_{4,ts} = 44.83 \times 10^{-2}\, rad\,/\sec$

5.8.2.1. Isotropic scaling of a thick beam

This test is focussed on the application of the tessellated theory to a thick beam with view to examining how rotary inertia is accommodated by the theory. The influence of rotary inertial is recognised to be small during the flexural deflection of a thin beam and consequently is often neglected. It is accounted for in Timoshenko beam theory but its influence on natural frequencies for any shear deformation mode is known to be limited [84]. The ability of the tessellated approach to predict the dynamical behaviour of a thick beam is therefore of some interest. The case study presented in section 5.7.1 is illustrated in Table 5.10 known as Case I which is represented in this section for further analysis to verify the TCM theory. The studied model is a Cantor set of the third complexity and under the boundary condition of clamped-free denoted by CF and under a shear concentrated load. A shear deformation is achievable by applying a shear force to the structure in the lateral direction that cause the beam to deflect by means of $+w_{ps}$ to deform the structure by applying a pure shear component, then allowing it to vibrate freely; In the same way, $+w_{ts}$ is achieved on the tessellated space by applying the Equation $Q_{ts} = \beta^{-1} F_{33} Q_{ps}$.

The lifted results in Figure 5.4 and Figure 5.5 are compared with the pre-fractal space models, and they give an indication that the analysis of a thick beam structure is predicted perfectly through comparing the displacement and slope variation with time. Furthermore, the instantaneous response is also plotted in Figure 5.4 to confirm the static deflection of the beam at 0.56 unit of time. By doing so the numerical results has proved its efficiency in predicting the results on the pre-fractal space.

5.8.2.2. Isotropic scaling of thin beam

For the next cases, the studied models testing the most widely used structures in engineering applications, which are beams in static lateral loading and lateral vibration. Due to the importance of such models, it is found necessary to understand the ability and the limitation of the TCM theory in analysing different boundary conditions (BC) and load cases. For example and in this analysis, the structure is tested under four different combinations of boundary conditions (BC)

Table 5.10: Studied case for pre-fractal and tessellated beams on $\hat{E}_3$ and $\hat{T}_3$.

Studied cases	Boundary condition	Excitations source	Figure
Case I: Isotropic scaling	CF	Shear Stress Q	
Case II: Isotropic scaling	PP	Lateral Displacement w	
Case III: Isotropic scaling	CF	Lateral Displacement w	
Case IV: Isotropic scaling	CP	Lateral Displacement w	
Case V: Isotropic scaling	CC	Concentrated Force Q	
Case VI: Anisotropic scaling	CC	Lateral Displacement w	
Case VII: Anisotropic scaling	PP	Lateral Displacement w	
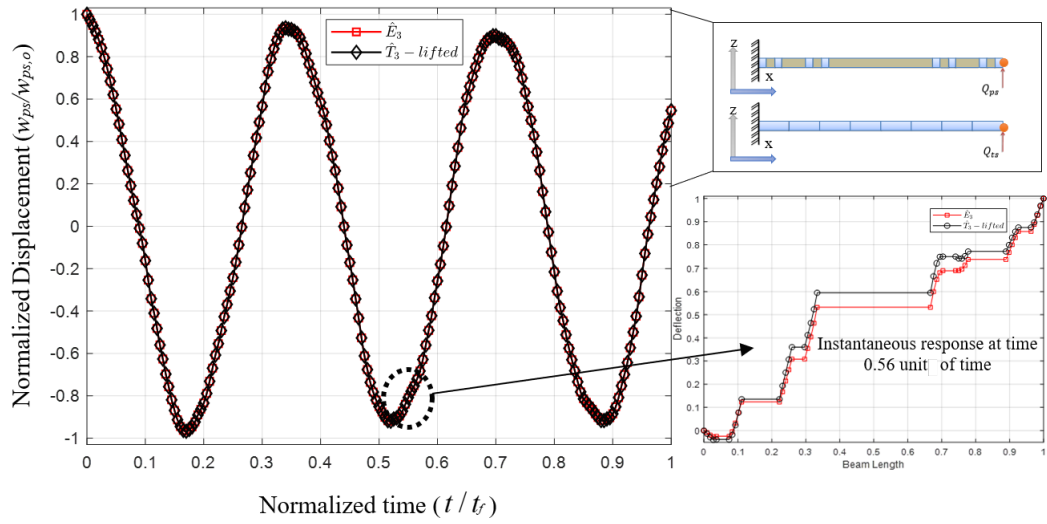
Figure 5.4: Transient displacement response on $\hat{E}_3$ compared to lifted results from $\hat{T}_3$ for a cantilever beam at the free end.
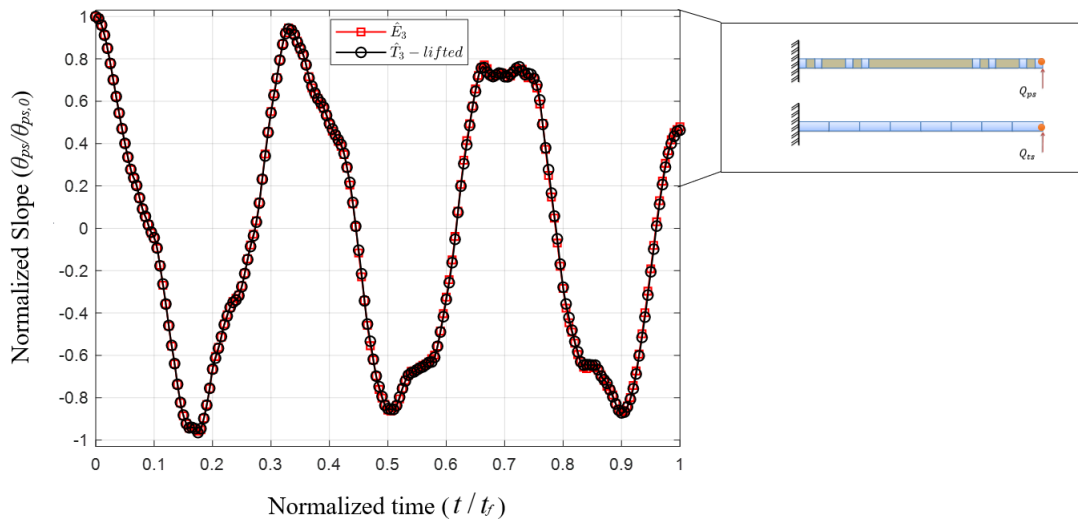
Figure 5.5: Transient slope response on $\hat{E}_3$ compared to lifted results from $\hat{T}_3$ for a cantilever beam at the free end.

such as: Clamped-Free (CF); and Clamped-Pinned (CP); excitations sources at different applied location; with two cases of different lateral disturbance sources: Displacement (w), and Concentrated Force (Q); with different locations of applying the deforming sources. All the studied models in this section are chosen to have $k = 3$. All the studied models in this section use the isotropic scaling process to create the tessellated space and consequent models. So basically, this section is more concerned with understanding the possibility of applying different combinations of boundary conditions (BC) and sources of initial loading. Furthermore, a forced vibration case is also been considered.

5.8.2.2.1. Symmetric pinned-pinned BC under initial displacement

The model presented in section 5.7.2 is represented here to validate the TCM theory numerically. This model illustrates an isotropic scaling of a beam under a pinned (PP) boundary condition as indicated in Table 5.10, Case II. The structure is initially deformed by an arbitrary displacement in the lateral direction then it is left to vibrate freely. Since the scaling map is isotropic then the material of the tessellated models remains isotropic as listed in Table 4.1. The transient FE analysis took place on the pre-fractal and the tessellated space correspondingly. The results of lateral deflection versus time for both pre-fractal and the tessellated models are depicted in Figure 5.6. The temporal variation of the velocity of the structure at the place of the applied initial displacement is presented in Figure 5.7.

5.8.2.2.2. Unsymmetric clamped-free BC under initial displacement

The model is under CF boundary conditions and lateral displacement of an arbitrary magnitude, see Table 5.10, Case III. The isotropic tessellated model is built by using the same procedure mentioned earlier, and its material properties are listed in Table 4.1. It is essential to investigate more the effect of boundary condition (BC) on the frequency analysis which is influence clearly the transient response.

The transient response is presented in Figures 5.8 and 5.9. These figures show the transient responses in measures of displacement and slope on the pre-fractal space
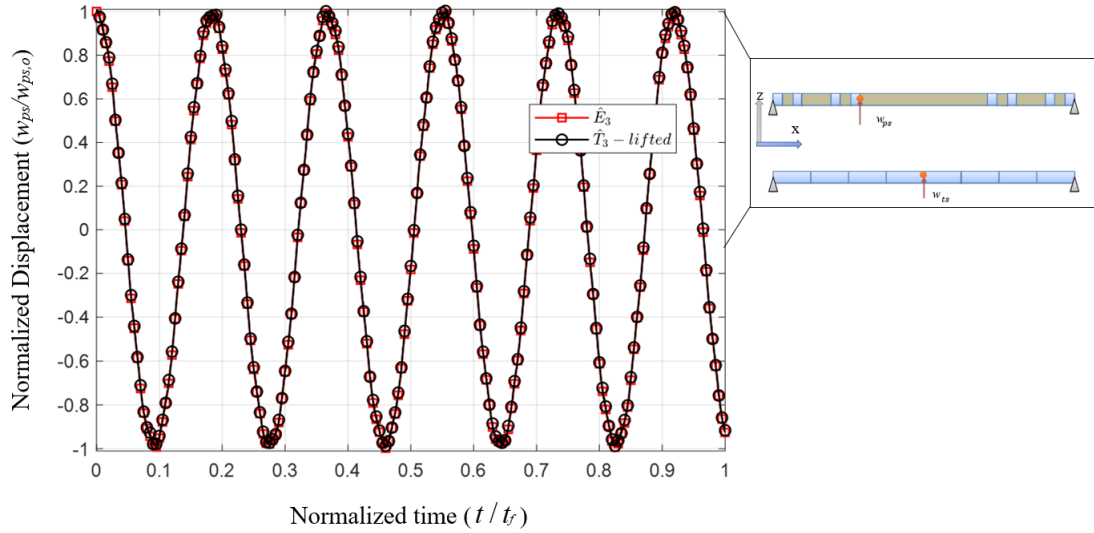
Figure 5.6: Transient displacement response on $\hat{E}_3$ compared to lifted results from $\hat{T}_3$ for a pinned beam measured at the point of initial displacement.
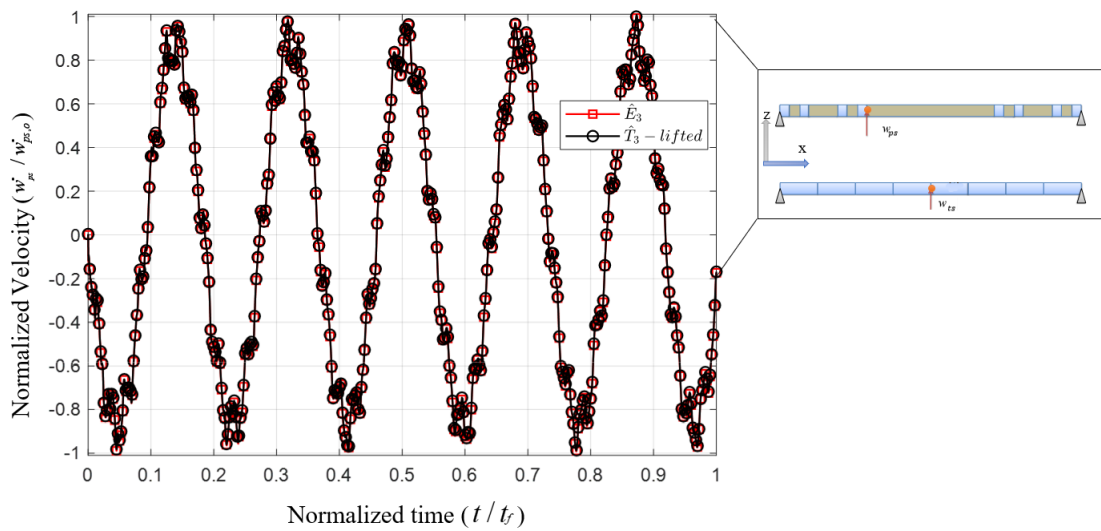
Figure 5.7: Transient velocity response on $\hat{E}_3$ compared to lifted results from $\hat{T}_3$ for a pinned beam measured at the point of initial displacement.

126

and the reversed tessellated responses. The time unit is been normalised through the final maximum time on both models, which is denoted by t_f. This analysis proves that the tessellated space has shown a significant agreement in predicting the response on the pre-fractal space, while testing different BC combinations. Furthermore, the instantaneous beam responses plotted and compared at 0.04 unit of time, with a perfect match on both spaces achieved in terms of lateral deflection.

5.8.2.2.3. Unsymmetric clamped-pinned BC under initial displacement

To test further an unsymmetrical boundary condition such as a clamped pinned case, this is denoted by (CP). Case IV in Table 5.10, is gives an excellent demonstration to apply of unsymmetric boundary conditions for an isotropic tessellated model. Displacement of an arbitrary magnitude of a unit length is applied on the left edge of the main hole see Case IV, Table 5.10. Then by using Equation (5.18) the excitation magnitude and direction are calculated on the tessellated space.

Then by removing the excitation and allowing the structure to vibrate freely, the transient response can be measured and is plotted in Figure 5.10 at the mid-left edge of both structures. As mentioned earlier the reversed tessellate results, which are obtained by using equation $dx_{ts} = F_{11} \cdot dx_{ps}$. and Equation (5.10), and Equation (5.34) are presented in Figures 5.10 to 5.12. This proves that the TCM theory managed to get a perfectly match to the pre-fractal results whose error can be considered as a numerical accumulative error. Similar to the previous sections, the instantaneous beam lateral deflection at (1) normalised unit of time is plotted and compared with the reverse tessellated response. The results showed a good match on both spaces as in Figure 5.10.

Furthermore, the modal energy is also been investigated numerically. At 1 unit of time, the changes in kinetic energy (H) with time is been studied and compared on both spaces. Similarly to the strain energy (M) is also recorded and compared on both spaces. Figure 5.13 demonstrates the relation between the kinetic and the strain energy for both models. The kinetic energy is found to follow $H_{ts} = 0.5 \int m_{ts} v_{ts}^2 dx_{ts}$ and by using a contravariant relationship $H_{ts} = \alpha^{-\rho} \alpha^{-2v} F_{11} F_{33} H_{ps}$. This is equal to $H_{ts} = \alpha^{-\rho} \beta^{-2} F_{11} F_{33} H_{ps}$. And the results
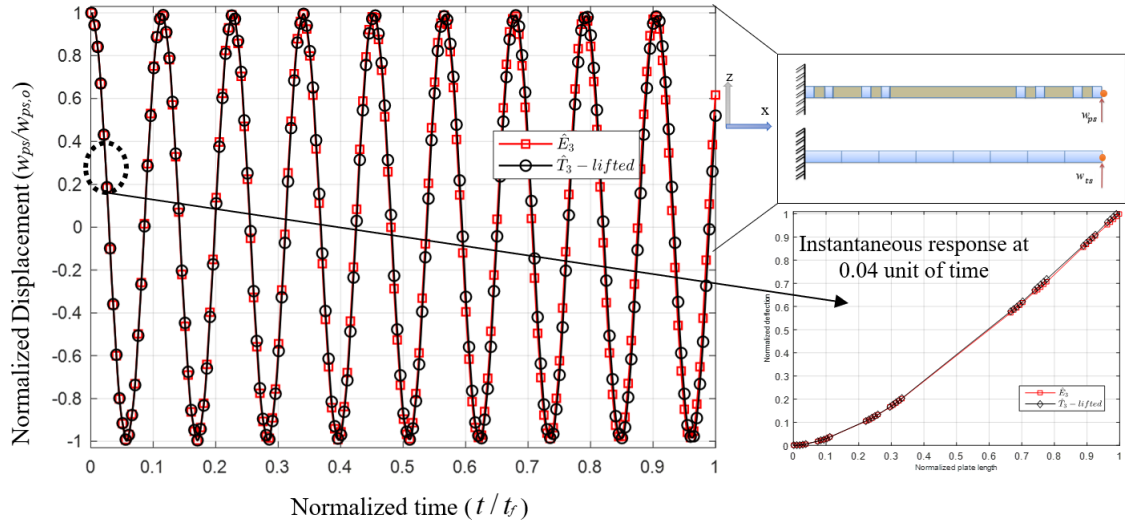
Figure 5.8: Transient lateral response by displacement unit on $\hat{E}_3$ compared to lifted results from $\hat{T}_3$ for a cantilever beam measured at the free end.
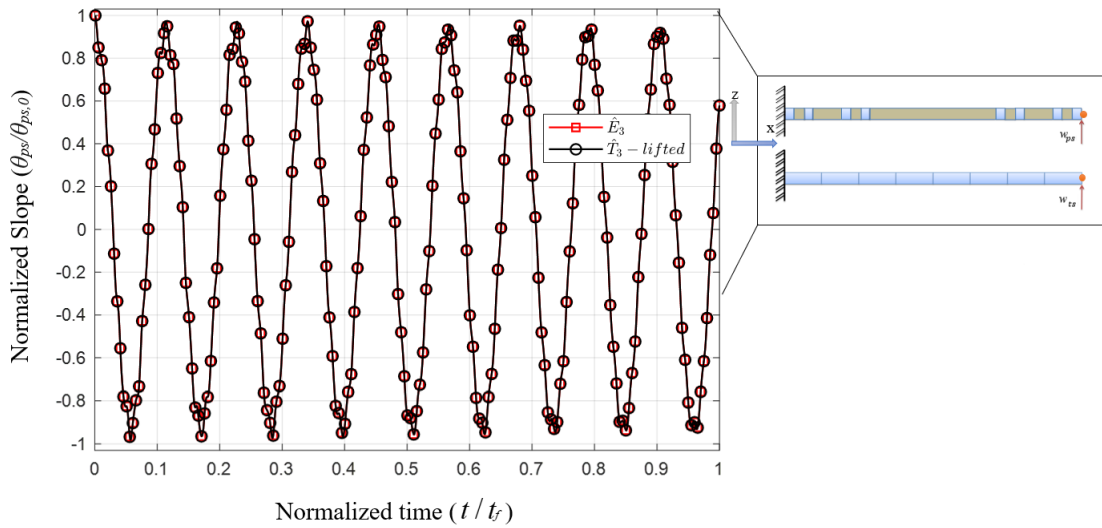
Figure 5.9: Transient velocity response on $\hat{E}_3$ compared to lifted results from $\hat{T}_3$ for a cantilever beam measured at the free end.
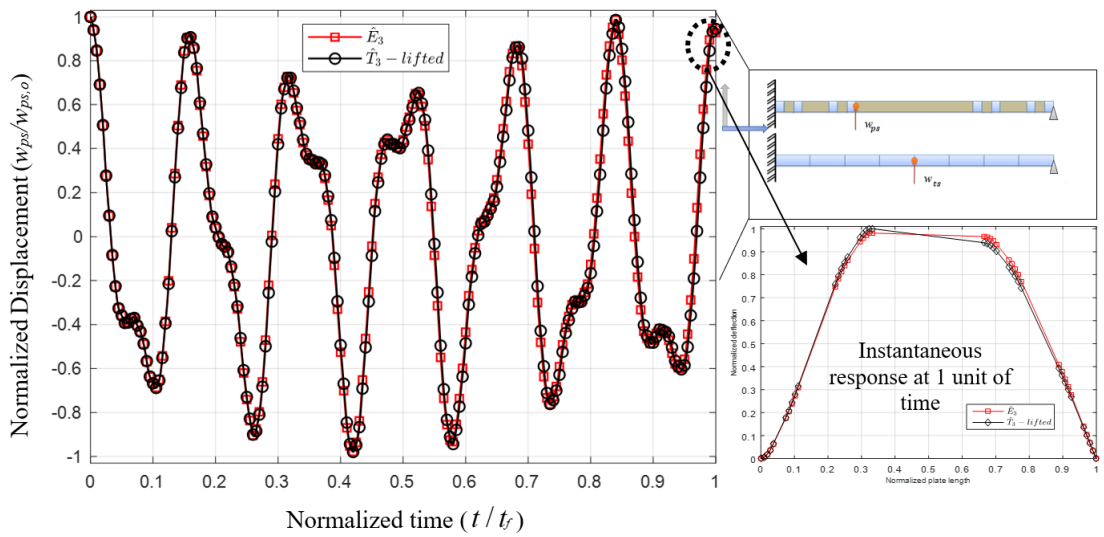
Figure 5.10: Transient lateral response by displacement unit on $\hat{E}_3$ compared to the lifted $\hat{T}_3$ under clamped-pinned boundary conditions measured at point of applied displacement.
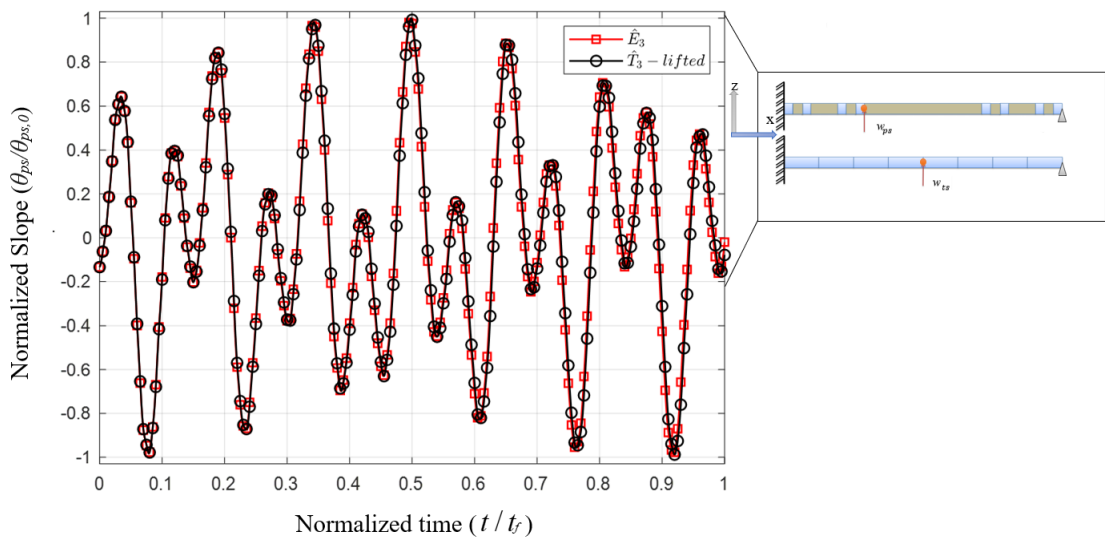
Figure 5.11: Transient lateral response by slope unit on $\hat{E}_3$ compared to the lifted $\hat{T}_3$ under clamped-pinned boundary conditions measured at point of applied displacement.
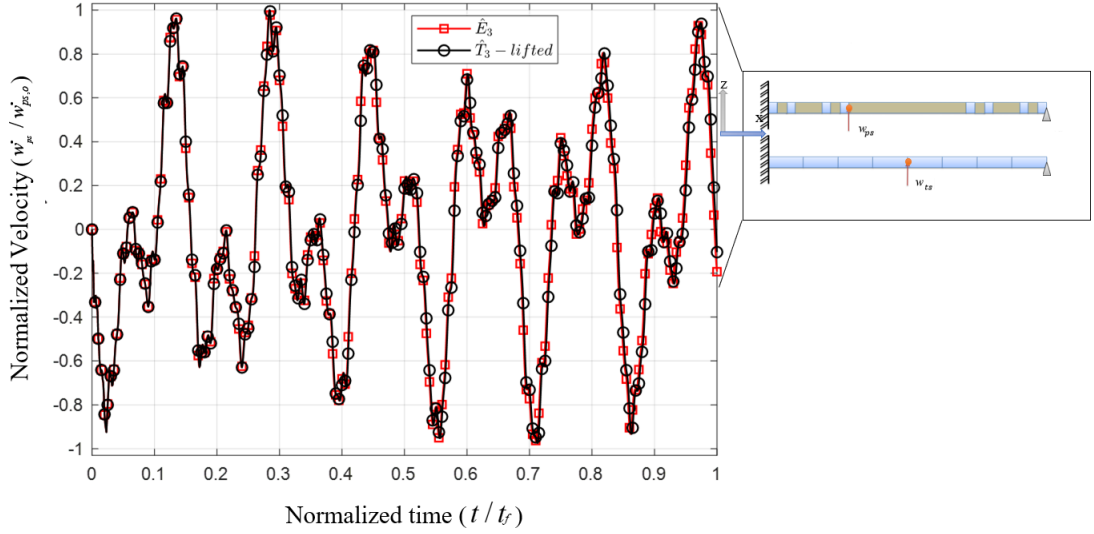
Figure 5.12: Transient lateral response by velocity unit on $\hat{E}_3$ compared to the lifted $\hat{T}_3$ under clamped-pinned boundary conditions measured at point of applied displacement.

have proved to follow equation $H_{ts} = H_{ps}$ and similarly the strain energy $M_{ts} = M_{ps}$. This proves the point that kinetic and strain energy are scalable.

5.8.2.2.4. Symmetric clamped BC under initial force

In this case study, the structure is under a CC boundary condition while a force of arbitrary magnitude (Q_{ps}) displaces the pre-fractal model. Force scaling should follow $Q_{ts} = \beta^{-1} F_{33} Q_{ps}$. Q_{ts} is the magnitude of the force which is applied on the isotropic tessellated model [77], see Case V in Table 5.10. The structure is deformed by utilising a concentrated force in the lateral direction at the left edge of the middle-main hole. The analysis is run on the two spaces separately and the results are compared after using the tessellated reverse-results. The reversed responses are plotted against the main real space results (pre-fractal) to check if the TCM captured the real analysis. Figure 5.14 and Figure 5.15 demonstrate the ability of the TCM method in predicting the pre-fractal results, while the instantaneous beam lateral deflection is compared at the end of the analysis and the results showed a great agreement with what expected. This analysis demonstrates the possibility of using a concentrated load as the initial cause of deflection to the studied structure.

130
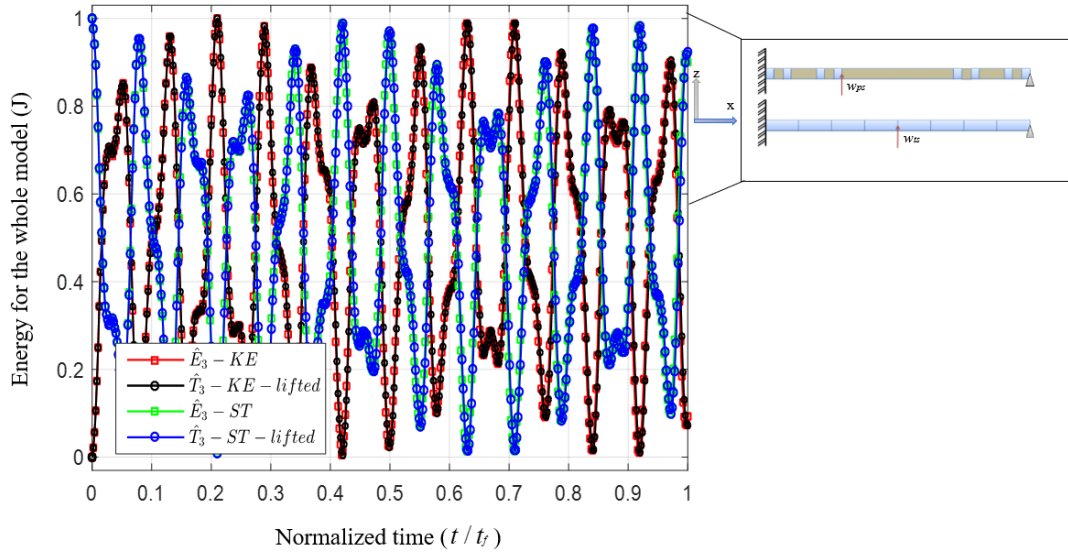
Figure 5.13: The change in the kinetic energy and the strain energy with the time, for the whole model on $\hat{E}_3$ compared with its reversed $\hat{T}_3$ structure.

5.8.2.2.5. Anisotropic scaling of thin beam

In this case study, two approaches are used to create two different tessellated spaces. This is completed by using the anisotropic scaling function, see Equation (5.39), where $F_{11} = (3/2)^3$. So, by using a different combination of linear scaling tensor mappings, different tessellated models can be built, but it is important to maintain the same rules of closing the holes in the axial directions, which in this case are use $F_{11} = (3/2)^3$. The material properties and dimensions are listed in Table 4.2. Most interestingly the constant scalars used in this study are illustrated in the same table. Two cases are listed in this analysis as follows.

5.8.2.2.6. Symmetric clamped BC under initial displacement

The boundary condition for this case is CC, where a displacement of an arbitrary unit of length is applied at the main-left hole's edge (see Table 5.10 for Case VI). In this case study, two approaches are used to create two different tessellated spaces. All three models are under CC boundary condition with displacement as a deforming source is applied on the pre-fractal and mapped into the tessellated space by using Equation (5.18), but for this case, it is essential to use F_{33} , which

131
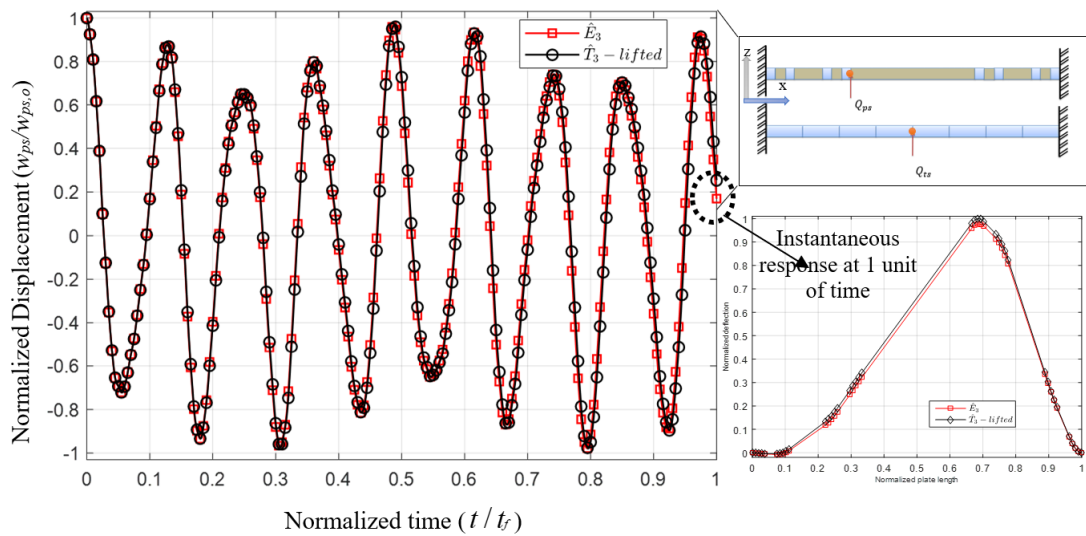
Figure 5.14: Transient lateral response by displacement unit on $\hat{E}_3$ compared to the lifted results on $\hat{T}_3$ for a clamped-clamped boundary conditions measured at the point of applied force.
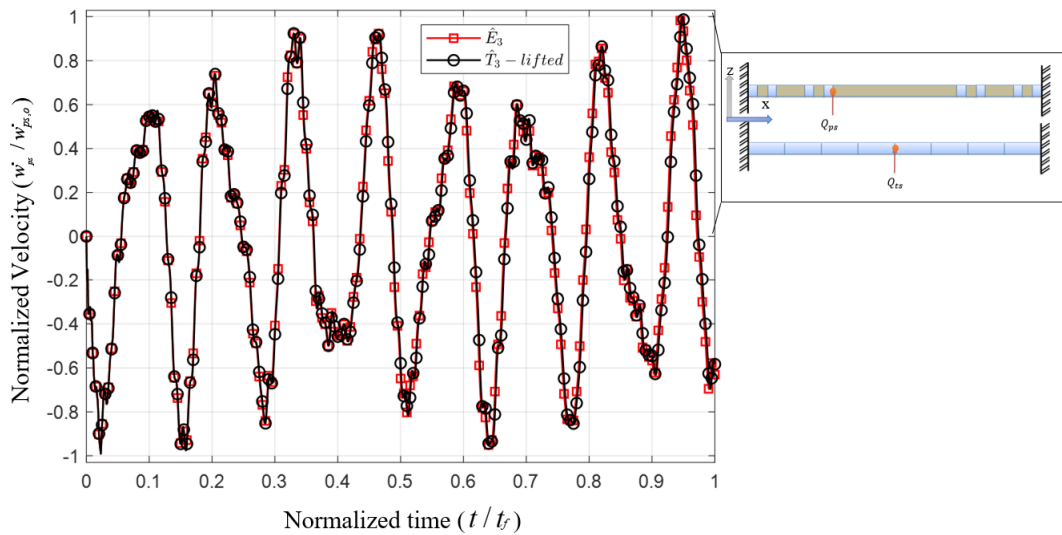
Figure 5.15: Transient lateral response by velocity unit on $\hat{E}_3$ compared to the lifted results on $\hat{T}_3$ for a clamped-clamped boundary conditions measured at the point of applied force.

is entirely different for each scaled case. Similar to the previous cases the results are shown in Figures 5.16 and 5.17, which expand the sense of using the TCM in anisotropic scaling cases, which is investigated in this form for the first time in literature. The instantaneous lateral deformation is also tested at 0.2 unit of normalised time, see Figure 5.16.

5.8.2.2.7. Symmetric pinned BC under initial displacement

Table 5.10 Case VII illustrates the final case study in this work for free vibration. A similar initial deflection is applied inn this case study. The analysis is carried out by using one of the choices of the hole-fill maps. The tessellated model is built by using the first choice in Equation (5.39). The structures are under a PP boundary condition with a lateral displacement as mentioned earlier, this is shown in Figures 5.18 and 5.19. In this analysis all the possible transient responses are investigated in this work and plotted in Figure 5.18 in terms of lateral displacement, slope and velocity varied with time. It can be seen that the analysis after a period of time accumulates more error and this is due to the numerical solver.
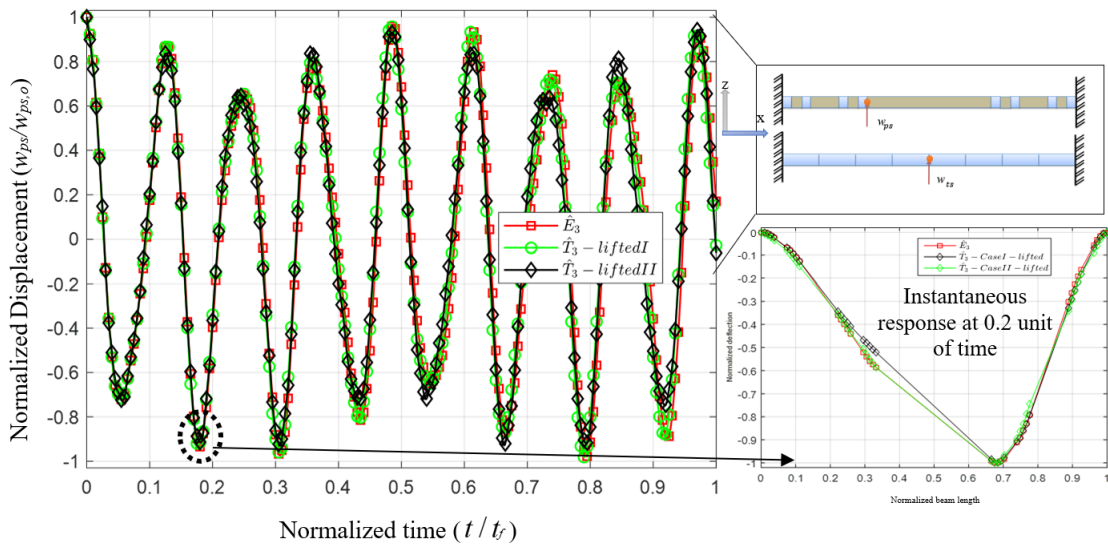
Figure 5.16: Transient lateral response by displacement unit on $\hat{E}_3$ compared to the lifted results on the anisotropic $\hat{T}_3$ for a clamped-clamped boundary conditions measured at the point of applied displacement.
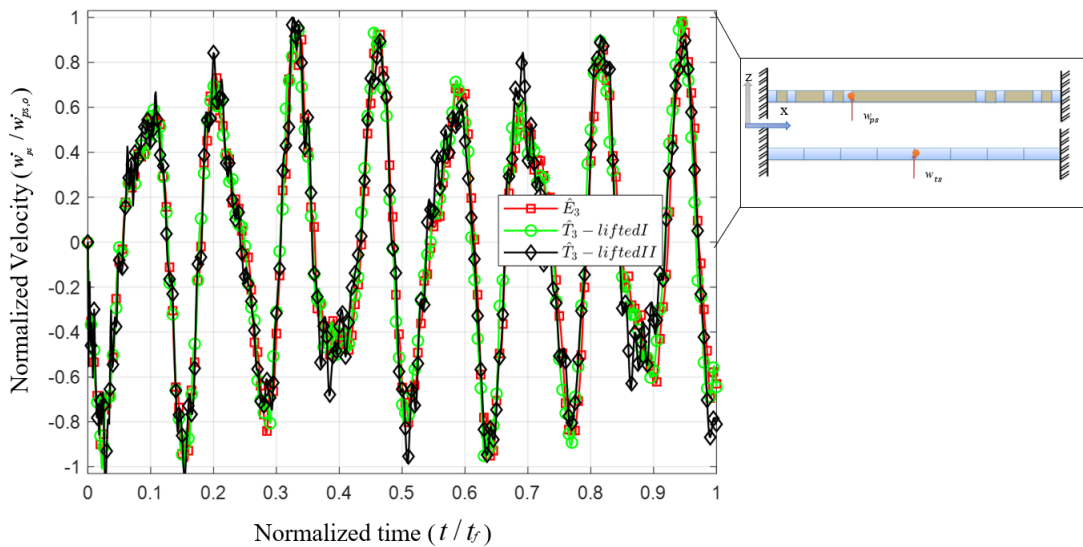
Figure 5.17: Transient lateral response by velocity unit on $\hat{E}_3$ compared to the lifted results on the anisotropic $\hat{T}_3$ for a clamped-clamped boundary conditions measured at the point of applied displacement.
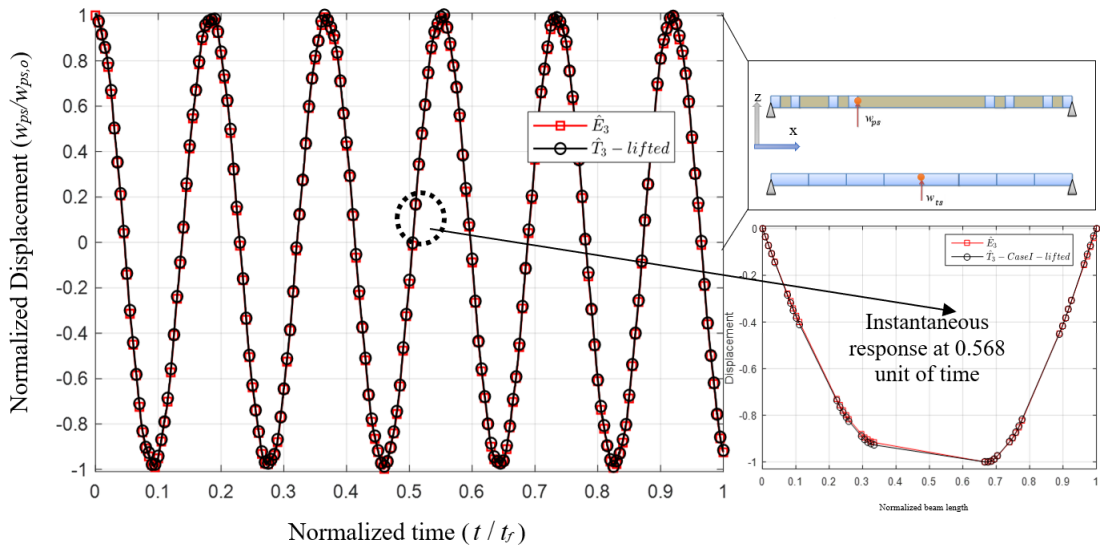
Figure 5.18: Transient lateral response by displacement unit on $\hat{E}_3$ compared to the lifted results on the anisotropic $\hat{T}_3$ for a pinned-pinned boundary conditions measured at the point of applied displacement.
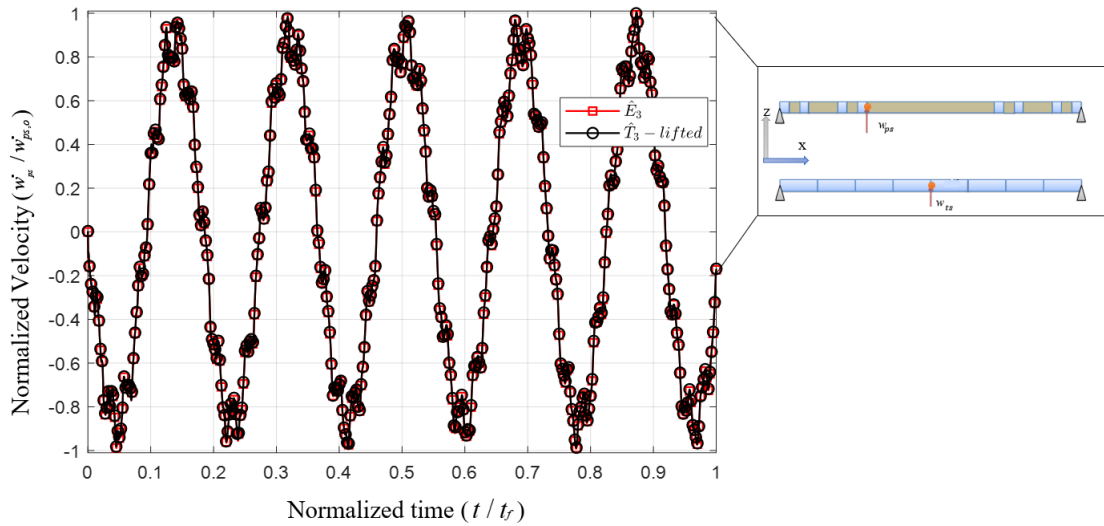
Figure 5.19: Transient lateral response by velocity unit on $\hat{E}_3$ compared to the lifted results on the anisotropic $\hat{T}_3$ for a pinned-pinned boundary conditions measured at the point of applied displacement.

5.9   Forced vibration analysis

The forced vibration analysis for isotropic scaling cases can be found in reference [77], where an isotropic tessellated model has shown a great ability in replicating the real (pre-fractal) model. In this case study two anisotropic scaling cases are investigated. Those cases are defined by Equation (5.39). Similar to the previous section where a separate analysis is carried out on each space separately then the results are compared on the pre-fractal model.

So, the last case study is a beam under a clamped-pinned boundary condition as indicated in Table 5.12 /Case IV, but with a forced vibration. The structure is tested by applying a force of arbitrary magnitude in the lateral direction at the second natural frequency for each model. The 2nd natural frequency is found numerically equal to 0.1317 (rad/ sec) for the pre-fractal model. On the other hand, the natural frequencies are 0.13204 and 0.13098 (rad/sec) for the tessellated models for Case I and Case II correspondingly. The harmonic forces are expressed as $Q_{ts} = A\cos(\omega_{2,ts}t_{ts}) + B\sin(\omega_{2,ts}t_{ts})$ where $A = B/2$. The results are taken at the right edge of the hole and they are listed in Figures 5.20 and 5.21 in terms of lateral displacement and velocity where a near perfect match is achieved. The DN is a mathematical mapping to the pre-fractal hole-behaviour. It is fallow the mapping of a liner equations only.
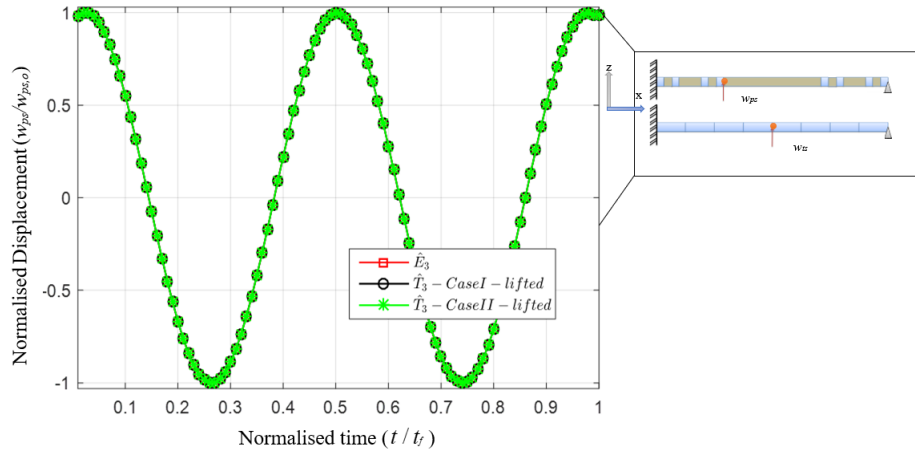
Figure 5.20: Transient lateral response by displacement unit on $\hat{E}_3$ compared to the lifted results on the anisotropic $\hat{T}_3$ for a clamped-pinned boundary conditions for forced vibration measured at the point of applied force.
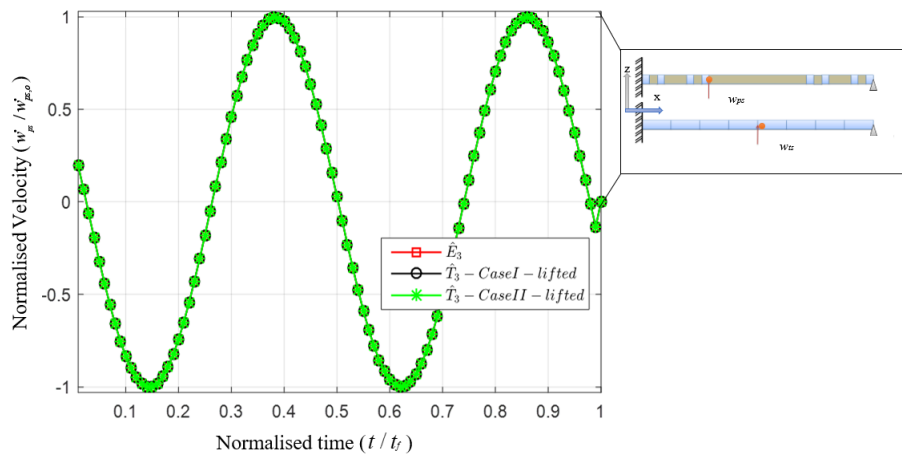
Figure 5.21: Transient lateral response by velocity unit on $\hat{E}_3$ compared to the lifted results on the anisotropic $\hat{T}_3$ for a clamped-pinned boundary conditions for forced vibration measured at the point of applied force.

5.10   Conclusions

All the presented figures proved that the TCM succeeded in capturing the physics. This is done with the following remarks:

1. Deriving transport equations and implementing the conserved continuum laws for general dynamic analysis are achieved in this chapter. This is accomplished by creating the rules of direct and reverse maps.

2. Using the discontinuity network, to overcome a problem that could not be solved in [15] where the response in the tessellated space is found to have a linear jumps in the lateral deflection that would effects the studied models. This is shown in the instantaneous response in Figures 5.8, 5.10, 5.14, 5.16, and 5.18.

3. The analytical analysis is used to test the tessellated models when compared to the numerical analysis with a very good accuracy.

4. Frequency analysis for the isotropic and the anisotropic cases are found matching on both spaces with very acceptable results.

5. The flexibility of the TCM theory to run different BC is remarkable even when tested for different scaled spaces.

6. The transient and instantaneous beam deflections for wider options of BC are matched for real cases with an acceptable accuracy.

7. Using anisotropic scaling factors shows excellent results in matching the physics of a discrete system; this is presented by using different random values of F.

Chapter 6

Dynamic 2-D Analysis of TCM

6.1 Introduction

This chapter answers the main question of this project, can the TCM theory can be used to replace the dynamic analysis of 2-D discontinuous problems in pre-fractal space by creating a hypothetical continuous space named as tessellation? This assumption is also involves solving the problem in the hypothetical continuum space independently from the original one. The outcomes of this analysis can be related through implementing a reverse rule to give the continuum results a physical meaning .

The main reason for choosing the TCM method in creating an entire environment to support the implementation of analytical and numerical approaches, is to re-place the analysis on the pre-fractal space. But due to the fact that 2-D structures in vibration analysis rarely have an analytical solution, the analytical solution will not be considered in this chapter, unlike the previous ones, and the main focus remains on the numerical calculations. All this is possible by using the commercial FE software ABAQUS.

The creation of the chosen pre-fractal type in this work always considers the use of the iterated function system (IFS). This process is also used in creating the tessellated models, and includes creating its geometry accompanied by the hole-fill maps that will close the holes on the tessellated models. Meanwhile, forming the tessellation space is neither arbitrary nor unique. A detailed discussion on this topic is given in Chapter Three, Section 3.2. Due to the complexity of the used models a Python code is used to build those geometries in $\hat{E}$ and $\hat{T}$

space. The Python programming language also includes the implementation of the mathematical calculations for the studied 2-D cases for models type $k = 3$. It is also still important to mention that this work is still in the early stages of verification. For this reason, it is crucial to run the analysis independently on the pre-fractal space as well as running the analysis on the tessellated, then comparing the results afterward through implementing a reverse scaling rule.

From the previous chapters, the TCM theory is developed and verified to test static case studies for one-dimensional (1-D) and two-dimensional (2-D) structures; and through dynamic cases for 1-D structures in solid mechanics analysis. In this chapter the framework for applying the TCM theory in testing 2-D holey structures such as the pre-fractal models is introduced and verified. Through tracking the development of this theory, it is found that many techniques such as the hole fill-map techniques, discontinuity network, and the reverse mapping is well established at this point and are therefore ready to be tested. This is crucial to assist running the analysis on the hypothetical space.

This work tests the frame procedure derived in Chapter 5, where the dynamical analysis of 1-D pre-fractal structure known as the Cantor set is tested by the TCM theory, and a small strain theory is applied for a holey structure that follows the Euler-Bernoulli and Rayleigh beam theories. It is also worth mentioning that the approach developed in chapter 5 and tested in this chapter is been updated further in next chapter. This updated methodology is found to predicted the natural frequency at higher accuracy than the one used in this section with some limitation. This method is include scaling the density by considering the momentum equations.

Similar analysis is carried out in this chapter for the 2-D pre-fractal model known as the Sierpinski Carpet. Also a small strain theory is applied for a holey structure that follows the Mindlin-plate theory. The results confirm the statement that the TCM theory can be used as an alternative approach for analysing the pre-fractal models without the need to deal with their space complexity. This statement is achieved in this chapter. Section 6.2 introduces the general procedure to implement the TCM. It is followed by Section 6.3, which presents the numerical method and the case studies. The chapter ends with conclusions in Section 6.4.

6.2 The general procedure to implement TCM in 2-D pre-fractal models

One of the challenges that faced the previous work in this field is the complexity of dealing with the studied models such as the Sierpinski Capet after mapping it into the tessellated space as in [54]. This chapter takes the work a step further from where it started, it enable the users to use an automatic code to create the hypothetical models. So, in order to deal with such models, Python code is used to handle the TCM calculations and the procedure steps, from building the interested model's geometries to calculating the corresponding material properties and finding the scaled relations between both models. And the reason behind using Python as the constructing language is because Python has shown great ability in dealing with the iterated function system (IFS), which in principal are sets of equations that can be used to create both models. Those mathematical equations are presented in Appendix A. It is found that creating the models on the pre-fractal space is much easier than on the tessellated one. For example, the equations listed in Appendix A, Table A-1 are applied directly through eight lines of codes. On the other hand, the tessellated models are built by applying the concept of the hole-fill maps beside the IFS. This will lead to apply the equation listed in Appendix A, Table 1. Those equations are completely different form the equations listed in Appendix A, Table A-2 because they depends on the (x, y) coordinates (see Appendix C). For this reason, constructing the tessellated geometry can be considered harder than creating the pre-fractal one, from a programming perspective.

Moreover, through linking the relations between the deformed and the real geometries the F-function can be calculated. More information about the hole-fill maps is discussed later in this work. Finding the values of these functions is essential to link the material properties and the boundary condition and later to find the reverse-maps for the tessellated results to be compared with the results of the real space. At the end, it is crucial to illustrate the problem size that Python is dealing with for the selected case studies. For example, for the case of $k = 1$ Python code has to assign the material properties and dimensions for 64 parts. This number is applicable to both models, although for the tessellated model the

material properties are anisotropic and completely different from one case to another. So it is irrelevant to mention all the material properties here. Besides, this difficulty becomes greater when dealing with structures such as $\hat{T}_2$. This model has 512 parts, and the number of elements on the studied models reaches to 4096 for $\hat{T}_3$. The TCM theory can be applied in five steps. These steps are used to create the tessellated models, which are extensively listed in reference [77] and in Chapter 3, where the work mainly consists of applying four steps to construct these models. But they are briefly mentioned here and extended to cope with using the Python code:

6.2.1 Step I: Model geometries

This step is concerned with building the models in the pre-fractal and in the tessellated, but with more focus on how to construct the tessellated one. As mentioned earlier, the pre-fractals and tessellation models are created separately by relying on the iterated function schemes (IFS). Those systems of equation are listed in Appendix A for the Sierpinski Carpet. The contraction maps that involve building the pre-fractal models as presented in Table A-1 in the same appendix. In the same manner, the tessellated model is constructed through the maps that are demonstrated in Table A-2. However, to understand the principles behind creating these equations, a further step is needed, which is insertion of an initial triangular meshes on the pre-fractal models as in Figure 6.1 (see Appendix C). Then these models are allowed to undergo the IFS. Basically, these maps are performed on the pre-fractal models first. For example, the maps that create a model type k are presented as $\hat{E}_k = \bigcup_i S_i(\hat{E}_{k-1})$. Again, S_i represents the IFS functions that are presented in Appendix A, Table A-1. Moreover, it also can be represented by $S_k = A_k \cdot A_k + c_k$ [6] (see the same appendix). In a similar manner, the tessellated models, are presented mathematically by $\hat{T}_k = \bigcup_i P_i(\hat{T}_{k-1})$, where P_i produces the maps required to create the tessellated models by the IFS and the hole-filling maps. These functions are contraction maps that involve in building the tessellations through closing the holes in the pre-fractal models. These maps are presented in Appendix A, Table A-2. Please note, that $\hat{E}_0 = \hat{T}_0$ and to create $\hat{T}_1$ the equation $\hat{T}_1 = \bigcup_i P_i(\hat{T}_0)$ can be used. So this process always considers applying the IFS mapping on the continuous model (closed hole model) from

the previous iteration. This mean that the model of type $(k-1)$ must be run on different (smalls) scale than the final model. And the concept of applying the hole fill-map can be explained by identifying the centre of the pre-fractal's holes. Then following equation $\Phi_{new} = (\Phi_{old} - \delta \tan(\theta))/\alpha$, which determine's the new coordinates for the tessellated model type $(k-i)$, where i is iteration number $0 \geq i \geq k$, Φ is the model coordinates before and after the mapping; θ is the angle between the model's lines before and after closing the holes; δ is the half hole length; and α is the number of elements that are going to be stretched to fill the hole, see Figure 6.2.

Finally, it is crucial to mention here that by closing the holes on the tessel-

(a)   (b)
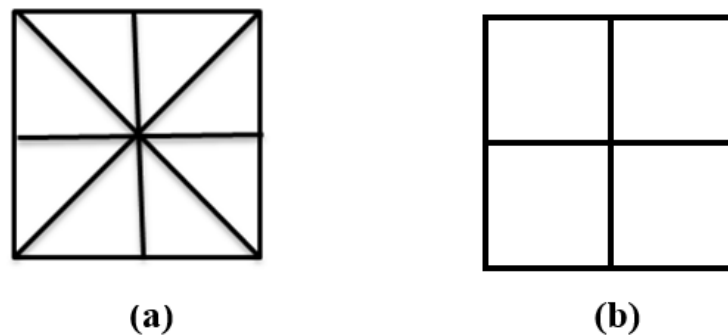
Figure 6.1: Basic mesh on the pre-fractal under different mesh type: (a) considering the TCM techniques (b) FE square mesh pattern.

lated space the structure is going to have individual nodes that have the same coordinates. And basically, this is the location that can be used to apply the discontinuity network denoted by DN [55]. The DN is found to accommodate the jumps in the field on the continuous space. This is highly dependent on the case study that is being analysed. The tested models are presented in Figures 3.2 - 3.4. Furthermore, these figures are also illustrate the DN distributed on the tessellated models and represented by red lines.
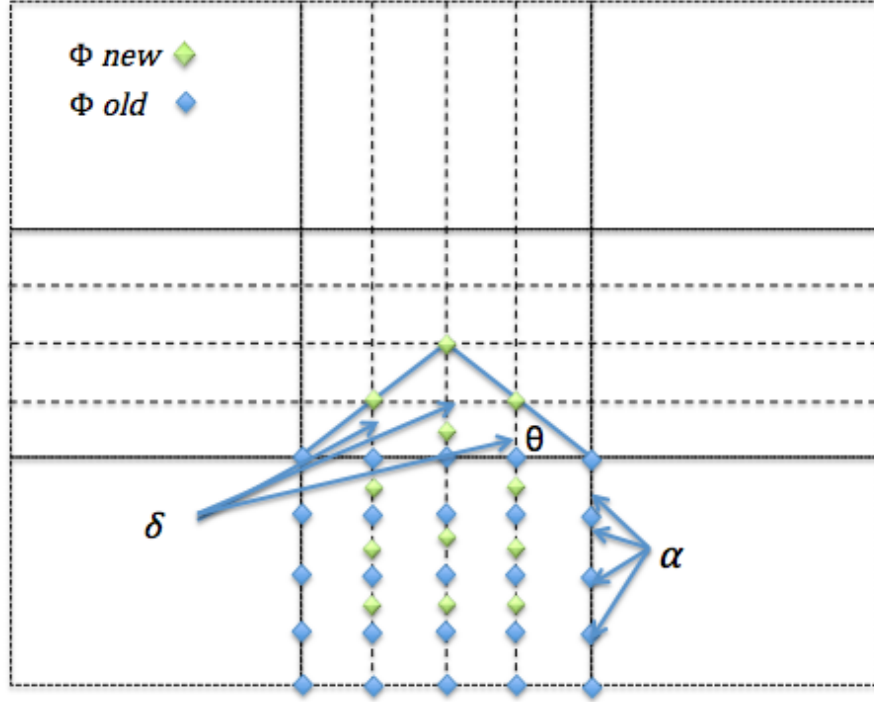
Figure 6.2: The concept of using the hole-filling maps.

6.2.2 Step II: Direct mapping

The previous step is completed in such a way as to ensure the same numbers of elements are produced after scaling the pre-fractal models into the tessellated space. The most important section in this work is to find the geometrical links between the deformed and the initial models. To create the 2-D models by the direct mapping is found challenging due to the high numbers of elements that are used in this case study. For this reason, Python code is found more straightforward to deal automatically with the models' coordinates on both spaces, since the coordinates on the $\hat{E}_k$ and $\hat{T}_k$ have the same number of elements on each model. This stage links each tile on both models together, which is possible by using Nanson's identity. A spatial link in the physical space (where the pre-fractal resides) is related to its corresponding tessellated space (where the tessellation resides) by the relationship $dx_{ts} = F \cdot dx_{ps}$, where F is the hole-fill map and plays a fundamental role in the Similitude theory as mentioned earlier. Due to the complexity of the 2-D models, a Python code is used to implement Nanson's identity represented by $d\underline{V}^*_{ts} = Jd\underline{V}^*_{ps}$ and $d\underline{\Gamma}^*_{ts} = Jd\underline{\Gamma}^*_{ps} \cdot F^{-T}$ [71], to

calculate the F-Function or what is called the 2nd-order mapping tensor by using the following equations:

$$
\begin{bmatrix} \alpha_{ts,1} \\ \beta_{ts,1} \\ \alpha_{ts,2} \\ \beta_{ts,2} \end{bmatrix} = \begin{bmatrix} \alpha_{ps,1} & \beta_{ps,1} & 0 & 0 \\ 0 & 0 & \alpha_{ps,1} & \beta_{ps,1} \\ \alpha_{ps,2} & \beta_{ps,2} & 0 & 0 \\ 0 & 0 & \alpha_{ps,2} & \beta_{ps,2} \end{bmatrix} \begin{bmatrix} F_{11} \\ F_{12} \\ F_{21} \\ F_{22} \end{bmatrix}
\tag{6.1}
$$

where α is the x-axis component to the first chosen edge of the basic mesh on either space, while β is the y-axis component of the chosen edge of the basic mesh on either space, the subscript (1 or 2) in these variables indicates the first and second chosen edges (remember in this study we are using a basic mesh in the shape of triangular elements, so by relating any two edges to form the F-function on both spaces, this is completely enough to establish the full link between both spaces), while ps and ts are denote for the pre-fractal and the tessellated space.

In general, the F-Function is a 2nd-order tensor that can be created directly through equation (6.1) and takes the following shape [69]:

$$
F = \begin{bmatrix} F_{11} & F_{12} & F_{13} \\ F_{21} & F_{22} & F_{23} \\ F_{31} & F_{32} & F_{33} \end{bmatrix}
\tag{6.2}
$$

For the current study, the structure is scaled in 2-D space. This means F_{13}, F_{23}, F_{31} and $F_{32} = 0$. This is unlike the approach considered for 1-D structures [77] and [80], where the model had the same F-Function.

As mentioned earlier, the 2-D models are divided into eight segments that are distributed evenly on the whole studied model. So, for example, for the geometry of $k = 1$ there are around 64 elements; and each element has its own mapping functions. The F-Function is defined correspondingly. For this reason, it is found, and very essential to use an orientable programming language such as Python.

6.2.3   Step III: Material properties

The second most crucial reason behind using Python code is to calculate the material properties and assign them into their correct location. Calculating the

material properties and assigning them into the correct location is highly linked with calculation of the corresponding F-functions and geometrical coordinates. So after finding the values of the F-function, it is possible now to apply the rules that are outlined in Chapter 5 which include the use of the scaling rules by paying extra attention to the constant scalar. So, two main equations are used in this section after calculating the F-Function tensors, which are the density and the elasticity equations represented by Equation (5.10) and (5.34). The constant values are discussed in Chapter 5. For a demonstration of how the material properties are created on the tessellated space, Figures 4.13 is showing the normalised principle of Young's modulus which is calculated by Equation (5.34). This is demonstrated on the tessellated models of the third complexity. For this reason, the material properties of models tested on $\hat{T}$ space could not be presented in this work.

It is also worth mentioning that these constant mappings incorporated some scaling limitations that are chosen to fit the TCM method for this cases of analysis, which is also found to match the chosen values during the static analysis, i.e. $\alpha^\rho, \alpha^u, \alpha^v$ and α^e are following the values listed in Table 6.1. From the previous analysis to the model, its found that the α^ρ does not affect the results since it is concerned with scaling structure density. For this reason, it is chosen to have a unit value, see Table 6.1. On the other hand, α^u and α^v are found to have the same magnitude, but α^v incorporates the time scaling factor while α^u, which is concerned with the displacement, is not. For this reason the relationship between the displacement factor is selected to follow $\alpha^u = \beta$ and velocity constant $\alpha^u = h^{-1}\alpha^v$. The time scaling factor is represented by h. For more details about how to find these constant, see reference [77] Also the material properties provided for the tessellated space of an isotropic material and their values can be fed into the numerical solver with the aid of reference [85 and 86].

6.2.4   Step IV: Boundary conditions

In order to create the same space that mimics the pre-fractal space, the same boundary condition must be used in this type of analysis. And depending on the studied cases, the boundary must be scaled from the pre-fractal space. For

Table 6.1: Scaling constant values.

Equation needed	Contravariant and Covariant Rules
Volume	α^{ρ}
Displacement	α^{u}
Velocity	$\alpha^{v} = h\beta^{-1}$
Time	$h = 1$
Energy	$\alpha^{e} = \alpha^{-\rho}(\beta^{-1}\alpha^{v})^{2}$

example, in the case of applying a displacement as an initial boundary condition or as a source of deforming the models, these values must be scaled by following the relationship $\alpha^{\rho}\underline{u} = \alpha^{u}F^{-1} \cdot \underline{u}_{ts}$. And due to the fact that the 2-D models consist of different scaled parts, extra care must be taken for this case while assigning the applied deforming source, because the F values are functions of the coordinates in the (x, y) system.

Using a clamped or fixed boundary condition where all six degrees of freedom for a node are constrained gives the same constrained boundary conditions on the tessellation.

Similarly, for stress constrains Equation (5.14) applies (i.e. $\underline{\underline{\sigma}}_{ps} = \alpha^{v}JF^{-1} \cdot \underline{\underline{\sigma}}_{ts} \cdot F^{-T}$), which approves that free-stress boundary conditions are must be identical on each space. A comparable approach can be held for the stress at the hole's edges on the pre-fractal space. This is must be maintained the same, while closing the hole's edges on the tessellated space.

Finally, after creating the tessellated geometry and in order to maintain applying the same boundary conditions on the closed holes, it is found that it is necessary to match the boundary conditions that are used on the pre-fractal and especially the one that is used around the closed holes [55].

6.2.5 Step V: Analysis and post-processing

This is the second main step of applying the TCM theory in analysing the pre-fractal models. Reaching this step declares that the tested models on the pre-fractal and the tessellated spaces are ready for further analysis by any solver. Even though the fact that the tessellation models are considered as a replica to

the real model, their response still lacks the physical meaning. This means that it is necessary to use the reversed mapped rules that were mentioned earlier. This process is equal in importance to the step of creating the models in the first place. So, to apply the reverse maps of Equation (5.13) and Equation (5.18) is essential and depends on which response we are after, It also might need Equation (5.14) with the aid of Equation (4.25); this purely depends on the tested cases. This is true for all fields on tessellation which can subsequently be lifted back to the pre-fractal using the scaling identities.

6.3   Numerical analysis and verification

This study is concerned with testing the pre-fractal structure known as a Sierpinski Carpet for three different geometries, where $k = 1, 2,$ and 3 . All these geometries with their corresponding tessellated structures are presented in Figures (3.2, 3.3 and 3.4). Due to the fact that analytical solutions for a 2-D plate with perforation is hardly exist in the engineering fields. This analysis is carried out with the concept of using a relative error. So by using the same tool to analyse the studied models and using the exact same type of procedure with the same mesh types, and numbers of elements beside using the same time step for the FE solver. All of this is necessary to reduce the differences between the pre-fractal and the tessellated models. So, by carrying out such analysis, it can be judged whether the solver is dealing with the same problem or not. For this reason, the only verification that is needed in analysing 2-D models is a relative error. This is the procedure that has been carried out through the work, which is unlike the previous work that is presented earlier in Chapter 4 and Chapter 5.

All the cases presented in this study are built with the aid of using Python code. Mainly, the analysis is run on the tessellated space, then the tessellated results are compared with the pre-fractal results after being scaled back into the pre-fractal space. This is done by using the reverse equations mentioned earlier in Section 6.2. A shell element is used to represent the 2-D models on both spaces, which has general pre-fractal material properties and general geometrical features as presented in Table 5.1.

First, to verify the tested models, a mesh study is found to be essential. In the

following sections, it is found vital to run a mesh study first to find the best elements and a minimum number of meshes to represent the studied models by the numerical solver ABAQUS. Moreover, due to the fact, that these models are constrained with a specific mesh type, it is also found necessary to compare the results presented by a parametric mesh study with the results presented by the TCM theory. Different geometries are tested under different boundary conditions and different loading sources. Two main areas are investigated, frequency analysis and dynamical response with time (for more details see Appendix C):

6.3.1 Solver verification

It is important to mention that ABAQUS normally uses Mindlin-thick plate theory to avoid the shear locking when using a shell element [85]. In this analysis the eigenvalue problem to find the natural frequencies of small vibration must be examined. The governing equation of motion listed in ABAQUS solver is as follows [72]:

$$\eta^2[M] + \eta[C] + [K]\phi = 0 \qquad (6.3)$$

where $[M]$ is the mass matrix; while, $[C]$ is the damping matrix; $[K]$ is the stiffness matrix. Moreover, η is the eigenvalues, and $\{\phi\}$ is the vibration mode vector. A Lanczos eigen-solver is used in this study to solve the FE equations for extracting the extreme eigenvalues and the corresponding eigenvectors of a sparse symmetric generalised eigen-problem. Moreover, modal analysis is used to find the structural responses at the first natural frequency. This type of analysis provides a time history analysis for a linear system, where the model is under a form of excitation during a specified time. Then the model is projected onto the chosen eigen-modes used for the dynamic representations by using the following equation [72]:

$$\ddot{q}_i + B_{ij}\dot{q}_j + \omega_i^2 q_i = (f_t)_i \qquad (6.4)$$

$$(f_t)_i = f_{t-Vt} + \frac{Vf}{Vt}Vt \qquad (6.5)$$

where i and j are the indices span of the eigenvalues; B_{ij} is the projected viscous damping matrix; q_i are the generalised coordinates of the chosen mode i (the amplitude of the response in this mode); ω_i is the natural frequency of the

undamped mode which is equal to $\omega_i = (k_i/m_i)^{0.5}$ [81] and [83] and must be calculated by a previous frequency analysis step; Finally $(f_t)i$ is the magnitude of the force applied to the system at that selected mode.

More importantly to mention, from all the numerical analysis executed by the commercial FE software ABAQUS (version 6.13), using shell elements, it is found that the best element is SR8 [72] for both pre-fractal and tessellated structures. It is also imperative to investigate the accuracy of the used mesh on both models. But it is not possible to apply a controlled mesh study on the tessellated model and more importantly there are the restriction in using such a basic mesh which is consists of 8 elements and is extremely linked to the mesh chosen on the pre-fractal. For these reasons a mesh study could be performed by running a mesh study on the pre-fractal models only. Then this is compared with results on the tessellated space in terms of frequency analysis and mode shapes. For this reason, a mesh study is found to be crucial in choosing the minimum number of elements on the pre-fractal models to give the optimum results. This study is essential to investigate the current limitation of considering the used meshes for the TCM theory compared to the best performance on the pre-fractal models that could be achieved.

6.3.1.1. Mesh sensitivity

A convergence study is always essential in numerical calculations especially in the absence of experimental results. This study is vital to define the type and number of elements that are going to be used in this study, which alternatively defines the model size. In verifying the TCM for 2-D pre-fractal analysis, it is important to ensure running the same type of analysis throughout the whole study. So, in this work, a convergence study is carried out on the pre-fractal models instead of testing the tessellated models. This is due to the limitation of applying such techniques (mesh convergence study) on the tessellated model, due to the shape of its geometry. Furthermore, the TCM theory has some limitations towards the initial mesh conducted on the studied models. This mesh must follow a certain pattern (i.e, as illustrated in Figure 3.2). By following this pattern, it is found that the number of elements for each case study type k is limited to a certain number of elements. These numbers of elements are illustrated in Table

4.4. This table indicates that 64 elements are necessary to mesh the models for the case $k = 1$, for both models the pre-fractal and tessellated. For the case of $k = 2$ the models entail 512 elements on both spaces. Finally, 4096 is the total number of elements used on $k = 3$. The mesh patterns used in verifying the TCM theory are presented in Figure 6.1 a. This is important to be highlighted because the conclusions are crucial for defining the next step.

The following analysis performs a convergence mesh study by using square mesh patterns on the pre-fractal models as illustrated in Figure 6.1 b. This type of mesh is widely used in the field. The analysis in this section is accomplished by testing the pre-fractal models for three different geometries $k = 1, 2$, and 3. This is done by reviewing the first 4 natural frequencies of non-uniform perforated plates by using the mesh illustrated in Figure 6.1 b. The studied models have shared the material properties listed in Table 4.3 (A detailed mesh study is performed on the Vicsek pre-fractal models and the results are recorded in Appendix D).

The numerical solver results show that the best element type for this study is the SR8. This element gives the best results for all the tested models of the pre-fractals. Furthermore, to find the minimum number of elements by testing the stability of the calculated natural frequency while alternating the meshes size is crucial to have solid results. This is performed through using 5 different sets of mesh size for all the tested pre-fractal models. Figures 6.3, 6.4 and 6.5 show the mesh study on different pre-fractal models. Except Figure 6.3 ignores the results when the mesh size is 0.3 unit of length, for a better presentation to the results. Therefore, Figures 6.3 to 6.5 clearly show that the minimum number of elements that give a stable prediction of the interested frequencies for the first three pre-fractal geometries are (0.037, 0.025 and 0.00833) per unit of length. This would create about (512, 1024 and 8192) number of elements on each studied model correspondingly. This obviously indicates that the minimum number of elements needed to get a stable result on $\hat{E}_1$ is only 512, while the TCM theory limited this number to only 64; While for the higher studied pre-fractal models such as $k = 3$ the minimum number of elements that the theory allows are 4096 while Figure 6.5 recommends to use 8192 number of elements. This is true for all the studied models if compared with Table 4.4. So to understand the accuracy of the current used mesh on the TCM theory, this is carried out in the next section.

6.3.1.2. Mesh pattern accuracy

Moreover, as mentioned in the previous section it is almost impossible to have consistency in the tested results if the mesh study is tested on the tessellated models due to the complexity of their geometrical shapes and the difficulty of controlling the mesh shapes. For this reason, the analysis in this section is also centred on testing the pre-fractal models. Even though, running the analysis on the pre-fractal models are a costly process compared to the problem size and it is a time-consuming. However, this is necessary for the sake of verifying the tested results' accuracy.

The tested models are two cases of Sierpinski Carpet of the third complexity under a Clamped-Clamped-Clamped-Clamped, which is denoted by a 'CCCC' boundary condition. The material properties of the studied models are presented in Table 4.3 with the thickness 0.05 unit of length. The numbers of elements on the studied cases are 4096 for Case 1, while the number of elements in Case 2 is 8192. Case 1 represents the case of the basic mesh that is used to verify the TCM theory, see Table 4.4, while Case 2 represents the standard mesh used in the previous section. In general, Table 6.2 gives the natural frequencies for two mesh's patterns, also listing their absolute relative error. The mode shape of the studied cases are following the legend in Figure 6.6 to indicate the normalised deflection on the studied plates. The mode shapes are presented in Table 6.3, where only the first three mode shapes are presented and compared. Table 6.3 obviously shows that even by using a small number of elements, the mode shape can be obtained with a very good accuracy with a maximum absolute relative error of 0.03 percentage.

To run a frequency analysis on 2-D models, it is important to mention the naming system for these mode shapes. The mode shapes which have no nodal lines, for example, the very first mode of vibration of plates is the first bending modes that are represented by a dark line. The mode shapes which have only one nodal line along the y-axis ($j = 1$) would be the pure torsional modes. As the value of j increases to 2 then two nodal lines are formed along the y-axis. Similarly, the mode shapes which have only one nodal line along the x-axis ($i = 1$) would be
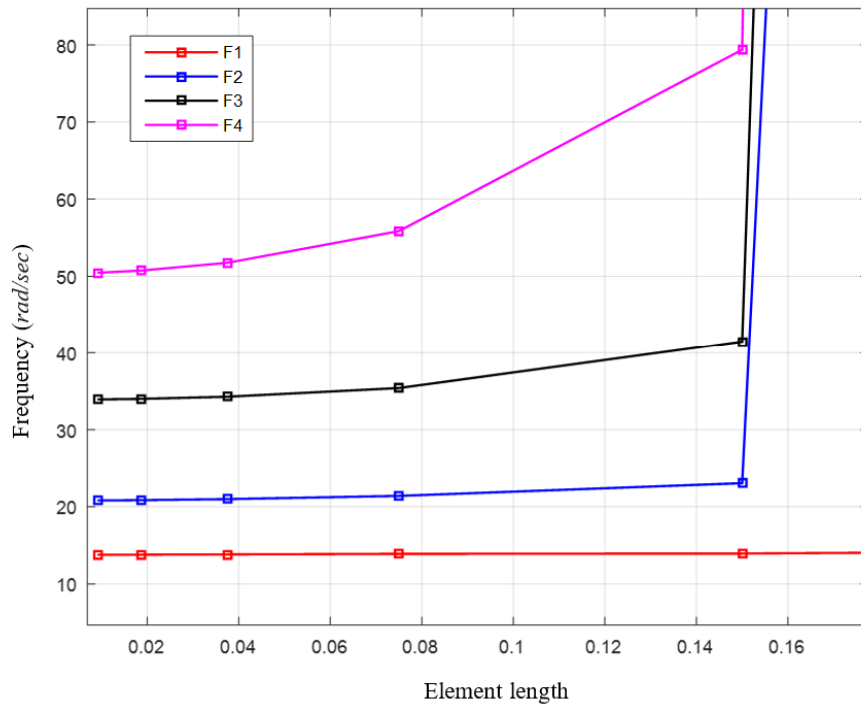
Figure 6.3: Mesh sensitivity study for pre-fractal geometry $\hat{E}_1$.
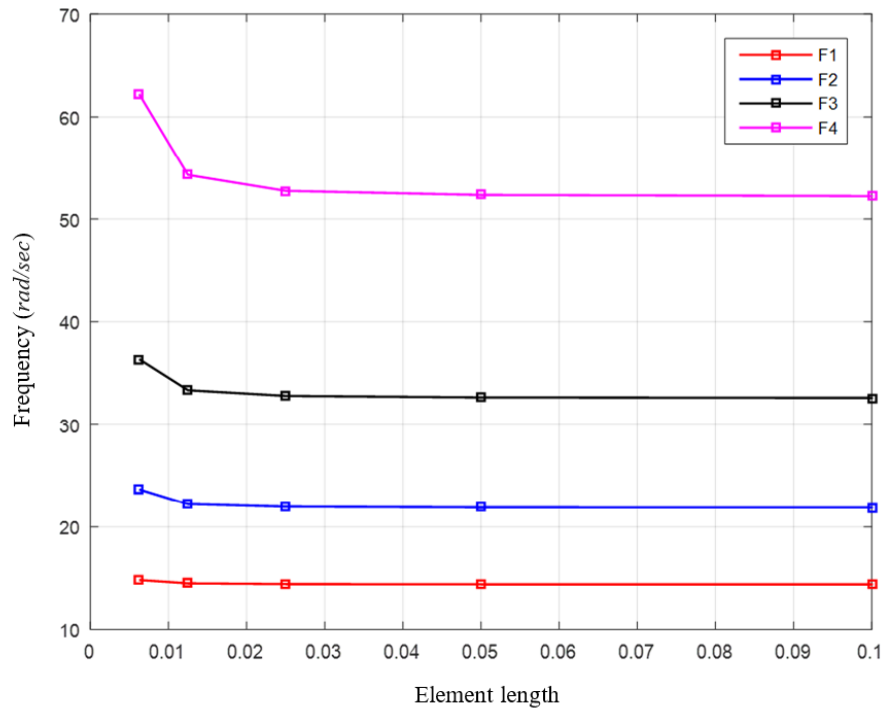
Figure 6.4: Mesh sensitivity study for pre-fractal geometry $\hat{E}_2$.
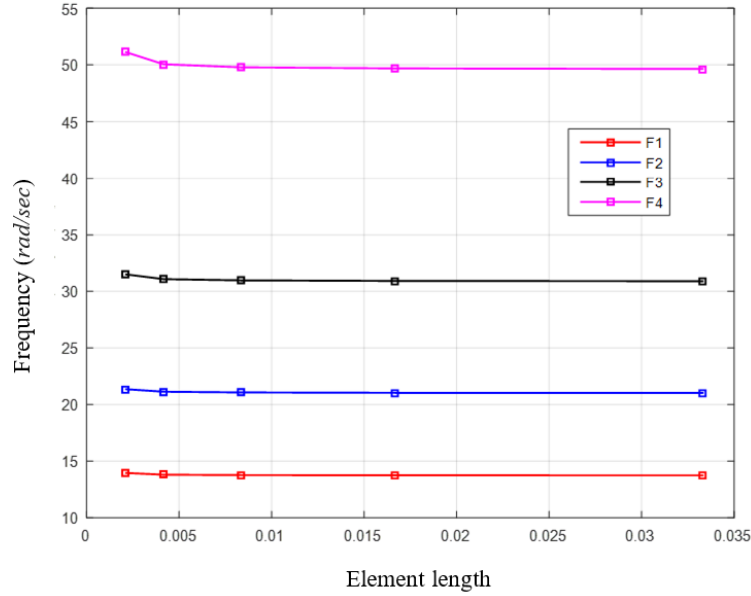
Figure 6.5: Mesh sensitivity study for pre-fractal geometry $\hat{E}_2$.

the pure bending modes. For example, mode 4 of the plate with aspect ratio 1 are represent to model lines one parallel to the x-axis and the others are parallel to the y-axis, this is identified as $(1,1)$. When the value of i increases to 2 and 3, the third and fourth pure bending modes, respectively, are formed. The mode shapes which have combinations of both nodal lines are stated as composite modes. So each mode of vibration can be represented by (i, j) to identify the plate's modes of vibration.

In Table 6.3 the mode shape which has no nodal line, for example, is the first mode shape which represent the first bending mode and its signified by $(0,0)$, while the figures with only one nodal line present the pure modes of vibration like $(1,0)$ as in Table 6.3 the second mode which depends on the axis that the nodal lines are parallel to. This is the naming system that is used to describe the mode shapes in the following sections.

6.3.2 Theory verification

Based on the analysis run in the previous section, the dynamical models are built and tested correspondingly. The studied models are shell 2-D models, for the case of pre-fractal with overall dimensions of $\ell_o \times \ell_o = 0.9 \times 0.9$ per unit
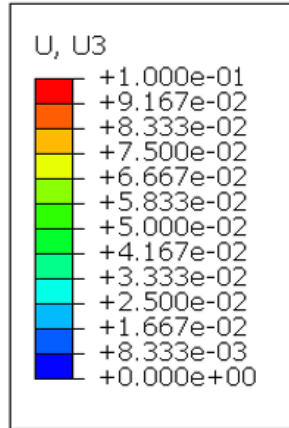
Figure 6.6: Displacement legend for frequency analysis

Table 6.2: Differences in the natural frequencies: analytical vs numerical.
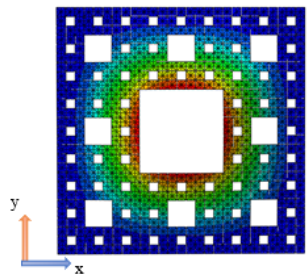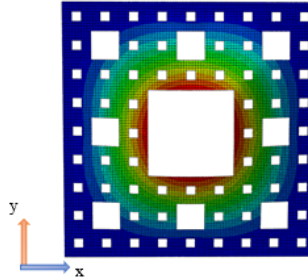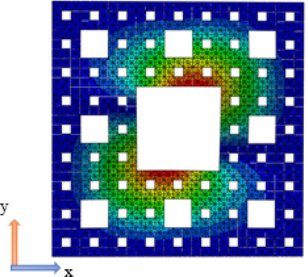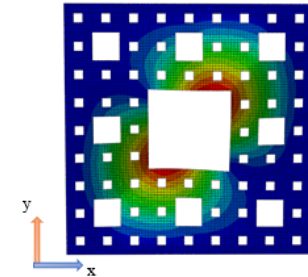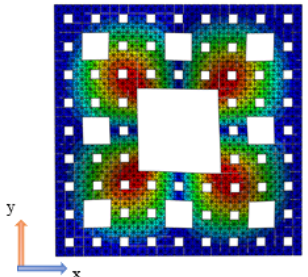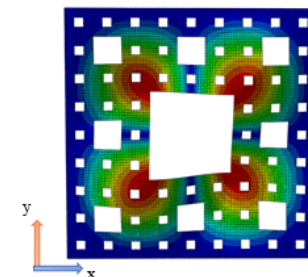
Mode Shape n	Case I $\omega_{n,Case1}^{num}$ (rad/sec)	Case II $\omega_{n,Case2}^{num}$ (rad/sec)	Error $\left|\frac{\omega_{n,Case2}^{ana}-\omega_{n,Case1}^{num}}{\omega_{n,Case2}^{ana}}\right|$
(0,0)	560.71	545.99	0.0269
(1,0)	828.65	802.32	0.0328
(1,1)	1229.9	1191.8	0.0319

of length while the rest of the material properties are indicated in Table 4.3. This model is used in the tessellated but the geometry are continuous unlike the pre-fractal model, see Figures 3.2 to 3.4.

The pre-fractal geometry is created by applying the IFS function that is mentioned earlier. On the other hand, the tessellated models are built by using Equations (5.10) and (5.34) while the boundary conditions are kept the same as the pre-fractal models and by using Equation (5.18) to duplicate the excitation or deforming sources.

In the end, this section concentrates on comparing the relative response between both spaces, so the results accuracy existed in the tested models remains relative. Keeping this in mind, the analysis in this section is performed by testing different boundary conditions as a combination of Clamped and Pinned boundary conditions cases. Furthermore, two types of analysis are carried out, the frequency

Table 6.3: Mode shape comparison for different mesh studied under an overall material assignment.

Mode shape number	Mode shape pre-fractal Case1	Mode shape pre-fractal Case 2
(0,0)	$\omega_{1,Case1} = 560.71 \quad rad/sec$	$\omega_{1,Case2} = 545.99 \quad rad/sec$
(1,0)	$\omega_{2,Case1} = 828.65 \quad rad/sec$	$\omega_{2,Case2} = 802.32 \quad rad/sec$
(1,1)	$\omega_{3,Case1} = 1229.90 \quad rad/sec$	$\omega_{3,Case2} = 1191.80 \quad rad/sec$

analysis and dynamic responses.

6.3.2.1. Frequency analysis

To ensure the integrity of any newly designed models, frequency analysis is the first frontier to provide enough information about the of ability and the possible problems. Moreover, as mentioned earlier, the pre-fractal models are relatively new models that have been avoided in engineering designs due to the complexity that is required to investigate their behaviour. So this is the third most important section in this study because it shines the light on the possibilities to use such structures. And most importantly, it is imperative to use this section to investigate the possibility of using the TCM theory in mimicking the pre-fractal model's behaviour. For this reason, it is found necessary to test different pre-fractal models under different boundary conditions.

The main three pre-fractal models are tested in this section, and each model is tested for two different boundary conditions. This is due to the fact that the natural frequency is dependent on the boundary conditions, and it is essential to understand the trends of the TCM theory in predicting the pre-fractal model's responses due to the effect of changing the boundary condition while increasing the studied model's complexity. So, this analysis is focused on the models presented in Figures 3.2, 3.3, and 3.4. The material properties and dimensions for the tested models are listed in Table 4.3, this is for the pre-fractal models, while the tessellated model is created by considering Equation (5.10) and (5.34) with the aid of the hole fill-maps, as is widely discussed in Section 6.2 and in the previous chapters. Three main cases are presented and as follow:

6.3.2.1.1. Case I: Structure type $k = 1$

Sierpinski Carpet of the first complexity is tested in this section. The pre-fractal models and its corresponding tessellated models are presented in Figure 3.2. The material properties are listed in Table 4.3. And due to the mentioned complexity of the tessellated model, it is impractical to list the material properties which consist of 64 different elements. Also, the model is under Clamped-Clamped-Clamped-Clamped boundary condition denoted by CCCC. The clamped edges, all the six degrees of freedom are constrained, three transition degrees of free-

dom, and other three rotational components are equal to zeros at the constrained edges. First, the frequency analysis is investigated for the first four natural frequencies. The natural frequencies as listed in Table 6.4, and their mode shapes are presented in Table 6.5. It is also found that the maximum absolute error at the second natural frequency is 4.53×10^{-2} for the CCCC case. But it also noted that the predicted mode shapes are a little shifted. This is due to the limited number of element on both spaces. Despite this fact, the models' results are close, and this is the purpose of this study, which can be denoted as verified.

In a similar manner, the second boundary condition is CPCP, where 'P' rep-

Table 6.4: The natural frequency comparison in both space for a structure type $k = 1$ under CCCC BC

Mode n	Physical-natural frequency $\omega_{n,ps}^{num}$ (rad/sec)	Tessellated-natural frequency $\omega_{n,ts}^{num}$ (rad/sec)	Absolute relative error $\left| \frac{\omega_{n,ps}^{num} - \omega_{n,ts}^{num}}{\omega_{n,ps}^{num}} \right|$
(0,0)	1257.80	1249.90	6.28×10^{-3}
(1,0)	1880.50	1795.30	4.53×10^{-2}
(0,1)	1874.00	1843.20	1.64×10^{-2}
(1,1)	2489.90	2440.50	1.98×10^{-2}

resents a pinned boundary condition. For the case of a pin the three-transition degrees of freedom are constrained to be 0, for example $(u, v, w) = 0$. The natural frequencies are presented in Table 6.6 and the mode shapes are presented in Table 6.7 for the first four mode shapes. It is found that the highest absolute relative percentage error is at the second natural frequency with 0.087 relative error. And similar to the first tested cases in this section, it is found that the tessellated mode shapes are worse than the case where all the edges are clamped (CCCC). But both analyses gave good equivalent results when compared with their original physical models.

6.3.2.1.2. Case II: Structure type $k = 2$

The second complexity of Sierpinski Carpet with its corresponding tessellated models are tested here. The pre-fractal type $k = 2$ and the tessellated model are

Table 6.5: Mode shapes of Sierpinski Carpet $\hat{E}_1$ and its corresponding tessellated under CCCC BC.
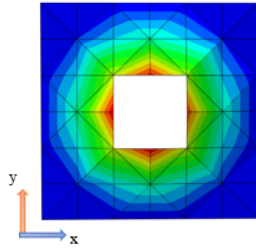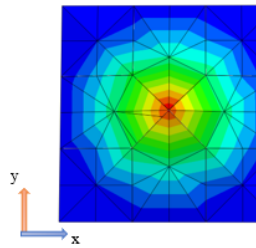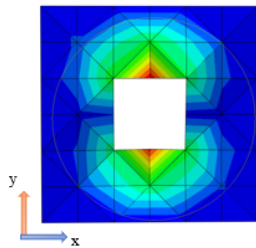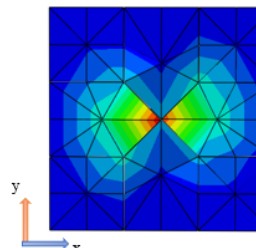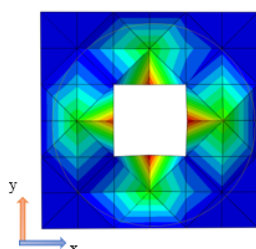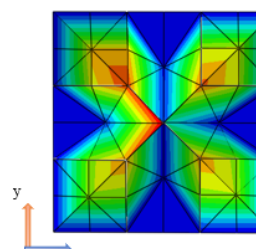
Mode Shape	Mode shape pre-fractal space	Mode shape tessellated space
(0,0)	$\omega_{1,ps} = 1257.80 \quad rad/\sec$	$\omega_{1,ts} = 1249.90 \quad rad/\sec$
(1,0)	$\omega_{2,ps} = 1880.50 \quad rad/\sec$	$\omega_{2,ts}^{x} = 1795.30 \quad rad/\sec$
(0,1)	$\omega_{3,ps} = 1874.00 \quad rad/\sec$	$\omega_{3,ts} = 1843.20 \quad rad/\sec$
(1,1)	$\omega_{4,ps} = 2489.90 \quad rad/\sec$	$\omega_{4,ts} = 2440.5 \quad rad/\sec$

Table 6.6: The natural frequency comparison in both spaces for a structure type $k = 1$ under CPCP BC.
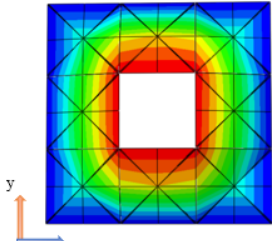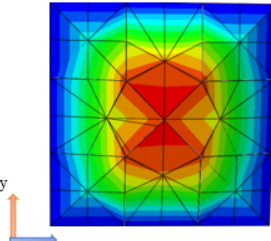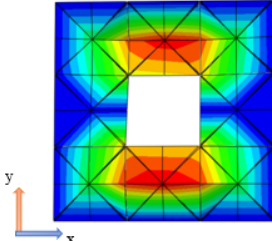
Mode n	Physical-natural frequency $\omega_{n,ps}^{num}$(rad/sec)	Tessellated-natural frequency $\omega_{n,ts}^{num}$ (rad/sec)	Absolute relative error $\left\lvert \frac{\omega_{n,ps}^{num} - \omega_{n,ts}^{num}}{\omega_{n,ps}^{num}} \right\rvert$
(0,0)	1337.60	1352.70	0.01129
(1,0)	1936.70	2104.90	0.08685
(0,1)	2453.70	2660.70	0.08436
(1,1)	3503.20	3591.00	0.02448

illustrated in Figure 3.3. Both models are constructed from 512 different tiles. Testing a non uniform perforation can be noticed in this section as in Figure 3.3 a, where there are two different types of holes on the physical model. The first has the dimension $\ell_o/3 \times \ell_o/3$, while the second hole has $\ell_o/3^2 \times \ell_o/3^2$. For the case of pre-fractal model, the same material properties are assigned for each tile. Those material properties are listed in Table 4.3. On the tessellated model, each element of those 512 has different material and geometrical properties, as has been discussed earlier.

Two different boundary conditions are tested in this case, too. The first is a Clamped- Clamped-Clamped-Clamped boundary condition, while the second boundary condition is pinned from all the edges, which is denoted by 'PPPP'. The natural frequencies are presented for two different cases for a nonuniform perforated structure as indicated by the Euclidean coordinate system. Table 6.8 and Table 6.9 are demonstrate the natural frequency and the mode shapes for the CCCC case. In the same manner, the second case is tested under PPPP boundary conditions, where the natural frequencies are presented in a unit of rad/sec as in Table 6.10, and their mode shapes are presented in Table 6.11.

The results trending is in a quite interest, where It is found that the highest error is at the fourth natural frequency for the CCCC cases, although the second case is showing the highest error at the first natural frequency when the structure is under PPPP case study. It is clearly that the highest absolute relative error is 0.00384 and 0.0164 at the fourth mode shapes for both models. And in the same manner, the predicted mode shapes for both studied boundary condition cases

Table 6.7: Mode shapes of Sierpinski Carpet $\hat{E}_1$ and its corresponding tessellated under CPCP BC.

Mode Shape	Mode shape pre-fractal space	Mode shape tessellated space
(0,0)	$\omega_{1,ps} = 1337.60 \quad rad/\sec$	$\omega_{1,ts} = 1352.70 \quad rad/\sec$
(1,0)	$\omega_{2,ps} = 1936.70 \quad rad/\sec$	$\omega_{2,ts} = 2104.90 \quad rad/\sec$
(0,1)	$\omega_{3,ps} = 2453.70 \quad rad/\sec$	$\omega_{3,ts} = 2660.70 \quad rad/\sec$
(1,1)	$\omega_{4,ps} = 3505.20 \quad rad/\sec$	$\omega_{4,ts} = 3591.00 \quad rad/\sec$

are improved than the previous case when $k = 1$.

Table 6.8: The natural frequency comparison in both space for a structure type $k = 2$ under CCCC BC

Mode n	Physical- natural frequency $\omega_{n,ps}^{num}$ (rad/sec)	Tessellated- natural frequency $\omega_{n,ts}^{num}$ (rad/sec)	Absolute relative error $\left\lvert \frac{\omega_{n,ps}^{num} - \omega_{n,ts}^{num}}{\omega_{n,ps}^{num}} \right\rvert$
(0,0)	1105.90	1107.80	0.00172
(1,0)	1569.80	1567.70	0.001338
(0,1)	1570.60	1568.80	0.001146
(1,1)	2315.70	2306.90	0.00380

6.3.2.1.3. Case III: Structure type $k = 3$

The tessellated has shown very promising results when handling the random perforated structure. This is proves its capability in mimicking the physical structures with high efficiency. A further step can be taken to analysis a more complicated model. A pre-fractal of the third complexity as indicated in Figure 3.4, presents a square plate with three different type of holes. These holes dimension are $\ell_o/3^{k-i}$, where $i = 0, 1, 2, ..., (k-1)$ with number of holes $(1, 8,$ and $64)$ corresponding to i values. With testing two types of boundary conditions, it is found necessary to carry out the same boundary conditions cases that are investigated in Case II, to investigate the effect of running a higher model complexity compared to the previous results.

So, the results for the CCCC boundary condition presented in Table 6.12 and Table 6.13 in terms of natural frequency and mode shapes show a comparison between the pre-fractal and the tessellated models. In the same manner, the second tested set of boundary condition are illustrated in Table 6.14 and Table 6.15 . From the point of view of verifying the models in case of $k = 3$ it is found that the maximum absolute relative errors between the predicted results from both spaces, are found to be equal to $0.00604, 0.016467$ at the 2nd mode shape for the CCCC and PPPP boundary conditions, in Table 6.12 and 6.14. On the other hand, and to investigate the degree of the accuracy while testing higher pre-fractal models, it is obvious as the degree of the model complexity increases

Table 6.9: Mode shapes of Sierpinski Carpet $\hat{E}_2$ and its corresponding tessellated under CCCC BC.
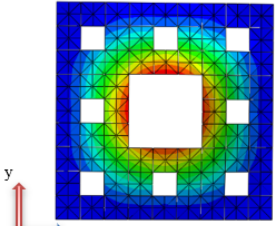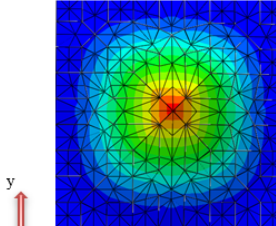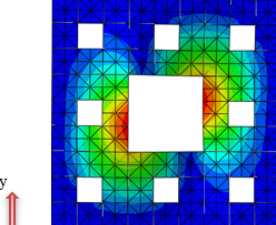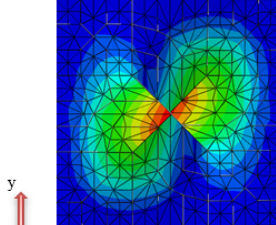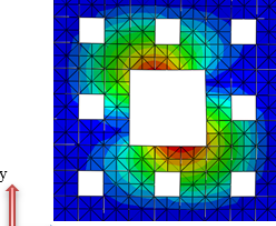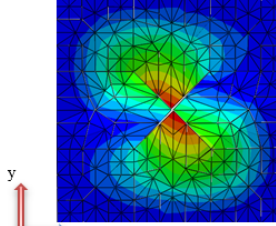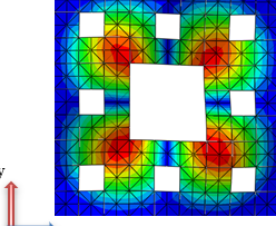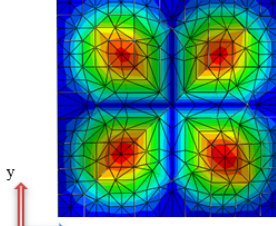
Mode Shape	Mode shape pre-fractal space	Mode shape tessellated space
(0,0)	$\omega_{1,ps} = 1105.0 \quad rad/\sec$	$\omega_{1,ts} = 1107.8 \quad rad/\sec$
(1,0)	$\omega_{2,ps}^{x} = 1569.8 \quad rad/\sec$	$\omega_{2,ts}^{x} = 1567.7 \quad rad/\sec$
(0,1)	$\omega_{3,ps}^{x} = 1570.6 \quad rad/\sec$	$\omega_{3,ts}^{x} = 1568.8 \quad rad/\sec$
(1,1)	$\omega_{4,ps}^{x} = 2315.7 \quad rad/\sec$	$\omega_{4,ts}^{x} = 2306.9 \quad rad/\sec$

163

Table 6.10: The natural frequency comparison in both space for a structure type $k = 2$ under PPPP BC.

Mode n	Physical-natural frequency $\omega_{n,ps}^{num}$ (rad/sec)	Tessellated-natural frequency $\omega_{n,ts}^{num}$ (rad/sec)	Absolute relative error $\left\vert \frac{\omega_{n,ps}^{num} - \omega_{n,ts}^{num}}{\omega_{n,ps}^{num}} \right\vert$
(0,0)	511.28	558.56	0.09247
(1,0)	1066.20	1067.70	0.00141
(0,1)	1066.30	1060.80	0.005158
(1,1)	1756.10	1784.90	0.01640

the predicted results improved significantly too if compared with the previous two studied cases. This effect is also noticed while analysing pre-fractal models especially when testing geometries higher than $k = 2$.

6.3.2.2. Dynamical analysis

After investigating the natural frequencies for different models and different boundary conditions the next step remains less crucial since the static analysis has been confirmed in Chapter 4 for the studied models. The frequency analysis has also been verified in Section 6.3.2.1. So, the following step can be considered minor in its importance to verify the TCM theory. Besides, numerical solvers tend to accumulate error while calculating such models when testing the transient response.

In this section, three different pre-fractal geometries of Sierpinski Carpet are tested for their dynamical response. The general theme of the analysis in this section, is done by examining the response on each space separately, then the results are compared after reverse-mapping the tessellated transient responses into the real space. The models are tested under transition base excitation; then the structure response is recorded in terms of transit lateral deformation, velocity and change of slope with time. The location of the recorded data is represented by a green dot at the left edge of the main hole for all the studied cases.

The first studied model, in this section, is presented in Figure 3.2. This model is considered to be a holey-structure under a CPCP boundary condition and a lateral base excitation. In the same manner, it is corresponding tessellated model

Table 6.11: Mode shapes of Sierpinski Carpet $\hat{E}_2$ and its corresponding tessellated under PPPP BC.
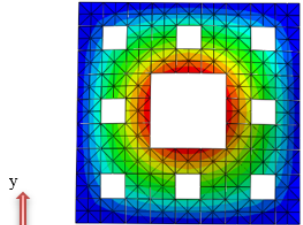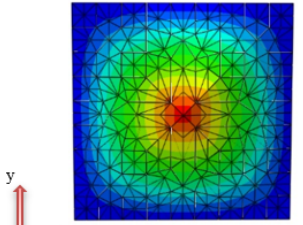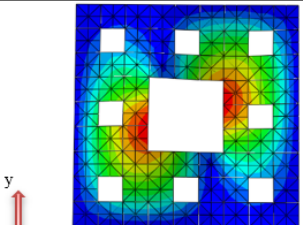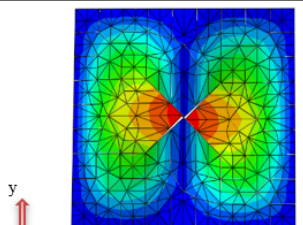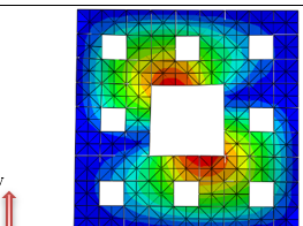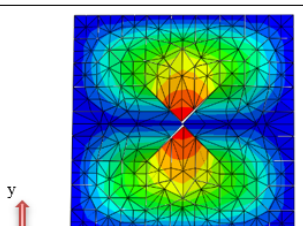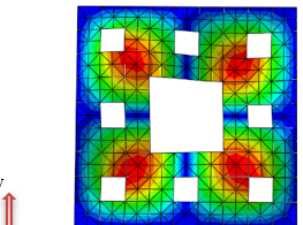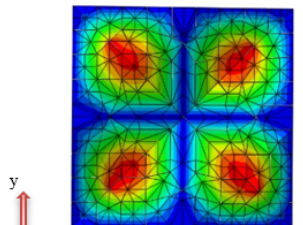
Mode Shape	Mode shape pre-fractal space	Mode shape tessellated space
(0,0)	$\omega_{1,ps} = 511.28 \quad rad/\sec$	$\omega_{1,ts} = 558.56 \quad rad/\sec$
(1,0)	$\omega_{2,ps} = 1066.2 \quad rad/\sec$	$\omega_{2,ts} = 1067.7 \quad rad/\sec$
(0,1)	$\omega_{3,ps} = 1066.3 \quad rad/\sec$	$\omega_{3,ts} = 1060.8 \quad rad/\sec$
(1,1)	$\omega_{4,ps} = 1756.1 \quad rad/\sec$	$\omega_{4,ts} = 1784.9 \quad rad/\sec$

Table 6.12: The natural frequency comparison in both space for a structure type $k = 3$ under CCCC BC.

Mode n	Physical-natural frequency $\omega_{n,ps}^{num}$ (rad/sec)	Tessellated-natural frequency $\omega_{n,ts}^{num}$ (rad/sec)	Absolute relative error $\left\| \frac{\omega_{n,ps}^{num} - \omega_{n,ts}^{num}}{\omega_{n,ps}^{num}} \right\|$
(0,0)	1006.90	1011.30	0.00437
(1,0)	1423.80	1432.40	0.00604
(0,1)	1423.90	1432.50	0.00604
(1,1)	2075.10	2078.90	0.00183

is presented in Figure 3.2. The tessellated model is under the same boundary condition and excitation motion. By running the analysis on both spaces, the structural response is compared in terms of lateral displacement, slope and finally by velocity measures. The responses are demonstrated in Figures 6.6, 6.7 and 6.8 correspondingly, where an excellent match is achieved by comparing the pre-fractal results with the reverse tessellated results. The reverse-tessellated responses are calculated by using Equation (5.18) to scale the displacement and by using the spatial derivative in Equation (5.18). And finally, by using Equation (5.13), the velocity reverse-response is calculated.
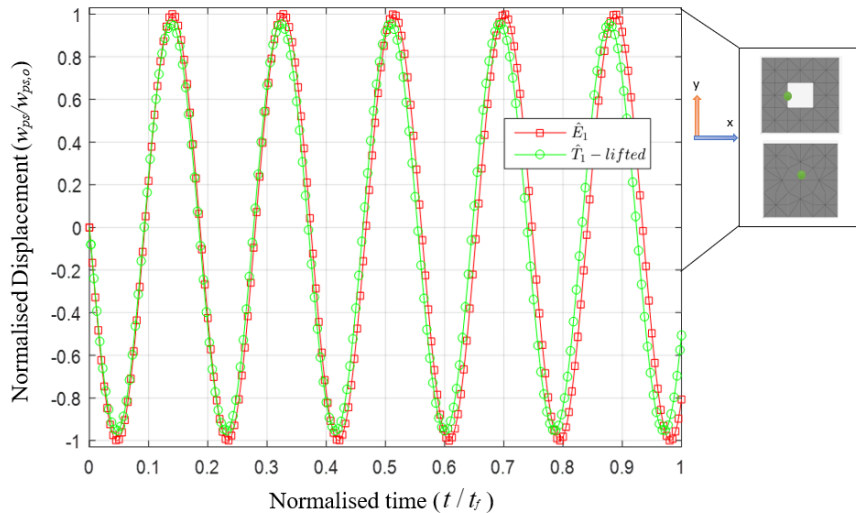
Figure 6.7: Transient lateral response in terms of displacement on $\hat{E}_1$ compared to $\hat{T}_1$ under CPCP boundary condition taken at the green spot.

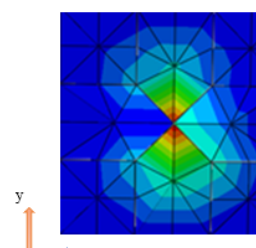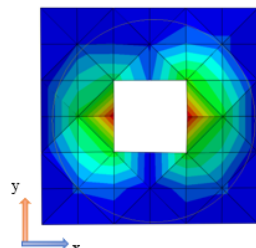Table 6.13: Mode shapes of Sierpinski Carpet $\hat{E}_3$ and its corresponding tessellated under CCCC BC.

Mode Shape	Mode shape pre-fractal space	Mode shape tessellated space
(0,0)	 $\omega_{1,ps} = 1006.9 \quad rad/\sec$	 $\omega_{1,ts} = 1011.3 \quad rad/\sec$
(1,0)	 $\omega_{2,ps} = 1423.8 \quad rad/\sec$	 $\omega_{2,ts} = 1432.4 \quad rad/\sec$
(0,1)	 $\omega_{3,ps} = 1423.9 \quad rad/\sec$	 $\omega_{3,ts} = 1432.5 \quad rad/\sec$
(1,1)	 $\omega_{4,ps} = 2075.1 \quad rad/\sec$	 $\omega_{4,ts} = 2078.9 \quad rad/\sec$

Figure 6.8: Transient lateral response in terms of slope on $\hat{E}_1$ compared to $\hat{T}_1$ under CPCP boundary condition taken at the green spot.
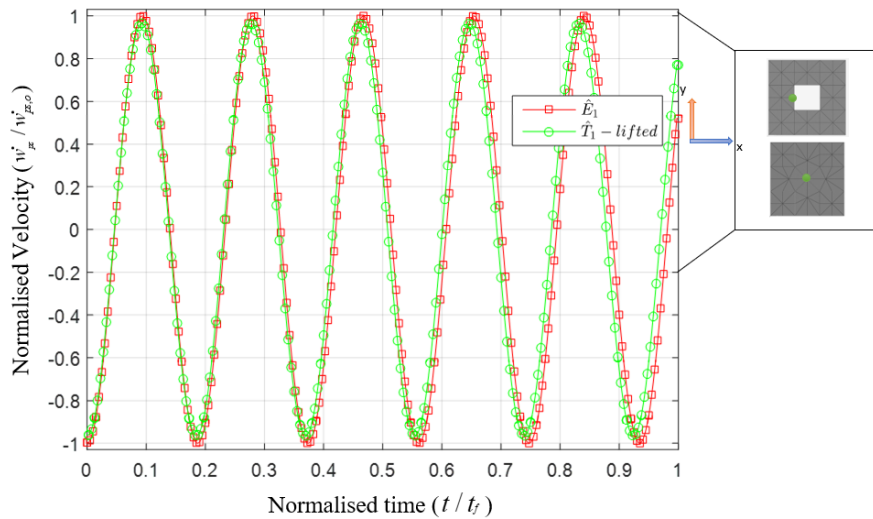
Figure 6.9: Transient lateral response in terms of velocity on $\hat{E}_1$ compared to $\hat{T}_1$ under CPCP boundary condition taken at the green spot.

Table 6.14: The natural frequency comparison in both space for a structure type $k = 3$ under CPCP BC.

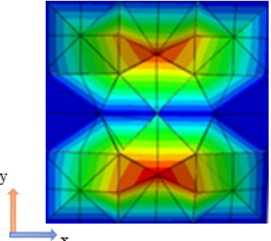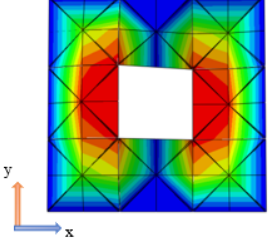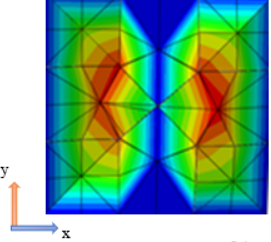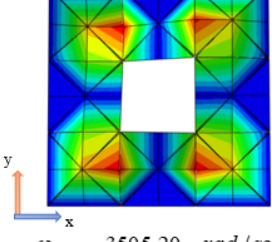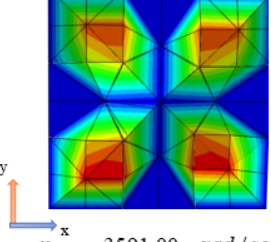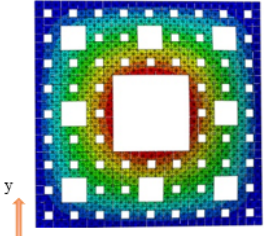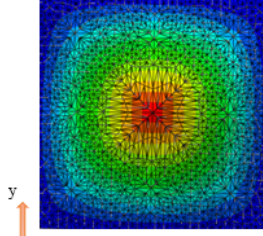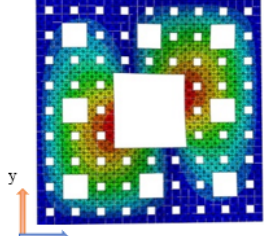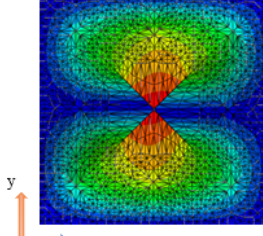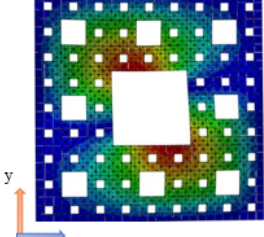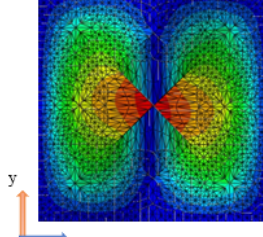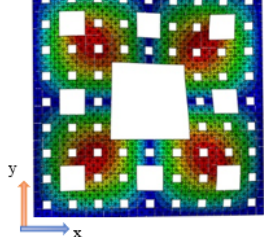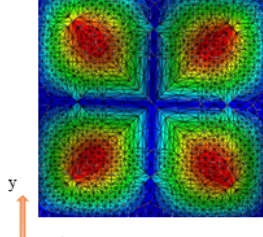| Mode n	Physical- natural frequency $\omega_{n,ps}^{num}$ (rad/sec)	Tessellated- n natural frequency $\omega_{n,ts}^{num}$ (rad/sec)	Absolute relative error $\left| \frac{\omega_{n,ps}^{num} - \omega_{n,ts}^{num}}{\omega_{n,ps}^{num}} \right|$
(0,0)	452.67	450.40	0.005015
(1,0)	949.74	934.07	0.016499
(0,1)	949.75	934.11	0.016467
(1,1)	1544.3	1532.00	0.007965

Similar to the first studied model, Figure 3.3 presents the studied models in this case. A Sierpinski Carpet of the second complexity is tested here. For this case study, the structure is experiences a dynamical excitation in the form of base motion. This is applicable to both models. The boundary condition, in this case, is CCCC.

It is of interest to see the effects of the dynamical excitation on the structural response of a pre-fractal, and how well the tessellated model captures the real structure response. All the measured responses are collected at the left-edge-side of the main hole of the studied models. And the transient response in terms of lateral deformation are listed in Figure 6.10, which clearly shows that the tessellated models succeed in capturing the pre-fractal model of type $k = 2$. And in the same manner, the slope and the time integration to lateral displacement are presented in Figures 6.11 and 6.12, correspondingly.

Furthermore, there is a shifting in the predicted results, and this shifting can be identified as simply a numerical error.// Finally, the last studied model in this work, is presented in Figure 3.4 with its tessellated model. It is interesting to mention that the hole's dimensions are $(\ell_o/3^{k-i} \times \ell_o/3^{k-i})$, where $k = 1, 2$, and 3 , while the number of holes are varied for each size. All this would increase the level of complexity on both studied models. Dynamic model analysis is performed on the studied structures. This is basically achieved by applying an initial excitation to the structure boundary conditions. The measured results are presented in Figures 6.13 to 6.15. Those Figures include the pre-fractal responses plotted against the reversed tessellated results. The reversed tessellated results

Table 6.15: Mode shapes of Sierpinski Carpet $\hat{E}_3$ and its corresponding tessellated under CPCP BC.

Mode Shape	Mode shape pre-fractal space	Mode shape tessellated space
(0,0)	$\omega_{1,ps} = 452.67 \quad rad/\sec$	$\omega_{1,ts} = 450.4 \quad rad/\sec$
(1,0)	$\omega_{2,ps} = 949.74 \quad rad/\sec$	$\omega_{2,ts} = 934.07 \quad rad/\sec$
(0,1)	$\omega_{3,ps} = 949.75 \quad rad/\sec$	$\omega_{3,ts} = 934.11 \quad rad/\sec$
(1,1)	$\omega_{4,ps} = 1544.3 \quad rad/\sec$	$\omega_{4,ts}^x = 1532 \quad rad/\sec$

Figure 6.10: Transient lateral response in terms of displacement on $\hat{E}_2$ compared to $\hat{T}_2$ under CCCC boundary condition taken at the green spot.
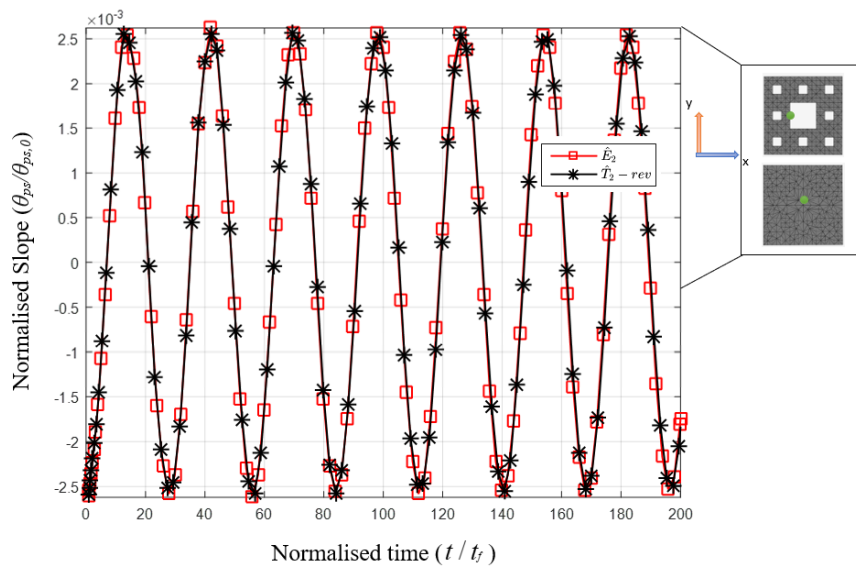
Figure 6.11: Transient lateral response in terms of slope on $\hat{E}_2$ compared to $\hat{T}_2$ under CCCC boundary condition taken at the green spot.
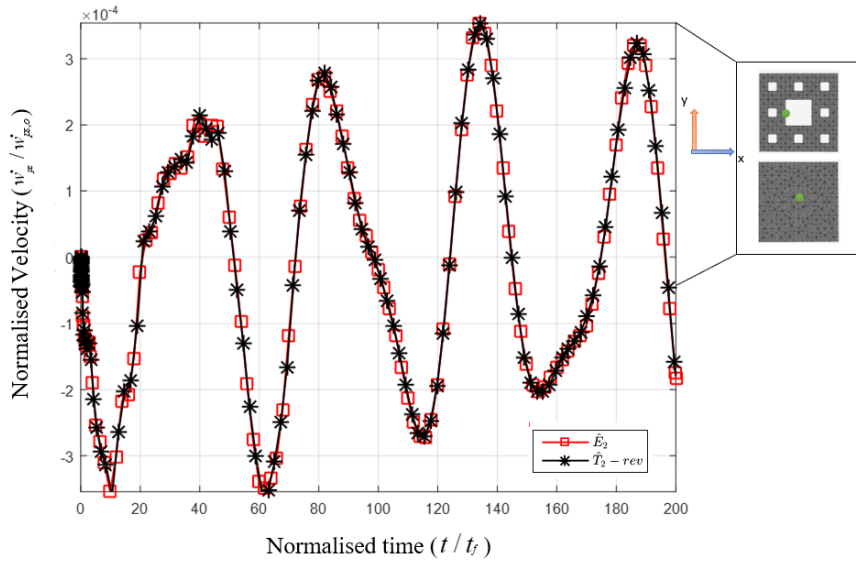
Figure 6.12: Transient lateral response in terms of velocity on $\hat{E}_2$ compared to $\hat{E}_2$ under CCCC boundary condition taken at the green spot.

are calculated by applying Equations (5.13), (5.18) and (4.25) with the aid of the hole-filling maps $dx_{ts} = F \cdot dx_{ps}$.
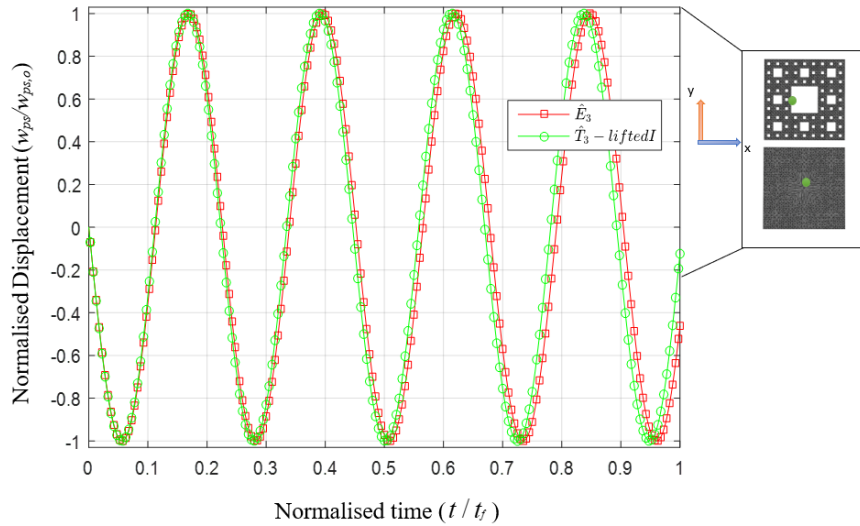
Figure 6.13: Transient lateral response in terms of displacement on $\hat{E}_3$ compared to $\hat{T}_3$ under CCCC boundary condition taken at the green spot.
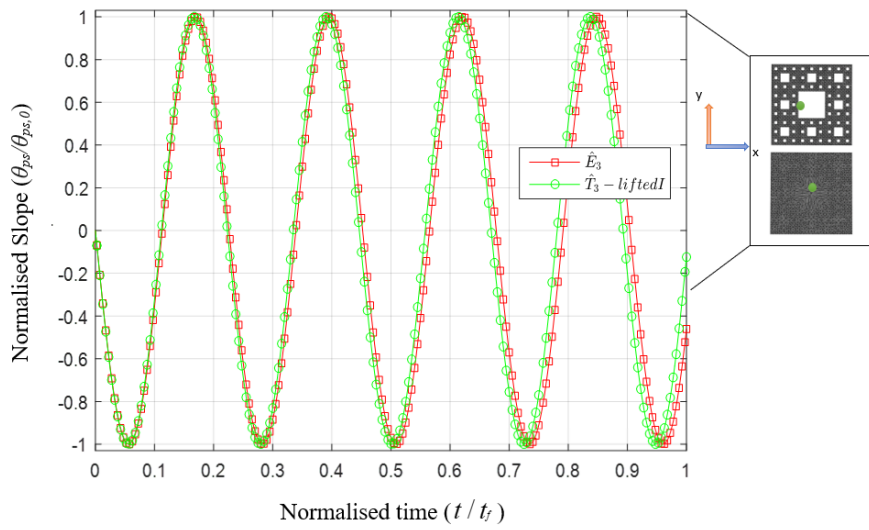
Figure 6.14: Transient lateral response in terms of slsope on $\hat{E}_3$ compared to $\hat{T}_3$ under CCCC boundary condition taken at the green spot.
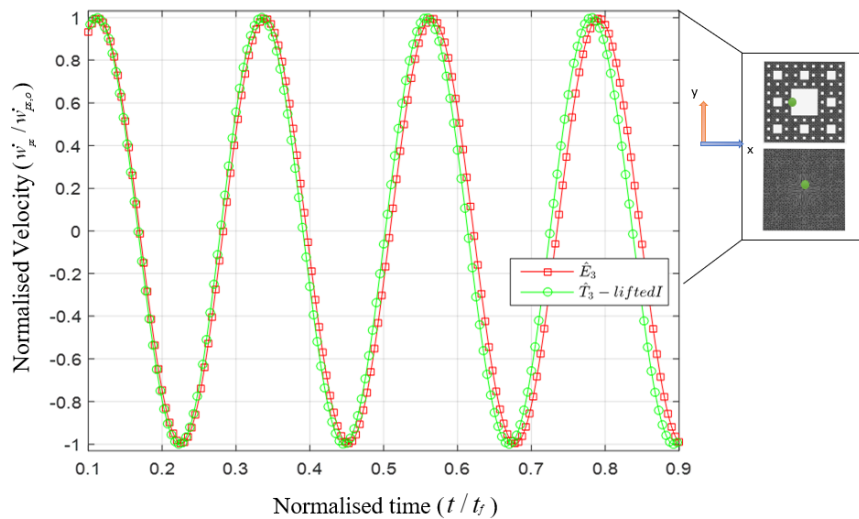
Figure 6.15: Transient lateral response in terms of velocity on $\hat{E}_3$ compared to $\hat{T}_3$ under CCCC boundary condition taken at the green spot.

6.4   Summary

All the presented Figures proved that the TCM succeeded in capturing the physics for the pre-fractal models. This is done with the following remarks:

1. Implement the transport equations which include using the conserved continuum laws on the pre-fractal space to create the tessellated space for dynamic analysis on 2-D models are achieved in this chapter. This leads to creating direct mapping-rules that create the tessellated models; and the reversed mapping-rules to transport the results from the tessellated space into the pre-fractal space.

2. Applying local and anisotropic scaling maps to create an alternative space, that simulates the original space, showed excellent results in matching the physics of a discrete system. This approach is presented and verified for the first time in literature.

3. Implementing a Python code has eased the process of creating the tested models on both spaces and widen the horizon for a possible application. Besides, implement Python to generate the hole-fill maps, can be considered on different geometries that are not systematically iterated as in the pre-fractal models.

4. The basic mesh for the lower pre-fractal models is found to lack accuracy due to the current limitation of the theory. The lack of accuracy disappears when testing higher pre-fractal geometries such as $k = 2$ and 3.

5. The current limitation of the TCM method are tested regarding the number of elements that are used to create the initial mesh on both models, pre-fractal and tessellation. The triangular mesh elements is found to give a very good result when compared with the results that are run on square mesh type elements. Both analyses are run on the pre-fractal models with almost half the number of elements for higher k , see Tables 6.2 and 6.3.

6. The TCM theory are controls the mesh number and distribution on the 2-D models. Although a very good match between the results is achieved, this

is found to limit the accuracy of the results on the real models for lower k models as in Tables 6.4 to 6.7.

7. Running a dynamical analysis on the tessellated space has given promising results when compared with the pre-fractal with a negligible error. So, the TCM approach successfully predicted the dynamical analysis for the 2-D pre-fractal models, as it shown in Figures 6.6 to 6.8.

Chapter 7

Conclusion and Future Work

7.1 Introduction

This chapter presents the main conclusions that are drawn from testing the TCM method's accuracy in predicting the results of the pre-fractal space, where this theory is constructed to replace the analysis run on the pre-fractal space. A general introduction to the presented theory is stated briefly in section 7.2. This is followed by listing the main points of essential conclusions of this research in section 7.3. At the end of this chapter, a list of possible future works is presented.

7.2 Preface of TCM theory

This research offers an entirely new method to analyse vibration on pre-fractal space without involving the complexity of the pre-fractal analysis. The TCM method is built on the concept of creating an alternative space that can reflect the pre-fractal model. This method creates a continuum model whose structural geometry is fabricated by using hole-fill maps. This approach is used for the first time. The material properties of the created structure are calculated by applying transport equations that map the material properties of pre-fractal space to create the tessellation. ABAQUS software is used in order to find the results numerically on both spaces (pre-fractal and tessellated). The tested 2-D model's geometry is prepared by using Python. Moreover, implementing the required equations to calculate the mapped material properties is also executed using

Python code.

Another approach is also implemented in this study and for the first time in the literature, which is the Discontinuity Network (DN). The TCM approach results confirm that the tessellated approach has successfully managed to find the correct pre-fractal responses on different dimensions, and under different boundary conditions and deforming sources.

7.3 Conclusions

The transport theory is a general theory that is applied to different aspects in engineering, as was concluded in Chapter Two, but this is the first time that the transport theory has been considered on a local scaling process. This is known as the tessellated continuum mechanics (TCM) theory.

The claim of this work is centred on the concept of replacing the analysis of a porous structure, known as the pre-fractal, by creating an equivalent continuum model known as tessellated structure. This claim is established in 1-D and 2-D structures. The achieved results are found to give a good prove that the TCM is an excellent alternative approach to analyse the pre-a fractal models. To verify the TCM theory, this analysis is carried out by running a detailed analysis on the tessellated continuum models. Then, at the same time similar analysis is had to be carried out on the pre-fractal models. At the end the results are compared after A pre-fractal structure in 1-D space is known as a Cantor set. The Cantor set is a non-physical structure that needs to be linked in a specific way to force the structure to behave as a physical structure. This issue is overcome when analysing a 2-D structure. All this achieved with the following conclusions:

1. Testing the isotropic and the anisotropic scaling for 1-D structures is found to give the same results with minor differences that have no effect on the solution, while on the 2-D space the structure must be mapped only by using an anisotropic linear scaling function on a local basis. This is demonstrates the beauty of creating the tessellated structure, which uses a non-unique local expansion is used. This would enable researchers to use any possible shapes that would force the studied structure geometries to be continuous.

2. Applying the DN in 1-D models is proven to give accurate results while testing the lateral vibration analysis. This overcomes the difficulties that were faced in the first work prepared in this field for a Cantor set under cantilevered boundary conditions [15]. Unlike the 2-D models where the structure can have the DN or not, this only depends on the studied cases. To reframe this "The jump condition represented by the DN is found to give a perfect match on 1-D pre-fractal structures, but has a minor effect on 2-D structures". As matter of fact it is found that the DN is no more than applying similar boundary conditions to those applied on the pre-fractal structure.

3. One of the bigger difficulties that face researchers when running analysis on the tessellated space has been easily overcome in this work. This is achieved by applying a local scaling on each tile of the pre-fractal model. This is done manually for the 1-D models. But for the 2-D models, a Python code eases this process significantly by applying the TCM rules directly at the first stage of designing the program. So, based on the transport theory, the transport equation derives the main rules to create the tessellated space. For example, the density scaling rules are listed in Equation (5.10). Material properties represented as Young's modulus of elasticity are given by Equation (5.34). Each segment on the tessellated structure has its own density, and Young's modulus values which are completely dependent on the geometrical mapping of the structure.

4. A parametric study on the pre-fractal space is performed. It is demonstrated that the SR8 element is the best to represent the studied models, with minimum numbers of element for the first three pre-fractal models as $(512, 1024$ and $8192)$ with a unit length of mesh $(0.037, 0.025$ and $0.00833)$ for model types $k = 1, 2$ and 3. It is also shown that at the higher pre-fractal structures, there is no need to use a higher density mesh to capture all the selected mode shapes. Using a mesh size of the dimension of the smallest hole size can give very stable results compared with the lower pre-fractal structure in the 2-D analysis.

5. Applying a higher mesh on the basic meshed elements on pre-fractal space

is found to be effective, although this can be improved to use higher mesh densities before creating the tessellated structure. Increasing the mesh on the pre-fractal space is accomplished by increasing the number of tiles. Then, these tiles can be mapped to create the tessellated space perfectly. This would create numbers of mesh for the first three pre-fractal models $(64, 512$ and $4096)$. These values are proven to give better results than the one mentioned earlier in point 4 (this demonstrated in 6.3.1.2).

In all the tested cases, linear vibration analysis for analytical and numerical analysis is carried out by the ABAQUS software. Two different pre-fractals are tested in this work. For 1-D space, a pre-fractal of type Cantor Set is tested. On the other hand, in 2-D space, a pre-fractal known as a Sierpinski Carpet is been tested.

Furthermore, in the case of the 2-D cases, a thin plate with a linear small deformation theory is implemented. Most of the studied cases are tested under free vibration analysis. Furthermore, a forced vibration is found to give good results when tested by the TCM theory [77] and in Section 5.9.

6. Different tessellation geometries are numerically proven to give a better demonstration to the studied cases under different boundary conditions and excitation sources. The deformation distribution on the pre-fractal space is a cubic function, while the DN is represented by a linear equation. Its shown that the continuity in the tessellated has no effects on the response. The continuity on the tessellated space is enforced by deformation measures. The deformation difference between both spaces is proportional, and it is shown to be scalable. This is known as the DN, which is used to link the pre-fractal in 1-D space.

7. The analytical solution on 1-D pre-fractal Cantor Set is driven from the governing partial differential equation on the pre-fractal space, where the results showed a good matching with the numerical results.

8. On the other hand, the investigation of the lateral vibration case study is expanded to test different boundary conditions. Clamped-Clamped (CC), Clamped-Pinned (CP), and Clamped-Free (CF) (at both ends) are studied. The author founds that the tessellated structure has successfully

demonstrated the pre-fractal response under displacement excitation and forced excitation with an accurate range. However, the only error found was due to the accumulated numerical errors.

9. Similarity, the investigation of the lateral vibration case study for 2-D is expanded to test different boundary conditions. Clamped-Clamped (CCCC), Clamped-Pinned (PPPP), or Clamped-Free (CPCP) are studied. It is also found that the tessellated structure has successfully predicted the pre-fractal response under displacement and pressure excitation with an accurate range. Also, the only error was due to accumulated numerical errors.

10. Moreover, three types of analysis are carried out, the static deformation, dynamic, and frequency. These responses are tested and compared by running the same scaled analysis on the pre-fractal and the tessellated spaces separately. The compared results in the static analysis are shown to match perfectly, while a minor error is found while running the dynamical analysis. Finally, frequency analysis results also follows the same error range as the dynamical analysis.

11. The TCM is found to have a less accuracy when dealing with lower pre-fractal complexity. This is shown obviously in the static and in the dynamic analysis for model type K=1.
   Also the number of mesh on the tessellated is completely depends on the initial mesh that is been set on the pre-fractal.

7.4   Future work

Some possible work that can be done in this area is listed in details as follow:

1. Three-dimensional (3-D) model can be built up by using a programming language; Python code is the easiest method for solving the problem of implementing the iterated function system. An example for a 3-D model is shown in Figure 1.3. This can be done by the following:

- Modifying hole-fill maps to create the tessellated geometry in 3-D, where it will be represented by the following equation :

$$F = \begin{bmatrix} F_{11} & F_{12} & F_{13} \\ F_{21} & F_{22} & F_{23} \\ F_{31} & F_{32} & F_{33} \end{bmatrix} \tag{7.1}$$

In this case the shear F-Function components are no longer equal to zero.

- Studying the effect of scaling the thickness in the 3-D model rather than a shell structure.

- Applying the theory to different analysis types such as structures under shear forces, for analysis in different applications.

- Testing the theory to different hole-fill maps shapes on the tessellated space. For example Figure 7.1 shows the basis mesh on the pre-fractal space. The hole-fill maps in Figure 7.1 (b) is different than the Figure 7.1 (c) (notice the middle centre shifting. Figure 7.1 (d) is showing a scaling in the thickness.
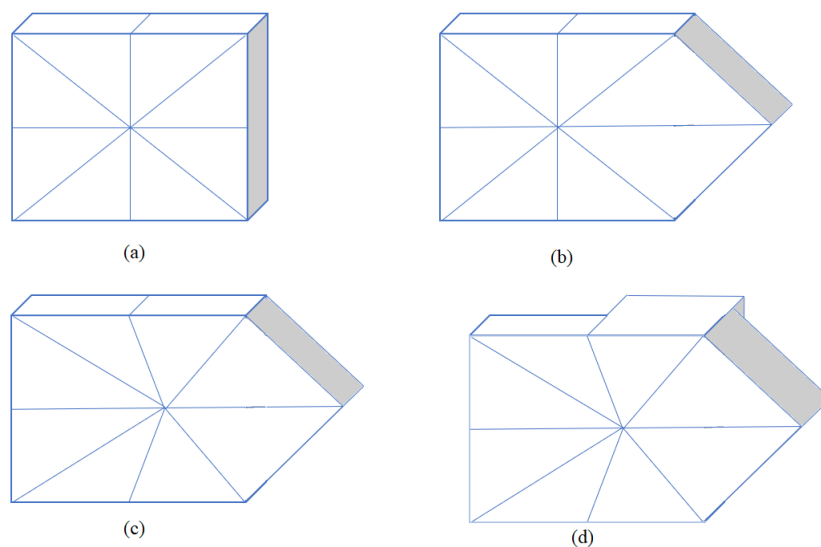
Figure 7.1: Choosing different Hole-Fill maps options.

2. Testing if the theory can be implemented in geometries that are not related to pre-fractals models. For a simple case study see Figure 7.2. This can be

advanced by finding a different approach for creating the hole-filling map techniques (the author suggests using artificial intelligent techniques (AI) to fill the holes). This is important because there is one rule that controls the formation of the new geometry which maintains triangular shapes of the tiles for the reasons of maintaining a linear mapping. This can be challenging unless using AI techniques.

(a)   (b)
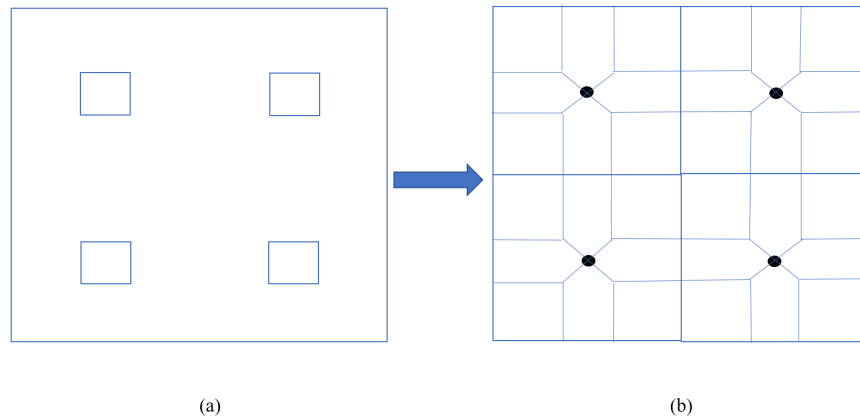
Figure 7.2: Applying the TCM theory on uniform plate perforation

3. Different pre-fractal structures can be implemented that do not following the IFS pre-fractals, such as the work done using the Vicsek fractal. In more detail for the 1-D models, a Von Koch fractal can be used to modify the hole-fill maps to cope with a pre-fractal behaving as a beam structure that is created in (x, y) space rather than the Cantor set which is created by alternating the beam length in one direction (x-axis). Another geometry that can also be tested is listed in the following figure:
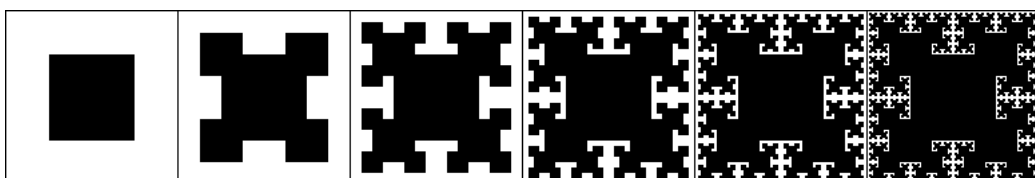
Figure 7.3: Testing the 2-D hole fill map for a T-fractal geometry

4. In this work, the frequency results predicted by ABAQUS is found to be limited for the first few natural frequencies (these frequencies are the most important one because these frequencies are most likely to be tested during operation). The natural frequency range can be increased by using a second approach that is also gives a better accuracy. This approach is considering the momentum scaling equations to find an alternative scaling rules for density. And the author did not use the momentum equation in this thesis but can be found in [97]. Although this work is still under progress, it is found to be best to mention here for further improvement.

5. Non-linear vibration analysis can be tested for example by changing the structure thickness for each tile on the pre-fractal space, or by using high elastic material properties.

References

1. A. Preumont, R. Bastaits, and G. Rodrigues, Active optics for large segmented mirrors: Scale effects. Elsevier, 2009. 19(8): p. 1286-1293.

2. Wikipedia. Hubble space telescope. 2016; Available from: Telescope Structure and Mechanisms.

3. OSE-executive, OWLconcept design report. 2006.

4. R. Bastaits, G. Rodrigues, B. Mokrani and A. Preumont, Active optics of large segmented mirrors: Dynamics and control. Journal of Guidance, Control, and Dynamics, 2009. 32(6): p. 1795-1803.

5. P. Leifsson, Fractal sets and dimensions, in Applied Mathematics. 2006, Link Opines University.

6. M. F. Bransley, Fractals everywhere. 1993: Academia Press, Inc.

7. V. E. Tarasov, Fractional hydrodynamic equations for fractal media. Annals of Physics, 2005. 318: p. 286-307.

8. M. Ostoja-Starzewski, Extremum and variational principles for elastic and inelastic media with fractal geometries. Acta Mechanica, 2009. 205(1): p. 161-170.

9. S. Butera, and M. D. Paola, A physically based connection between fractional calculus and fractal geometry. Annals of Physics, 2014. 350: p. 146-158.

10. M. G. Blyth, and C. Pozrikidis, Heat conduction across irregular and fractal-like surfaces. International Journal of Heat and Mass Transfer, 2003. 46: p. 1329-1339.

11. Davey, K. and R. Prosser, Analytical solutions for heat transfer on fractal and pre-fractal domains. Applied Mathematical Modeling, 2013. 37: p. 554-569.

12. E. Motheau, T. Lederlin, J. L. Florenceiano, and P. Bruel , LES investigation of the flow through an effusion-cooled aeronautical combustor model. Flow Turbulence and Combustion, 2012. 88(1): p. 169-189.

13. V. Mironovs, A. Tatarinov, and S. Gorbacova. Expanding application of perforated metal materials in construction and architecture. in Materials Science and Engineering. 2017.

14. B. Mandelbrot, The fractal geometry of nature. 1977: W. H . Freeman and Company.

15. K. Davey and M.T.A. Rasgado, Analytical solutions for vibrating fractal composite rods and beams. Applied Mathematical Modeling, 2011. 35(3): p. 1194-1209.

16. C. Shull, V. Ravikumar, and T. H. K. Frederking, Hydrodynamic characterization of perforated plate flow passages, in Advances in Cryogenic Engineering. 1994.

17. R. V. Waterhouse, Measuring the sound attenuation of space absorbers for jet-engine test cells. The Journal of the Acoustical Society of America, 1954. 26(5).

18. M. A. Temiz, I. L. Arteaga, and A. Hirschberg, Sound absorption measurements for micro-perforated plates: The Effect of Edge Profile. EURONOISE 2015, 2015. 43(20).

19. S. Sizilard, Theory of plates classes and numerical methods. 1974, New Jersey: Hall, Inc.

20. S. Timoshenko, Vibration problems in engineering, 3rd ed. 1944.

21. W. J. O'Donnell, Design of perforated plates. Journal of Engineering for Industry, 1962. 84(3): p. 307-319.

22. M. J. Jhunga, Y. H. Choia, and Y.H. Ryua. Equivalent material properties of perforated structure for free vibration analysis. in 20th International Conference on Structural Mechanics in Reactor Technology. 2009. Espoo, Finland: Structural Mechanics In Reactor Technology.

23. G. Aksu, and R. Ali, Determination of dynamic characteristics of rectangular plates with cutouts using a finite difference formulation. Journal of Sound and Vibration, 1967. 44(1): p. 147-158.

24. S. Choi, K. H. Jeong, and J. Park, Free vibration analysis of perforated plates using equivalent elastic properties. Journal of Knee Nuclear Society, 1988. 30(4): p. 416-423.

25. C. G. Boay, Free vibration of laminated composite plates with a central circular hole. Composite Structures, 1996. 35(4): p. 357-368.

26. S. C. Baik, K. H. Oh, and D. N. Lee, Analysis of the deformation of a perforated sheet under uniaxial tension. Journal of Materials Processing Technology, 1996. 58.

27. M. Imregn, Three case studies in finite element model updating. Shock and Vibration, 2(2), 1995, p. 119-131.

28. D. L. Kaap, M. A. Sprague, and R. L. Engelstad, A finite element benchmark for the dynamic analysis of perforated plates with a square penetration pattern. Fusion Technology Institute University of Wisconsin 1997.

29. K. Kalita, and S. Haldar, Free vibration analysis of rectangular plates with central cutout. Cogent Engineering, 2015. 3(1).

30. J. Jhung, and Myung-Jo, Equivalent material properties of perforated plate with triangular or square penetration pattern for dynamic analysis, in Korea Institute of Nuclear Safety 2006: 19 Guseong-dong, Yuseong-gu, Daejeon Korea p. 305-338.

31. O. R. Nandagopan, S. Ranjithkumar, and C. G. Nandakumar, Shock analysis of water backed perforated plate subjected to underwater explosion. Journal of The Institution of Engineers 2016. 97(3): p. 291-298.

32. K. Falconer, Hausdorff measure and dimension, in Fractal geometry: Mathematical foundations and applications, 2nd ed. 2005, Wiley Online Library.

33. N. Bajorin, T. Chen, A. Dagan, C. Emmons, M. Hussein, M. Khalil, P. Mody, B. Steinhurst, and A. Teplyaev, Vibration modes of 3^n-gaskets and other fractals. Journal Of Physics A: Mathematical And Theoretical, 2008. 21.

34. K. S. Birdi, Physical applications of fractals in: Fractals in Chemistry, Geochemistry, and Biophysics. 1993, Springer: Boston, MA.

35. K. Gil'mutdinov, P. A. Ushakov, and R. El-Khazali, Fractal elements and their applications. 2017, Springer, Cham: Switzerland.

36. R. Khalil, M. Al Horani, A. Yousef, and M. Sababheh, A new definition of fractional derivative. Journal of Computational and Applied Mathematics, 2014. 264: p. 65-70.

37. G. Jumarie, Table of some basic fractional calculus formulae derived from a modified Riemann?Liouville derivative for non-differentiable functions. Applied Mathematics Letters, 2009. 22(3): p. 378-385.

38. M. V. Berry, Z.V. Lewis, and J.F. Nye. On the Weierstrass-Mandelbrot fractal function. in mathematical, physical and engineering sciences. 1980. Royal Society.

39. G. Goldstein, and H. Benaroya, Fractal modelling of a one dimensional layered medium. Applied mathematical modelling 1989. 13: p. 555-558.

40. B. Sapoval, O Haeberle, and S. Russ, Acoustical properties of irregular and fractal cavities. Acoustical Society of American, 1997, 102(4).

41. A. Carpinteri, N. Pugno, and A. Sapora, Free vibration analysis of a Von Koch beam. International Journal of Solids and Structures, 2010. 47: p. 1555-1562.

42. Y. Tremblay, A. J. Roberts, and D. P. Costa, Fractal landscape method: An alternative approach to measuring area-restricted searching behavior. Journal of Experimental Biology, 2007. 210(6): p. 935-945.

43. A. J. Salim, and J. K. Ali. Design of internal dual band printed monopole antenna based on Peano-type fractal geometry for WLAN USB Dongle. in PIERS Proceedings. 2011. Suzhou, China: Progress In Electromagnetic Research Symposium Proceedings,.

44. T. Ozaki, and M. Nishigori, Crystal thickness dependence of pre-fractal domain structures in triglycine sulfate. Journal of the Korean Physical Society, 1988. 32(3).

45. D. S. Grebenkov, A. Rozanova-Pierrat, and B. Sapoval, Faster diffusion across an irregular boundary. 2012, Physical Review Letters.

46. S. Castineira-Ibanez, D. Tarrazo-Serrano, C. Rubio, P. Candelas , and A. Uris , An ultrasonic lens design based on pre-fractal structures. 2016: p. 7

47. M. Ostoja-Starzewsk, Towards thermo-elasticity of fractal media. Journal of Thermal Stresses, 2007. 30(9-10): p. 889-896.

48. C. S. Jog, Continuum mechanics: Foundations and applications of mechanics. 3rd ed. Vol. 1. 2015, Cambridge: Cambridge University Press.

49. C. Xu, H. Chen, Z. Liu, and Z. Cheng, Condition monitoring of milling tool wear based on fractal dimension of vibration signals. Strojniski Vestnik 2009. 55(1): p. 15-25.

50. T. Liu, and K. Zhu, Intelligent robust milling tool wear monitoring via fractal analysis of cutting force, in 2017 13th IEEE Conference on Automation Science and Engineering 2017, IEEE: Xi'an, China.

51. S. T. S. Bukkapatnam, S. R. T. Kumara, and A. Lakhtakia, Fractal estimation of flank wear in turning. Journal of Dynamic Systems, Measurement, and Control, 2000. 122(1): p. 89-245.

52. Z. Q. Wang, G. Y. Zhang, and B. Liu, Detection of wear condition of micro milling cutters based on length fractal dimension. Applied Mechanics and Materials, 2014. 577: p. 697-700.

53. K. Davey, R. Prosser, and C. Jiang, Heat transfer through fractal-like porous media: A tessellated continuum approach. Computers & Structures, 2015. 151: p. 58-72.

54. K. Davey, C. Jiang, and R. Prosser, Tessellated continuum mechanics: A Galerkin finite element method. Computers & Structures, 2016. 175: p. 157-183.

55. C. Jiang, K. Davey, and R. Prosser, A tessellated continuum approach to thermal analysis: Discontinuity Networks. Continuum Mechanics and Thermodynamics, 2017. 29(1): p. 145-186.

56. K. Davey, R. Darvizeh, and A. Al-Tamimi, Finite Similitude in metal forming, in MATEC Web of Conferences. 2016.

57. A. Al-Tamimi, R. Darvizeh, and K. Davey, Scaling of metal forming processes. Procedia Engineering, 2017. 207: p. 1069-1074.

58. K. Davey, R. Darvizeh, and A. Al-Tamimi, Scaled metal forming experiments: A transport equation approach. International Journal of Solids and Structures 2017. 125.

59. R. Ochoa-Cabrero, T. Alonso-Rasgado, and K. Davey, Scaling in biomechanical experimentation: A Finite Similitude approach. Journal of The Royal Society Interface, 2018. 15(143).

60. M. Moghaddam, R. Darvizeh, K. Davey, and A. Darvizeh, Scaling of the powder compaction process. International Journal of Solids and Structures, 2018. 144-145: p. 192-212.

61. K. Davey, R. Darvizeh, A. Golbaf, and H. Sadeghi, The law of Finite Similitude. in submission process to Proceedings of the Royal Society of London, 2018.

62. C. S. Jog, Continuum mechanics: Foundations and applications of mechanics. 3rd ed. Vol. 1. 2015, Cambridge: Cambridge University Press.

63. Y. C. Fung, A first course in continuum mechanics. 1st ed. 1696, United State of America: Prentice-Hall, Inc.

64. H. R. P. S. Pawlik, Elasticity theory and applications. 1980, United State of America: John Wiley & Sons, Inc.

65. J. Vass, On the geometry of IFS fractals and its applications, in Applied Mathematics. 2013, University of Waterloo: Waterloo, Ontario, Canada. p. 132.

66. S. C. Cowin, Basic continuum kinematics, in continuum mechanics of anisotropic materials,. 2013, Springer.

67. S. Demko, Construction of fractal object with Iterated Function System. ACM, 1985. 19: p. 271-278.

68. P. C. Chou, Elasticity tensor, dyadic and engineering approaches. W.W.Hagerty. 1967, United State of America: D. Van Nostrand Company,Inc.

69. W. Flugge, Tensor analysis and continuum mechanics. 1972: Springer-Verlag Berlin Heidelberg GmH.

70. J. D. Clayton, Mathematical foundations in nonlinear mechanics of crystals, solid mechanics and its applications 2011, Springer Science.

71. S. Flugge, Practical quantum mechanics. 1974: Springer-Verlag Berlin Heidlberg 1999.

72. M. Smith, ABAQUS/Standard user?s manual, Version 6.14. 2014: Simulia.

73. W. J. Stronge, Static Deflection, in dynamic models for structural plasticity, London. 1993, Springer.

74. B. Zohuri, Dimensional analysis and self-similarity methods for engineers and scientists. 2015: Springer.

75. S. S. Rao, The finite element method in engineering. 1st ed. 1982, United Kingdom: Pergamon Press.

76. D. B. Ingham, and I. Pop, Transport phenomena in porous media. 1998: Elsevier.

77. K. Davey, R. Darvizeh, and Z. Sedqi. Tessellated continuum mechanics: forced vibration of cantor Dust-Like structures. in 2017 Fourth International Conference on Mathematics and Computers in Sciences and in Industry (MCSI). 2017.

78. C. T. F. Ross, Finite element methods in engineering science. 1935: Redwood Press limited.

79. A. P. Boresi, and K.P. Chong, Elasticity in engineering mechanics. 3rd ed. 1987, United State of America: Elsevier.

80. K. Davey, R. Darvizeh, and Z. Sedqi, A tessellated continuum approach for the static analysis of perforated structures. Unpublished paper, 2018.

81. S. S. Rao, Mechanical vibration. 3rd ed. J. Albanese. 1995, United State of America Addison-Wesley Publishing Company, Inc.

82. J. Wu, Analytical and numerical methods for vibration analyses. 2015: John Wiley & Sons Singapore Pte. Ltd.

83. R. D. Blevins, Formulas for natural frequencies and mode shapes. Van Nostrand, 1979.

84. S. Timoshenko and S. W-Krieger, Theory of plates and shells. McGraw, Inc. 1959.

85. T. Lewinski, Plates, laminates and shells: asymptotic analysis and homogenization 2000, London: World Scientific.

86. P. G. Ciarlet, Introduction to linear shell theory. Series in applied mathematics. P.G. Ciarlet and P.L. Lions. 1998, France.

87. K. Lp, P. Tse, and T. Lai, Material characterization for orthotropic shells using modal analysis and Rayleigh-Ritz models. Composites Part B Engineering, 1998. 29(4): p. 397-409.

88. G. v. Rossum, A brief timeline of Python, G.v. Rossum, Editor. 2009.

89. A. Sweigart, Automate the boring stuff with python: Practical programming for total beginners. 1st ed. 2015.

90. T. Radcliffe, Python vs. Java: Duck typing, parsing on whitespace and other cool differences, in ActiveState. 2018, The open source language company: United Kingdom.

91. EDUCBA. Python vs C++. 2019; Available from: https://www.educba.com /python-vs-c-plus-plus/.

92. P. Norvig, Python for LISP programmers. 2000.

93. G. Khera, Dive deep into Python vs Perl debate ? What should I learn Python or Perl? 2016, TecMint.

94. G.V. Rossum, Comparing python to other languages. 1997, Python Python^{tm}.

95. M. Griffel, Ruby vs. Python. 2018, One Month web site.

96. J. Zelles, Python programming: An introduction to computer science. 2nd ed. 2010: Sherwood, Oregon : Franklin, Beedle & Associates.

97. K. Davey, R. Darvizeh, and Z. Sedqi, A tessellated continuum approach: A Similitude Approach to Holey-Beam Vibration,Applied Mathematical modelling , 2018.

Appendix A
Per-fractal IFS Equations

A.1. Maps for the Sierpinski Carpet

The mapping results on the pre-fractal and the tessellated space should be used the mapping listed in Table 1 and Table 2. For each table, the x and y are denoting to the dimensionless coordinates, where $x = X / \ell_0$ and in a similar way $y = Y / \ell_0$.

Table A-1. Scaling maps for Sierpinski Carpet [55].

$S_1(x,y) = \left(\dfrac{x}{3}, \dfrac{y}{3} \right)$	$S_2(x,y) = \left(\dfrac{\ell_0}{3} + \dfrac{x}{3}, \dfrac{y}{3} \right)$
$S_3(x,y) = \left(\dfrac{2\ell_0}{3} + \dfrac{x}{3}, \dfrac{y}{3} \right)$	$S_4(x,y) = \left(\dfrac{x}{3}, \dfrac{\ell_0}{3} + \dfrac{y}{3} \right)$
$S_5(x,y) = \left(\dfrac{2\ell_0}{3} + \dfrac{x}{3}, \dfrac{\ell_0}{3} + \dfrac{y}{3} \right)$	$S_6(x,y) = \left(\dfrac{x}{3}, \dfrac{2\ell_0}{3} + \dfrac{y}{3} \right)$
$S_7(x,y) = \left(\dfrac{\ell_0}{3} + \dfrac{x}{3}, \dfrac{2\ell_0}{3} + \dfrac{y}{3} \right)$	$S_8(x,y) = \left(\dfrac{2\ell_0}{3} + \dfrac{x}{3}, \dfrac{2\ell_0}{3} + \dfrac{y}{3} \right)$

Table A-2. Scaling maps for the tessellated geometry mirrored the Sierpinski Carpet [55].

$P_2(x,y)$	$P_{21}(x,y) = \left(\dfrac{1}{3} + \dfrac{x}{3}, \dfrac{1}{3} + \dfrac{y}{3} \right)$	if $y \geq 2x$ and $1/3 \leq x \leq 1/2$
	$P_{22}(x,y) = \left(\dfrac{1}{3} + \dfrac{x}{3}, \dfrac{1}{3} - \dfrac{x}{3} + \dfrac{y}{3} \right)$	if $y \geq 2(1-x)$ and $1/2 \leq x \leq 2/3$
	$P_{23}(x,y) = \left(\dfrac{x}{2}, \dfrac{1}{3} + \dfrac{y}{3} \right)$	if $y \geq 2x$ and $1/3 \leq x \leq 1/2$ and if $y \geq 2(1-x)$ and $1/2 \leq x \leq 2/3$
$P_4(x,y)$	$P_{41}(x,y) = \left(\dfrac{1}{3} + \dfrac{x}{3}, \dfrac{1}{3} + \dfrac{y}{3} \right)$	if $y \leq x/2$ and $2/3 \leq x \leq 1$

	$P_{42}(x,y) = \left(\dfrac{1}{3} + \dfrac{x}{3} - \dfrac{y}{3}, \dfrac{1}{3} + \dfrac{y}{3}\right)$	if $y \geq (1 - x/2)$ and $2/3 \leq x \leq 1$
	$P_{43}(x,y) = \left(\dfrac{x}{2}, \dfrac{1}{3} + \dfrac{y}{3}\right)$	if $y \geq x/2$ and $2/3 \leq x \leq 1$ and if $y \geq (1 - x/2)$ and $2/3 \leq x \leq 1$
$P_5(x,y)$	$P_{51}(x,y) = \left(\dfrac{2}{3} + \dfrac{x}{3} - \dfrac{y}{3}, \dfrac{1}{3} + \dfrac{y}{3}\right)$	if $2y \leq 1 - x$ and $0 \leq x \leq 1/3$
	$P_{52}(x,y) = \left(\dfrac{1}{3} + \dfrac{x}{3} + \dfrac{y}{3}, \dfrac{1}{3} + \dfrac{y}{3}\right)$	if $2y \geq 1 - x$ and $0 \leq x \leq 1/3$
	$P_{53}(x,y) = \left(\dfrac{1}{2} + \dfrac{x}{2}, \dfrac{1}{3} + \dfrac{y}{3}\right)$	if $2y \geq 1 - x$ and $0 \leq x \leq 1/3$ and if $2y \leq 1 - x$ and $0 \leq x \leq 1/3$
$P_7(x,y)$	$P_{71}(x,y) = \left(\dfrac{1}{3} + \dfrac{x}{3}, \dfrac{2}{3} - \dfrac{x}{3} + \dfrac{y}{3}\right)$	if $y \leq 1/2 - x/2$ and $1/3 \leq x \leq 1/2$
	$P_{72}(x,y) = \left(\dfrac{1}{3} + \dfrac{x}{3}, \dfrac{1}{3} - \dfrac{x}{3} + \dfrac{y}{3}\right)$	if $y \leq 2x - 1$ and $1/2 \leq x \leq 2/3$
	$P_{73}(x,y) = \left(\dfrac{1}{3} + \dfrac{x}{3}, \dfrac{1}{2} + \dfrac{y}{2}\right)$	if $y \geq 1/2 - x/2$ and $1/3 \leq x \leq 1/2$ and if $y \geq 2x - 1$ and $1/2 \leq x \leq 2/3$

A.2. Maps for the Vicsek Fractal

The Vicsek Fractal is constructed by the five affine contraction maps in the following Table. For each table, the x and y are denoting to the dimensionless coordinates, where $x = X/\ell_0$ and in a similar way $y = Y/\ell_0$.

Table A-3 Contraction maps for Vicsek Fractal [55].

$S_1(x,y) = \left(\dfrac{x}{3}, \dfrac{\ell_0}{3} + \dfrac{y}{3}\right)$	$S_2(x,y) = \left(\dfrac{\ell_0}{3} + \dfrac{x}{3}, \dfrac{\ell_0}{3} + \dfrac{y}{3}\right)$
$S_3(x,y) = \left(\dfrac{\ell_0}{3} + \dfrac{x}{3}, \dfrac{y}{3}\right)$	$S_4(x,y) = \left(\dfrac{2\ell_0}{3} + \dfrac{x}{3}, \dfrac{\ell_0}{3} + \dfrac{y}{3}\right)$
$S_5(x,y) = \left(\dfrac{\ell_0}{3} + \dfrac{x}{3}, \dfrac{2\ell_0}{3} + \dfrac{y}{3}\right)$	

Two sets of expansion maps termed (a) and (b) are defined in Tables 25 and 26, respectively. The effect of these maps is shown visually in Figures 22 and 23, where disparate tessellations are displayed.

Table A-4. Expansion maps (a) for Vicsek Fractal [55].

$P_1(x,y)$	$P_{11}(x,y)=\left(\dfrac{x}{3},-\dfrac{x}{3}+\dfrac{2y}{3}+\dfrac{\ell_0}{3}\right)$	if $y \ge x$ and $y \ge -x+1$
	$P_{12}(x,y)=\left(\dfrac{x}{3},\dfrac{y}{3}+\dfrac{\ell_0}{3}\right)$	if $y \le x$ and $y \ge -x+1$
	$P_{13}(x,y)=\left(\dfrac{x}{3},\dfrac{x}{3}+\dfrac{2y}{3}\right)$	if $y \le x$ and $y \le -x+1$
	$P_{14}(x,y)=\left(\dfrac{x}{3},y\right)$	if $y \ge x$ and $y \le -x+1$
	$P_2(x,y)=\left(\dfrac{\ell_0}{3}+\dfrac{x}{3},\dfrac{\ell_0}{3}+\dfrac{y}{3}\right)$	
$P_3(x,y)$	$P_{31}(x,y)=\left(\dfrac{x}{3}+\dfrac{\ell_0}{3},\dfrac{y}{3}\right)$	if $y \ge x$ and $y \ge -x+1$
	$P_{32}(x,y)=\left(\dfrac{2x}{3}-\dfrac{y}{3}+\dfrac{\ell_0}{3},\dfrac{y}{3}\right)$	if $y \le x$ and $y \ge -x+1$
	$P_{33}(x,y)=\left(x,\dfrac{y}{3}\right)$	if $y \le x$ and $y \le -x+1$
	$P_{34}(x,y)=\left(\dfrac{2x}{3}+\dfrac{y}{3},\dfrac{y}{3}\right)$	if $y \ge x$ and $y \le -x+1$
$P_4(x,y)$	$P_{41}(x,y)=\left(\dfrac{x}{3}+\dfrac{2}{3},\dfrac{x}{3}+\dfrac{2y}{3}\right)$	if $y \ge x$ and $y \ge -x+1$
	$P_{42}(x,y)=\left(\dfrac{x}{3}+\dfrac{2}{3},y\right)$	if $y \le x$ and $y \ge -x+1$

	$P_{43}(x,y) = \left(\dfrac{x}{3} + \dfrac{2\ell_0}{3}, -\dfrac{x}{3} + \dfrac{2y}{3} + \dfrac{\ell_0}{3} \right)$	if $y \leq x$ and $y \leq -x + 1$
	$P_{44}(x,y) = \left(\dfrac{x}{3} + \dfrac{2}{3}, \dfrac{y}{3} + \dfrac{\ell_0}{3} \right)$	if $y \geq x$ and $y \leq -x + 1$
$P_5(x,y)$	$P_{51}(x,y) = \left(x, \dfrac{y}{3} + \dfrac{2\ell_0}{3} \right)$	if $y \geq x$ and $y \geq -x + 1$
	$P_{52}(x,y) = \left(\dfrac{2x}{3} + \dfrac{y}{3}, \dfrac{y}{3} + \dfrac{2\ell_0}{3} \right)$	if $y \leq x$ and $y \geq -x + 1$
	$P_{53}(x,y) = \left(\dfrac{x}{3} + \dfrac{1}{3}, \dfrac{y}{3} + \dfrac{2\ell_0}{3} \right)$	if $y \leq x$ and $y \leq -x + 1$
	$P_{54}(x,y) = \left(\dfrac{2x}{3} - \dfrac{y}{3} + \dfrac{\ell_0}{3}, \dfrac{y}{3} + \dfrac{2\ell_0}{3} \right)$	if $y \geq x$ and $y \leq -x + 1$

Appendix B

Analytical Equation for Fractal Structures

B.1. The Cantor Set type *k=3*

The lateral deflection on the tessellated space of *k=3* is represented by Equation (4.23). The following results are showing the lateral deflection for each segments (the even number of equations are explaining the linear behaviour of the holes):

1. $\dfrac{Ql^3}{EI}\left(\dfrac{\hat{x}_{ps}^2}{2}-\dfrac{\hat{x}_{ps}^3}{6}\right)$ $\hspace{2cm}$ $0 \le \hat{x}_{ps} \le 1/27$

2. $\dfrac{40Fl^3}{59049EI}+\dfrac{53Fl^2}{1458EI}\left(\hat{x}_{ps}-\dfrac{1}{27}\right)$ $\hspace{1cm}$ $1/27 \le \hat{x}_{ps} \le 2/27$

3. $\dfrac{Ql^3}{EI}\left(\dfrac{\hat{x}_{ps}^2}{2}-\dfrac{\hat{x}_{ps}^3}{6}\right)+\dfrac{53\,F\,l^2}{1458\,EI}\hat{x}_{ps}+\dfrac{239\,Fl^3}{118098\,EI}$ $\hspace{1cm}$ $2/27 \le \hat{x}_{ps} \le 3/27$

4. $\dfrac{1}{3}\left(\dfrac{53\,Fl^2}{1458\,EI}\right)+\dfrac{239\,Fl^3}{118098\,EI}+\left(\dfrac{53\,Fl^2}{1458\,EI}+\dfrac{F\left(-\dfrac{1}{162}+\dfrac{1}{9}\right)}{EI}\right)\left(\hat{x}_{ps}-\dfrac{1}{9}\right)$ $\hspace{1cm}$ $3/27 \le \hat{x}_{ps} \le 6/27$

5. $\dfrac{Ql^3}{EI}\left(\dfrac{\hat{x}_{ps}^2}{2}-\dfrac{\hat{x}_{ps}^3}{6}\right)+\left(\dfrac{53\,F\,l^2}{1458\,EI}+\dfrac{F\left(-\dfrac{1}{162}+\dfrac{1}{18}\right)}{EI}\right)\hat{x}_{ps}+\dfrac{53\,F\,l^2}{13122\,EI}+\dfrac{239\,Fl^3}{118098\,EI}+\dfrac{F\left(-\dfrac{1}{4374}+\dfrac{1}{162}\right)}{EI}+$

$\dfrac{1}{9}\left(\dfrac{53\,F\,l^2}{1458\,EI}+\dfrac{F\left(-\dfrac{1}{162}+\dfrac{1}{18}\right)}{EI}\right)l$

$6/27 \le \hat{x}_{ps} \le 7/27$

6. $\dfrac{7}{27}\left(\dfrac{53\,F\,l^2}{1458\,EI}+\dfrac{F\left(-\dfrac{1}{162}+\dfrac{1}{18}\right)}{EI}\right)+\dfrac{53\,F\,l^2}{13122\,EI}+\dfrac{239\,Fl^3}{118098\,EI}+\dfrac{F\left(-\dfrac{1}{4374}+\dfrac{1}{162}\right)}{EI}+$

$\dfrac{1}{9}\left(\dfrac{53\,F\,l^2}{1458\,EI}+\dfrac{F\left(-\dfrac{1}{162}+\dfrac{1}{18}\right)}{EI}\right)l+\left(\dfrac{53\,F\,l^2}{1458\,EI}+\dfrac{F\left(-\dfrac{1}{162}+\dfrac{1}{18}\right)}{EI}+\dfrac{F\left(-\dfrac{49}{1458}+\dfrac{71}{27}\right)}{EI}\right)\left(\hat{x}_{ps}-\dfrac{1}{27}\right)$

$7/27 \le \hat{x}_{ps} \le 8/27$

7. $\dfrac{Ql^3}{EI}\left(\dfrac{\hat{x}_{ps}^2}{2}-\dfrac{\hat{x}_{ps}^3}{6}\right)+\left(\dfrac{53\,F\,l^2}{1458\,EI}+\dfrac{F\left(-\dfrac{1}{162}+\dfrac{1}{18}\right)}{EI}+\dfrac{F\left(-\dfrac{1}{162}+\dfrac{1}{18}\right)}{EI}+\dfrac{F\left(-\dfrac{1}{18}+\dfrac{1}{3}\right)}{EI}\right)\hat{x}_{ps}+$

$$\frac{7}{27}\left(\frac{53\,F\,l^2}{1458\,EI}+\frac{F\left(-\frac{1}{162}+\frac{1}{18}\right)}{EI}+\frac{F\left(-\frac{1}{162}+\frac{1}{18}\right)}{EI}\right)+\left(\begin{array}{l}\frac{7}{27}\left(\frac{53\,F\,l^2}{1458\,EI}+\frac{F\left(-\frac{1}{162}+\frac{1}{18}\right)}{EI}+\frac{F\left(-\frac{1}{162}+\frac{1}{18}\right)}{EI}\right)+\\[4pt]\left(\frac{53\,F\,l^2}{13122\,EI}+\frac{239\,Fl^3}{118098\,EI}+\frac{F\left(-\frac{1}{4374}+\frac{1}{162}\right)}{EI}+\frac{1}{9}\left(\frac{53\,F\,l^2}{1458\,EI}+\frac{F\left(-\frac{1}{162}+\frac{1}{18}\right)}{EI}\right)\right)l+\\[4pt]\frac{F\left(-\frac{343}{118098}+\frac{491}{1458}\right)}{EI}+\frac{23}{27}\left(\left(\frac{53\,F\,l^2}{1458\,EI}+\frac{F\left(-\frac{1}{162}+\frac{1}{18}\right)}{EI}+\frac{F\left(-\frac{1}{162}+\frac{1}{18}\right)}{EI}\right)+\frac{F\left(-\frac{49}{1458}+\frac{71}{27}\right)}{EI}\right)l+\\[4pt]\frac{F\left(-\frac{343}{118098}+\frac{491}{1458}\right)}{EI}+\frac{23}{27}\left(\left(\frac{53\,F\,l^2}{1458\,EI}+\frac{F\left(-\frac{1}{162}+\frac{1}{18}\right)}{EI}+\frac{F\left(-\frac{1}{162}+\frac{1}{18}\right)}{EI}\right)+\frac{F\left(-\frac{49}{1458}+\frac{71}{27}\right)}{EI}\right)l\end{array}\right)$$

$$8/27 \le \hat{x}_{ps} \le 9/27$$

8.
$$\frac{1}{3}\left(\frac{53\,F\,l^2}{1458\,EI}+\frac{F\left(-\frac{1}{162}+\frac{1}{18}\right)}{EI}+\frac{F\left(-\frac{1}{162}+\frac{1}{18}\right)}{EI}\right)+\frac{7}{27}\left(\frac{53\,F\,l^2}{1458\,EI}+\frac{F\left(-\frac{1}{162}+\frac{1}{18}\right)}{EI}\right)+\frac{53\,F\,l^2}{13122\,EI}+\frac{239\,Fl^3}{118098\,EI}+$$

$$\frac{F\left(-\frac{1}{4374}+\frac{1}{162}\right)}{EI}+\frac{1}{9}\left(\frac{53\,F\,l^2}{1458\,EI}+\frac{F\left(-\frac{1}{162}+\frac{1}{18}\right)}{EI}\right)l+\frac{F\left(-\frac{343}{118098}+\frac{491}{1458}\right)}{EI}+\frac{23}{27}\left(\frac{53\,F\,l^2}{1458\,EI}+\frac{F\left(-\frac{1}{162}+\frac{1}{18}\right)}{EI}+\frac{F\left(-\frac{49}{1458}+\frac{71}{27}\right)}{EI}\right)l$$

$$\frac{F\left(-\frac{1}{162}+\frac{1}{18}\right)}{EI}+\left(\frac{53\,F\,l^2}{1458\,EI}+\frac{F\left(-\frac{1}{162}+\frac{1}{18}\right)}{EI}+\frac{F\left(-\frac{1}{162}+\frac{1}{18}\right)}{EI}+\frac{F\left(-\frac{1}{18}+\frac{1}{3}\right)}{EI}\right)\left(\hat{x}_{ps}-\frac{1}{3}\right)$$

$$9/27 \le x_{ps} \le 19/27$$

9.
$$\frac{Ql^3}{EI}\left(\frac{\hat{x}_{ps}^2}{2}-\frac{\hat{x}_{ps}^3}{6}\right)+\left(\frac{53\,F\,l^2}{1458\,EI}+\frac{F\left(-\frac{1}{162}+\frac{1}{18}\right)}{EI}+\frac{F\left(-\frac{1}{162}+\frac{1}{18}\right)}{EI}+\frac{F\left(-\frac{1}{18}+\frac{1}{3}\right)}{EI}\right)\hat{x}_{ps}+$$

$$\left(\begin{array}{l}\frac{1}{3}\left(\frac{53\,F\,l^2}{1458\,EI}+\frac{F\left(-\frac{1}{162}+\frac{1}{18}\right)}{EI}+\frac{F\left(-\frac{1}{162}+\frac{1}{18}\right)}{EI}\right)+\frac{7}{27}\left(\frac{53\,F\,l^2}{1458\,EI}+\frac{F\left(-\frac{1}{162}+\frac{1}{18}\right)}{EI}+\frac{F\left(-\frac{1}{162}+\frac{1}{18}\right)}{EI}\right)+\\[4pt]\left(\frac{7}{27}\left(\frac{53\,F\,l^2}{1458\,EI}+\frac{F\left(-\frac{1}{162}+\frac{1}{18}\right)}{EI}+\frac{F\left(-\frac{1}{162}+\frac{1}{18}\right)}{EI}\right)+\frac{53\,F\,l^2}{13122\,EI}+\frac{239\,Fl^3}{118098\,EI}+\frac{F\left(-\frac{1}{4374}+\frac{1}{162}\right)}{EI}+\right.\\[4pt]\left.\frac{1}{9}\left(\frac{53\,F\,l^2}{1458\,EI}+\frac{F\left(-\frac{1}{162}+\frac{1}{18}\right)}{EI}\right)l+\frac{F\left(-\frac{343}{118098}+\frac{491}{1458}\right)}{EI}+\frac{23}{27}\left(\left(\frac{53\,F\,l^2}{1458\,EI}+\frac{F\left(-\frac{1}{162}+\frac{1}{18}\right)}{EI}+\frac{F\left(-\frac{1}{162}+\frac{1}{18}\right)}{EI}\right)+\frac{F\left(-\frac{49}{1458}+\frac{71}{27}\right)}{EI}\right)l\right)\\[4pt]+\frac{F\left(-\frac{343}{118098}+\frac{491}{1458}\right)}{EI}+\frac{23}{27}\left(\left(\frac{53\,F\,l^2}{1458\,EI}+\frac{F\left(-\frac{1}{162}+\frac{1}{18}\right)}{EI}+\frac{F\left(-\frac{1}{162}+\frac{1}{18}\right)}{EI}\right)+\frac{F\left(-\frac{49}{1458}+\frac{71}{27}\right)}{EI}\right)l+\frac{F\left(-\frac{1}{162}+\frac{1}{18}\right)}{EI}+\\[4pt]\left(\frac{53\,F\,l^2}{1458\,EI}+\frac{F\left(-\frac{1}{162}+\frac{1}{18}\right)}{EI}+\frac{F\left(-\frac{1}{162}+\frac{1}{18}\right)}{EI}+\frac{F\left(-\frac{1}{162}+\frac{1}{18}\right)}{EI}\right)\left(-\frac{1}{3}+\frac{21}{3}\right)\end{array}\right)$$

$$19/27 \le x_{ps} \le 20/27$$

$$\frac{1}{3}\left(\frac{53\,F\,l^2}{1458\,EI}+\frac{F\left(-\frac{1}{162}+\frac{1}{18}\right)}{EI}+\frac{F\left(-\frac{1}{162}+\frac{1}{18}\right)}{EI}\right)+\frac{7}{27}\left(\frac{53\,F\,l^2}{1458\,EI}+\frac{F\left(-\frac{1}{162}+\frac{1}{18}\right)}{EI}+\frac{F\left(-\frac{1}{162}+\frac{1}{18}\right)}{EI}\right)$$

$$\frac{7}{27}\left(\frac{53\,F\,l^2}{1458\,EI}+\frac{F\left(-\frac{1}{162}+\frac{1}{18}\right)}{EI}+\frac{F\left(-\frac{1}{162}+\frac{1}{18}\right)}{EI}\right)+\frac{53\,F\,l^2}{13122\,EI}+\frac{239\,Fl^3}{118098\,EI}+\frac{F\left(-\frac{1}{4374}+\frac{1}{162}\right)}{EI}+$$

$$+\frac{1}{9}\left(\frac{53\,F\,l^2}{1458\,EI}+\frac{F\left(-\frac{1}{162}+\frac{1}{18}\right)}{EI}\right)l+\frac{F\left(-\frac{343}{118098}+\frac{491}{1458}\right)}{EI}+$$

$$\frac{23}{27}\left(\left(\frac{53\,F\,l^2}{1458\,EI}+\frac{F\left(-\frac{1}{162}+\frac{1}{18}\right)}{EI}+\frac{F\left(-\frac{1}{162}+\frac{1}{18}\right)}{EI}\right)+\frac{F\left(-\frac{49}{1458}+\frac{71}{27}\right)}{EI}\right)l$$

$$+\frac{F\left(-\frac{343}{118098}+\frac{491}{1458}\right)}{EI}+\frac{23}{27}\left(\left(\frac{53\,F\,l^2}{1458\,EI}+\frac{F\left(-\frac{1}{162}+\frac{1}{18}\right)}{EI}+\frac{F\left(-\frac{1}{162}+\frac{1}{18}\right)}{EI}\right)+\frac{F\left(-\frac{49}{1458}+\frac{71}{27}\right)}{EI}\right)l+$$

10.
$$\frac{F\left(-\frac{1}{162}+\frac{1}{18}\right)}{EI}+\left(\frac{53\,F\,l^2}{1458\,EI}+\frac{F\left(-\frac{1}{162}+\frac{1}{18}\right)}{EI}+\frac{F\left(-\frac{1}{162}+\frac{1}{18}\right)}{EI}+\frac{F\left(-\frac{1}{162}+\frac{1}{18}\right)}{EI}\right)\left(-\frac{1}{3}+\frac{21}{3}\right)+$$

$$\frac{19}{27}\left(\frac{53\,F\,l^2}{1458\,EI}+\frac{F\left(-\frac{1}{162}+\frac{1}{18}\right)}{EI}+\frac{F\left(-\frac{1}{162}+\frac{1}{18}\right)}{EI}+\frac{F\left(-\frac{1}{18}+\frac{1}{3}\right)}{EI}\right)+$$

$$\left(\frac{53\,F\,l^2}{1458\,EI}+\frac{F\left(-\frac{1}{162}+\frac{1}{18}\right)}{EI}+\frac{F\left(-\frac{1}{162}+\frac{1}{18}\right)}{EI}+\frac{F\left(-\frac{1}{18}+\frac{1}{3}\right)}{EI}+\frac{F\left(-\frac{119}{27}+\frac{19}{1458}\right)}{EI}\right)\left(\hat{x}_{ps}-\frac{1}{27}\right)$$

$20/27 \le x_{ps} \le 21/27$

11.
$$\frac{1}{3}\left(\frac{53\,F\,l^2}{1458\,EI}+\frac{F\left(-\frac{1}{162}+\frac{1}{18}\right)}{EI}+\frac{F\left(-\frac{1}{162}+\frac{1}{18}\right)}{EI}\right)+\frac{7}{27}\left(\frac{53\,F\,l^2}{1458\,EI}+\frac{F\left(-\frac{1}{162}+\frac{1}{18}\right)}{EI}+\frac{F\left(-\frac{1}{162}+\frac{1}{18}\right)}{EI}\right)+$$

$$\frac{7}{27}\left(\frac{53\,F\,l^2}{1458\,EI}+\frac{F\left(-\frac{1}{162}+\frac{1}{18}\right)}{EI}+\frac{F\left(-\frac{1}{162}+\frac{1}{18}\right)}{EI}\right)+\frac{53\,F\,l^2}{13122\,EI}+\frac{239\,Fl^3}{118098\,EI}+\frac{F\left(-\frac{1}{4374}+\frac{1}{162}\right)}{EI}+$$

$$\frac{1}{9}\left(\frac{53\,F\,l^2}{1458\,EI}+\frac{F\left(-\frac{1}{162}+\frac{1}{18}\right)}{EI}\right)l+\frac{F\left(-\frac{343}{118098}+\frac{491}{1458}\right)}{EI}+$$

$$\frac{23}{27}\left(\left(\frac{53\,F\,l^2}{1458\,EI}+\frac{F\left(-\frac{1}{162}+\frac{1}{18}\right)}{EI}+\frac{F\left(-\frac{1}{162}+\frac{1}{18}\right)}{EI}\right)+\frac{F\left(-\frac{49}{1458}+\frac{71}{27}\right)}{EI}\right)l$$

$$+\frac{F\left(-\frac{343}{118098}+\frac{491}{1458}\right)}{EI}+\frac{23}{27}\left(\left(\frac{53\,F\,l^2}{1458\,EI}+\frac{F\left(-\frac{1}{162}+\frac{1}{18}\right)}{EI}+\frac{F\left(-\frac{1}{162}+\frac{1}{18}\right)}{EI}\right)+\frac{F\left(-\frac{49}{1458}+\frac{71}{27}\right)}{EI}\right)l+$$

$$\frac{F\left(-\frac{1}{162}+\frac{1}{18}\right)}{EI}+\left(\frac{53\,F\,l^2}{1458\,EI}+\frac{F\left(-\frac{1}{162}+\frac{1}{18}\right)}{EI}+\frac{F\left(-\frac{1}{162}+\frac{1}{18}\right)}{EI}+\frac{F\left(-\frac{1}{162}+\frac{1}{18}\right)}{EI}\right)\left(-\frac{1}{3}+\frac{21}{3}\right)+$$

$$\frac{19}{27}\left(\frac{53\,F\,l^2}{1458\,EI}+\frac{F\left(-\frac{1}{162}+\frac{1}{18}\right)}{EI}+\frac{F\left(-\frac{1}{162}+\frac{1}{18}\right)}{EI}+\frac{F\left(-\frac{1}{18}+\frac{1}{3}\right)}{EI}\right)+\frac{F\left(-\frac{119}{11458}-\frac{19^3}{118098}\right)}{EI}+$$

$$\frac{19}{27}l\left(\frac{53\,F\,l^2}{1458\,EI}+\frac{F\left(-\frac{1}{162}+\frac{1}{18}\right)}{EI}+\frac{F\left(-\frac{1}{162}+\frac{1}{18}\right)}{EI}+\frac{F\left(-\frac{1}{18}+\frac{1}{3}\right)}{EI}+\frac{F\left(-\frac{119}{27}-\frac{19^2}{1458}\right)}{EI}\right)$$

$$+\frac{Ql^3}{EI}\left(\frac{\hat{x}_{ps}^2}{2}-\frac{\hat{x}_{ps}^3}{6}\right)+\left(\frac{53\,F\,l^2}{1458\,EI}+\frac{F\left(-\frac{1}{162}+\frac{1}{18}\right)}{EI}+\frac{F\left(-\frac{1}{162}+\frac{1}{18}\right)}{EI}+\frac{F\left(-\frac{1}{18}+\frac{1}{3}\right)}{EI}+\frac{F\left(-\frac{119}{27}-\frac{19^2}{1458}\right)}{EI}\right)\hat{x}_{ps} \qquad 21/27\le x_{ps}\le 22/27$$

12.

$$\frac{1}{3}\left(\frac{53\,F\,l^2}{1458\,EI}+\frac{F\left(-\frac{1}{162}+\frac{1}{18}\right)}{EI}+\frac{F\left(-\frac{1}{162}+\frac{1}{18}\right)}{EI}\right)+\frac{7}{27}\left(\frac{53\,F\,l^2}{1458\,EI}+\frac{F\left(-\frac{1}{162}+\frac{1}{18}\right)}{EI}+\frac{F\left(-\frac{1}{162}+\frac{1}{18}\right)}{EI}\right)+$$

$$\left(\frac{7}{27}\left(\frac{53\,F\,l^2}{1458\,EI}+\frac{F\left(-\frac{1}{162}+\frac{1}{18}\right)}{EI}+\frac{F\left(-\frac{1}{162}+\frac{1}{18}\right)}{EI}\right)+\frac{53\,F\,l^2}{13122\,EI}+\frac{239\,Fl^3}{118098\,EI}+\frac{F\left(-\frac{1}{4374}+\frac{1}{162}\right)}{EI}+\right.$$

$$\frac{1}{9}\left(\frac{53\,F\,l^2}{1458\,EI}+\frac{F\left(-\frac{1}{162}+\frac{1}{18}\right)}{EI}\right)l+\frac{F\left(-\frac{343}{118098}+\frac{491}{1458}\right)}{EI}+\frac{23}{27}\left(\left(\frac{53\,F\,l^2}{1458\,EI}+\frac{F\left(-\frac{1}{162}+\frac{1}{18}\right)}{EI}+\frac{F\left(-\frac{1}{162}+\frac{1}{18}\right)}{EI}\right)+\frac{F\left(-\frac{49}{1458}+\frac{71}{27}\right)}{EI}\right)l$$

$$+\frac{F\left(-\frac{343}{118098}+\frac{491}{1458}\right)}{EI}+\frac{23}{27}\left(\left(\frac{53\,F\,l^2}{1458\,EI}+\frac{F\left(-\frac{1}{162}+\frac{1}{18}\right)}{EI}+\frac{F\left(-\frac{1}{162}+\frac{1}{18}\right)}{EI}\right)+\frac{F\left(-\frac{49}{1458}+\frac{71}{27}\right)}{EI}\right)l+\frac{F\left(-\frac{1}{162}+\frac{1}{18}\right)}{EI}+$$

$$\left(\frac{53\,F\,l^2}{1458\,EI}+\frac{F\left(-\frac{1}{162}+\frac{1}{18}\right)}{EI}+\frac{F\left(-\frac{1}{162}+\frac{1}{18}\right)}{EI}+\frac{F\left(-\frac{1}{162}+\frac{1}{18}\right)}{EI}\right)\left(-\frac{1}{3}+\frac{21}{3}\right)+$$

$$\frac{19}{27}\left(\frac{53\,F\,l^2}{1458\,EI}+\frac{F\left(-\frac{1}{162}+\frac{1}{18}\right)}{EI}+\frac{F\left(-\frac{1}{162}+\frac{1}{18}\right)}{EI}+\frac{F\left(-\frac{1}{18}+\frac{1}{3}\right)}{EI}\right)+$$

$$\frac{F\left(-\frac{119}{11458}-\frac{19^3}{118098}\right)}{EI}+\frac{19}{27}l\left(\frac{53\,F\,l^2}{1458\,EI}+\frac{F\left(-\frac{1}{162}+\frac{1}{18}\right)}{EI}+\frac{F\left(-\frac{1}{162}+\frac{1}{18}\right)}{EI}+\frac{F\left(-\frac{1}{18}+\frac{1}{3}\right)}{EI}+\frac{F\left(-\frac{119}{27}-\frac{19^2}{1458}\right)}{EI}\right)+$$

$$\frac{2l}{27}\left(\frac{53\,F\,l^2}{1458\,EI}+\frac{F\left(-\frac{1}{162}+\frac{1}{18}\right)}{EI}+\frac{F\left(-\frac{1}{162}+\frac{1}{18}\right)}{EI}+\frac{F\left(-\frac{1}{18}+\frac{1}{3}\right)}{EI}+\frac{F\left(-\frac{119}{27}-\frac{19^2}{1458}\right)}{EI}\right)+\frac{158Fl^3}{59049EI}+$$

$$\left(\frac{53\,F\,l^2}{1458\,EI}+\frac{F\left(-\frac{1}{162}+\frac{1}{18}\right)}{EI}+\frac{F\left(-\frac{1}{162}+\frac{1}{18}\right)}{EI}+\frac{F\left(-\frac{1}{18}+\frac{1}{3}\right)}{EI}+\frac{F\left(-\frac{119}{27}-\frac{19^2}{1458}\right)}{EI}+\frac{52Fl^2}{729EI}\right)\left(\hat{x}_{ps}-\frac{1}{9}\right)$$

$22/27\le x_{ps}\le 24/27$

13.

$$\frac{Ql^3}{EI}\left(\frac{\hat{x}_{ps}^2}{2}-\frac{\hat{x}_{ps}^3}{6}\right)+\left(\frac{53\,F\,l^2}{1458\,EI}+\frac{F\left(-\frac{1}{162}+\frac{1}{18}\right)}{EI}+\frac{F\left(-\frac{1}{162}+\frac{1}{18}\right)}{EI}+\frac{F\left(-\frac{1}{18}+\frac{1}{3}\right)}{EI}+\frac{F\left(-\frac{119}{27}-\frac{19^2}{1458}\right)}{EI}+\frac{52\,F\,l^2}{729\,EI}\right)\hat{x}_{ps}$$

$$\left(\frac{1}{3}\left(\frac{53\,F\,l^2}{1458\,EI}+\frac{F\left(-\frac{1}{162}+\frac{1}{18}\right)}{EI}+\frac{F\left(-\frac{1}{162}+\frac{1}{18}\right)}{EI}\right)+\frac{7}{27}\left(\frac{53\,F\,l^2}{1458\,EI}+\frac{F\left(-\frac{1}{162}+\frac{1}{18}\right)}{EI}+\frac{F\left(-\frac{1}{162}+\frac{1}{18}\right)}{EI}\right)+\right.$$

$$\frac{7}{27}\left(\frac{53\,F\,l^2}{1458\,EI}+\frac{F\left(-\frac{1}{162}+\frac{1}{18}\right)}{EI}+\frac{F\left(-\frac{1}{162}+\frac{1}{18}\right)}{EI}\right)+\frac{53\,F\,l^2}{13122\,EI}+\frac{239\,Fl^3}{118098\,EI}+\frac{F\left(-\frac{1}{4374}+\frac{1}{162}\right)}{EI}+$$

$$\frac{1}{9}\left(\frac{53\,F\,l^2}{1458\,EI}+\frac{F\left(-\frac{1}{162}+\frac{1}{18}\right)}{EI}\right)l+\frac{F\left(-\frac{343}{118098}+\frac{491}{1458}\right)}{EI}+$$

$$\frac{23}{27}\left(\left(\frac{53\,F\,l^2}{1458\,EI}+\frac{F\left(-\frac{1}{162}+\frac{1}{18}\right)}{EI}+\frac{F\left(-\frac{1}{162}+\frac{1}{18}\right)}{EI}\right)+\frac{F\left(-\frac{49}{1458}+\frac{71}{27}\right)}{EI}\right)l$$

$$+\frac{F\left(-\frac{343}{118098}+\frac{491}{1458}\right)}{EI}+\frac{23}{27}\left(\left(\frac{53\,F\,l^2}{1458\,EI}+\frac{F\left(-\frac{1}{162}+\frac{1}{18}\right)}{EI}+\frac{F\left(-\frac{1}{162}+\frac{1}{18}\right)}{EI}\right)+\frac{F\left(-\frac{49}{1458}+\frac{71}{27}\right)}{EI}\right)l+$$

$$\frac{F\left(-\frac{1}{162}+\frac{1}{18}\right)}{EI}+\left(\frac{53\,F\,l^2}{1458\,EI}+\frac{F\left(-\frac{1}{162}+\frac{1}{18}\right)}{EI}+\frac{F\left(-\frac{1}{162}+\frac{1}{18}\right)}{EI}+\frac{F\left(-\frac{1}{162}+\frac{1}{18}\right)}{EI}\right)\left(-\frac{1}{3}+\frac{21}{3}\right)+$$

$$\frac{19}{27}\left(\frac{53\,F\,l^2}{1458\,EI}+\frac{F\left(-\frac{1}{162}+\frac{1}{18}\right)}{EI}+\frac{F\left(-\frac{1}{162}+\frac{1}{18}\right)}{EI}+\frac{F\left(-\frac{1}{18}+\frac{1}{3}\right)}{EI}\right)+\frac{F\left(-\frac{119}{11458}-\frac{19^3}{118098}\right)}{EI}+$$

$$\frac{19}{27}l\left(\frac{53\,F\,l^2}{1458\,EI}+\frac{F\left(-\frac{1}{162}+\frac{1}{18}\right)}{EI}+\frac{F\left(-\frac{1}{162}+\frac{1}{18}\right)}{EI}+\frac{F\left(-\frac{1}{18}+\frac{1}{3}\right)}{EI}+\frac{F\left(-\frac{119}{27}-\frac{19^2}{1458}\right)}{EI}\right)+$$

$$\frac{2l}{27}\left(\frac{53\,F\,l^2}{1458\,EI}+\frac{F\left(-\frac{1}{162}+\frac{1}{18}\right)}{EI}+\frac{F\left(-\frac{1}{162}+\frac{1}{18}\right)}{EI}+\frac{F\left(-\frac{1}{18}+\frac{1}{3}\right)}{EI}+\frac{F\left(-\frac{119}{27}-\frac{19^2}{1458}\right)}{EI}\right)+$$

$$\left.\frac{158\,Fl^3}{59049\,EI}+\frac{7}{9}l\left(\frac{53\,F\,l^2}{1458\,EI}+\frac{F\left(-\frac{1}{162}+\frac{1}{18}\right)}{EI}+\frac{F\left(-\frac{1}{162}+\frac{1}{18}\right)}{EI}+\frac{F\left(-\frac{1}{18}+\frac{1}{3}\right)}{EI}+\frac{F\left(-\frac{119}{27}-\frac{19^2}{1458}\right)}{EI}+\frac{52\,F\,l^2}{729\,EI}\right)\right)$$

$$24 \leq \hat{x}_{ps} \leq 25/27$$

$$\frac{25}{27}\left(\frac{53\,F\,l^2}{1458\,EI}+\frac{F\left(-\frac{1}{162}+\frac{1}{18}\right)}{EI}+\frac{F\left(-\frac{1}{162}+\frac{1}{18}\right)}{EI}+\frac{F\left(-\frac{1}{18}+\frac{1}{3}\right)}{EI}+\frac{F\left(-\frac{119}{27}-\frac{19^2}{1458}\right)}{EI}+\frac{52\,F\,l^2}{729\,EI}\right.$$
$$\left.+\frac{F\left(-\frac{625}{1458}-\frac{25l}{27}\right)}{EI}\right)+$$

$$\frac{25}{27}\left(\frac{53\,F\,l^2}{1458\,EI}+\frac{F\left(-\frac{1}{162}+\frac{1}{18}\right)}{EI}+\frac{F\left(-\frac{1}{162}+\frac{1}{18}\right)}{EI}+\frac{F\left(-\frac{1}{18}+\frac{1}{3}\right)}{EI}+\frac{F\left(-\frac{119}{27}-\frac{19^2}{1458}\right)}{EI}+\frac{52\,F\,l^2}{729\,EI}\right)+$$

$$\frac{1}{3}\left(\frac{53\,F\,l^2}{1458\,EI}+\frac{F\left(-\frac{1}{162}+\frac{1}{18}\right)}{EI}+\frac{F\left(-\frac{1}{162}+\frac{1}{18}\right)}{EI}\right)+\frac{7}{27}\left(\frac{53\,F\,l^2}{1458\,EI}+\frac{F\left(-\frac{1}{162}+\frac{1}{18}\right)}{EI}+\frac{F\left(-\frac{1}{162}+\frac{1}{18}\right)}{EI}\right)+$$

$$\left(\begin{array}{l}\frac{7}{27}\left(\frac{53\,F\,l^2}{1458\,EI}+\frac{F\left(-\frac{1}{162}+\frac{1}{18}\right)}{EI}+\frac{F\left(-\frac{1}{162}+\frac{1}{18}\right)}{EI}\right)+\frac{53\,F\,l^2}{13122\,EI}+\frac{239\,Fl^3}{118098\,EI}+\frac{F\left(-\frac{1}{4374}+\frac{1}{162}\right)}{EI}+\\[2em]\frac{1}{9}\left(\frac{53\,F\,l^2}{1458\,EI}+\frac{F\left(-\frac{1}{162}+\frac{1}{18}\right)}{EI}\right)l+\frac{F\left(-\frac{343}{118098}+\frac{491}{1458}\right)}{EI}+\\[2em]\frac{23}{27}\left(\left(\frac{53\,F\,l^2}{1458\,EI}+\frac{F\left(-\frac{1}{162}+\frac{1}{18}\right)}{EI}+\frac{F\left(-\frac{1}{162}+\frac{1}{18}\right)}{EI}\right)+\frac{F\left(-\frac{49}{1458}+\frac{71}{27}\right)}{EI}\right)l\end{array}\right)$$

14.

$$+\frac{F\left(-\frac{343}{118098}+\frac{491}{1458}\right)}{EI}+\frac{23}{27}\left(\left(\frac{53\,F\,l^2}{1458\,EI}+\frac{F\left(-\frac{1}{162}+\frac{1}{18}\right)}{EI}+\frac{F\left(-\frac{1}{162}+\frac{1}{18}\right)}{EI}\right)+\frac{F\left(-\frac{49}{1458}+\frac{71}{27}\right)}{EI}\right)l+$$

$$\frac{F\left(-\frac{1}{162}+\frac{1}{18}\right)}{EI}+\left(\frac{53\,F\,l^2}{1458\,EI}+\frac{F\left(-\frac{1}{162}+\frac{1}{18}\right)}{EI}+\frac{F\left(-\frac{1}{162}+\frac{1}{18}\right)}{EI}+\frac{F\left(-\frac{1}{162}+\frac{1}{18}\right)}{EI}\right)\left(-\frac{1}{3}+\frac{21}{3}\right)+$$

$$\frac{19}{27}\left(\frac{53\,F\,l^2}{1458\,EI}+\frac{F\left(-\frac{1}{162}+\frac{1}{18}\right)}{EI}+\frac{F\left(-\frac{1}{162}+\frac{1}{18}\right)}{EI}+\frac{F\left(-\frac{1}{18}+\frac{1}{3}\right)}{EI}\right)+\frac{F\left(-\frac{119}{11458}-\frac{19^3}{118098}\right)}{EI}+$$

$$\frac{19}{27}l\left(\frac{53\,F\,l^2}{1458\,EI}+\frac{F\left(-\frac{1}{162}+\frac{1}{18}\right)}{EI}+\frac{F\left(-\frac{1}{162}+\frac{1}{18}\right)}{EI}+\frac{F\left(-\frac{1}{18}+\frac{1}{3}\right)}{EI}+\frac{F\left(-\frac{119}{27}-\frac{19^2}{1458}\right)}{EI}\right)$$

$$+\frac{2l}{27}\left(\frac{53\,F\,l^2}{1458\,EI}+\frac{F\left(-\frac{1}{162}+\frac{1}{18}\right)}{EI}+\frac{F\left(-\frac{1}{162}+\frac{1}{18}\right)}{EI}+\frac{F\left(-\frac{1}{18}+\frac{1}{3}\right)}{EI}+\frac{F\left(-\frac{119}{27}-\frac{19^2}{1458}\right)}{EI}\right)+$$

$$\frac{158Fl^3}{59049EI}+\frac{7}{9}l\left(\begin{array}{l}\frac{53\,F\,l^2}{1458\,EI}+\frac{F\left(-\frac{1}{162}+\frac{1}{18}\right)}{EI}+\frac{F\left(-\frac{1}{162}+\frac{1}{18}\right)}{EI}+\frac{F\left(-\frac{1}{18}+\frac{1}{3}\right)}{EI}+\\[1.5em]\frac{F\left(-\frac{119}{27}-\frac{19^2}{1458}\right)}{EI}+\frac{52\,F\,l^2}{729\,EI}\end{array}\right)+$$

$$\frac{F\left(-\frac{15325}{118098}-\frac{625l}{1458}\right)}{EI}+\frac{25}{27}\left(\frac{53\,F\,l^2}{1458\,EI}+\frac{F\left(-\frac{1}{162}+\frac{1}{18}\right)}{EI}+\frac{F\left(-\frac{1}{162}+\frac{1}{18}\right)}{EI}+\frac{F\left(-\frac{1}{18}+\frac{1}{3}\right)}{EI}+\frac{F\left(-\frac{119}{27}-\frac{19^2}{1458}\right)}{EI}+\frac{52\,F\,l^2}{729\,EI}+\frac{F\left(-\frac{625}{1458}-\frac{25l}{27}\right)}{EI}\right)l+$$

$$25\le\hat{x}_{ps}\le26\,/\,27$$

$$\frac{F\left(-\frac{15325}{118098}-\frac{625l}{1458}\right)}{EI}+\left(\frac{53\,F\,l^2}{1458\,EI}+\frac{F\left(-\frac{1}{162}+\frac{1}{18}\right)}{EI}+\frac{F\left(-\frac{1}{162}+\frac{1}{18}\right)}{EI}+\frac{F\left(-\frac{1}{18}+\frac{1}{3}\right)}{EI}+\frac{F\left(-\frac{119}{27}-\frac{19^2}{1458}\right)}{EI}+\frac{52\,F\,l^2}{729\,EI}+\frac{F\left(-\frac{625}{1458}-\frac{25l}{27}\right)}{EI}\right)\left(\hat{x}_{ps}-\frac{1}{27}\right)$$

$$\frac{Ql^3}{EI}\left(\frac{\hat{x}_{ps}^2}{2}-\frac{\hat{x}_{ps}^3}{6}\right)+\left(\frac{53\,F\,l^2}{1458\,EI}+\frac{F\left(-\frac{1}{162}+\frac{1}{18}\right)}{EI}+\frac{F\left(-\frac{1}{162}+\frac{1}{18}\right)}{EI}+\frac{F\left(-\frac{1}{18}+\frac{1}{3}\right)}{EI}+\frac{F\left(-\frac{119}{27}-\frac{19^2}{1458}\right)}{EI}+\frac{52\,F\,l^2}{729\,EI}+\frac{F\left(-\frac{625}{1458}-\frac{25l}{27}\right)}{EI}\right)\hat{x}_{ps}+$$

15.

$$\begin{aligned}&\frac{25}{27}\left(\frac{53\,F\,l^2}{1458\,EI}+\frac{F\left(-\frac{1}{162}+\frac{1}{18}\right)}{EI}+\frac{F\left(-\frac{1}{162}+\frac{1}{18}\right)}{EI}+\frac{F\left(-\frac{1}{18}+\frac{1}{3}\right)}{EI}+\frac{F\left(-\frac{119}{27}-\frac{19^2}{1458}\right)}{EI}+\frac{52\,F\,l^2}{729\,EI}\right)+\\[4pt]&\frac{1}{3}\left(\frac{53\,F\,l^2}{1458\,EI}+\frac{F\left(-\frac{1}{162}+\frac{1}{18}\right)}{EI}+\frac{F\left(-\frac{1}{162}+\frac{1}{18}\right)}{EI}\right)+\frac{7}{27}\left(\frac{53\,F\,l^2}{1458\,EI}+\frac{F\left(-\frac{1}{162}+\frac{1}{18}\right)}{EI}+\frac{F\left(-\frac{1}{162}+\frac{1}{18}\right)}{EI}\right)+\\[4pt]&\frac{7}{27}\left(\frac{53\,F\,l^2}{1458\,EI}+\frac{F\left(-\frac{1}{162}+\frac{1}{18}\right)}{EI}+\frac{F\left(-\frac{1}{162}+\frac{1}{18}\right)}{EI}\right)+\frac{53\,F\,l^2}{13122\,EI}+\frac{239\,Fl^3}{118098\,EI}+\frac{F\left(-\frac{1}{4374}+\frac{1}{162}\right)}{EI}+\\[4pt]&\frac{1}{9}\left(\frac{53\,F\,l^2}{1458\,EI}+\frac{F\left(-\frac{1}{162}+\frac{1}{18}\right)}{EI}\right)l+\frac{F\left(-\frac{343}{118098}+\frac{491}{1458}\right)}{EI}+\\[4pt]&\frac{23}{27}\left(\left(\frac{53\,F\,l^2}{1458\,EI}+\frac{F\left(-\frac{1}{162}+\frac{1}{18}\right)}{EI}+\frac{F\left(-\frac{1}{162}+\frac{1}{18}\right)}{EI}\right)+\frac{F\left(-\frac{49}{1458}+\frac{71}{27}\right)}{EI}\right)l\\[4pt]&+\frac{F\left(-\frac{343}{118098}+\frac{491}{1458}\right)}{EI}+\frac{23}{27}\left(\left(\frac{53\,F\,l^2}{1458\,EI}+\frac{F\left(-\frac{1}{162}+\frac{1}{18}\right)}{EI}+\frac{F\left(-\frac{1}{162}+\frac{1}{18}\right)}{EI}\right)+\frac{F\left(-\frac{49}{1458}+\frac{71}{27}\right)}{EI}\right)l+\\[4pt]&\frac{F\left(-\frac{1}{162}+\frac{1}{18}\right)}{EI}+\left(\frac{53\,F\,l^2}{1458\,EI}+\frac{F\left(-\frac{1}{162}+\frac{1}{18}\right)}{EI}+\frac{F\left(-\frac{1}{162}+\frac{1}{18}\right)}{EI}+\frac{F\left(-\frac{1}{18}+\frac{1}{3}\right)}{EI}\right)\left(-\frac{1}{3}+\frac{21}{3}\right)+\\[4pt]&\frac{19}{27}\left(\frac{53\,F\,l^2}{1458\,EI}+\frac{F\left(-\frac{1}{162}+\frac{1}{18}\right)}{EI}+\frac{F\left(-\frac{1}{162}+\frac{1}{18}\right)}{EI}+\frac{F\left(-\frac{1}{18}+\frac{1}{3}\right)}{EI}\right)+\frac{F\left(-\frac{119}{11458}-\frac{19^3}{118098}\right)}{EI}+\end{aligned}$$

$$26\le\hat{x}_{ps}\le27\,/\,27$$

203

$$\frac{19}{27}\,l\left(\frac{53\,F\,l^2}{1458\,EI}+\frac{F\left(-\frac{1}{162}+\frac{1}{18}\right)}{EI}+\frac{F\left(-\frac{1}{162}+\frac{1}{18}\right)}{EI}+\frac{F\left(-\frac{1}{18}+\frac{1}{3}\right)}{EI}+\frac{F\left(-\frac{119}{27}-\frac{19^2}{1458}\right)}{EI}\right)+$$

$$\frac{2\,A_7\,l}{27}+\frac{158Fl^3}{59049\,EI}+\frac{7}{9}\,l\left(\frac{53\,F\,l^2}{1458\,EI}+\frac{F\left(-\frac{1}{162}+\frac{1}{18}\right)}{EI}+\frac{F\left(-\frac{1}{162}+\frac{1}{18}\right)}{EI}+\frac{F\left(-\frac{1}{18}+\frac{1}{3}\right)}{EI}+\frac{F\left(-\frac{119}{27}-\frac{19^2}{1458}\right)}{EI}+\frac{52\,F\,l^2}{729\,EI}\right)+$$

$$\frac{F\left(-\frac{15325}{118098}-\frac{625l}{1458}\right)}{EI}+\frac{25}{27}\left(\frac{53\,F\,l^2}{1458\,EI}+\frac{F\left(-\frac{1}{162}+\frac{1}{18}\right)}{EI}+\frac{F\left(-\frac{1}{162}+\frac{1}{18}\right)}{EI}+\frac{F\left(-\frac{1}{18}+\frac{1}{3}\right)}{EI}+\frac{F\left(-\frac{119}{27}-\frac{19^2}{1458}\right)}{EI}+\frac{52\,F\,l^2}{729\,EI}+\frac{F\left(-\frac{625}{1458}-\frac{25l}{27}\right)}{EI}\right)l$$

Appendix C
Python code in building the 2-D models

C.1. Introduction

This section explains the main features of the Python code used to create the 2-D models on the pre-fractal and tessellated space by applying the mathematical equations of TCM theory. Dealing with 2-D models as a Sierpinski Carpet by Python codes is found to be essential due to the complexity of the models studied. In this section, two Python codes are presented. The first is to build the pre-fractal models and the second is to build the tessellated models:

C.2. Programming languages

Python was first released in 1991 by Guido van Rossum [88]. Python is a high-level open-source[1] programming language. It is mainly used for Rapid Application Development and as an application extension language (glue language[2]). It also supports object-oriented programming (most programs work on the basis of logic; on the other hand, object-oriented programming is concentrated on the object that concerns the programmers rather than the logic) with classes.

One of the most interesting features in Python is that it has a polymorphic list [3] [89] beside its dictionary types; all this enables Python to have rich syntactic support, such that it adds up to a language that is considered straightforward for developing a prototype and other ad-hoc programming tasks[4], without undermining maintainability. Python is always compared to the interpreted

---

[1] Open-source language refers to a programming language that falls within the parameters of open-source protocol. This basically means that the language is not proprietary, and with certain provisions (depending on the open-source license), can be modified or built upon in a manner that is open to the public.

[2] Glue Language refers to a language that has been designed to write and manage programs and code that link two different software components. It does not add any functional value to the core software. Examples include VBScript, Ruby, Perl, and PHP besides Python.

[3] Polymorphic list: are the well-defined lists with the ability to use different variables of different types.

[4] Ad-hoc programming tasks: this a Latin phrase that means a programming tasks that is just relevant to a specific task with a special situation to solve a problem, as a systematic approach.

languages such as Java, JavaScript, Perl, Tcl, and Scheme [90-95]. A comparisons to C++, Common Lisp, and Ruby. For example, Python runs slower than JAVA, but its code is 3-5 times shorter than JAVA (a low-level implementation language) and 5-10 times shorter the C++ code. More favourably, it does not need to declare its variables or arguments type. Most of all, it does not need great efforts to track its code because it uses a rich syntax which is built directly into the code. For all the reasons mentioned, Python is better for use as a glue language compared to other programming languages.

Moreover, Python is designed to support common programming methodologies, such as data structure design and object-oriented programming. This would expedite the tasks to the programmer to correct errors or develop the code himself without destroying its maintainability [96]. Python is like the Tcl programming language in its availability as a glue programming language, but Python can be considered stronger on data structures and faster in executing codes. Finally, it can be run on different software very easily such as Mac OS X, Windows, Linux, and Unix.

C.3. Creating the pre-fractal models

Python is a user-friendly language that is straightforward to use; as well as easy error tracking due to the fact that the language is an object-oriented language and polymorphic (which refers to a well-defined list with the ability to use different variables of different types). Python was released in 1991 [88] (as mentioned in Chapter 2). It is considered a high-level programming language; open source; with limitless application. (Section 2.5 lists a more detailed comparison between the main programming languages and Python).

Sierpinski Carpet is indicated in Figures C-1,a to C-3,a for $k = 1:3$, with material properties shown in Table C-1. These structures are created by defining two main factors, the Sierpinski Carpet length and the level of complexity (k), where k is a value that indicates the increase in number of a pre-fractal complexity. In order

to handle the geometrical complexity of such behaviour, it found that the best way to carry out the work is using Python. Besides all the previously listed advantages, the main reason for using a programming language in this study is that implementing the Iteration Function System (IFS) in creating pre-fractal is easy to be handled by Python. In this section, Python code is developed to build pre-fractal models in ABAQUS through the following steps:

C.3.1. Generating the Coordinates

To create a pre-fractal geometry eight main contracting mapping equations [55] are listed in Appendix A Table A-1, which is used to generate the Sierpinski Carpet geometry. These equations are defined in Python in the form of functions as follows:

```
def S1x(x):return ((x/3.))
def S1y(y):return ((y/3.))
def S2x(x):return ((Length/3.)+(x/3.))
def S2y(y):return ((y/3.))
def S3x(x):return ((Length*(2./3.))+(x/3.))
def S3y(y):return ((y/3.))
def S4x(x):return ((x/3.))
def S4y(y):return ((Length/3.)+(y/3.))
def S5x(x):return ((Length*(2./3.))+(x/3.))
def S5y(y):return ((Length/3.)+(y/3.))
def S6x(x):return ((x/3.))
def S6y(y):return (((Length*(2./3.))+y/3.))
def S7x(x):return ((Length/3.)+(x/3.))
def S7y(y):return ((Length*(2./3.))+(y/3.))
def S8x(x):return ((Length*(2./3.))+(x/3.))
def S8y(y):return ((Length*(2./3.))+(y/3.))
```

(a) $\hat{E}_1$ (b) $\hat{T}_1$
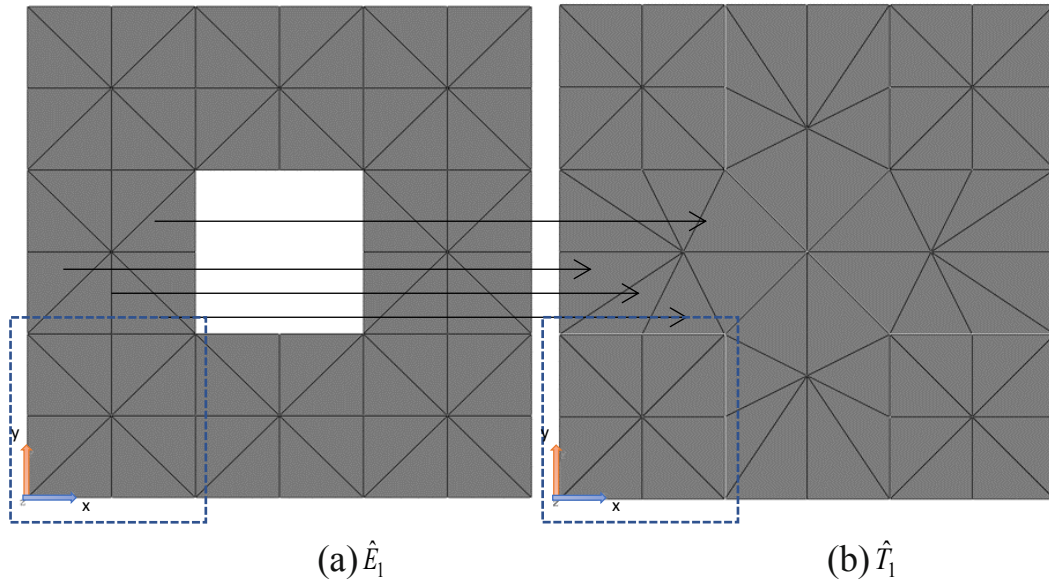
Figure C-1. Sierpinski Carpet case study of $k = 1$.

(a) $\hat{E}_2$ (b) $\hat{T}_2$
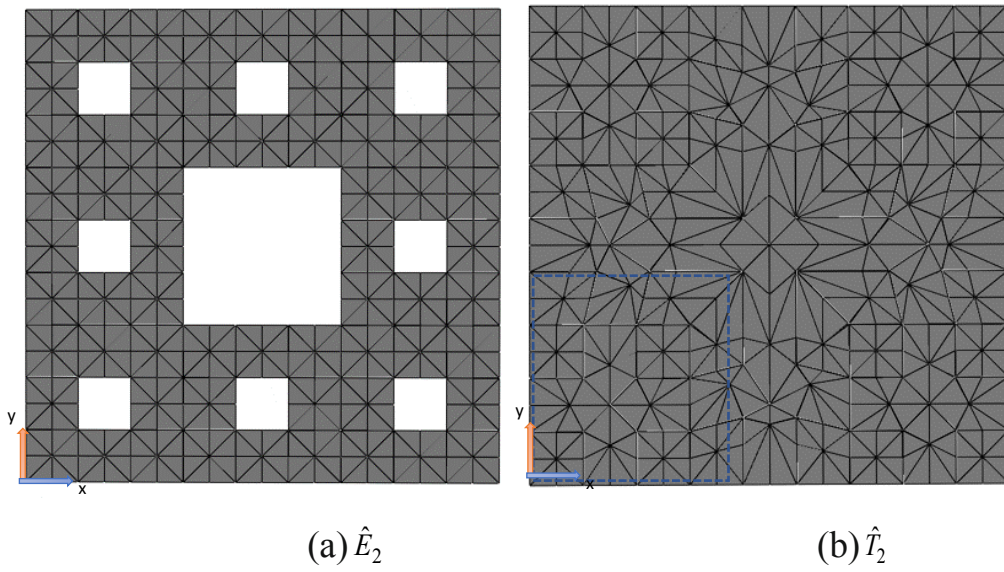
Figure C-2. Sierpinski Carpet case study of $k = 2$.

(a) $\hat{E}_3$ (b) $\hat{T}_3$
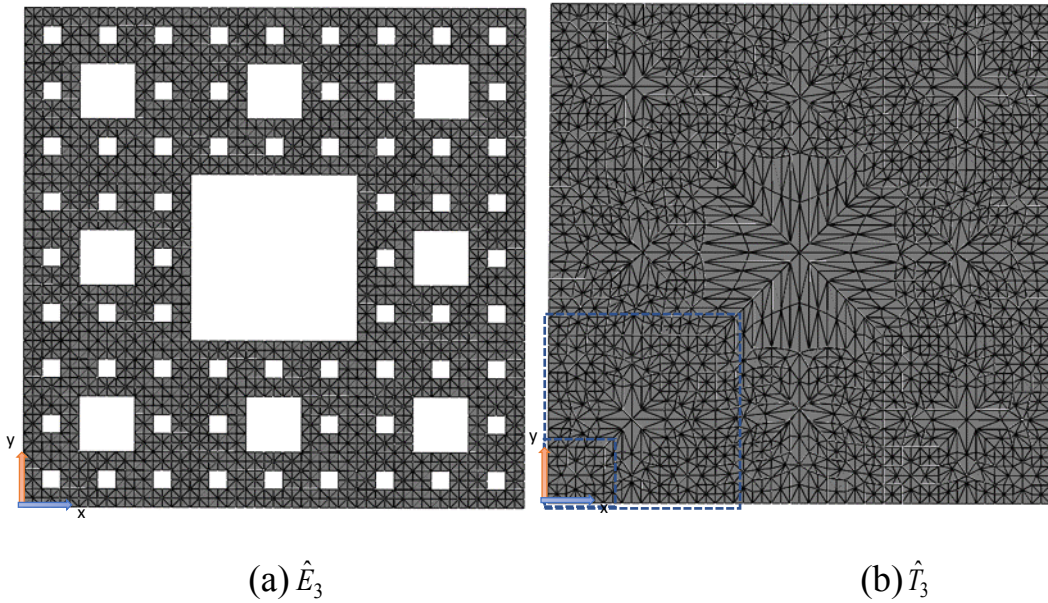
Figure C-3. Sierpinski Carpet case study of $k = 3$.

Table C-1. Material properties and dimensions for Sierpinski Carpet

Properties	Values
Length (m)	0.9
Width (m)	0.9
Thickness (m)	(0.001-0.1)
Density (kg/m^3)	2698.8
Elasticity (N/m^2)	68.9$\times 10^9$
Poisson's ratio	0.3

The coordinates of the main holes are recorded in matrix form, named as (E1x) and (E1y). These matrices list the hole edge coordinates and are used by the following codes:

```
i=1
for ii in range(8):
    E2x.append(list(map((globals()['S'+str(ii+1)+'x']),
      (globals()['E1x']))))
    E2y.append(list(map((globals()['S'+str(ii+1)+'y']),
```

```
                        (globals()['E1y']))))
            XX12=[]
            YY12=[]
            for ii in range (N+1-1):
              XX12.append(globals()['E'+str(ii)+'x'])
              YY12.append(globals()['E'+str(ii)+'y'])
            XX1=XX12+E2x
            YY1=YY12+E2y
```

The first two main lines call the function listed earlier, while the last two main lines group the newly generated coordinates in final matrices named as XX1 and YY1. These matrices list the coordinates of the holes. These lines can be repeated according to the level of complexity k. All these new matrices are added up to generate the new holes.

Creating the matrix in this form would ease its plotting by the sketching command in ABAQUS Python. (The full code is listed in Appendix D.)

C.3.2. Sketching the model

The Sierpinski Carpet is shown in Figure C.1. It is constructed by plotting a main square shell shape with dimensions of ($\ell_o \times \ell_o$), followed by plotting the other holes' square coordinates. Step one has provided the coordinates of the square holes in the form of five separated (x, y) coordinate groups. These coordinates beside the coordinates of the basic square of dimensions ($\ell_o / 3^k \times \ell_o / 3^k$) are calculated in matrix XX1 and YY1. These coordinates are plotted through employing the following lines of codes in Python:

```
mdb.models['Model-1'].ConstrainedSketch(name='__profile__',
sheetSize=2.0)
for e in range(len(XX1)):
        XX=XX1[e-1]
        YY=YY1[e-1]
        for q in range(len(XX)):
mdb.models['Model-1'].sketches['__profile__'].Line(point1=(XX[q-
1],YY[q-1]), point2=(XX[q],YY[q] ))
mdb.models['Model-1'].Part(dimensionality=THREE_D, name='Carpet-1',
type=DEFORMABLE_BODY)
```

```
mdb.models['Model-1'].parts['Carpet-
    1'].BaseShell(sketch=mdb.models['Model-1'].sketches['__profile__'])
```

These lines create all the 2-D shell base deformable structures. The command (mdb.models['Model-1'].sketches['__profile__'].Line(point1=(XX[q-1], YY[q-1]), point2=(XX[q],YY[q]))) plots the hole coordinates provided in Step 1. In this step, five straight lines are drawn to create each hole. Finally, the structure is created by a final line and the model name is set as "Carpet-1".

C.3.3. Assembly

In the pre-fractal structure, the code assembles one structure only; this is performed by the following code:

```
mdb.models['Model-1'].rootAssembly.DatumCsysByDefault CARTESIAN)
mdb.models['Model-1'].rootAssembly.Instance(dependent=ON,   name='Carpet-
1', part= mdb.models['Model-1'].parts['Carpet-1'])
```

C.3.4. Assign material properties

The material properties and cross-sectional area are assigned in this step. The material properties, in the form of elasticity and density units, are assigned to the required section directly through the computer-aided environment (CAE) window. Then, assigning the created section to the model "Carpet-1", (Check Appendix D).

C.3.5. Setting analysis steps

Any analysis steps are created directly in the computer-aided environment (CAE) in ABAQUS.

C.3.6. Meshing

The initial mesh on the pre-fractal structure is necessary because it is considered the initial step to create the tessellated geometry, as in Appendix E. Due to the discontinuity of the model, the partition function is needed to accomplish this task, where it is used directly in CAE in ABAQUS.

Further, the mesh code is listed below and can be run inside loops:

```
name='T'+str(BB_forw[ii])+'_'+str(iRow)+'_'+str(jCol)+'_'+str(i)+'_'+str(j)
 mdb.models['Model-1'].parts[name].deleteMesh()
mdb.models['Model-1'].parts[name].seedPart(deviationFactor=0.1,
minSizeFactor=0.1, size=0.1)
mdb.models['Model-1'].parts[name].generatemesh()
```

C.4. Tessellated models

The main reason behind using Python as a programming language is that it can implement the IFS to create pre-fractal geometries in a more comfortable and more compact way. The main focus of this work is to create a tessellated model which includes the geometry and calculate the equivalent material properties of these models. This is accomplished by executing nine steps to build a complete Python code that shapes any tessellated geometry, which is accomplished in this work throughout the following steps:

C.4.1. Creating the coordinates (Hole-filling map structure)

This is the most challenging part of the work; no one has ever previously come up with an approach to create such a structure (tessellated) using code. One of the critical elements of this approach is using the IFS, that is, creating the geometrical shape of the pre-fractal. Then, we vary the current geometry through using the hole-fill maps to fill the holes. In order to make the structure continuous, the hole-fill map is built through the following steps:

1- Mesh the structure into a triangular shape and list the coordinates.

2- Identify the centre coordinates.

3- Deform the meshed area around the holes, using hole-fill maps, which is mainly through the use of trigonometric equations.

4- After closing the holes, and applying the same boundary condition, it is also possible to use the discontinuity network DN on the closed holes.

5- Arrange the coordinates in order to input them into ABAQUS for the drawing section.

All these steps are mathematically developed in Chapter Three and implemented mainly in Python. All the listed steps are constructed in Python code for the pre-fractal:

1-   Calculating the pre-fractal coordinates (as mentioned in Section 2).

2-   After preparing the coordinates of the initial pre-fractal $\hat{E}_1$, this step is always followed by applying the hole-fill map to create the next model, which, in this case, is a $\hat{T}_1$. This model is a continuous structure, see Figure C-1 (b), that is created from Figure C-1 (a). Alternatively, this procedure can be described as deforming the triangular elements of the pre-fractal while keeping the elements' thickness the same. This is true for $\hat{E}_1$, but to create the next $\hat{T}_1$ as in Figure C-2 or for $\hat{T}_1$ as in Figure C-3, the structure must be mapped according to the same $\hat{E}_1$ mappings, while the next mapping step must be followed to fill the hole existing in the current $\hat{E}_1$ geometry, by following the block diagram plotted in Figure C-4. This is can be completed by identifying the holes' coordinates. On the other hand, it is important to mention that the basic mesh generated on the pre-fractal models, which is mapped to create the tessellated models, is named as the basic shape and illustrated in Figure C-5. Furthermore, this figure illustrates the initial mesh that was recommended in reference [54]. Also, this figure is represented in a matrix form as in Figure C-6

Figure C-6. For example, the coordinates of Figure C-6 belong to pre-fractal type $k = 1$. The hole centres are indicated by the centre of the shape which is ($\ell_o / 2, \ell_o / 2$).

For higher-order structures such as $k > 1$, the hole-fill maps are calculated through applying trigonometric equations, where it i essential to calculate the number of nodes in a direction normal to the hole's stretched edges. This depends on using the following equation to find the newly deformed

coordinates $Y_{new} = (Y_{old} - \delta \tan(\theta))/\alpha$. This equation can simply express the relationship between the new and the old coordinates (before and after applying the hole-fill maps), where Y_{new} are the new coordinates to be calculated; Y_{old} are the old coordinates (normally those representing the tessellated structure of $(k-1)$; δ is the half-length of the hole that needs to be covered; θ, is the angle between the old and new stretched edges (for Sierpinski Carpet, this is always 45^0); and finally, α is the number of elements that are going to be stretched to cover the hole.
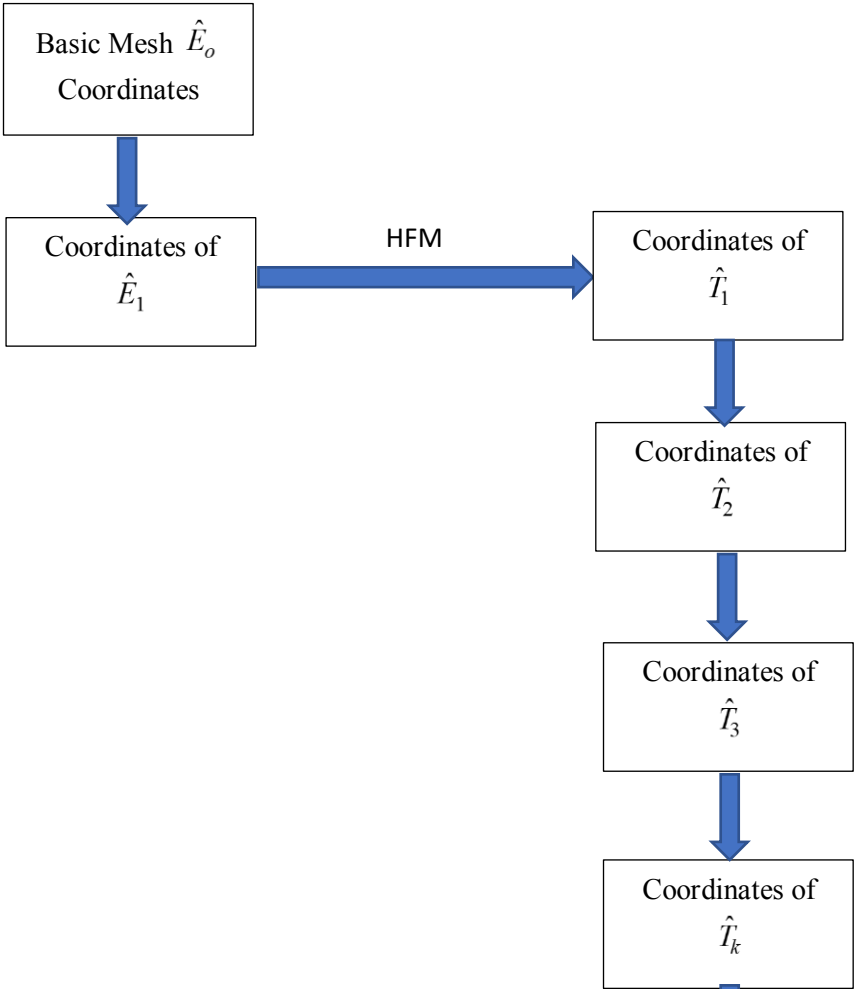
.

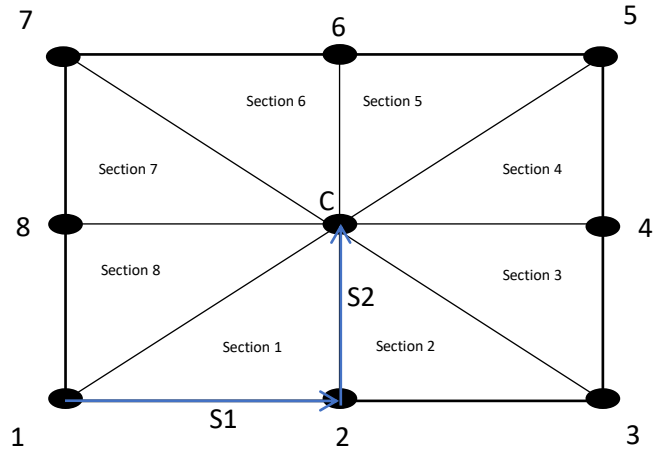Figure C-4. Block Diagram of how to create the coordinates matrix

Figure C-5. Basic mesh shape on any structure k

$$
MPx =
\begin{bmatrix}
\begin{bmatrix} 0 & \ell_0/6 & \ell_0/3 \\ 0 & \ell_0/6 & \ell_0/3 \\ 0 & \ell_0/6 & \ell_0/3 \end{bmatrix} &
\begin{bmatrix} \ell_0/3 & \ell_0/2 & 2\ell_0/3 \\ \ell_0/3 & \ell_0/2 & 2\ell_0/3 \\ \ell_0/3 & \ell_0/2 & 2\ell_0/3 \end{bmatrix} &
\begin{bmatrix} 2\ell_0/3 & 5\ell_0/6 & \ell_0 \\ 2\ell_0/3 & 5\ell_0/6 & \ell_0 \\ 2\ell_0/3 & 5\ell_0/6 & \ell_0 \end{bmatrix} \\[12pt]
\begin{bmatrix} 0 & \ell_0/6 & \ell_0/3 \\ 0 & 3\ell_0/12 & \ell_0/2 \\ 0 & \ell_0/6 & \ell_0/3 \end{bmatrix} &
\begin{bmatrix} 0 & 0 & 0 \\ 0 & 0 & 0 \\ 0 & 0 & 0 \end{bmatrix} &
\begin{bmatrix} 2\ell_0/3 & 5\ell_0/6 & \ell_0 \\ \ell_0/2 & 9\ell_0/12 & \ell_0 \\ 2\ell_0/3 & 5\ell_0/6 & \ell_0 \end{bmatrix} \\[12pt]
\begin{bmatrix} 0 & \ell_0/6 & \ell_0/3 \\ 0 & \ell_0/6 & \ell_0/3 \\ 0 & \ell_0/6 & \ell_0/3 \end{bmatrix} &
\begin{bmatrix} \ell_0/3 & \ell_0/2 & 2\ell_0/3 \\ \ell_0/3 & \ell_0/2 & 2\ell_0/3 \\ \ell_0/3 & \ell_0/2 & 2\ell_0/3 \end{bmatrix} &
\begin{bmatrix} 2\ell_0/3 & 5\ell_0/6 & \ell_0 \\ 2\ell_0/3 & 5\ell_0/6 & \ell_0 \\ 2\ell_0/3 & 5\ell_0/6 & \ell_0 \end{bmatrix}
\end{bmatrix}
\quad \dots (1)
$$

$$
MPy =
\begin{bmatrix}
\begin{bmatrix} 0 & 0 & 0 \\ \ell_0/6 & \ell_0/6 & \ell_0/6 \\ \ell_0/3 & \ell_0/3 & \ell_0/3 \end{bmatrix} &
\begin{bmatrix} 0 & 0 & 0 \\ \ell_0/6 & 3\ell_0/12 & \ell_0/6 \\ \ell_0/3 & \ell_0/3 & \ell_0/3 \end{bmatrix} &
\begin{bmatrix} 0 & 0 & 0 \\ \ell_0/6 & \ell_0/6 & \ell_0/6 \\ \ell_0/3 & \ell_0/3 & \ell_0/3 \end{bmatrix} \\[12pt]
\begin{bmatrix} \ell_0/3 & \ell_0/3 & \ell_0/3 \\ \ell_0/2 & \ell_0/2 & \ell_0/2 \\ 2\ell_0/3 & 2\ell_0/3 & 2\ell_0/3 \end{bmatrix} &
\begin{bmatrix} 0 & 0 & 0 \\ 0 & 0 & 0 \\ 0 & 0 & 0 \end{bmatrix} &
\begin{bmatrix} \ell_0/3 & \ell_0/3 & \ell_0/3 \\ \ell_0/2 & \ell_0/2 & \ell_0/2 \\ 2\ell_0/3 & 2\ell_0/3 & 2\ell_0/3 \end{bmatrix} \\[12pt]
\begin{bmatrix} 2\ell_0/3 & 2\ell_0/3 & 2\ell_0/3 \\ 5\ell_0/6 & 5\ell_0/6 & 5\ell_0/6 \\ \ell_0 & \ell_0 & \ell_0 \end{bmatrix} &
\begin{bmatrix} 2\ell_0/3 & \ell_0/2 & 2\ell_0/3 \\ 5\ell_0/6 & 9\ell_0/12 & 5\ell_0/6 \\ \ell_0 & \ell_0 & \ell_0 \end{bmatrix} &
\begin{bmatrix} 2\ell_0/3 & 2\ell_0/3 & 2\ell_0/3 \\ 5\ell_0/6 & 5\ell_0/6 & 5\ell_0/6 \\ \ell_0 & \ell_0 & \ell_0 \end{bmatrix}
\end{bmatrix}
\quad \dots (2)
$$

Figure C-6. Tessellated coordinates after applying the hole-fill map

Now, the explanation above can be repe]ated in code language. So, to create pre-fractal coordinates base on the initial mesh presented in Figure C-5, a defined function in Python can be used. The function name is (PSCoordinatedMatrixGeneratr). The brief code of the function is illustrated below, see Figure C-7:

```
def PSCoordinatedMatrixGeneratr(Lengthx,Lengthy,N):
    # N==1
    lsx=Lengthx/(3.)**N
    lsy=Lengthy/(3.)**N
MP1x0=np.array([[0.0,lsx/2.,lsx],[0.0,lsx/2.,lsx],[0.0,lsx/2.,lsx]])
#MT1[i,j]=[(((lsx*i)for i in range(3))*(3*j) for j  in range(3))]
    MP1y0=np.array([[0.0]*3,[lsx/2.0]*3,[lsx]*3])
MPx=[[MP1x0,MP1x0+lsx,MP1x0+(lsx*2)],[MP1x0,np.zeros((3,3)),MP1x
0+(lsx*2)],[MP1x0,MP1x0+lsx,MP1x0+(lsx*2)]]
MPy=[[MP1y0,MP1y0,MP1y0],[MP1y0+(lsy),np.zeros((3,3)),MP1y0+(lsy)
],[MP1y0+(2*lsy),MP1y0+(2*lsy),MP1y0+(2*lsy)]]
    MPx1=np.array(MPx)
    MPy1=MPy
return(MPx,MPy)
```
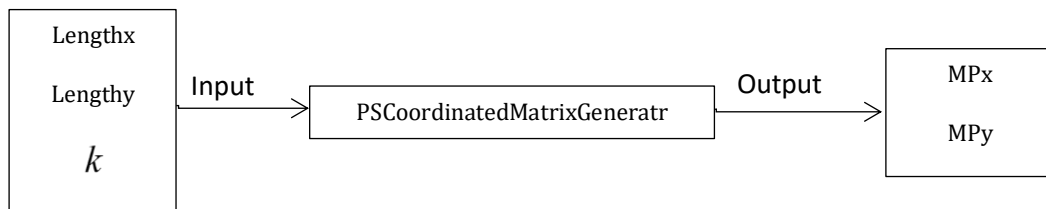

Figure C-7. Block diagram explaining the use of the
PSCoordinatedMatrixGeneratr function

where k is the pre-fractal level of complexity; Lengthx and Lengthy are the dimensions of the basic shape that are created on the pre-fractal structure (see Figure C-1).

Figure C-7 shows the inputs and the outputs of the Function being discussed. By way of further explanation, this function creates the matrices MPx and MPy. These matrices are of 3*3*3*3 dimension. For example, the coordinates in the shape of (x, y) for the $\hat{E}_1$ in a matrix form are presented in Figure C-6.

Figure C-1 can be built through calculating the coordinates of the pre-fractal structure using the following automatic code; this code can work for any value of k:

```
#1-Basic Shape
BB_inv=[(N-i)for i in range(N)]
BB_forw=[(i+1)for i in range(N)]
if N==1:
    lsx=Lengthx
    lsy=Lengthy
    fg=PSCoordinatedMatrixGeneratr(lsx,lsy,BB_forw[i])
    MPSx=fg[0]
    MPSy=fg[1]
else:
    i=0
    lsx=(Lengthx/(3.**(BB_forw[i])))
    lsy=(Lengthy/(3.**(BB_forw[i])))
    fg=PSCoordinatedMatrixGeneratr(lsx,lsy,BB_inv[i])
    MPSx=fg[0]
    MPSy=fg[1]
```

On the other hand, to create the tessellated structure basically uses the initial coordinates on the pre-fractal (provided from function PSCoordinatedMatrixGeneratr). For a better illustration of using the hole-fill maps, see Figure C-8. This diagram shows the steps to create a tessellated structure for $k = 2$, which is represented by the dashed green lines in Figure C-6. This is managed by following the next chart:

```
┌─────────────────────────────────────────┐
│      Measuring the WI at each Columns     │
└─────────────────────────────────────────┘
                    │
                    ▼
┌─────────────────────────────────────────┐
│      Changing the (3*3*3*3) Matrix into   │
│                   (9*9)                   │
└─────────────────────────────────────────┘
                    │
                    ▼
┌─────────────────────────────────────────┐
│        Distinguishing the sides of Matrix │
│             according to columns:         │
│                                           │
│        Jo=1,-1, theta=theta1, theta2      │
└─────────────────────────────────────────┘
                    │
                    ▼
┌─────────────────────────────────────────┐
│    Distinguishing the rows will determine │
│     percentage of extension at each point │
└─────────────────────────────────────────┘
                    │
                    ▼
┌─────────────────────────────────────────┐
│       Implementing the HFM at the Holes   │
│                   centres                 │
└─────────────────────────────────────────┘
                    │
                    ▼
┌─────────────────────────────────────────┐
│     Applying a rotation function to create│
│             the other matrix diagonal     │
└─────────────────────────────────────────┘
                    │
                    ▼
┌─────────────────────────────────────────┐
│    Rearranging the Matrix into sets of (3*3)│
└─────────────────────────────────────────┘
                    │
                    ▼
┌─────────────────────────────────────────┐
│        Adding Up the Whole New Matrix     │
└─────────────────────────────────────────┘
```
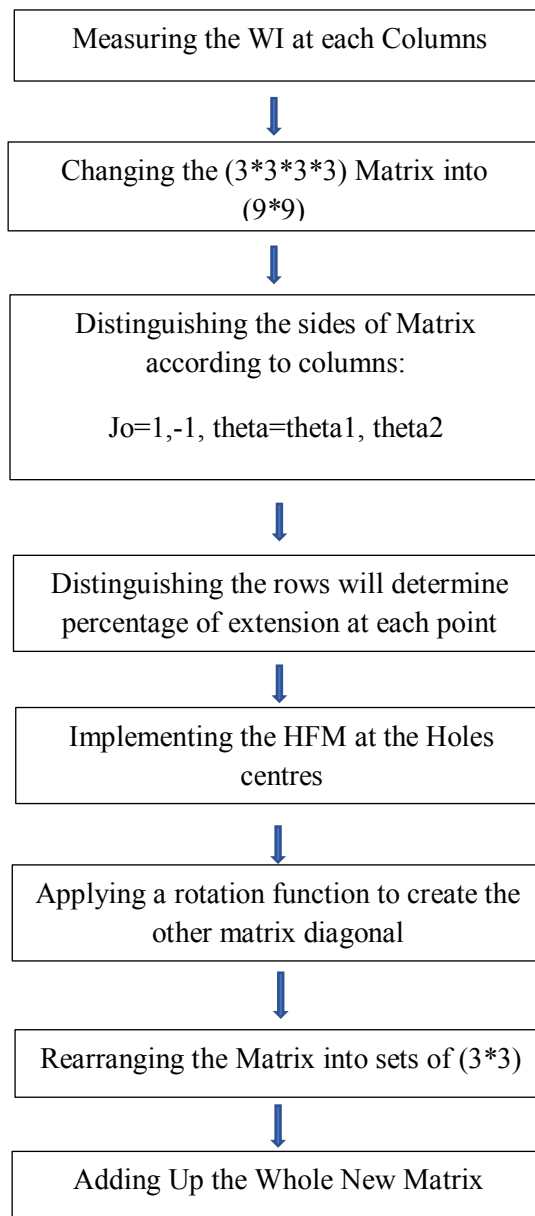
Figure C-8. Block diagram representing the steps of applying the hole-filling maps method

where WI is the length of holes at each section.

At this stage, the coordinates of the pre-fractal are obtained in the form of two matrices named as (MPSx, MPSy), using the steps established in Figure C-8 in relation to how to use the hole-fill maps techniques to obtain the tessellated coordinates named by (MTx, MTy). Again, the minimum lengths of the basic mesh are (lsx, lsy), and the original Sierpinski Carpet model lengths are

218

(Lengthx, Lengthy); finally, the level of complexity is k. This function is represented in Figure C-9:
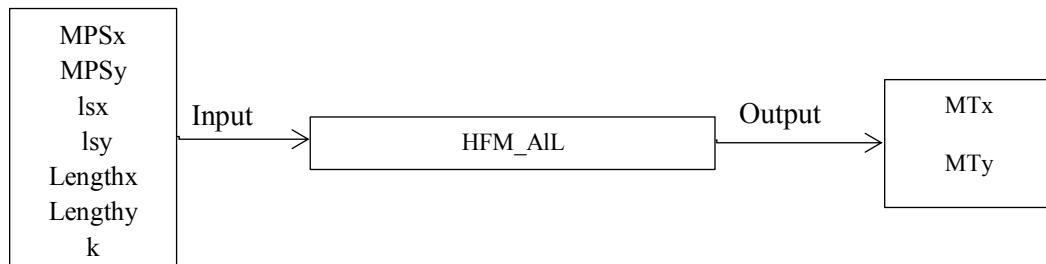

Figure C-9. Block diagram explaining the use of the HFM_AlL function

C.4.2. Sketching the models

This section concerns plotting the model; defining the element types and dimensions; and setting the parts' names. In order to do this, the coordinates of the generated tessellated structure should be changed into vectors. "MattoVect" is the function that is used to rearrange the coordinates correspondingly (Figure C-10). This is important in order to draw eight straight lines to create the small parts that will compose the whole structure. This is shown clearly in the function block diagram and the following code:

Figure C-10. Block diagram explaining the use of the MattoVect function where M_T_x and M_T_y are the tessellated coordinates of matrix (3×3) after they have been changed into matrices of vectors, for example, the matrix in Figure C-6 Figure C-6/ Equation (1), the MT1x[0][0] would become as M_T_x[0][0]=[0,0.15,0.3,0.3,0.3,0.15,0,0,0] while M_T_y[0][0] =[0,0,0,0.15,0.3,0.3,0.3,0.15,0]. Finally, by using the following command inside loops depending on the level of complexities, the structure can be plotted:

219

```
ii=0
Ni=1
MT1x=MTx
MT1y=MTy
for i in range(3):
    for j in range(3):
        if i==1 and j==1:
            pass
        else:
            XX=M_T_x[i][j]
    YY=M_T_y[i][j]
            M_T_x_c[i][j]
            M_T_y_c[i][j]
            #To build the Outer diameter
            w=j
            mdb.models['Model-
1'].ConstrainedSketch(name='__profile__', sheetSize=(Lengthx*2.0))
                for q in range(len(XX)):
                    mdb.models['Model-
1'].sketches['__profile__'].Line(point1=(XX[q-1],YY[q-1]),
point2=(XX[q],YY[q] ))
            Name='T'+str(BB_forw[ii])+'_'+str(i)+'_'+str(j)
            mdb.models['Model-1'].Part(dimensionality=THREE_D,
name= Name, type=DEFORMABLE_BODY)
            mdb.models['Model-
1'].parts[Name].BaseShell(sketch=mdb.models['Model-
1'].sketches['__profile__'])
            mdb.models['Model-
1'].rootAssembly.DatumCsysByDefault(CARTESIAN)
            mdb.models['Model-
1'].rootAssembly.Instance(dependent=ON, name=Name,
part=mdb.models['Model-1'].parts[Name])
```

C.4.3. Partitioning

This part is vital to create the initial mesh on each segment of the tessellated structure. Due to the hole-fill maps, each part in the diagonal needs to be stretched differently from every other. The partitioning creates the eight parts on each tessellated tail, where these parts will have different material properties. ABAQUS needs Parts Names, Parts Centres, Right Edge Datum and surroundings points to sketch the geometry.

For example, to create a part name matrix, the following line must be inside loops which depend on the number of complexities:

Name='T2'_'+str(iRow)+'_'+str(jCol)+'_'+str(i)+'_'+str(j)

where iRow, jCol, i , and j are indices referring to the loops used. The datum point at each part to partition the structure is created by selecting points on the right-hand side of each part via the following lines:

```
mdb.models['Model-1'].parts[Name].DatumPointByCoordinate(coords=
(M_T_x[iRow][jCol][i][j][2], M_T_y[iRow][jCol][i][j][2], 0.0))
mdb.models['Model-1'].parts[Name].DatumPointByCoordinate(coords=
(M_T_x[iRow][jCol][i][j][2],M_T_y[iRow][jCol][i][j][4], 0.0))
mdb.models['Model-1'].parts[Name].DatumAxisByTwoPoint(point1
=mdb.models['Model-          1'].parts[Name].datums[2],point2=mdb.models
['Model-1'] .parts[Name] . datums[3])
```

After selecting the part name, by picking the centre of each part and creating the datum, sketching a sequence of lines to create the partitioning is completed through the following lines of code:

```
mdb.models['Model-1'].parts[Name].projectReferencesOntoSketch
  (filter=COPLANAR_EDGES, sketch=mdb.models['Model-1'] .
   sketches['__profile__'])
for q in range(len(M_T_x[iRow][jCol][i][j])):
        mdb.models['Model-1'].sketches['__profile__'].Line(point1=
        (M_T_x[iRow][jCol][i][j][q-1], M_T_y[iRow][jCol][i][j][q-1]),
        point2= (M_T_x_c[iRow][jCol][i][j],
        M_T_y_c[iRow][jCol][i][j]))
```

C.4.4. Calculating F_function "F"

This is the most important part that forces the researcher to use Python in order to create the structure and use the TCM theory to implement the mathematical formulas directly to find the scaled material properties and other factors.

In this section, the link between the physical part and the hypothetical one is created by using the theory illustrated in Chapter 3.

Preparing the coordinates for the initial mesh on the pre-fractal structure is essential. This is completed by using the previous code of

(PSCoordinatedMatrixGeneratr). The pre-fractal coordinate is created by using the contraction and shifting methods, while the Tessellated coordinated created by applying the hole-fill map on its pre-fractal model as mentioned earlier.

The main links between both spaces are by the F_Function, which is a second-order tensor that is used to scale the discrete parts of the pre-fractal structure linearly into the continuous model of the tessellated. This is completed by finding the following matrix:

$$F = \begin{bmatrix} F_{11} & F_{12} & F_{13} \\ F_{21} & F_{22} & F_{23} \\ F_{31} & F_{32} & F_{33} \end{bmatrix}$$

(C-1)

For the current study, the structure is scaled in two dimensions. This means F_{13}, F_{23}, F_{31} and $F_{32} = 0$. For this reason, the F_Function equation is reduced to the following configurations:

$$\begin{bmatrix} \alpha_{xts,1} \\ \beta_{yts,1} \\ \alpha_{xts,2} \\ \beta_{yts,2} \end{bmatrix} = \begin{bmatrix} \alpha_{xps,1} & \beta_{yps,1} & 0 & 0 \\ 0 & 0 & \alpha_{xps,1} & \beta_{yps,1} \\ \alpha_{xps,2} & \beta_{yps,2} & 0 & 0 \\ 0 & 0 & \alpha_{xps,2} & \beta_{yps,2} \end{bmatrix} \begin{bmatrix} F_{11} \\ F_{12} \\ F_{21} \\ F_{22} \end{bmatrix}$$

(C-2)

where $\alpha_{xps,1}$ is the x-axial coordinates for the pre-fractal structure for the basic shape of mesh from Figure C-5. $\beta_{yts,1}$ is the y-axial coordinates for the tessellated structure for the basic shape of mesh from Figure C-5. $F_{11} - F_{22}$ are the linear scaling functions.

The equation above in effect calculates the changes in the length differences between two shapes, as in Figure C-5. This is represented by the triangular edges S1 and S2 in the same Figure. The only constraint is the order in which a side is chosen to relate to the other space where the same rules must be preserved. Other than this, any side of any of the triangular segments that form the basic shape can be chosen.

The flowcharts in Figure C-11 explain the translation by two matrices. The first is describing the x-axis and the second one defines the y-axis coordinates in the following form for $\hat{E}_1$:

For illustration, the coordinates of the structure basic mesh area represented in Figure C-1 is presented in Equation (C-3).

$$(x, y) = \left(\begin{bmatrix} 0 & \ell_0/6 & \ell_0/3 \\ 0 & \ell_0/6 & \ell_0/3 \\ 0 & \ell_0/6 & \ell_0/3 \end{bmatrix}, \begin{bmatrix} 0 & 0 & 0 \\ \ell_0/6 & \ell_0/6 & \ell_0/6 \\ \ell_0/3 & \ell_0/3 & \ell_0/3 \end{bmatrix} \right) \qquad \text{(C-3)}$$

This Equation forms a matrix of order 3×3, which must be changed into vector x_Vector$^\times$ y_Vector, which are 9×9 elements, by using the following symbolic code:

```
x_Vector=[x[0][0], x[0][1], x[0][2],
x[1][2],x[2][2],x[2][1],x[2][0],x[1][0],x[0][0]]
y_Vector=[y[0][0], y[0][1], y[0][2], y[1][2], y[2][2], y[2][1], y[2][0],
y[1][0], y[0][0]]
cx_Center=[x[1][1]]
cy_Center=[y[1][1]]
```
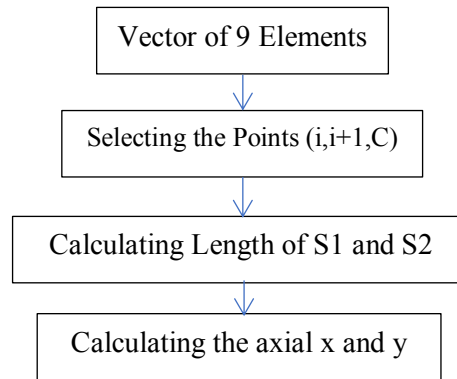

Figure C-11. Block diagram explaining the use of the FFunctionAny function

This code can be used inside a loop; see the main code in Appendix D to see how to make the code automatic through selecting the right order of the meshed triangular points to find the axial length of each triangular side. This is achieved by the following lines:

```python
Dis1=((Point20_x-Point10_x)**2+(Point20_y-Point10_y)**2)**0.5
        Dis2=((Point30_x-Point20_x)**2+(Point30_y-Point20_y) **2)
          **0.5
        x_Comp1=(Point20_x-Point10_x)
        y_Comp1=(Point20_y-Point10_y)
        th1=TheetaCalculation(x_Comp1,y_Comp1)
        Alfax1_0=Dis1*(math.cos((th1)))
        Betay1_0=Dis1*(math.sin((th1)))
def TheetaCalculation (x,y):
    x_Comp=x
    y_Comp=y
    if (y_Comp==0.)or(x_Comp==0.):
                #Finding Theeta on the normal plans
        if (y_Comp==0.) and (x_Comp==0.):
            th_Deg=0.0
        elif (y_Comp==0.) and (x_Comp>0.):
            th_Deg=0.0
        elif (y_Comp>0.) and (x_Comp==0.):
            th_Deg=90.
        elif (y_Comp==0.) and (x_Comp<0.):
            th_Deg=180.
        elif (y_Comp<0.) and (x_Comp==0.):
            th_Deg=270.
        th_Rad_New=math.radians(th_Deg)
    else:
                #Correcting theeta on the any quarters
        th_Deg=math.degrees(math.atan(y_Comp/x_Comp))
        if (y_Comp>0) and (x_Comp>0):
            th_Deg_New=th_Deg
        elif (y_Comp>0) and (x_Comp<0):
            th_Deg_New=180.0+th_Deg
        elif (y_Comp<0) and (x_Comp<0):
            th_Deg_New=th_Deg+180.
        elif (y_Comp<0) and (x_Comp>0):
            th_Deg_New=th_Deg+360.
        th_Rad_New=math.radians(th_Deg_New)
    return(th_Rad_New)
```

Finally, we use Equation (C-5) in the function FFunctionAll2. The following lines show how to use both functions to create the F_Function or the hole-fill maps:

```
F_BSAll=[]
 F1=[]#For Test Only for T1 Here
 for iRow in [0,1,2]:
    for iCol in [0,1,2]:
        if iRow==1 and iCol==1:
    pass
        else:
        F_BS=FFunctionAny(MPSx[iRow][iCol],MPSy[iRow][iCol])
        F_Str=FFunctionAny(MT1x[iRow][iCol],MT1y[iRow][iCol])
        F0=FFunctionAll2(F_BS,F_Str)
        F1.append(F0)
```

The previous lines of the code call the two main defined F-functions, which
are: FFunctionAny and FFunctionAll2.

The first function is used to find the normal component for shapes (meshes)
in each space as can be seen in Figure C-12. The last function performs two
main purposes. The first purpose is to arrange and apply Equation
(C-3). This is illustrated in Figure C-13.
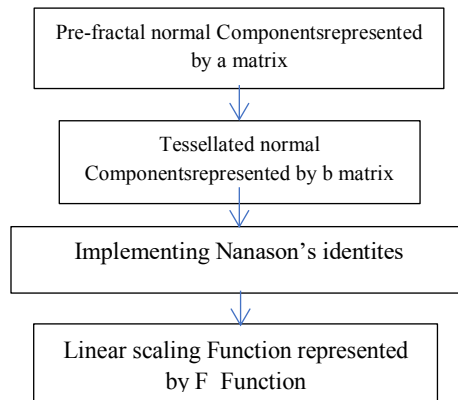
Figure C-12. Block diagram explaining the use of the FFunctionAll2
function.

Figure C-13. Block diagram explaining the use of the
PSCoordinatedMatrixGeneratr function.

225

C.4.5. Assigning the material properties

This section requires dealing with calculating the material properties and thickness mathematically, while the second section is concerned with preparing and setting the material name with its coordinates. This is illustrated by the following block diagram in Figure C-14.
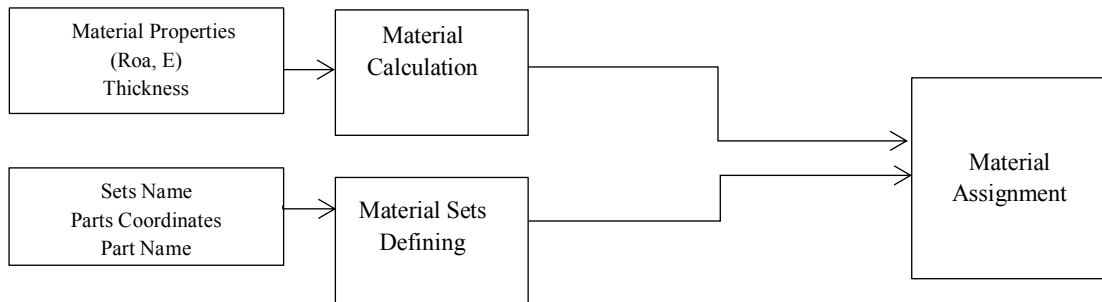
Figure C-14. Block diagram explaining the main material assigning function.

The scaling equations that are derived in the previous chapter, such as Equations (5.10), (5.34), and (4.25) are implemented here to automate the procedure to find the density and material elasticity properties from the material properties of the pre-fractal structure, see Figure C-15:
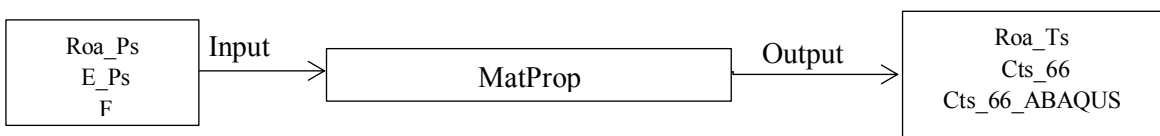
Figure C-15. Block diagram explaining the use of the MatProp function.

where Roa-Ps is pre-fractal density; E-Ps is the elasticity of the pre-fractal. On the other hand, the function outputs are Roa_Ts and Cts_66, which are the density and the $[3 \times 3]$ Elasticity anisotropic matrix that describe the tessellated structure. Finally, Cts_66_ABAQUS are the elasticity matrices that can be used as input for ABAQUS directly where only the 21 values are needed, see the following Figure:

$$\begin{Bmatrix} \sigma_{11} \\ \sigma_{22} \\ \sigma_{33} \\ \sigma_{12} \\ \sigma_{13} \\ \sigma_{23} \end{Bmatrix} = \begin{bmatrix} D_{1111} & D_{1122} & D_{1133} & D_{1112} & D_{1113} & D_{1123} \\ & D_{2222} & D_{2233} & D_{2212} & D_{2213} & D_{2223} \\ & & D_{3333} & D_{3312} & D_{3313} & D_{3323} \\ & & & D_{1212} & D_{1213} & D_{1223} \\ & sym & & & D_{1313} & D_{1323} \\ & & & & & D_{2323} \end{bmatrix} \begin{Bmatrix} \varepsilon_{11} \\ \varepsilon_{22} \\ \varepsilon_{33} \\ \gamma_{12} \\ \gamma_{13} \\ \gamma_{23} \end{Bmatrix} = [D^{el}] \begin{Bmatrix} \varepsilon_{11} \\ \varepsilon_{22} \\ \varepsilon_{33} \\ \gamma_{12} \\ \gamma_{13} \\ \gamma_{23} \end{Bmatrix}.$$

Figure C-16. Elasticity matrix as it been defined in ABAQUS manual [72]

The second section requires the tessellated matrix of form $[3 \times 3 \times 3 \times 3]$, exactly as for the coordinates of the tessellated structure of complexity $k = 1$. This section also provides the user with the possibility of changing the tessellation thickness, where th_Ps is the thickness of the pre-fractal structure, by using tessellated theory geometry mapping. However, for the present time, the thickness is kept the same to maintain the continuity of the structure. The second section also prepares the centre coordinates of the triangular shapes of the meshed parts on the tessellated space; this is represented by Traingul10_Center_x and Traingul10_Center_x matrices. This is accomplished by using the area function, which is illustrated in Figure C-17:
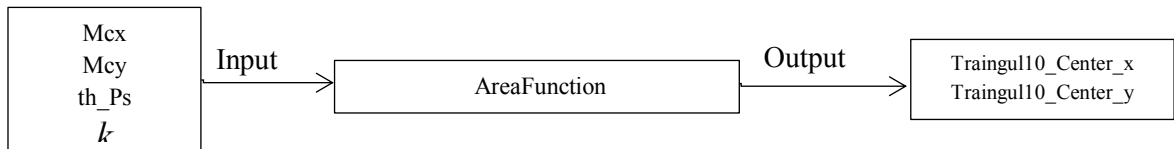

Figure C-17. Block diagram explaining the use of the area function.

The code in Figure C-17 is presented by the following lines:

g=AreaFunction(MTx,MTy,th_Ps,k)

th_Ts=g[2]

Traingul10_Center_x=g[3]

Traingul10_Center_y=g[4]

Then this is followed by defining the sets naming and assigned it to the correct coordinates by the following codes

```
For ii in range (3):
    For iRow in range (3):
        For jCol in range (3):
Name='T'+str(BB_forw[ii])+'_'+str(iRow)+'_'+str(jCol)
Mat_Name.append(Name)
mdb.models['Model-1'].parts[Name_All[ielemnet]].Set(faces=
mdb.models['Model-
1'].parts[Name_All[ielemnet]].faces.findAt((((np.float64(Traingul10_Center_
x[ielemnet][q]), np.float64(Traingul10_Center_y[ielemnet][q]), 0.0), )),
name='Set-'+str(q))
mdb.models['Model-
1'].parts[Name_All[ielemnet]].SectionAssignment(offset=0.0,  offsetField='',
offsetType=MIDDLE_SURFACE,                region=mdb.models['Model-
1'].parts[Name_All[ielemnet]].sets['Set-'+str(q)],
sectionName='Sec_'+Mat_Name
[ielemnet][q],thicknessAssignment=FROM_SECTION)
```

At this point the material assigning can be used by:

```
mdb.models['Model-1'].Material(name='Mat_'+Mat_Name[ielemnet][q])
```

```
mdb.models['Model-1'].materials['Mat_'+Mat_Name[ielemnet][q]].
Density(table= ((Roa_Ts[ielemnet][q], ), ))
```

```
mdb.models['Model-1'].materials['Mat_'+Mat_Name[ielemnet][q]].
Elastic(table=(Cts_66_ABAQUS [ielemnet][q], ), type=ANISOTROPIC)
```

```
mdb.models['Model-1'].HomogeneousShellSection(idealization=
NO_IDEALIZATION, integrationRule=SIMPSON, material='Mat_'+Mat_
Name[ielemnet][q], name='Sec_'+Mat_Name[ielemnet][q], numIntPts=5,
poissonDefinition=DEFAULT,         preIntegrate=OFF,         temperature=
GRADIENT,   thickness=   np.float64   (th_Ts[q]),   thicknessField='',
thicknessModulus=None, thicknessType=UNIFORM, useDensity=OFF)
```

C.4.6. Tying interaction

For tying, the user needs to provide 2 types of surface (Master and Slave). This can be done by providing the part names and their corresponding coordinates. Moreover, since this work requires many of tying commands, the author found that the structure can be tied through following anti clock-wise

procedure to tie the structure (see Figure C-18). The following Figure shows the master surfaces and the slave denoted by the blue line and the red lines respectively. Starting from parts 0 (P0) through to 7 (P7), this procedure is found to be the most straightforward and easiest to use inside automatic loops, see Figure C-19:
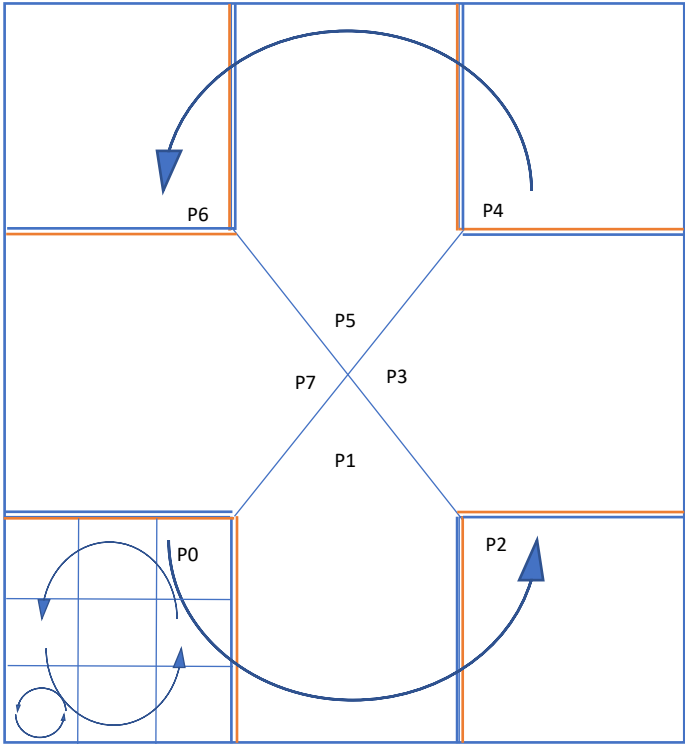

Figure C-18. Symbolic sketch showing the directions of assigning the tying function in ABAQUS
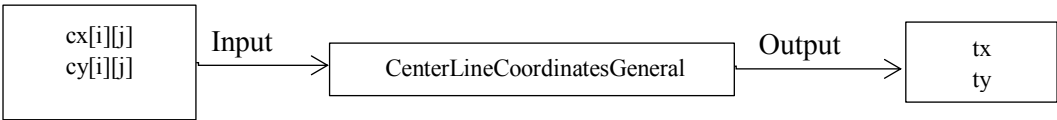

Figure C-19. Block diagram explaining the use of the CenterLineCoordinatesGeneral function

where cx[i][j] are the coordinate matrix and tx, ty are the edges coordinates to be tied.

C.4.7. Meshing

By reaching this step, the coordinates of the tessellated structure as an x-axis matrix and y-axis matrix are completed. At this step, the tessellated structure is created easily by running two programs, where the main program holds the main equations. The second parts encompass all the functions used to carry out the work.

Remarks:

One of the issues with tying, especially, when using the "find" function to find a surface, is that it is found to have an exact value of the coordinates with accuracy of 1×10^{-6}. This case has failed with higher tessellated complexity. For this reason, the code needed to be updated. In order to use the code to create higher tessellated geometry, different methods (such as the Boolean, get Box Function command in ABAQUS) must be used. This problem arose when $k=3$, but for the present, it is fixed manually.

Appendix D
2-D Pre-fractal analysis as Structures

D.1 Vicsek fractal models

The Vicsek fractal has many names, such as the Vicesk snowflake or the Vicsek or box fractal. It is suggested by Tamas Vicsek. It is in the shape of 5 squares linked by each other as shown in Figure D-1. And similar to the Sierpinski Carpet, the structure is created by 5 different maps see Appendix A Table (A-3 and A-4). Figure D-1 shows different pre-fractal structures of Vicsek fractal type. Vicsek is an interesting geometry that can be used in multi-engineering applications. For example, it can be used as antennas and in heat exchange configuration. Although this work is concentrated on studying perforated structure, but studying the Vicsek fractal can form a challenge to the TCM theory. For these reasons, it is essential to understand, its dynamical characteristic. This is possible by using commercial FE software. A mesh study is implemented to find the best shell element type that is going to represent the models with the minimum number of elements in order to minimise the analysis size and reduce the time cost. Moreover, the dynamical characteristic of the fractal structure is investigated by running a frequency analysis. This is accomplished by the following sections:

D.1.1. Element and mesh study sensitivity

The first five natural frequencies are selected to test the best element types that needs the minimum number of elements. This analysis is run on different pre-fractal structures like k=1, 2 and 3 as in Figures D-1, while the material properties are listed in Table D-1. The best element type for $k=1$ is a shell element type STRI65 with a minimum element size of 0.075 per unit length [72] and the reuslts did not included there. The rest four tested cases (S3, S3R, STRI3, and STRI65) of the pre-fractal models type k=2 and 3 are listed in Figure D-3 -D-10. In similar way a pre-fractal of type $k=2$ is sufficicantly represented by a shell element of

type STRI65 with minimum element length of 0.0225 (see Figure D-3). Finally, the last Vicsek pre-fractal of the third complexity is illustrated in Figure D-10, with element length 0.03 for the Element type STRI65 are 0.03.
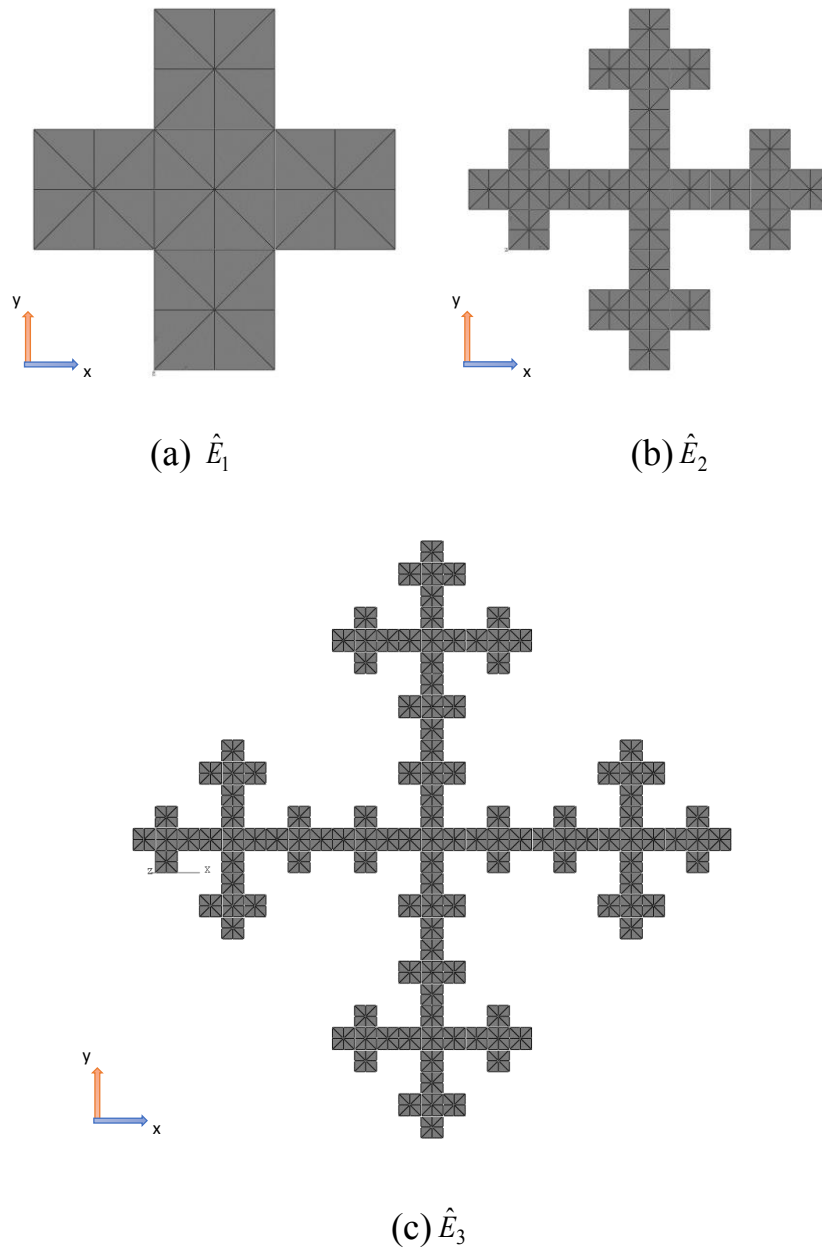

(a) $\hat{E}_1$ (b) $\hat{E}_2$

(c) $\hat{E}_3$

Figure D-1. Vicsek fractal for three different geometries k

Table D-1. Material properties and the dimensions for Vicsek fractal

Properties	Values
Length (m)	$0.9 \times k$
Width (m)	$0.9 \times k$
Thickness (m)	0.01
Density (kg/m^3)	2698.8
Elasticity (N/m^2)	68.9×10^9
Poisson's ratio	0.3
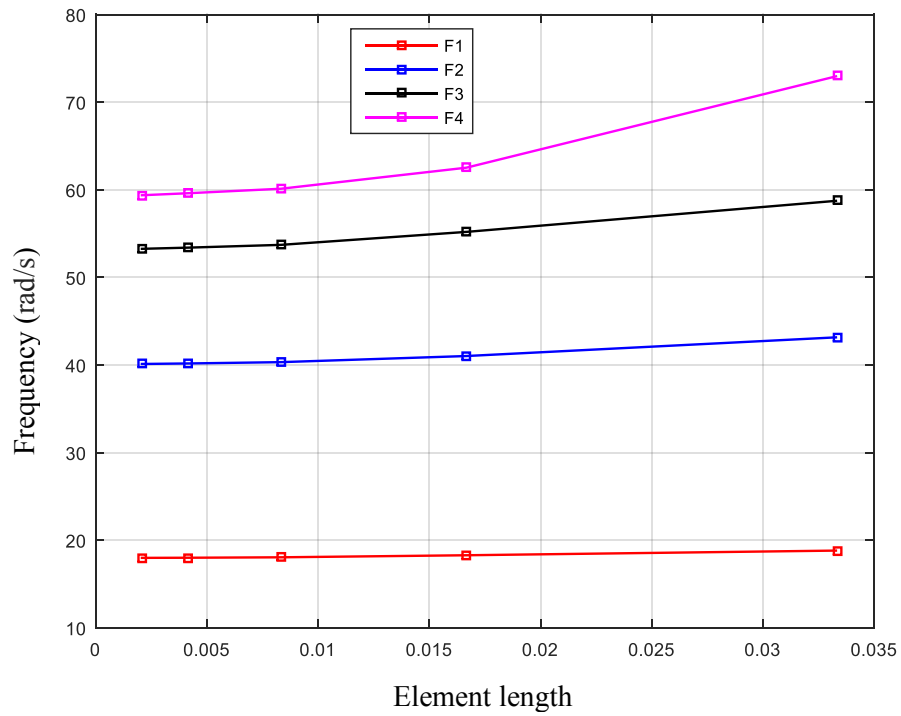
Figure D-3. Meshes sizes study for ps geometry $\hat{E}_2$ using element type S3
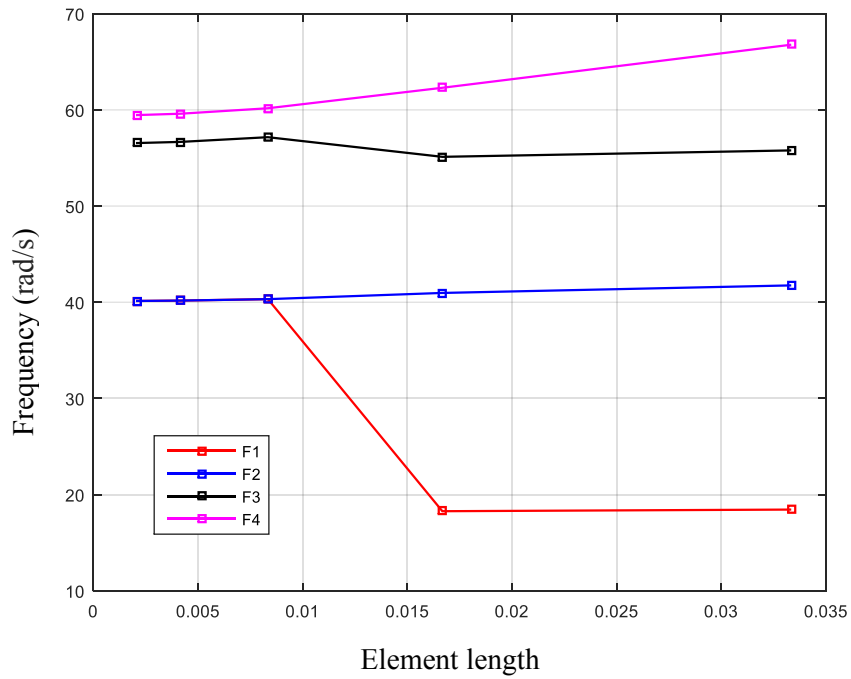
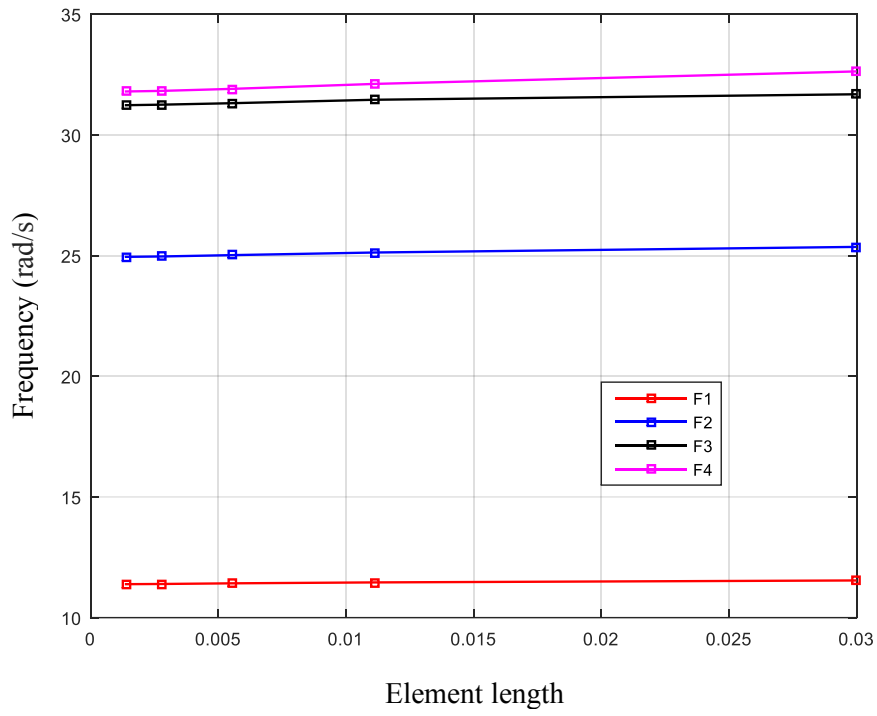Figure D-4. Meshes sizes study for ps geometry $\hat{E}_2$ using element type S3R
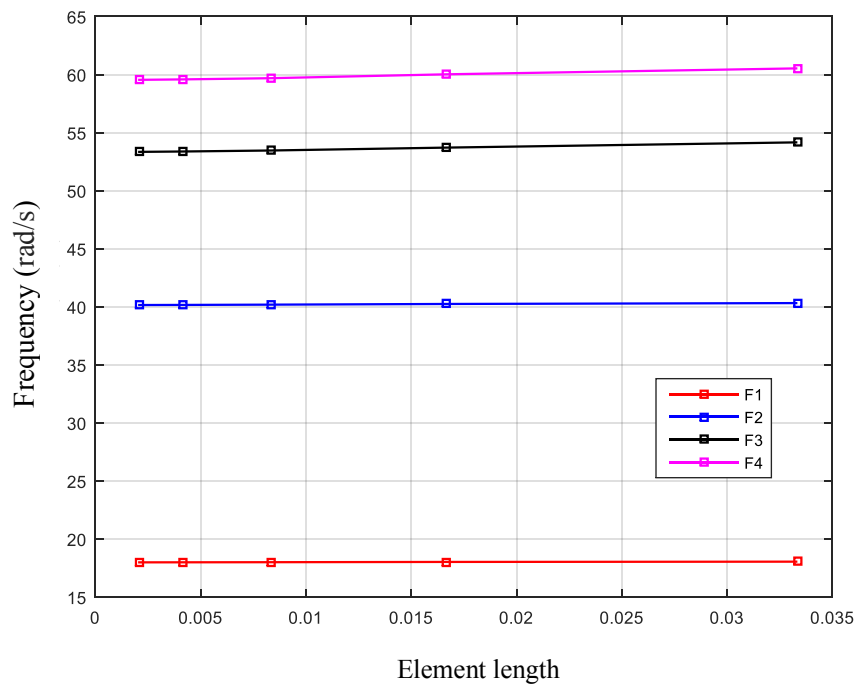
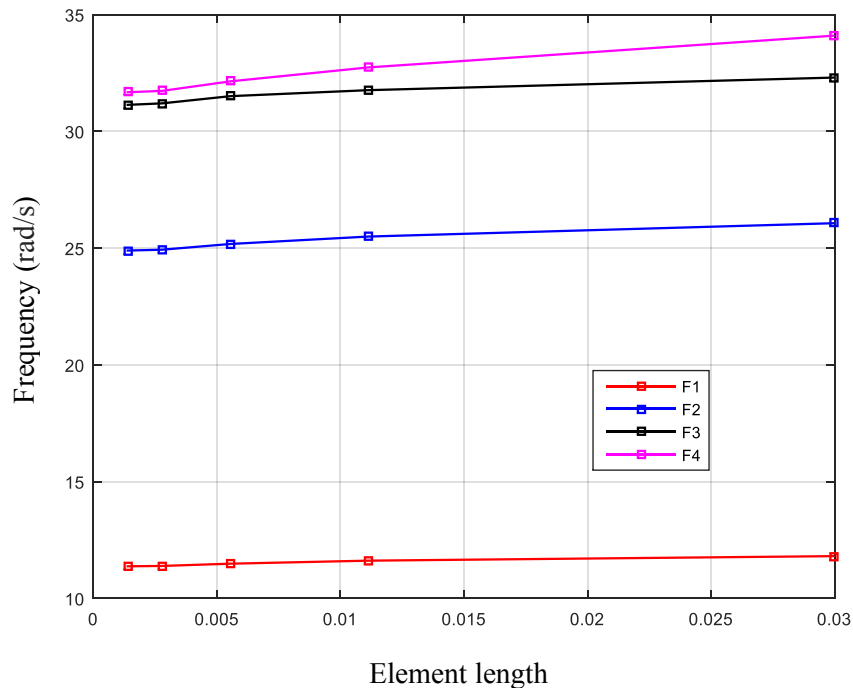Figure D-5. Meshes sizes study for ps geometry $\hat{E}_2$ using element type STRI3
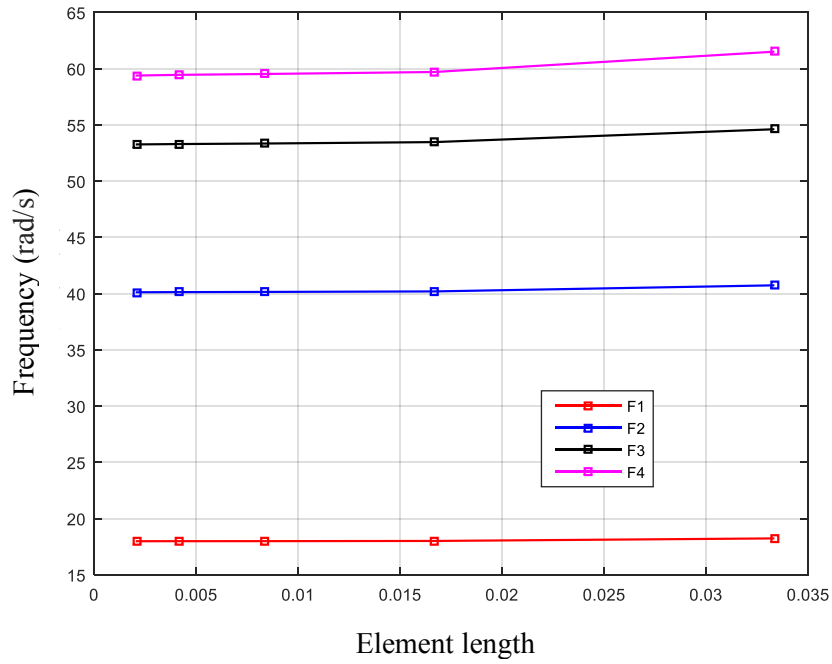
Figure D-6. Meshes sizes study for ps geometry $\hat{E}_2$ using element type STRI65
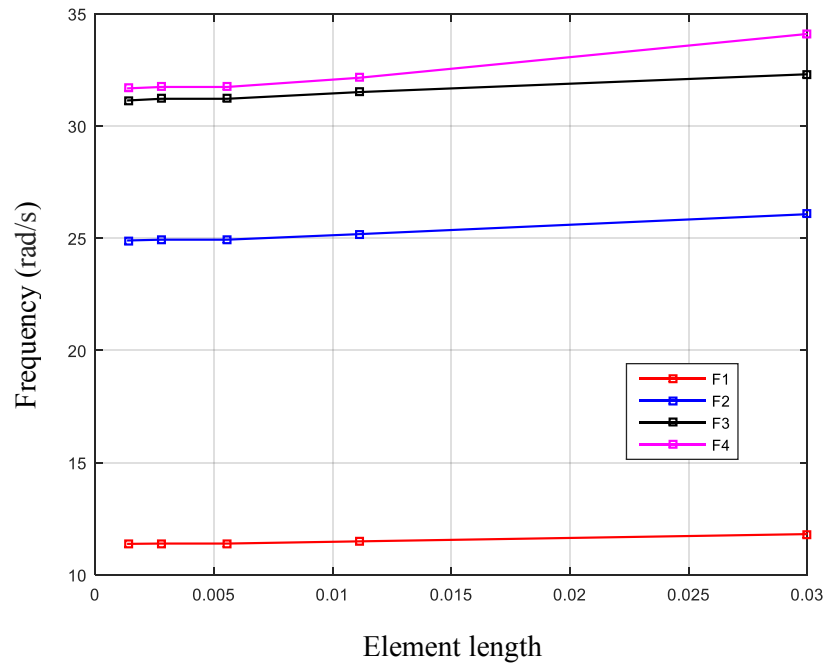
Figure D-7. Meshes sizes study for ps geometry $\hat{E}_3$ using element type S3

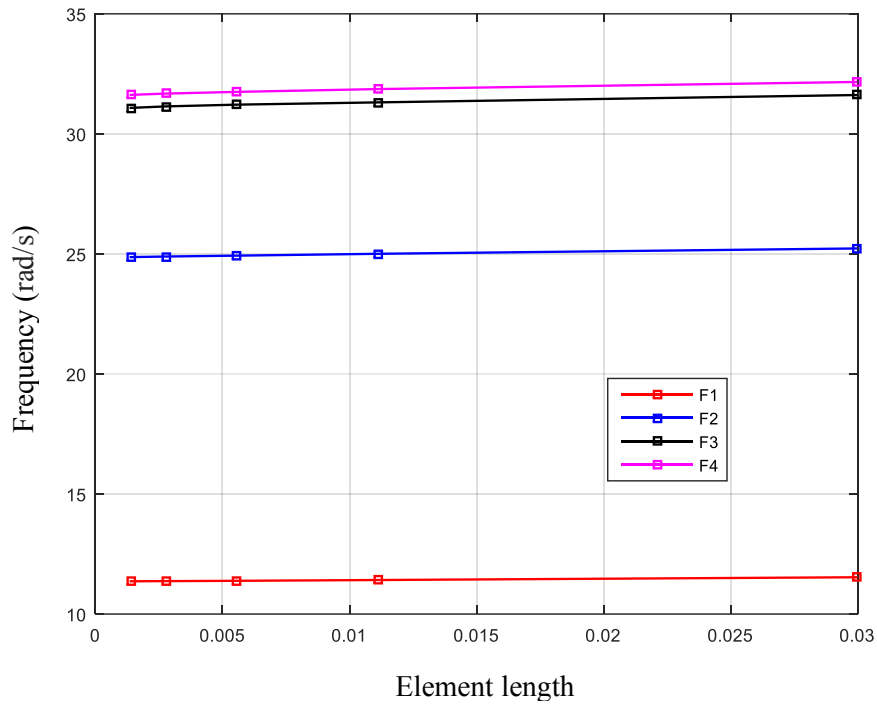Figure D-8. Meshes sizes study for ps geometry $\hat{E}_3$ using element type STRI3

Figure D-9. Meshes sizes study for ps geometry $\hat{E}_3$ using element type S3R

Figure D-10. Meshes sizes study for ps geometry $\hat{E}_3$ using element type STRI65

D.1.2. Thickness Sensitivity

It is necessary to understand the frequency tends when changing the thickness of the Vicsek pre-fractal. The frequency analysis for the first pre-fractal structure is found to increase while increasing the thickness of the structure this true for the all studied cases and for all the frequencies. The trends of the increase are a non-linear way (see Figure D-11-Figure D-13). Except in the higher cases such as when $k = 2$ and 3.
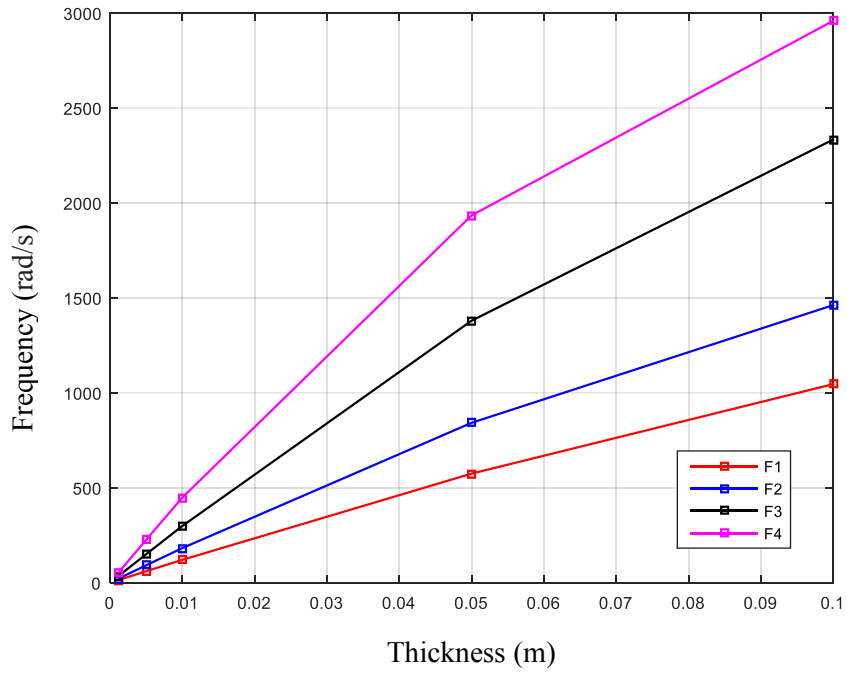
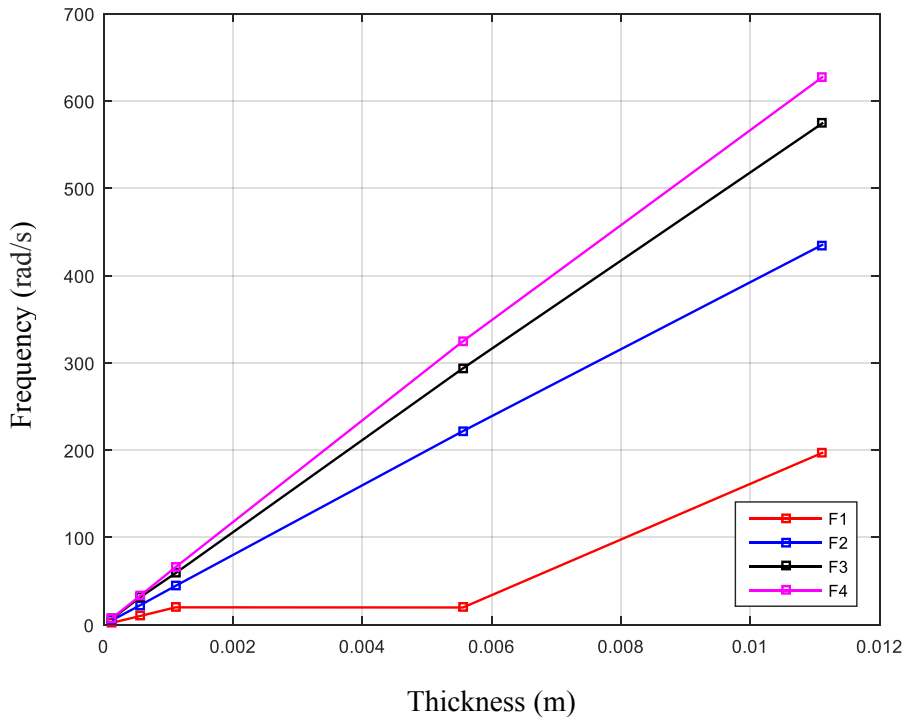Figure D-11. Structure thickness study for ps geometry $\hat{E}_1$

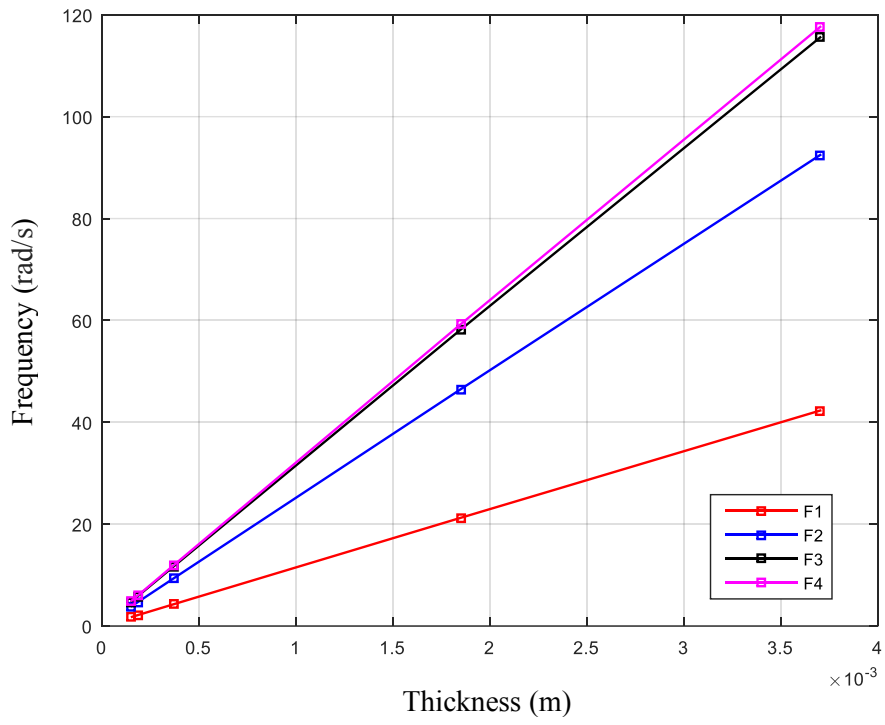Figure D-12. Structure thickness study for ps geometry $\hat{E}_2$

238

Figure D-13. Structure thickness study for pre-fractal geometry $\hat{E}_3$